Journal of Research of the National Bureau of Standards Vol. 46, No. 4, April 1951 Research Paper 2195

Analysis of Symmetrical Waveguide Junctions[1]

David M. Kerns

Previous theory of consequences of symmetry in waveguide junctions has made limited use of mathematical tools available in the theory of group representations and has been limited to the consideration of nondissipative junctions. In this paper group-theoretical technique is utilized more fully (in much the same way as in the analysis of the vibration of symmetrical molecules) in the formulation of an improved and general technique for the analysis of symmetrical waveguide junctions subject merely to the requirement of linearity.

A waveguide junction, for the purpose of this paper, is a linear electromagnetic system possessing ideal waveguide leads, and is considered to be subject to excitation solely through the effects of nonattenuated modes in the waveguide leads. Under the conditions of the problem, an arbitrary electric (or magnetic) field in a waveguide junction is expressible linearly in terms of a finite number of linearly independent electric (or magnetic) basis fields. From any given ordered pair of electric (or magnetic) basis fields one can in principle calculate a complex number—an element of the admittance (or impedance) matrix characterizing the junction (relative to the choice of basis fields). The geometric concept of rotation and reflection of fields (and structures) is discussed in terms of a rotation-reflection operator, and the symmetry of a junction is characterized by a group of rotation-reflection operations under which the structure is invariant. A general procedure is given for the construction of a basis in which the basis fields transform according to irreducible representations of the symmetry group involved. Such basis fields are said to be of particular symmetry species and from the special properties of such fields follow the physical results, of which perhaps the most conspicuous is the vanishing of the matrix element between two fields of distinct symmetry species.

I. Introduction

This paper is concerned with symmetry properties in "waveguide junctions." A waveguide junction, for the purpose of this paper, is a linear electromagnetic system possessing ideal waveguide leads and is considered to be subject to excitation solely through the effects of nonattenuated waveguide modes in the waveguide leads. The electromagnetic boundary-value problem presented by a waveguide junction is, in general, impracticably difficult to solve. Nevertheless, important information concerning the characteristics of a waveguide junction in its primary function as a device for transferring power from one waveguide-mode to another is derivable with relatively little labor from general properties, such as reciprocity, losslessness, and, in particular, symmetry. Many waveguide junctions used in microwave practice do in fact possess useful and interesting properties in virtue of symmetry. A few simple examples of such junctions are shown in figure 1.

The literature on the present subject is not extensive. The book, *Principles of microwave circuits*,[2] contains a valuable and fairly comprehensive treatment applying to nondissipative waveguide junctions. A report by Slater[3] is mainly concerned with the analysis of nondissipative T-junctions having essentially a single symmetry element. A paper by Chodorow, Ginzton, and Kane[4] deals with one particularly interesting junction, which is a waveguide analogue of a Wheastone-bridge network.

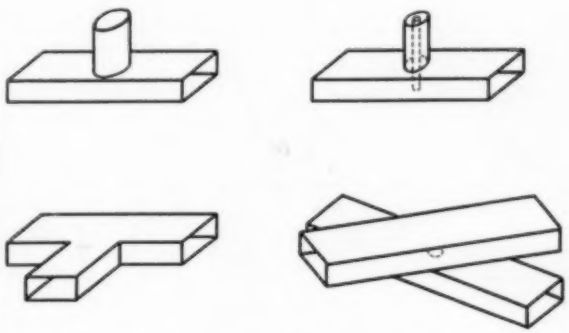

FIGURE 1. *Simple junctions possessing symmetry.*

There is to be found also the occasional and limited use of symmetry arguments in discussions primarily concerned with other matters.

The analytical technique employed in the book referred to in footnote 2 is partly formulated in general terms and partly indicated by the consideration of a series of examples. The technique used involves the restriction to nondissipative junctions as an explicit condition. The discussions contained in the papers referred to in footnotes 3 and 4 are of a more or less specific nature and, in the form given, are likewise subject to the restriction of no dissipation.

The object of the present paper is to develop a general theory of the consequences of symmetry in waveguide junctions of a general class: in the interior of a waveguide junction media that may be nonhomogeneous and anisotropic are permitted; dissipation, by reason of finite conductivity or radiation to infinity (or both), is permitted; fulfillment of the reciprocity condition is not required. Linear behavior and freedom from internal sources are as-

[1] A dissertation submitted to the faculty of the Graduate School of Arts and Sciences of the Catholic University of America in partial fulfillment of the requirements for the degree of Doctor of Philosophy.

[2] C. G. Montgomery, R. H. Dicke, and E. M. Purcell, Principles of microwave circuits, chapter 12 (McGraw-Hill Co., New York, N. Y., 1948).

[3] J. C. Slater, Technical Report No. 37, Electronics Research Lab., Mass. Inst. Tech. (Cambridge, Mass., 1947).

[4] M. Chodorow, E. L. Ginzton, and J. F. Kane, Proc. IRE **37**, 634 (1949).

sumed (the former being essential, the latter non-essential). A broad outline of the discussion follows.

The needed physical and mathematical formulation of the electromagnetic problem is given in section II. Under the conditions of the problem, an arbitrary electric (or magnetic) field in a waveguide junction is expressible linearly in terms of a finite number of linearly independent electric (or magnetic) basis fields. From any given ordered pair of basis fields of the same kind (electric or magnetic) one can in principle calculate a complex number—an element of the admittance (or impedance) matrix of the junction—which is a measure of the field of opposite kind associated with the second (or first) of the given pair of fields. The characterization of a junction by means of matrices is relative to the choice of basis fields; the basis fields first chosen might be described as "simple with respect to excitation." Formulas for change of basis are given.

The geometric concept of rotation and reflection of fields (and structures), taken up in section III, is discussed in terms of a rotation-reflection operator applicable to tensor point-functions.[5] The symmetry of a waveguide junction is characterized by a group of rotation-reflection operations under which the structure is invariant.

A method of symmetry analysis and the results obtained for the class of problems considered are presented in general terms in section IV (with some further results in appendix 2). The basis fields set up in section II do not necessarily exhibit particularly simple transformation properties under operations of the symmetry group; however, as is shown, it is possible to select linear combinations of the original basis fields to form new basis fields that do exhibit special transformation properties. Such fields are said to be of particular symmetry species. (If, for example, the symmetry group consists of only two operations, the identity and reflection in a plane, say, the two possible species are the familiar "even" and "odd." The general definition of symmetry species is provided by the theory of group representations, which theory indeed provides the natural mathematical tools for the analysis.) An important property of fields of the new basis is the vanishing of the matrix element between two fields of distinct symmetry species.

As might be expected, the method used here is in some respects very similar to methods used in the analysis of the vibration of symmetrical molecules. However, because dissipation (as well as failure of reciprocity) is permitted in the waveguide problem, the main part of the analysis here is formulated without reference to the question of eigenvalues of the matrices of a junction. The eigenvalue problem is discussed briefly in the latter part of section IV.

Three illustrative examples are considered in section V. In one of these examples the theoretical results previously obtained (footnote 4) for the waveguide Wheatstone bridge are presented in a more general context.

[5] *Tensor* is used in the general sense, a scalar being a tensor of rank 0, etc.

II. Electromagnetic Formulation

A waveguide junction may be described briefly as an electromagnetic system comprising an arbitrary number, n, of ideal waveguide "leads", which individually may be of arbitrary cross section, and a "coupling region" from which the waveguide leads emerge. Various aspects of the theory of waveguide junctions have been considered in recent years by a number of authors, and a considerable body of systematic theory[6 7 8] centering on the use of impedance, admittance and scattering matrices, has been built up. Nevertheless, for the purposes of this paper a formulation, which can be brief, but which is in some respects new and more complete, is needed. Part of the formulation will depend, of course, on certain rather well-known general results of the theory of waveguides (see footnotes 2 and 7).

The domain of the electromagnetic field in a waveguide junction will be denoted by V, the complete boundary of V will be denoted by S, and the inward normal unit vector on S will be denoted by $\boldsymbol{k}$. The surface S and also, in part, the boundary conditions to be imposed may be described (in two typical cases) as follows. If the domain is of infinite

FIGURE 2. *Slotted waveguide.*
Illustrating S_m, S_m' ($n=2$); S_∞ is not shown.

extent (fig. 2), V is bounded internally by n closed surfaces S_m+S_m' ($m=1, 2, \cdots, n$), where S_m is a transverse surface (the *terminal surface*) in the m^{th} waveguide and S_m, S_m' together enclose the termination of the m^{th} waveguide. Although V in this case is externally unbounded, it is convenient to employ a large spherical bounding surface S_∞ (of radius r), appropriate limiting processes being implied. The complete boundary of V is then $S=S_\infty+S_1+S_1'+\cdots+S_n+S_n'$. On all parts of S except the terminal surfaces, the field is to satisfy homogeneous boundary-conditions: on S_∞, lim $(r\boldsymbol{E})$ is bounded, and $\boldsymbol{E}$ satisfies the outward-radiation condition; on S_m', the tangential component $\boldsymbol{E}_t$ of $\boldsymbol{E}$ vanishes ($\boldsymbol{E}$ denoting the electric field). If the field is confined to a finite domain by a perfectly conducting metal surface (fig. 3), then $S=S_0+S_1+\cdots+S_n$, where S_0 coincides with the metal surface. In this case the homogeneous boundary condition is simply $\boldsymbol{E}_t=0$ on S_0. (If metal walls are considered finitely conducting, but are sufficiently thick, S_0 may be taken on the outer surface where $\boldsymbol{E}$, hence $\boldsymbol{E}_t$, is substantially zero.)

The whole of the space and structure within V can be regarded as a linear, source-free medium,

[6] See footnote 2.
[7] J. C. Slater, Rev. Mod. Phys. **18**, 441 (1946).
[8] D. M. Kerns, J. Research NBS **42**, 515 (1949). (The references cited are believed to be the ones most useful in connection with the present paper.)

which is in general nonhomogeneous and anisotropic. The conductivity and the electric and magnetic inductive capacities of the medium are to be given by the real point-functions $\sigma=\sigma(\boldsymbol{r})$, $\epsilon=\epsilon(\boldsymbol{r})$, $\mu=\mu(\boldsymbol{r})$, respectively. Anisotropy is taken into account by considering σ, ϵ, μ to be, in general, tensors of rank two.

The interior of the m^{th} waveguide lead is a cylindrical, source-free domain τ_m (of finite length) in which $\sigma\equiv 0$, μ, ϵ=scalar constants. τ_m is bounded by a cylindrical surface (also of finite length) on which the conductivity becomes infinite. The terminal surface S_m is a transverse section of τ_m; S_m

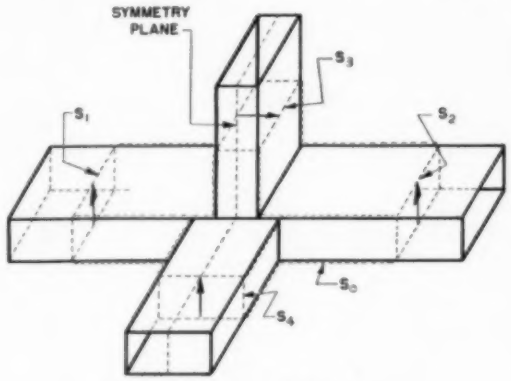

FIGURE 3. *Hybrid T-junction.*

Illustrating S_m and S_0 ($n=4$).

is to be a closed, connected (but not necessarily simply connected) plane surface bounded by a curve C_m (which may consist of one or more distinct parts). As the figures indicate, S_m is to be located within its waveguide lead at some distance from any discontinuity. (A portion of a waveguide lead may be included bodily within V, as in fig. 2; in any case the interior of a waveguide lead from the inner portion of the junction out to the terminal surface is an integral part of the domain V.)

Harmonic time-dependence, at angular frequency ω, is assumed; we shall deal with the complex electric and magnetic field (amplitudes) $\boldsymbol{E}=\boldsymbol{E}(\boldsymbol{r})$, $\boldsymbol{H}=\boldsymbol{H}(\boldsymbol{r})$, omitting the time-dependent factor $\exp(j\omega t)$. Within V, then, $\boldsymbol{E},\boldsymbol{H}$ satisfy Maxwell's equations in the form

$$\left.\begin{aligned}\nabla\times\boldsymbol{E}&=-j\omega\mu\cdot\boldsymbol{H},\\ \nabla\times\boldsymbol{H}&=(j\omega\epsilon+\sigma)\cdot\boldsymbol{E}.\end{aligned}\right\} \tag{1}$$

The rationalized meter-kilogram-second system of units is assumed.

Under the specified conditions holding on S and in V the electromagnetic field within V will be determined by the boundary conditions on the terminal surfaces. The ultimate sources of the field, which are to be found within the waveguide terminations (pictured in fig. 2, implied in other figures), are of interest only insofar as certain fields, of a single frequency ω, are caused to appear on the terminal surfaces. If, as is assumed, the terminal surface S_m is sufficiently far from any discontinuity (or any other departure from the conditions defining a waveguide lead), the contributions of attenuated waveguide modes to the field on S_m will be negligible. Thus only nonattenuated modes need be considered in describing the field on a terminal surface.[9] It is understood that the field of a single nonattenuated mode may and in general will involve both incident and emergent progressive components. Waveguide and frequency being given, the number ν_m of nonattenuated modes supported in the m^{th} waveguide is necessarily finite or zero; it is naturally assumed that $\nu_m \gtrless 1$. In general, *TEM*, *TM*, and *TE* modes will occur among the ν_m nonattenuated modes in waveguide m, but it will not be necessary to distinguish the several types of modes in the notation.

Of essential interest will be suitable expressions for the tangential (=transverse) components $\boldsymbol{E}_t,\boldsymbol{H}_t$ of the most general $\boldsymbol{E},\boldsymbol{H}$ on S_m consistent with the above conditions. Let the index μ ($\mu=1,2,\ \cdot\ \cdot\ \cdot,\ \nu_m$) identify the nonattenuated modes supported at frequency ω in waveguide m. From waveguide theory we know that $\boldsymbol{E}_t$ on S_m can be expressed in the form

$$\boldsymbol{E}(\boldsymbol{r}_m)_t=\sum_{\mu=1}^{\nu_m} v_{m\mu}\boldsymbol{e}^0_{m\mu}(\boldsymbol{r}_m), \qquad (\boldsymbol{r}_m \text{ on } S_m), \tag{2}$$

where $\boldsymbol{r}_m$ denotes $\boldsymbol{r}$ on S_m, the $v_{m\mu}$ are scalar coefficients, and the $\boldsymbol{e}^0_{m\mu}$ are derivable from eigenfunctions of certain two-dimensional boundary-value problems formulated for S_m and its perimeter C_m. The vector $\boldsymbol{e}^0_{m\mu}$, like $\boldsymbol{E}_t$, lies in the plane of S_m; $\boldsymbol{e}^0_{m\mu}$ is considered to be defined only for $\boldsymbol{r}$ on S_m. No coordinate-dependence is indicated for the $v_{m\mu}$ since S_m is considered to be in a fixed position in its waveguide lead. Similarly, $\boldsymbol{H}_t$ on S_m can be expanded in the form

$$\boldsymbol{H}(\boldsymbol{r}_m)_t=\sum_{\mu=1}^{\nu_m} i_{m\mu}\boldsymbol{h}^0_m(\boldsymbol{r}_m), \qquad (\boldsymbol{r}_m \text{ on } S_m); \tag{3}$$

here the $i_{m\mu}$ are scalar coefficients and the $\boldsymbol{h}^0_{m\mu}$ are defined by

$$\boldsymbol{h}^0_{m\mu}(\boldsymbol{r}_m)\equiv(\zeta_0\eta_{m\mu})\boldsymbol{k}_m\times\boldsymbol{e}^0_{m\mu}(\boldsymbol{r}_m), \tag{4}$$

where $\boldsymbol{k}_m$ denotes $\boldsymbol{k}$ on S_m, $\eta_{m\mu}$ is the wave-admittance of mode μ in waveguide m, and $\zeta_0=1$ ohm (see the following paragraph). The $\boldsymbol{e}^0_{m\mu}$ and the $\boldsymbol{h}^0_{m\mu}$ may be assumed to be real and to satisfy the orthogonality and normalization relation

$$\frac{1}{2}\int_{S_m}(\boldsymbol{e}^0_{m\mu}\times\boldsymbol{h}^0_{m\lambda})\cdot\boldsymbol{k}_m dS=\delta_{\mu\lambda}=\left\{\begin{matrix}1,\ \lambda=\mu\\ 0,\ \lambda\neq\mu\end{matrix}\right\}. \tag{5}$$

Equations 4 and 5 each represent combinations of what is necessary with what is convenient. In particular, eq 5 is automatically satisfied if modes μ,λ are not mutually degenerate or if one is a *TE* and the other a *TM* mode.

[9] Attenuated modes are excluded mainly because these higher-mode interactions are usually avoided in practice. The finiteness of the number of modes involved is the essential point so far as the subsequent analysis is concerned.

Clearly, $v_{m\mu}$ and $i_{m\mu}$ are respectively linear measures, relative to the *standard terminal fields* $\boldsymbol{e}^0_{m\mu}$ and $\boldsymbol{h}^0_{m\mu}$, of the contributions of mode μ to $\boldsymbol{E}_t$ and $\boldsymbol{H}_t$ on the terminal surface S_m. The variables $a_{m\mu}$, $b_{m\mu}$ defined by

$$2a_{m\mu}=v_{m\mu}+\zeta_0 i_{m\mu}, \qquad 2b_{m\mu}=v_{m\mu}-\zeta_0 i_{m\mu}, \tag{6}$$

will be employed to a very limited extent in this paper. $a_{m\mu}$ and $b_{m\mu}$ are respectively linear measures (relative to $\boldsymbol{e}^0_{m\mu}$) of the electric fields of the incident and emergent progressive components of mode μ at S_m. The second of eq 6 shows that if $b_{m\mu}=0$, then the corresponding value of $v_{m\mu}/i_{m\mu}$ (called the characteristic impedance of mode μ in waveguide m) is equal to ζ_0. So far as the present paper is concerned, ζ_0 may be considered to be primarily a dimensional constant inserted to bring about an attractive dimensional scheme. Indeed, from eq 4 and 5 one finds (considering $\delta_{\mu\kappa}$ and $\boldsymbol{k}_m$ to be dimensionless) $[\boldsymbol{e}^0_{m\mu}]=[\boldsymbol{h}^0_{m\mu}]=\text{meters}^{-1}$, and then from eq 2 and 3, $[v_{m\mu}]=$volts, $[i_{m\mu}]=$amperes.

It is appropriate to review the electromagnetic situation in the junction as a whole. For convenience let v and i denote the column matrices whose elements are respectively the N $v_{m\mu}$'s and the N $i_{m\mu}$'s, $N\equiv\nu_1+\nu_2+\cdots+\nu_n$. v uniquely determines and is uniquely determined by $\boldsymbol{E}_t$ on all the terminal surfaces; similarly, i determines and is determined by $\boldsymbol{H}_t$ on all the terminal surfaces. Now the specification of either $\boldsymbol{E}_t$ or $\boldsymbol{H}_t$ on all terminal surfaces (together with the homogeneous boundary condition holding elsewhere on S) is just sufficient to determine $\boldsymbol{E}$ and $\boldsymbol{H}$ throughout the domain V. Thus, if v is given, $\boldsymbol{E}$,$\boldsymbol{H}$, and i are determined; if i is given, $\boldsymbol{H}$,$\boldsymbol{E}$ and v are determined.[10] The existence of a homogeneous linear relation connecting v and i is implied. Moreover, there are (under the conditions of the problem) exactly N linearly independent electric fields possible in V; similarly, there are exactly N linearly independent magnetic fields possible in V. This fundamental property is expressed analytically in the following paragraph.

We define the *electric basis-field* $\boldsymbol{e}_{m\mu}$ as the electric field [11] in V corresponding to the special boundary condition implied by $v_{m\mu}=1$, $v_{l\lambda}=0$ $(l\lambda\neq m\mu)$. The connection, as well as the difference, between $\boldsymbol{e}_{m\mu}$ and $\boldsymbol{e}^0_{m\mu}$ is to be noted: $\boldsymbol{e}_{m\mu}$ is defined throughout V, its tangential component $(\boldsymbol{e}_{m\mu})_t$ reduces to $\boldsymbol{e}^0_{m\mu}$ on S_m, to zero on other terminal surfaces. From the boundary conditions it follows that the N $\boldsymbol{e}_{m\mu}$'s are linearly independent. The $\boldsymbol{E}$ in V corresponding to arbitrary v may be written

$$\boldsymbol{E}(\boldsymbol{r})=\sum_{m\mu}\boldsymbol{e}_{m\mu}(\boldsymbol{r})v_{m\mu}=\boldsymbol{e}v, \tag{7}$$

where $\boldsymbol{e}$ is the row matrix $\boldsymbol{e}=(\boldsymbol{e}_{11}\cdots\boldsymbol{e}_{m\mu}\cdots\boldsymbol{e}_{n\nu_n})$. Similarly, the *magnetic basis-field* $\boldsymbol{h}_{l\lambda}$ is defined as the magnetic field in V corresponding to the boundary condition $i_{l\lambda}=1$, $i_{k\kappa}=0$ $(k\kappa\neq l\lambda)$. The $\boldsymbol{H}$ in V corresponding to arbitrary i is then

$$\boldsymbol{H}(\boldsymbol{r})=\sum_{l\lambda}\boldsymbol{h}_{l\lambda}(\boldsymbol{r})i_{l\lambda}=\boldsymbol{h}i, \tag{8}$$

where $\boldsymbol{h}$ is the row matrix $\boldsymbol{h}=(\boldsymbol{h}_{11}\cdots\boldsymbol{h}_{l\lambda}\cdots\boldsymbol{h}_{n\nu_n})$. The possible $\boldsymbol{E}$'s and the possible $\boldsymbol{H}$'s are elements of linear vector spaces,[12] of dimension N. $\boldsymbol{E}$ has the *coordinates* v relative to the *basis* $\boldsymbol{e}$; $\boldsymbol{H}$ has the *coordinates* i relative to the *basis* $\boldsymbol{h}$. The particular basis fields introduced in eq 7 and 8 are the simplest ones to start out with; $\boldsymbol{e}$, $\boldsymbol{h}$, or both together will accordingly be called a primitive basis.

The usefulness of the following definition will become apparent. The *bracket* $[\boldsymbol{E}^1, \boldsymbol{H}^2]$ of any electric field $\boldsymbol{E}^1$ in V and any magnetic field $\boldsymbol{H}^2$ in V is defined by

$$[\boldsymbol{E}^1, \boldsymbol{H}^2]=\frac{1}{2}\sum_{m=1}^{n}\int_{S_m}(\boldsymbol{E}^1\times\overline{\boldsymbol{H}^2})\cdot\boldsymbol{k}_m dS, \tag{9}$$

where, as always in this paper, the superposed bar denotes the complex conjugate. It is to be emphasized that $\boldsymbol{E}^1$ and $\boldsymbol{H}^2$ are by no means necessarily associated electric and magnetic components of the same electromagnetic field. The most important algebraic property of the bracket is exemplified by

$$[(a\boldsymbol{E}^1+b\boldsymbol{E}^2), \boldsymbol{H}^3]=a[\boldsymbol{E}^1, \boldsymbol{H}^3]+b[\boldsymbol{E}^2, \boldsymbol{H}^3],$$

$$[\boldsymbol{E}^1, (c\boldsymbol{H}^2+d\boldsymbol{H}^3)]=[\boldsymbol{E}^1, \boldsymbol{H}^2]\overline{c}+[\boldsymbol{E}^1, \boldsymbol{H}^3]\overline{d},$$

where a, b, c, d are any constants. (There will be no need to define or use brackets of the type $[\boldsymbol{H}, \boldsymbol{E}]$.)

The orthonormalization of the standard terminal fields (as expressed in eq 5) has as an immediate consequence a corresponding property of the basis fields:

$$[\boldsymbol{e}_{m\mu}, \boldsymbol{h}_{l\lambda}]=\delta_{m\mu,\,l\lambda}, \tag{10}$$

where $\delta_{m\mu,\,l\lambda}=1$ for $m\mu=l\lambda$, $\delta_{m\mu,\,l\lambda}=0$ for $m\mu\neq l\lambda$. The coordinates (relative to the given basis) of arbitrary $\boldsymbol{E}$ and $\boldsymbol{H}$ in V may be defined by

$$[\boldsymbol{E}, \boldsymbol{h}_{l\lambda}]=v_{l\lambda}, \qquad [\boldsymbol{e}_{m\mu}, \boldsymbol{H}]=\overline{i}_{m\mu}, \tag{11}$$

for if $\boldsymbol{E}=\boldsymbol{e}v$ and $\boldsymbol{H}=\boldsymbol{h}i$, then, with the aid of eq 10, one finds that eq 11 do in fact yield $v_{l\lambda}$ and $\overline{i}_{m\mu}$. Let $\mathfrak{H}(\boldsymbol{e}_{l\lambda})$ denote the magnetic field associated with $\boldsymbol{e}_{l\lambda}$, and let $\mathfrak{E}(\boldsymbol{h}_{m\mu})$ denote the electric field associated with $\boldsymbol{h}_{m\mu}$ (so that $\nabla\times\boldsymbol{e}_{l\lambda}=-j\omega\mu\cdot\mathfrak{H}(\boldsymbol{e}_{l\lambda})$ and $\nabla\times\boldsymbol{h}_{m\mu}=(j\omega\epsilon+\sigma)\cdot\mathfrak{E}(\boldsymbol{h}_{m\mu})$). Replacing $\boldsymbol{E}$ and $\boldsymbol{H}$ in eq 11 by $\mathfrak{E}(\boldsymbol{h}_{m\mu})$ and $\mathfrak{H}(\boldsymbol{e}_{l\lambda})$, respectively, we write

$$[\mathfrak{E}(\boldsymbol{h}_{m\mu}), \boldsymbol{h}_{l\lambda}]=Z_{l\lambda,\,m\mu}, \qquad [\boldsymbol{e}_{m\mu}, \mathfrak{H}(\boldsymbol{e}_{l\lambda})]=\overline{Y}_{m\mu,\,l\lambda}, \tag{12}$$

thereby defining the N-dimensional square matrices Z and Y. (The first index-pair attached to the

[10] It may be assumed, with no appreciable loss of generality, that the electromagnetic field in V corresponding to arbitrarily prescribed v or i exists and is unique, and that $\boldsymbol{E}\equiv\boldsymbol{H}\equiv 0$ (throughout V) corresponds to $v=0$ or $i=0$. See paper in footnote 2, p. 134; also paper in footnote 8, p. 535.

[11] Possibly one might prefer to say that $\boldsymbol{e}_{m\mu}$ is a field of electric type inasmuch as the units of $\boldsymbol{e}_{m\mu}$ are those of $\boldsymbol{e}^0_{m\mu}$ and not those of $\boldsymbol{E}$.

[12] For the mathematical postulates defining such spaces, see, e. g., F. D. Murnaghan, Theory of group representations, p. 11 (Johns Hopkins Press, Baltimore, Md., 1938).

matrix element labels the row in both cases.) Now if $\boldsymbol{E}$ and $\boldsymbol{H}$ are associated ($\boldsymbol{E}=\mathfrak{E}(\boldsymbol{H})$, $\boldsymbol{H}=\mathfrak{H}(\boldsymbol{E})$), it is clear that

$$\boldsymbol{E}=\mathfrak{E}\left(\sum_{ka}\boldsymbol{h}_{ka}i_{ka}\right)=\sum_{ka}\mathfrak{E}(\boldsymbol{h}_{ka})\,i_{ka},$$

$$\boldsymbol{H}=\mathfrak{H}\left(\sum_{ka}\boldsymbol{e}_{ka}v_{ka}\right)=\sum_{ka}\mathfrak{H}(\boldsymbol{e}_{ka})\,v_{ka},$$

since $\mathfrak{E}$ and $\mathfrak{H}$ are linear functions of their arguments. By inserting these forms for $\boldsymbol{E}$ and $\boldsymbol{H}$ into eq 11 one finds

$$v_{l\lambda}=\sum_{ka}Z_{l\lambda,\,ka}i_{ka},\qquad \bar{i}_{m\mu}=\sum_{ka}\overline{Y}_{m\mu,\,ka}\bar{v}_{ka}. \tag{13}$$

Thus the coordinates of associated $\boldsymbol{E}$ and $\boldsymbol{H}$ are related by $v=Zi$ or, equivalently, by $i=Yv$. Z and Y are, respectively, the impedance and the admittance matrices (relative to the primitive basis) characteristic of the waveguide junction.

The bracket $[\boldsymbol{E},\boldsymbol{H}]$ of (associated) $\boldsymbol{E}$ and $\boldsymbol{H}$ is (directly from eq 9) the integral of the inward normal component of the complex Poynting's vector extended over the aggregate of the terminal surfaces. Thus the total (complex) power influx W across the terminal surface is

$$W=[\boldsymbol{E},\boldsymbol{H}]=\sum_{m\mu,l\lambda}v_{m\mu}[\boldsymbol{e}_{m\mu},\boldsymbol{h}_{l\lambda}]\,\bar{i}_{l\lambda}=i^{*}v. \tag{14}$$

Here and subsequently the star is used to denote the Hermitian conjugate (=transposed complex-conjugate) of a matrix. The additional expressions $W=i^{*}Zi=v^{*}Y^{*}v$ follow immediately from eq 13.

Consider the introduction of a new electric-field basis $\boldsymbol{e}'=(\boldsymbol{e}'_1\cdot\cdot\cdot\boldsymbol{e}'_N)$ related to the primitive basis $\boldsymbol{e}=(\boldsymbol{e}_{11}\cdot\cdot\cdot\boldsymbol{e}_{ns_n})$ by means of the linear transformation $\boldsymbol{e}'=\boldsymbol{e}\alpha$, where α is a unitary matrix ($\alpha^{*}=\alpha^{-1}$).[13] The postulate that eq 7, 14, 8 shall have invariant meaning determines the transformations of v, i, and $\boldsymbol{h}$ relative to that of $\boldsymbol{e}$. Namely, from

$$\boldsymbol{E}=\boldsymbol{e}v=\boldsymbol{e}'v', \tag{7}$$

$$W=i^{*}v=(i')^{*}v', \tag{14}$$

$$\boldsymbol{H}=\boldsymbol{h}i=\boldsymbol{h}'i', \tag{8}$$

and the given $\boldsymbol{e}'=\boldsymbol{e}\alpha$ one finds easily

$$\left.\begin{aligned}\boldsymbol{e}'&=\boldsymbol{e}\alpha, & v'&=\alpha^{-1}v,\\ \boldsymbol{h}'&=\boldsymbol{h}\alpha, & i'&=\alpha^{-1}i.\end{aligned}\right\} \tag{15}$$

And from eq 12

$$Z'=\alpha^{-1}Z\alpha,\qquad Y'=\alpha^{-1}Y\alpha. \tag{16}$$

(It should be noted that the formulas for $\boldsymbol{h}'$, i', Z', and Y' are written for unitary α and do not hold unless α is unitary.)

[13] Transformations with an arbitrary nonsingular α could be considered but will not be needed in this paper.

With the above provision for *change of basis* the electromagnetic formulation, as far as needed here, is essentially complete. It may be remarked that Z and Y can be regarded as metric tensors of the vector spaces of eq 7 and 8, respectively (the metric is not in general Hermitian, to be sure).[14] The scheme acquires additional meaning when it is recognized that for each bracket there is an expression involving volume integrals extended throughout the domain V (appendix, 1).

Although the discussion will relate primarily to Z, Y, and the corresponding basis fields, the results to be obtained for Z and Y will hold also for the scattering matrix S, which is defined as follows. Let

$$2a=v+\zeta_0 i,\qquad 2b=v-\zeta_0 i, \tag{17}$$

be the matrix form of eq 6. Then the scattering matrix furnishes the relation

$$b=Sa, \tag{18a}$$

and a simple calculation shows that

$$S=(Z-\zeta_0)(Z+\zeta_0)^{-1}, \tag{18b}$$

where ζ_0 is to be interpreted as a multiple of the N-dimensional unit matrix. Equations 17 and 18 will have invariant meaning under a change of basis provided

$$a'=\alpha^{-1}a,\qquad b'=\alpha^{-1}b,\qquad S'=\alpha^{-1}S\alpha. \tag{19}$$

The matrix ζ_0, which must transform like Z (from eq 17), is invariant under a unitary change of basis.

So far as the subsequent symmetry analysis is concerned, Z, Y, or S is an arbitrary nonsingular matrix subject only to the consequences of structural symmetry of the waveguide junction. (It may be understood that Z, Y, and S are such that the real part of W, $\mathrm{Re}(W)$, can not be negative, but this condition is not used in the analysis.) The following special conditions (of electrical origin) are of interest.

$$\left.\begin{aligned}&\text{I. The nondissipative condition } (\mathrm{Re}(W)\equiv 0)\text{: } Z, Y \text{ are skew-Hermitian; } S \text{ is unitary: } Z^{*}=-Z,\ Y^{*}=-Y,\ S^{*}=S^{-1}\\ &\text{II. The nonreactive condition } (\mathrm{Im}(W)\equiv 0)\text{: } Z, Y, S \text{ are Hermitian: e.g., } Z^{*}=Z.\\ &\text{III. The reciprocity condition: } Z, Y, S \text{ are symmetric: e.g., } Z_{m\mu,\,l\lambda}=Z_{l\lambda,\,m\mu}, \text{ or, in the matrix notation to be used, } \tilde{Z}=Z.\end{aligned}\right\} \tag{20}$$

These conditions may be incorporated, at will, after the main results have been obtained; of course, the more usual cases are III (alone) and the combination of III and I. The matrix conditions in I and II are

[14] For the mathematical postulates leading to a positive-definite Hermitian metric-tensor, see, e. g., Murnaghan, p. 17. To make connection with Murnaghan's notation, one may define

$$(\boldsymbol{E}^1|\boldsymbol{E}^2)=[\boldsymbol{E}^1,\mathfrak{H}(\boldsymbol{E}^2)]\text{(or }(\boldsymbol{H}^1|\boldsymbol{H}^2)=[\mathfrak{E}(\boldsymbol{H}^1),\boldsymbol{H}^2]).$$

invariant under transformations of the type needed, but the property $\tilde{Z}=Z$ is not (unless α is real).[15] In general $\tilde{Z}'$ is not simply equal to Z' but rather, from eq 16,

$$\tilde{Z}'=\tilde{\alpha}Z\tilde{\alpha}^{-1}=\tilde{\alpha}(\alpha Z'\alpha^{-1})\tilde{\alpha}^{-1}=(\tilde{\alpha}\alpha)Z'(\tilde{\alpha}\alpha)^{-1}. \quad (21)$$

Obviously Y' and S' are subject to the same condition when Y and S are symmetric.

III. The Rotation Operator; Symmetry Groups

The geometric concept of spatial rotation and reflection of a waveguide junction or of an electromagnetic field is represented and in fact analytically defined by certain transformations of the tensor point-functions involved (e. g., $\sigma(\boldsymbol{r})$, $\boldsymbol{e}_{mn}(\boldsymbol{r})$, $\boldsymbol{H}(\boldsymbol{r})$, etc.). These transformations are basic for what follows and will be set down presently. In the present context tensor components will be distinguished by the use of the letters x, y, z as indices, and a fixed, orthogonal three-dimensional basis is to be understood. The three unit vectors of such a basis plus an arbitrary origin O define a rectangular Cartesian coordinate-system Oxyz ($\boldsymbol{r}_x=x$).

For the present purpose the intrinsic geometric properties of a particular rotation are conveniently characterized by a tensor $\boldsymbol{R}$ (independent of $\boldsymbol{r}$) whose components R_{xy} are such that $R=(R_{xy})$ is a real orthogonal matrix. The determinant of R may be $+1$ or -1; a rotation (as the term is used here for convenience) may be termed proper or improper according as the determinant of R is $+1$ or -1.

As a preliminary to the complete expression of the desired transformation, we consider the transformation $\boldsymbol{F}(\boldsymbol{r})\to\boldsymbol{F}'(\boldsymbol{r})$ of a tensor $\boldsymbol{F}$ (of rank 0,1, or 2) furnished by

$$F'(\boldsymbol{r})=F(\boldsymbol{r}), \quad (22a)$$

$$F'_x(\boldsymbol{r})=\sum_y R_{xy}F_y(\boldsymbol{r}), \quad (22b)$$

or

$$F'_{xy}(\boldsymbol{r})=\sum_{\hat{x},\hat{y}} R_{x\hat{x}}R_{y\hat{y}}F_{\hat{x}\hat{y}}(\boldsymbol{r}). \quad (22c)$$

This may be called "local" rotation, inasmuch as the components of $\boldsymbol{F}'$ at the point $\boldsymbol{r}$ are related directly to those of $\boldsymbol{F}$ at the same point. It will be convenient to use the notation $\boldsymbol{r}'=\boldsymbol{R}\boldsymbol{r}$ for eq 22b when $\boldsymbol{F}(\boldsymbol{r})=\boldsymbol{r}$.

It may be noted that in electromagnetic theory it is customary (perhaps invariably so) to consider electric charge a scalar, thereby determining $\boldsymbol{E}$ as a vector and $\boldsymbol{H}$ as a pseudovector. Since a pseudovector is a (antisymmetric) tensor of rank two, eq 22c applies; but in terms of the usual pseudovectorial components, say H_x of $\boldsymbol{H}$, eq 22c becomes

$$H'_x(\boldsymbol{r})=\det(R)\sum_y R_{xy}H_y(\boldsymbol{r}), \quad (23)$$

where $\det(R)$ is the determinant of R. It is well to note also that in the present framework $\boldsymbol{E}\times\boldsymbol{H}$ is a vector and $\boldsymbol{E}\times\boldsymbol{H}\cdot\boldsymbol{k}$ is a scalar.

By combining a local rotation and a suitably related functional transformation, which may be called "parallel transport", we obtain the transformation to be termed *rotation of a tensor field* (or, briefly, rotation). In the sense of this term, the rotation corresponding to $\boldsymbol{R}$ applied to the tensor point-function $\boldsymbol{F}$ produces a new tensor point-function, to be denoted by $P_R\boldsymbol{F}$, whose components at the point $\boldsymbol{r}'=\boldsymbol{R}\boldsymbol{r}$ are equal respectively to those of the locally rotated $\boldsymbol{F}$ at the point $\boldsymbol{r}$. Thus, for all $\boldsymbol{r}$ in the domain V of definition of $\boldsymbol{F}$,

$$P_RF(\boldsymbol{r}')=F(\boldsymbol{r}), \quad (24a)$$[16]

$$[P_R\boldsymbol{F}(\boldsymbol{r}')]_x=\sum_y R_{xy}F_y(\boldsymbol{r}), \quad (24b)$$

$$[P_R\boldsymbol{F}(\boldsymbol{r}')]_{xy}=\sum_{\hat{x},\hat{y}} R_{x\hat{x}}R_{y\hat{y}}F_{\hat{x}\hat{y}}(\boldsymbol{r}). \quad (24c)$$

$P_R\boldsymbol{F}$ is defined in the rotated domain conveniently denoted by P_RV, P_RV being such that $\boldsymbol{r}'$ is in P_RV if $\boldsymbol{r}$ is in V. It should be observed that the meaning of a rotation depends upon the location of the origin O of Oxyz (at which point $\boldsymbol{F}$ undergoes only local rotation). By what amounts to a change in the designation of the independent variable, one may write, say for eq 24b,

$$[P_R\boldsymbol{F}(\boldsymbol{r})]_x=\sum_y R_{xy}F_y(\boldsymbol{R}^{-1}\boldsymbol{r}), \quad (25)$$

which holds for $\boldsymbol{r}$ in P_RV. In the later applications of eq 24 it will in fact generally be convenient to have $\boldsymbol{r}$ as the argument of $P_R\boldsymbol{F}$.

The analytical construction of eq 24 belies the simplicity of the underlying geometric picture: for proper rotations, at least, the transformation defines what might be described as a rigid motion (in which one point is fixed) of a tensor field; and for scalars and vectors, at least, the transformation is easily visualized. (Simple illustrations are given in fig. 4 and in connection with example A; section V.)

We impart operational meaning to the symbol P_R by saying that it stands for the operation (local rotation plus parallel transport) by which the function $P_R\boldsymbol{F}$ is produced from the function $\boldsymbol{F}$. It is convenient to describe the properties of the transformations 24 by describing the properties of P_R.

The properties of P_R to be listed now are all rather evident from the geometric picture corresponding to eq 24 and to some extent from eq 24 themselves. No proofs will be needed here. (a) P_R is linear:

$$P_R(c\boldsymbol{F}+d\boldsymbol{G})=cP_R\boldsymbol{F}+dP_R\boldsymbol{G},$$

[15] The fact that reciprocity is manifested in $\tilde{Z}=Z$ (in the primitive basis) depends upon the fact that the standard terminal fields are (by hypothesis) real.

[16] Equation 24a essentially reproduces Wigner's definition; eq 24b,c give the generalization needed here. E. Wigner, Gruppentheorie und ihre Anwendung auf die Quantenmechanik der Atomspektren, p. 113 (Vieweg and Sohn, Braunschweig, 1931).

where c, d are scalar constants and $\boldsymbol{F}$, $\boldsymbol{G}$ are tensors. (b) P_R is distributive with respect to tensor products in that

$$P_R(\boldsymbol{FG})=(P_R\boldsymbol{F})(P_R\boldsymbol{G}), \tag{26}$$

where on both sides the same type of tensor product is implied (e. g., $\mu\cdot\boldsymbol{H}, \boldsymbol{E}\times\bar{\boldsymbol{H}}$). (c) If the product

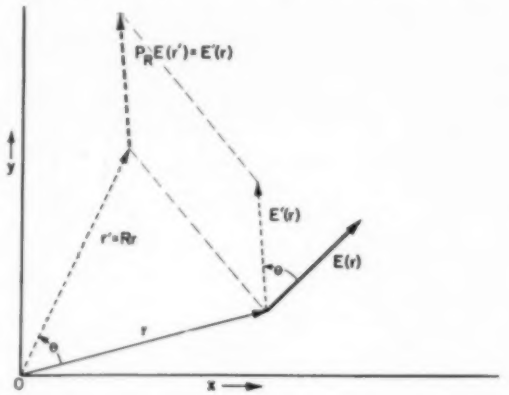

FIGURE 4. *Proper rotation of a vector.*

$\boldsymbol{FG}$ is a scalar (e. g., $\boldsymbol{F}=\boldsymbol{E}\cdot\sigma$, $\boldsymbol{G}=\bar{\boldsymbol{E}}, \boldsymbol{FG}=\boldsymbol{E}\cdot\sigma\cdot\bar{\boldsymbol{E}}$) then

$$\int_V \boldsymbol{FG}\,dV=\int_{P_RV}(P_R\boldsymbol{F})\,(P_R\boldsymbol{G})dV, \tag{27}$$

and in this sense P_R is unitary. The same property obviously holds also for surface integrals. (d) The identities

$$\left.\begin{aligned}\nabla_r[P_Rf(\boldsymbol{r})]&=P_R[\nabla_rf(\boldsymbol{r})],\\ \nabla_r\cdot[P_R\boldsymbol{E}(\boldsymbol{r})]&=P_R[\nabla_r\cdot\boldsymbol{E}(\boldsymbol{r})],\\ \nabla_r\times[P_R\boldsymbol{E}(\boldsymbol{r})]&=P_R[\nabla_r\times\boldsymbol{E}(\boldsymbol{r})],\end{aligned}\right\} \tag{28}$$

in which the subscript r denotes differentiations with respect to $\boldsymbol{r}$, lead to the statement that P_R commutes with the ∇-operations.

The *product* P_SP_R (of P_R *followed* by P_S) is defined by $(P_SP_R)\boldsymbol{F}\equiv P_S(P_R\boldsymbol{F})$ for arbitrary $\boldsymbol{F}$, where $P_S(P_R\boldsymbol{F})$ denotes the function produced from $\boldsymbol{F}$ by first applying P_R to $\boldsymbol{F}$ and then P_S to $P_R\boldsymbol{F}$. The product of two P-operations is itself a P-operation and in fact $P_SP_R=P_{SR}$, where the matrix representing $\boldsymbol{SR}$ is the matrix product SR. It is worth while to verify this multiplication law, say in the vector case. Letting $\boldsymbol{r}''=\boldsymbol{Sr}'=\boldsymbol{SRr}$ and thrice using eq 24b, one may write

$$\begin{aligned}\{P_S[P_R\boldsymbol{F}(\boldsymbol{r}'')]\}_x&=\sum_y S_{xy}[P_R\boldsymbol{F}(\boldsymbol{r}')]_y\\ &=\sum_{y,z}S_{xy}R_{yz}F_z(\boldsymbol{r})\\ &=\sum_z(SR)_{xz}F_z(\boldsymbol{r})=[P_{SR}\boldsymbol{F}(\boldsymbol{r}'')]_x.\end{aligned}$$

The equality of the first and last members, holding identically in $\boldsymbol{r}''$ for an arbitrary vector function[9] $\boldsymbol{F}$, shows in the vector case that P_SP_R as defined is equal to P_{SR}. Since the collection $\{R\}$ of all three-dimensional real orthogonal matrices, upon matrix multiplication, constitutes a group, it is clear that the collection $\{P_R\}$ of all rotations of a given tensor function, upon multiplication as defined, also constitutes a group; $\{R\}$ and $\{P_R\}$ are abstractly identical and may be identified as the three-dimensional rotation-reflection group. The groups of interest in the present discussion are subgroups [17] of this group, as will become clear from the content of the next few paragraphs.

A tensor function $\boldsymbol{F}$ will be said to be *invariant* with respect to the rotation P_R (in which O is a fixed point) if

$$P_R\boldsymbol{F}(\boldsymbol{r})=\boldsymbol{F}(\boldsymbol{r}), \tag{29}$$

for all $\boldsymbol{r}$ in the domain V of definition of $\boldsymbol{F}$. (For this equation to hold it is necessary that $P_RV=V$.) When eq 29 holds, P_R will be said to be a *covering operation of* $\boldsymbol{F}$.

For any choice of O, the corresponding set of covering operations $P_Q, P_R, P_S, \cdots$ of a given function constitutes a group. For, associative multiplication is defined within the set: $(P_RP_S)\boldsymbol{F}=P_R(P_S\boldsymbol{F})=P_R\boldsymbol{F}=\boldsymbol{F}$; moreover, the set contains the identity operation P_I (obviously) and the inverse of each of its operations: $P_S^{-1}\boldsymbol{F}=P_S^{-1}P_S\boldsymbol{F}=\boldsymbol{F}$. It may happen, of course, that a group of covering operations actually consists only of the single element P_I; this trivial case is obviously of no interest in what follows.

It may be recalled that the structure of a waveguide junction is described by three functions, $\sigma(\boldsymbol{r})$, $\mu(\boldsymbol{r})$, $\epsilon(\boldsymbol{r})$, which are in general tensors of rank two, defined in a region V. If σ,μ,ϵ are invariant with respect to P_R, we say that the structure is invariant with respect to P_R and that P_R is a covering operation of the structure. For any choice of O, the set of covering operations of a given structure will evidently be a group. If O is chosen so as to make the group of covering operations as large as possible, then this group may be said to characterize the symmetry of the structure and be called the symmetry group of the structure.[18] The symbol $\{P_R\}$, used above for the three-dimensional rotation-reflection group, will be used also for symmetry groups.

IV. Symmetry Analysis

Consider a waveguide junction having the symmetry group $\{P_R\}$, and let $\boldsymbol{E}$, $\boldsymbol{H}$ satisfy

$$\left.\begin{aligned}\nabla\times\boldsymbol{E}&=-j\omega\mu\cdot\boldsymbol{H}\\ \nabla\times\boldsymbol{H}&=(j\omega\epsilon+\sigma)\cdot\boldsymbol{E}\end{aligned}\right\}\text{in } V, \qquad \boldsymbol{E}_t=\boldsymbol{F}\text{ on } S, \tag{30}$$

[17] For a discussion of these groups, see, e. g., J. Rosenthal and G. M. Murphy, Rev. Mod. Phys. **8**, 317 (1936).

[18] If μ,ϵ are scalar constants and $\sigma\equiv O$ in V, then the necessary condition $P_RV=V$ contained in eq 29 becomes also sufficient and the symmetry group will be determined by V. In this way the present formulation includes cases in which symmetry is determined by geometrical figure alone.

where the vector function $\boldsymbol{F}$, defined on the complete boundary S of V, denotes in a unified notation any prescribed set of electric fields on the terminal surfaces and the homogeneous boundary condition holding on all other parts of S. Let the whole system—structure and field—be subjected, in imagination, at least, to the (proper or improper) rotation in space corresponding to P_R. One obtains an analytical description of the resulting situation by applying P_R to V, to S, and to both sides of each of the three equations above.

$$\left.\begin{aligned}\nabla\times(P_R\boldsymbol{E})&=-j\omega(P_R\mu)\cdot P_R\boldsymbol{H}\\ \nabla\times(P_R\boldsymbol{H})&=(j\omega P_R\epsilon+P_R\sigma)\cdot P_R\boldsymbol{E}\end{aligned}\right\}\text{in } P_RV,$$

$$P_R(\boldsymbol{E}_t)=P_R\boldsymbol{F} \text{ on } P_RS. \tag{31}$$

These equations hold formally whether or not the structure is invariant with respect to P_R; indeed, if P_R is a proper rotation, the configuration of the system relative to itself is in no way altered. However, the structure is by hypothesis invariant, so that eq 31 is equivalent to

$$\left.\begin{aligned}\nabla\times(P_R\boldsymbol{E})&=-j\omega\mu\cdot P_R\boldsymbol{H}\\ \nabla\times(P_R\boldsymbol{H}&=(j\omega\epsilon+\sigma)\cdot P_R\boldsymbol{E}\end{aligned}\right\}\text{in } V, \quad (P_R\boldsymbol{E})_t=P_R\boldsymbol{F} \text{ on } S. \tag{32}$$

The differential equations here are the same as those in eq 30; that is to say, the macroscopic Maxwell's equations of the problem are invariant with respect to P_R. The field $P_R\boldsymbol{E}$, $P_R\boldsymbol{H}$ appearing in eq 32, although closely related to the original $\boldsymbol{E}$, $\boldsymbol{H}$, is nevertheless a new field relative to the fixed axes Oxyz; and since the rotated structure is indistinguishable from the nonrotated one, $P_R\boldsymbol{E}$, $P_R\boldsymbol{H}$ may be counted as a new field relative to the structure. One may, of course, consider that only the field, and not the structure, is rotated.[19] The essential observations to be made here are: (a) If $\boldsymbol{E}$, $\boldsymbol{H}$ is a possible field in V, so also is $P_R\boldsymbol{E}$, $P_R\boldsymbol{H}$ (so that the vector spaces of eq 7, 8 are closed with respect to symmetry operations), (b) $P_R\boldsymbol{E}$, $P_R\boldsymbol{H}$ is essentially determined by the transformed terminal fields prescribed in eq 32, since the stated boundary conditions holding on all parts of S other than the terminal surfaces are not affected by P_R.

It follows from (a) above that the set of electric fields coinciding initially with the primitive basis $\boldsymbol{e}$ spans a representation of the symmetry group $\{P_R\}$. Namely, since $\boldsymbol{e}_{m\mu}$ is a possible electric field, $P_R\boldsymbol{e}_{m\mu}$ is also a possible electric field, and so $P_R\boldsymbol{e}_{m\mu}$ is expressible as a linear combination of primitive electric fields:

$$P_R\boldsymbol{e}_{m\mu}(\boldsymbol{r})=\sum_{l\lambda}\boldsymbol{e}_{l\lambda}(\boldsymbol{r})D(R)_{l\lambda,\,m\mu}. \tag{33}$$

(This equation is not to be regarded as defining a change of basis; the coefficient $D(R)_{l\lambda,\,m\mu}$ is to be regarded as a tensor component defined relative to the basis $\boldsymbol{e}$ of the N-dimensional vector space introduced in section II.) We take $D(R)_{l\lambda,\,m\mu}$ as the element in the $(l\lambda)^{\text{th}}$ row and the $(m\mu)^{\text{th}}$ column of an $N\times N$ matrix $D(R)$. These matrices constitute a representation of $\{P_R\}$. For, calculation of

$$\begin{aligned}P_Q(P_R\boldsymbol{e}_{m\mu})&=\sum_{l\lambda}(P_Q\boldsymbol{e}_{l\lambda})D(R)_{l\lambda,\,m\mu}\\ &=\sum_{l\lambda,\,k\kappa}\boldsymbol{e}_{k\kappa}D(Q)_{k\kappa,\,l\lambda}D(R)_{l\lambda,\,m\mu}\\ &=\sum_{k\kappa}\boldsymbol{e}_{k\kappa}[D(Q)D(R)]_{k\kappa,\,m\mu},\end{aligned}$$

and comparison of this result with

$$(P_Q\,P_R)\boldsymbol{e}_{m\mu}=\sum_{k\kappa}\boldsymbol{e}_{k\kappa}D(QR)_{k\kappa,\,m\mu},$$

shows that the matrix associated with the product P_QP_R is in fact the product, in the proper order, of the matrices individually associated with P_Q and P_R.

To determine further essential properties of $D(R)$ we utilize observation (b) above and consider the transformation of the terminal-surface boundary conditions that define $\boldsymbol{e}_{m\mu}$. Upon transformation by P_R, the standard terminal-field $\boldsymbol{e}^0_{m\mu}$, defined on terminal surface S_m in waveguide m, goes over into the field $P_R\boldsymbol{e}^0_{m\mu}$ defined on (and tangential to) the terminal surface in an equivalent waveguide whose index may be denoted by $R(m)$. $P_R\boldsymbol{e}^0_{m\mu}$ must accordingly be expressible linearly in terms of the standard terminal fields in waveguide $R(m)$. Thus, letting $R(m)=k$ to simplify the typography,

$$P_R\boldsymbol{e}^0_{m\mu}(\boldsymbol{r}_k)=\sum_{\kappa=1}^{\nu_k}\boldsymbol{e}^0_{k\kappa}(\boldsymbol{r}_k)D(R)_{k\kappa,\,m\mu}, \qquad (\boldsymbol{r}_k \text{ on } S_k). \tag{34}$$

Since the tangential components of $P_R\boldsymbol{e}_{m\mu}$ are zero on terminal surfaces other than S_k, eq 34 determines $P_R\boldsymbol{e}_{m\mu}$. Hence $D(R)_{l\lambda,\,m\mu}=0$, $l\neq R(m)$; also, since the standard terminal-fields are real, $D(R)$ must be real. The nonvanishing elements of $D(R)$ can be presented in a set of n submatrices $D(R)_{k,\,m}$ ($D(R)_{k,\,m}$ is square and of dimension ν_m). The arrangement of these submatrices within $D(R)$ is in accordance with the scheme of permutation, $m\rightarrow R(m)$, of terminal fields among equivalent waveguides. (In example A, section V, the permutation $1\rightarrow2$, $2\rightarrow1$, $3\rightarrow3$, $4\rightarrow4$ for $n=4$ occurs.) Thinking primarily of the general case $\nu_m>1$, but not excluding $\nu_m=1$, we determine the nature of the submatrices in the following manner. For the moment let two modes (in the same or in equivalent waveguides) be termed equivalent if they have equal wave-admittances, so that equivalent modes are not only "degenerate" but also of the same kind (*TE*, *TM*, or *TEM*). It is clear that the right-hand side of eq 34 can involve only modes equivalent to the μ^{th} mode in the m^{th} waveguide. Hence (assuming suitable ordering of mode indices) the nonvanishing elements of $D(R)_{k,\,m}$ will appear in smaller square

[19] This point of view is helpful in fixing the significance of the waveguide index $m(m=1,2,\cdots n)$, which is to be understood to identify a waveguide lead in a fixed spatial location.

submatrices ("steps") lying on the main diagonal of $D(R)_{k,m}$. Each step relates equivalent modes and is itself a real unitary (=real orthogonal) matrix. For, considering any two equivalent modes μ,μ' (distinct or not), one finds with the aid of eq 4, 5, 27, and 34,

$$\delta_{\mu\mu'}=(\zeta_0\eta_{m\mu})\int_{S_m}\boldsymbol{e}^0_{m\mu}\cdot\boldsymbol{e}^0_{m\mu'}\,dS$$

$$=(\zeta_0\eta_{m\mu})\int_{S_k}(P_R\boldsymbol{e}^0_{m\mu})\cdot(P_R\boldsymbol{e}^0_{m\mu'})\,dS$$

$$=\sum_{\kappa,\kappa'}\delta_{\kappa\kappa'}D(R)_{k\kappa,\,m\mu}D(R)_{k\kappa',\,m\mu'}=\sum_{\kappa}D(R)_{k\kappa,\,m\mu}D(R)_{k\kappa,\,m\mu'},$$

where $k=R(m)$, and $\eta_{m\mu}$ is the common value of the wave-admittances of the modes involved. Thus each step, hence each $D(R)_{k,m}$, hence $D(R)$ itself, is a real unitary matrix.

Parenthetically it may be noted that even if ν_m is large the dimension of an individual step ordinarily will not exceed two or three. (It can be shown that the highest symmetry degeneracy of waveguide modes is two-fold.) Of course, $\nu_m=1$ frequently occurs in actual problems; the submatrix $D(R)_{k,m}$ then consists of a single one-dimensional step and is necessarily equal to ±1.

The magnetic fields of the basis $\boldsymbol{h}$ transform under rotation according to the same group-representation as do the electric fields of the basis $\boldsymbol{e}$. Perhaps the most easily visualized proof of this is the following. From eq 34 and 4 one may obtain

$$P_R[\boldsymbol{h}^0_{m\mu}(\boldsymbol{r}_k)\times\boldsymbol{k}_m]=[\sum_{\kappa}\boldsymbol{h}^0_{k\kappa}(\boldsymbol{r}_k)D(R)_{k\kappa,\,m\mu}]\times\boldsymbol{k}_k,$$

$$(\boldsymbol{r}_k \text{ on } S_k;\ k=R(m))$$

where, again, the wave-admittances drop out. The left-hand side may be replaced by $[P_R\boldsymbol{h}^0_{m\mu}(\boldsymbol{r}_k)]\times\boldsymbol{k}_k$ (cf eq 26); and since the fields are transverse, $\boldsymbol{k}_k$ may be canceled from the resulting equation. Thus one obtains for the tangential component of $P_R\boldsymbol{h}_{m\mu}$ on S_k

$$P_R\boldsymbol{h}^0_{m\mu}(\boldsymbol{r}_k)=\sum_{\kappa}\boldsymbol{h}^0_{k\kappa}(\boldsymbol{r}_k)D(R)_{k\kappa,\,m\mu},$$

$$(\boldsymbol{r}_k \text{ on } S_k;\ k=R(m)). \quad (35)$$

Since the tangential components of $P_R\boldsymbol{h}_{m\mu}$ vanish on terminal surfaces other than S_k, eq 35 implies

$$P_R\boldsymbol{h}_{m\mu}(\boldsymbol{r})=\sum_{l\lambda}\boldsymbol{h}_{l\lambda}(\boldsymbol{r})D(R)_{l\lambda,\,m\mu},\qquad(\boldsymbol{r}\text{ in }V),\quad(36)$$

where $D(R)_{l\lambda,\,m\mu}=0$, $l\neq R(m)$, as above. In view of eq 34 and 35 it is clear that to determine $D(R)$ in a concrete case one may consider the transformation of either the electric or the magnetic standard terminal-fields. If the magnetic terminal-fields are considered, it should not be forgotten that they are pseudovectorial.

The transformation of an arbitrary electromagnetic state upon rotation by P_R is obviously determined by eq 33, 36 and is conveniently presented in matrix form. In matrix notation eq 33 and 36 become

$$P_R\boldsymbol{e}=\boldsymbol{e}D(R),\qquad P_R\boldsymbol{h}=\boldsymbol{h}D(R),\qquad(37)$$

where $P_R\boldsymbol{e}$ is interpreted simply as $(P_R\boldsymbol{e}_{11}\cdots P_R\boldsymbol{e}_{m\mu}\cdots P_R\boldsymbol{e}_{n\nu_n})$; $P_R\boldsymbol{h}$, similarly. For $\boldsymbol{E}=\boldsymbol{e}v$ and $\boldsymbol{H}=\boldsymbol{h}i$, then,

$$P_R\boldsymbol{E}=\boldsymbol{e}D(R)v=\boldsymbol{e}v_R,\qquad P_R\boldsymbol{H}=\boldsymbol{h}D(R)i=\boldsymbol{h}i_R,$$

where, by definition, $D(R)v=v_R$, $D(R)i=i_R$. That is to say, if $\boldsymbol{E}$ has the coordinates v relative to $\boldsymbol{e}$ as basis, then $P_R\boldsymbol{E}$ has the coordinates v_R relative to the same basis; similarly for $\boldsymbol{H}$. The interpretation of P_R as a matrix operator, defined with respect to v and i (which represent electromagnetic states) as operands, is immediate:

$$P_Rv\equiv D(R)v=v_R,\qquad P_Ri\equiv D(R)i=i_R.\quad(38)$$

The matrices $D(R)$ are, of course, basis-dependent. A unitary change of basis induces the similarity transformation

$$D(R)\rightarrow D'(R)=\alpha^{-1}D(R)\alpha,\qquad(39)$$

as is readily verified with aid of eq 15 and (choosing one of several possibilities) eq 37. The essential practical problem in symmetry analysis, briefly stated, is to find a basis—that is, to find a transforming matrix α—such that the representation D (of the symmetry group involved) whose matrices are $D(R)$ will be reduced-out [20] by the transformation 39. Such a basis, in which the matrices $D'(R)$ of the representation D' appear in reduced-out form, will be termed a *symmetry basis* and the corresponding coordinates, *symmetry coordinates*. The principal items to be considered in the remainder of the analysis are the construction of D', the construction of α, and the physical consequences; it is expedient to consider these items in this order.

A reduced-out representation D', in which the irreducible components of D are to appear explicitly, can in principle be written down as soon as the irreducible components of D are determined. Let χ denote the character of D, and let χ^p denote the character of the p^{th} irreducible representation D^p of the symmetry group involved.[21] Then, by a basic theorem, the nonnegative integer c_p that tells how many times D^p must appear in D' is given by [22]

$$c_p=(1/g)\sum_R\overline{\chi^p(R)}\chi(R),\qquad(40)$$

where g is the order of the symmetry group and the

[20] For the concepts and theorems of the theory of group representations that will be needed here it will be convenient to refer to Wigner (Gruppentheorie, cited in footnote 16), especially chapters IX and XII.

[21] Character tables are given, e. g., by Rosenthal and Murphy (footnote 17), and by G. Herzberg, Infrared and Raman spectra of polyatomic molecules (D. Van Nostrand Co., New York, 1945). Irreducible representations have apparently not been tabulated, but many of them are easily found (for one-dimensional representations, $D^p\equiv\chi^p$).

[22] Wigner, p. 95.

summation goes over the group.[23] (The complex conjugate taken in the right-hand side of eq 40, which makes the formula correct in general, is of no significance here because c_p is real in general and χ is real in the present problem.) Let the (distinct) nonequivalent irreducible representations actually contained in D (i. e., those for which $c_p \neq 0$) be numbered from 1 to t. Further, let $D^p(R)_{\pi\rho}$ denote the element in the π^{th} row and the ρ^{th} column of the matrix $D^p(R)$ of the irreducible representation D^p, which must be unitary and is considered known; and let l_p denote the dimension of D^p. For the element in the $(p\pi a)^{\text{th}}$ row and the $(q\rho b)^{\text{th}}$ column of the matrix $D'(R)$ we write

$$D'(R)_{p\pi a,\ q\rho b} = \delta_{pq}\delta_{ab}D^p(R)_{\pi\rho}, \tag{41}$$

where the indices are to have the ranges

$$a=1,2,\cdots,c_p; \qquad \pi=1,2,\cdots,l_p; \qquad p=1,2,\cdots,t;$$

$$b=1,2,\cdots,c_q; \qquad \rho=1,2,\cdots,l_q; \qquad q=1,2,\cdots,t.$$

(Whenever $l_p \neq l_q$, undefined symbols $D^p(R)_{\pi\rho}$ multiplied by zero occur in the right-hand side of eq 41; such "products" are defined to be zero.) The elements of $D'(R)$ furnished by eq 41 may, if desired, be arranged in such a way that $D'(R)$ takes the form

$$D'(R) = \begin{pmatrix} D^1(R) & \cdots & 0 & 0 & \cdots & 0 \\ \cdot & \cdot & \cdot & \cdot & \cdot & \cdot \\ 0 & \cdots & D^1(R) & 0 & \cdots & 0 \\ 0 & \cdots & 0 & D^2(R) & \cdots & 0 \\ \cdot & \cdot & \cdot & \cdot & \cdot & \cdot \\ 0 & \cdots & 0 & 0 & \cdots & D^t(R) \end{pmatrix}, \tag{42}$$

in which the matrix $D^1(R)$ appears c_1 times, $D^2(R)$ appears c_2 times, etc. (Any consistent scheme of ordering elements into matrices may be assumed, and it may be noted that an order other than one that leads to eq 42 will be convenient later.)

In the formation of D' by means of eq 41, the choice of the particular irreducible representation D^p among the unitary representations equivalent to D^p is merely a matter of convenience. (This question does not arise when $l_p=1$, of course.) However, an irreducible representation appearing more than once in D' is to be presented in identical form each time it appears, as indeed is insured by eq 41. The arbitrariness in D' implies an arbitrariness in the choice of a symmetry basis; of more interest in this paper, however, is further arbitrariness in a symmetry basis that remains after D' is assumed. This arbitrariness will appear in the course of the construction of the transforming matrix α and will be utilized in a brief discussion at the end of this section.

Let the row-matrices $\boldsymbol{e}'$, $\boldsymbol{h}'$ present the basis fields of a symmetry basis in which the matrices of D' are in fact given by eq 41. In this basis eq 37 become $P_R\boldsymbol{e}' = \boldsymbol{e}'D'(R)$, $P_R\boldsymbol{h}' = \boldsymbol{h}'D'(R)$; where, in accordance with the index notation established in eq 41, $\boldsymbol{e}' = (\boldsymbol{e}'_{p\pi a})$, $\boldsymbol{h}' = (\boldsymbol{h}'_{p\pi a})$. The characteristic transformation equations of basis fields in a symmetry basis follow directly from the form of $D'(R)$:

$$P_R\boldsymbol{e}'_{p\pi a} = \sum_{\rho=1}^{l_p} \boldsymbol{e}'_{p\rho a}D^p(R)_{\rho\pi}, \qquad P_R\boldsymbol{h}'_{p\pi a} = \sum_{\rho=1}^{l_p} \boldsymbol{h}'_{p\rho a}D^p(R)_{\rho\pi}. \tag{43a, b}$$

The l_p members of a set of basis fields (electric or magnetic) identified by fixed p and a transform among themselves according to the irreducible representation D^p of $\{P_R\}$, and they are said to be *partners* and to be of *symmetry species* p (relative to $\{P_R\}$). There are c_p sets of basis fields (electric or magnetic) of the species p, in accordance with the range $1,2,\cdots,c_p$ of the index a. More specifically, $\boldsymbol{e}'_{p\pi a}$ or $\boldsymbol{h}'_{p\pi a}$ is said to belong to the π^{th} row of the irreducible representation D^p; there are, again, c_p such electric or magnetic basis fields. The same terminology may be applied, of course, to other fields or other entities that transform under rotation according to an irreducible representation as in eq 43.

Let $\boldsymbol{e}'_{p\pi a}$ and $\boldsymbol{h}'_{p\pi a}$, which are to obey eq 43, be given by

$$\boldsymbol{e}'_{p\pi a} = \sum_{m\mu} \boldsymbol{e}_{m\mu}\alpha_{m\mu,\ p\pi a} \equiv \boldsymbol{e}\alpha_{p\pi a},$$

$$\boldsymbol{h}'_{p\pi a} = \sum_{m\mu} \boldsymbol{h}_{m\mu}\alpha_{m\mu,\ p\pi a} \equiv \boldsymbol{h}\alpha_{p\pi a},$$

where $\alpha_{p\pi a}$ denotes the $(p\pi a)^{\text{th}}$ column of the unitary transforming matrix α (cf eq 15 and the parenthetical remark following eq 16). (Note that the column matrix $\alpha_{p\pi a}$ presents the coordinates, relative to the primitive basis, of $\boldsymbol{e}'_{p\pi a}$ and $\boldsymbol{h}'_{p\pi a}$.) From either eq 43a or 43b we may derive an equation similar to eq 43 but applying to the $\alpha_{p\pi a}$. Namely, if in eq 43a we replace $\boldsymbol{e}'_{p\pi a}$ by $\boldsymbol{e}\alpha_{p\pi a}$ (and $\boldsymbol{e}'_{p\rho a}$ by $\boldsymbol{e}\alpha_{p\rho a}$) and then invoke the matrix interpretation of P_R (eq 37, 38) and abstract $\boldsymbol{e}$, we obtain

$$P_R\alpha_{p\pi a} = \sum_{\rho=1}^{l_p} \alpha_{p\rho a}D^p(R)_{\rho\pi}. \tag{44}$$

Thus $\alpha_{p\pi a}$, as well as $\boldsymbol{e}'_{p\pi a}$ and $\boldsymbol{h}'_{p\pi a}$, may be said to belong to the π^{th} row of the irreducible representation D^p. Conversely, it may be seen that if the columns of a unitary matrix obey eq 44, then the corresponding basis fields will obey eq 43. (Equation 44 is, moreover, equivalent to eq 39 and may be derived from that equation by equating the $(p\pi a)^{\text{th}}$ columns of the matrix products on the two sides of $D(R)\alpha = \alpha D'(R) - D'(R)$ being given by eq 41.)

A systematic procedure for the construction of α may be based upon eq 44, assuming that the matrices of the irreducible representations involved are known. (In a concrete problem various expedients, including judicious guessing, may often be employed to advantage.) We shall give the con-

[23] Only finite symmetry groups will be considered explicitly.

struction [24] almost in the form of a recipe, deferring the justification to the next paragraph. Define the $N\times 1$ matrix $v^{(\substack{p\\ \pi})}$ as a function of an arbitrary ($N\times 1$ matrix) v by means of the equation

$$v^{(\substack{p\\ \pi})}=(l_p/g)\sum_R \overline{D^p(R)}_{\pi\pi}P_R v, \tag{45a}$$

which may be written

$$v^{(\substack{p\\ \pi})}=[(l_p/g)\sum_R \overline{D^p(R)}_{\pi\pi}D(R)]v=G^{(\substack{p\\ \pi\pi})}v, \tag{45b}$$

thereby defining the $N\times N$ "generating" matrix $G^{(\substack{p\\ \pi\pi})}$. Corresponding to any set of N linearly independent v's, eq 45 yields a set of exactly c_p linearly independent $v^{(\substack{p\\ \pi})}$'s; each $v^{(\substack{p\\ \pi})}$, hence any linear combination of $v^{(\substack{p\\ \pi})}$'s, belongs to the π^{th} row of D^p. Select a set of c_p such combinations that are mutually orthogonal and normalized to unity (in the Hermitian sense): these may be taken as $\alpha_{p\pi 1}$, $\alpha_{p\pi 2}$, $\cdots$, $\alpha_{p\pi c_p}$. Define the matrix $G^{(\substack{p\\ \rho\pi})}$ and construct the l_p-1 partners of $\alpha_{p\pi a}$ by means of

$$\alpha_{p\rho a}=(l_p/g)\sum_R \overline{D^p(R)}_{\rho\pi}P_R\alpha_{p\pi a}, \tag{46a}$$

$$=[(l_p/g)\sum_R \overline{D^p(R)}_{\rho\pi}D(R)]\alpha_{p\pi a}\equiv G^{(\substack{p\\ \rho\pi})}\alpha_{p\pi a}, \tag{46b}$$

for $\rho=1, \cdots, \pi-1, \pi+1, \cdots, l_p$ and $a=1, 2, \cdots, c_p$. The $\alpha_{p\rho a}$'s so obtained will automatically satisfy $\alpha^*_{p\rho a}\alpha_{p\rho b}=\delta_{\rho\sigma}\delta_{ab}$. The procedure is to be carried out for each symmetry species ($p=1, 2, \cdots, t$); the orthogonality $\alpha^*_{p\pi a}\alpha_{q\rho b}=0$, $p\neq q$, will automatically hold. Thus one obtains altogther a complete set of column matrices that satisfy eq 44 and are properly orthonormalized to serve as columns of α.

For the most part, the above construction represents an immediate application of theorems given by Wigner.[25] Beyond this it is only necessary to show that (a) $G^{(\substack{p\\ \pi\pi})}$ is in fact of rank c_p and (b) $\alpha_{p\rho a}$ and $\alpha_{p\rho b}$, as given by eq 46, are orthogonal when $\alpha_{p\pi a}$ and $\alpha_{p\pi b}$ are. As for (a): since the representations D and D' are unitary and equivalent, there is no question of the existence of a unitary transformation connecting them. Hence the equation defining $G^{(\substack{p\\ \pi\pi})}$ may be transformed formally into

$$\alpha^{-1}G^{(\substack{p\\ \pi\pi})}\alpha=(l_p/g)\sum_R \overline{D^p(R)}_{\pi\pi}D'(R).$$

Considering $D'(R)$ in the form 42 (say) and applying the orthogonality theorem given below (eq 50) one finds that $\alpha^{-1}G^{(\substack{p\\ \pi\pi})}\alpha$ is a diagonal matrix having exactly c_p nonvanishing diagonal elements (each equal to 1), so that $\alpha^{-1}G^{(\substack{p\\ \pi\pi})}\alpha$, hence $G^{(\substack{p\\ \pi\pi})}$, is of rank c_p. As for (b): from the relation

$$(G^{(\substack{p\\ \rho\pi})})^*=(l_p/g)\sum_R D^p(R)_{\rho\pi}D(R)^*=$$

$$(l_p/g)\sum_R \overline{D^p(R^{-1})}_{\pi\rho}D(R^{-1})=G^{(\substack{p\\ \pi\rho})},$$

and the observation that, for a set of partners, eq 46 holds for all π,ρ (in their proper range),[26] one obtains

$$\alpha^*_{p\pi a}\alpha_{p\pi a}=\alpha^*_{p\pi a}(G^{(\substack{p\\ \rho\pi})})^*\alpha_{p\rho b}=\alpha^*_{p\pi a}G^{(\substack{p\\ \pi\rho})}\alpha_{p\rho b}=\alpha^*_{p\pi a}\alpha_{p\pi b},$$

which establishes (b).

Structural symmetry of a waveguide junction places certain restrictions on the form of the matrices Z, Y, and S (defined in eq 12, 18): some matrix elements may be forced to vanish, and the number of independent elements may be reduced materially,[27] as is well known in a variety of cases. One form of the governing equations may be found in the following way. The relation $v=Zi$ holds, of course, for any given electromagnetic state in the junction. If the fields are subjected to a symmetry operation, then $v\to v_R$, $i\to i_R$ (eq 38) and $v_R=Zi_R$ must hold, for v_R, i_R are coordinates of a possible state in the given invariant structure (cf footnote 19). Now $v_R=Zi_R$ is the same as $D(R)v=ZD(R)i$, v may be replaced by Zi, and i is arbitrary. Hence

$$D(R)Z=ZD(R), \qquad \text{every } R \text{ of } \{P_R\},$$

and we say that Z commutes with the representation D of the symmetry group. It immediately follows that $Z^{-1}(=Y)$ commutes with D and that $(Z-\zeta_0)$ and $(Z+\zeta_0)^{-1}$, hence $(Z-\zeta_0)(Z+\zeta_0)^{-1}(=S)$, commute with D. (In fact any rational matrix function of Z commutes with D.) Thus, if M denotes Z, Y, or S,

$$D(R)M=MD(R), \qquad \text{every } R \text{ of } \{P_R\}. \tag{47}$$

This equation contains the conditions imposed by symmetry upon the several matrices characterizing the junction. To find the consequences of eq 47 we consider it presented in a symmetry basis.

Upon transformation to a symmetry basis, M and D undergo one and the same similarity transformation (eq 15, 19, 39), and eq 47 becomes $D'(R)M'=M'D'(R)$. This may be written $M'=D'(R)^*M'D'(R)$, and for the element $M'_{p\pi a,\,q\rho b}$ of M' one obtains, using eq 41,

$$M'_{p\pi a,\,q\rho b}=\sum_{\sigma,\tau}\overline{D^p(R)}_{\sigma\pi}D^q(R)_{\tau\rho}M'_{p\sigma a,\,q\tau b}. \tag{48}$$

[24] The method to be given is essentially equivalent to one given (for the construction of molecular symmetry coordinates) by J. R. Nielson and L. H. Berryman, J. Chem. Phys. **17**, 659 (1949).

[25] Chap XII, eq 1, 3, 3a, 6, and 8. Compare eq 44, 45a, 46a with eq 1, 6, 3a, respectively. The reinterpretation of Wigner's equations with his functional P_R and f replaced by our matrix P_R and v is immediate.

[26] Wigner, Chap XII, eq 3a.

[27] Results more detailed than those to be obtained in the text are obtained in appendix, 2.

The g equations of this type (one for each R of $\{P_R\}$) may be added to obtain

$$g M'_{p\pi a,\,q\rho b} = \sum_{\sigma,\tau}\Big[\sum_R \overline{D^p(R)}_{\sigma\pi} D^q(R)_{\tau\rho}\Big] M'_{p\sigma a,\,q\tau b}. \quad (49)$$

Now according to the orthogonality theorem for unitary irreducible representations,[28]

$$\sum_R \overline{D^p(R)}_{\sigma\pi} D^q(R)_{\tau\rho} = \delta_{pq}\,\delta_{\sigma\tau}\,\delta_{\pi\rho}\,(g/l_p), \quad (50)$$

so that eq 49 becomes

$$\left.\begin{aligned} &M'_{p\pi a,\,q\rho b} = 0, \text{ unless } q=p \text{ and } \rho=\pi, \\ &M'_{p\pi a,\,p\pi b} = (1/l_p)\sum_\sigma M'_{p\sigma a,\,p\sigma b} \equiv m^p_{ab}, \end{aligned}\right\} \quad (51)$$

where m^p_{ab} is a constant independent of π. M' is determined by the values of the $c_1^2 + c_2^2 + \cdots + c_t^2$ constants m^p_{ab}, which are arbitrary so far as symmetry of the junction is concerned. A convenient step-matrix form for M' is obtained by arranging elements in dictionary-like order according to the values of the indices ρ, π, a in the sequence $p\pi a$. (The sequence $pa\pi$ yields $D'(R)$ in the form 42.) If $t=2$, for example, and $l_1=2$, $c_1=2$, $l_2=2$, $c_2=1$, then M' will have the particular step form

	$s\pi a$	$s\pi b$	$s\rho a$	$s\rho b$	$t\pi a$	$t\rho a$
$s\pi a$	m^s_{aa}	m^s_{ab}	0	0	0	0
$s\pi b$	m^s_{ba}	m^s_{bb}	0	0	0	0
$s\rho a$	0	0	m^s_{aa}	m^s_{ab}	0	0
$s\rho b$	0	0	m^s_{ba}	m^s_{bb}	0	0
$t\pi a$	0	0	0	0	m^t_{aa}	0
$t\rho a$	0	0	0	0	0	m^t_{aa}

The general M' will have, for each p, l_p identical steps of dimension c_p. (If $c_p=1$, every p, the steps are elements and M' is diagonal.)

Additional restrictions on M' corresponding to the conditions discussed in section II, eq 20, 21, are readily imposed. To fulfill I or II, M must satisfy one of the conditions $M^*=-M$, $M^*=M$, $M^*=M^{-1}$; and M' must satisfy the same condition. The reciprocity condition (III) requires $\tilde{M}=M$, and M' must satisfy

$$\tilde{M}' = (\tilde{\alpha}\alpha)\,M'\,(\tilde{\alpha}\alpha)^{-1}, \quad (52)$$

—or simply $\tilde{M}'=M'$ when α is real.

The form of M may obviously be found from that of M' by calculating $M=\alpha M'\alpha^{-1}$.

[28] Wigner, p. 91.

It is of interest to consider briefly the special case in which M is a *normal* [29] matrix. Either of the conditions I and II is sufficient to insure that M be normal.[30] When M is normal, M can be reduced to diagonal form by transformation to a suitably chosen symmetry basis. This statement is easily established by considering the transformation needed to diagonalize M'. If M is normal, so also is M'; from the form of M' (eq 51) it is evident that M' can be diagonalized by transformation with a unitary matrix β of the form

$$\beta_{p\pi a,\,q\rho b} = 0, \text{ unless } p=q \text{ and } \pi=\rho,$$

$$\beta_{p\pi a,\,p\pi b} = \beta^p_{ab},$$

where β^p is a suitable unitary matrix of dimension c_p. (The argument is trivial if $c_p=1$, every p.) The change of basis corresponding to this transformation may be denoted $\boldsymbol{e}' \to \boldsymbol{e}''$, where $\boldsymbol{e}'' = \boldsymbol{e}'\beta = \boldsymbol{e}(\alpha\beta)$, and we have

$$M' \to M'' = \beta^{-1}M'\beta = (\alpha\beta)^{-1}M(\alpha\beta),$$

where the diagonal matrix M'' presents the eigenvalues of M, and the columns of the combined transforming matrix $\alpha\beta$ are eigenvectors of M. Let us put $\alpha\beta=\gamma$ and examine the $(p\pi a)^{th}$ column of γ. From the form of β,

$$\gamma_{p\pi a} = \sum_{b=1}^{c_p} \beta^p_{ab}\alpha_{p\pi b}; \quad (53)$$

that is, the eigenvector $\gamma_{p\pi a}$ is a linear combination of the columns of α that belong to the π^{th} row of the irreducible representation D^p. Equation 53 is in fact an expression of the indeterminacy that appeared in the construction of α (following eq 45). Hence γ is, as it were, a possible α, and the basis $\boldsymbol{e}''$ is a symmetry basis.

The degeneracies (of the eigenvalues of M) that arise in consequence of symmetry may be made wholly explicit by a consideration of the formulas at hand. The eigenvector $\gamma_{p\pi a}$ of M belongs to the eigenvalue $M''_{p\pi a,\,p\pi a}$ presented in M''; according to eq 51 (applied to M'') $M''_{p\pi a,\,p\pi a} = \lambda^p_a$, say, where λ^p_a is independent of π. Hence the l_p eigenvectors $\gamma_{p\pi a}$ for $\pi=1,2,\ldots,l_p$ all belong to the eigenvalue λ^p_a. These eigenvectors are certainly linearly independent (being columns of a unitary matrix), and so the eigenvalue λ^p_a is at least l_p-fold degenerate. This degeneracy is necessitated by the symmetry of the waveguide junction and may be termed *symmetry degeneracy*. Degeneracy higher than that necessitated by structural symmetry, when it occurs, may be termed *accidental*, as is customary in mathematically similar circumstances.

[29] A matrix that satisfies $MM^*=M^*M$ is said to be a normal matrix; $MM^*=M^*M$ is a necessary and sufficient condition that M be reducible to diagonal form by a similarity transformation with a unitary matrix. See e. g., Murnaghan, Theory of group representations, p. 26.

[30] Although M may be and indeed usually will be symmetric (reciprocity), this condition is neither necessary nor sufficient to insure that M be normal.

V. Examples

In order to illustrate some of the text material by means of examples, we shall consider the waveguide junctions shown in figures 3, 5, and 6. The parameters σ, μ, ϵ in the interior of the junctions may be the most general consistent with the assumed symmetry in the respective cases. Although the figures indicate specific external geometries, it will be recognized that the exact manner in which the waveguides join is of no importance here, provided that this also is consistent with the assumed symmetries. Lowest-mode operation is assumed in all waveguides ($\nu_m=1$, $m=1,2,\ldots,n$); the heavy arrows in the figures, considered as localized vectors, suffice to characterize the electric terminal-fields for the lowest mode in rectangular waveguide. In applying the notation of the text, unneeded indices will be dropped; for example, $\boldsymbol{e}^0_{m\mu}$, $\boldsymbol{e}_{m\mu}$ will be written simply as $\boldsymbol{e}^0_m$, $\boldsymbol{e}_m$ (since $\nu_m=1$).

Example A. The junction shown in figure 3 has the single symmetry plane and the external geometry of a junction widely known as a "magic T". Let the indicated symmetry plane be $x=0$ of Oxyz. The symmetry group P_R consists of the identity P_I and the reflection P_S in the plane; the corresponding matrices $R=(R_{xy})$ are

$$I=\begin{pmatrix}1&0&0\\0&1&0\\0&0&1\end{pmatrix}, \qquad S=\begin{pmatrix}-1&0&0\\0&1&0\\0&0&1\end{pmatrix}.$$

(Det $(S)=-1$; P_S is a particular improper rotation.) An inspection of the figure makes it clear that

$$P_S\boldsymbol{e}^0_1=\boldsymbol{e}^0_2, \qquad P_S\boldsymbol{e}^0_2=\boldsymbol{e}^0_1, \qquad P_S\boldsymbol{e}^0_3=-\boldsymbol{e}^0_3, \qquad P_S\boldsymbol{e}^0_4=\boldsymbol{e}^0_4,$$

(cf eq 34); hence

$$P_S\boldsymbol{e}_1=\boldsymbol{e}_2, \qquad P_S\boldsymbol{e}_2=\boldsymbol{e}_1, \qquad P_S\boldsymbol{e}_3=-\boldsymbol{e}_3, \qquad P_S\boldsymbol{e}_4=\boldsymbol{e}_4,$$

(cf eq 33), and so the $N\times N$ $(=4\times4)$ representation D is

$$D(I)=\begin{pmatrix}1&0&0&0\\0&1&0&0\\0&0&1&0\\0&0&0&1\end{pmatrix}, \qquad D(S)=\begin{pmatrix}0&1&0&0\\1&0&0&0\\0&0&-1&0\\0&0&0&1\end{pmatrix}.$$

($D(I)$ is always the N-dimensional unit matrix, of course.) D is real and unitary, as it must be. The character χ of D is $\chi(I)=4$, $\chi(S)=0$.

$\{P_R\}$ has two irreducible representations; both are one-dimensional:

$$D^p: \qquad D^p(I)=(1), \qquad D^p(S)=(1).$$

$$D^q: \qquad D^q(I)=(1), \qquad D^q(S)=(-1).$$

(The 1×1 matrices are unitary.) Since D^p and D^q are one-dimensional, $\chi^p\equiv D^p$ and $\chi^q\equiv D^q$. From eq 40,

$$c_p=(1/2)(1\cdot4+1\cdot0)=2, \qquad c_q=(1/2)(1\cdot4+(-1)\cdot0)=2,$$

and a reduced-out representation D' (cf eq 41, 42) is given by

$$D'(I)=\begin{pmatrix}1&0&0&0\\0&1&0&0\\0&0&1&0\\0&0&0&1\end{pmatrix}, \qquad D'(S)=\begin{pmatrix}1&0&0&0\\0&1&0&0\\0&0&-1&0\\0&0&0&-1\end{pmatrix}.$$

For the symmetry basis $\boldsymbol{e}'$, $\boldsymbol{h}'$ we write

$$\boldsymbol{e}'=(\boldsymbol{e}'_{pa}\,\boldsymbol{e}'_{pb}\,\boldsymbol{e}'_{qa}\,\boldsymbol{e}'_{qb}), \qquad (\boldsymbol{h}'=\boldsymbol{h}'_{pa}\,\boldsymbol{h}'_{pb}\,\boldsymbol{h}'_{qa}\,\boldsymbol{h}'_{qb});$$

the basis fields must transforms according to eq 43 Thus, for example,

$$P_I\boldsymbol{e}'_{pa}=D^p(I)\boldsymbol{e}'_{pa}=(1)\boldsymbol{e}'_{pa}, \qquad P_S\boldsymbol{e}'_{pa}=D^p(S)\boldsymbol{e}'_{pa}=(1)\boldsymbol{e}'_{pa},$$

$$P_I\boldsymbol{e}'_{qa}=D^q(I)\boldsymbol{e}'_{qa}=(1)\boldsymbol{e}'_{qa}, \qquad P_S\boldsymbol{e}'_{qa}=D^q(S)\boldsymbol{e}'_{qa}=(-1)\boldsymbol{e}'_{qa}.$$

The same equations hold with a replaced by b, and $\boldsymbol{h}'$ transforms in the same way as does $\boldsymbol{e}'$. Fields of species p and q may, respectively, be termed symmetric and antisymmetric (or even and odd) with respect to reflection in the plane $x=0$. Now $\boldsymbol{e}_4$ is already symmetric and $\boldsymbol{e}_3$ is already antisymmetric; one may choose $\boldsymbol{e}'_{pa}=\boldsymbol{e}_4$, $\boldsymbol{e}'_{qa}=\boldsymbol{e}_3$. Suitable linear combinations to form one further electric basis-field of each species may be found immediately by inspection in this problem; a simple choice is $\boldsymbol{e}'_{pb}=(\boldsymbol{e}_1+\boldsymbol{e}_2)/\sqrt{2}$, $\boldsymbol{e}'_{qb}=(\boldsymbol{e}_1-\boldsymbol{e}_2)/\sqrt{2}$. The transformation $\boldsymbol{e}'=\boldsymbol{e}\alpha$ so determined is

$$(\boldsymbol{e}'_{pa}\,\boldsymbol{e}'_{pb}\,\boldsymbol{e}'_{qa}\,\boldsymbol{e}'_{qb})=(\boldsymbol{e}_1\,\boldsymbol{e}_2\,\boldsymbol{e}_3\,\boldsymbol{e}_4)\begin{pmatrix}0&1/\sqrt{2}&0&1/\sqrt{2}\\0&1/\sqrt{2}&0&-1/\sqrt{2}\\0&0&1&0\\1&0&0&0\end{pmatrix}$$

and we see that α is unitary, as is required, and also that α is real, as is convenient (but not always possible). (One may verify $D'(S)=\alpha^{-1}D(S)\alpha$ for the above matrices.) From eq 51, M' must be of the form

$$M'=\begin{pmatrix}m^p_{aa}&m^p_{ab}&0&0\\m^p_{ba}&m^p_{bb}&0&0\\0&0&m^q_{aa}&m^q_{ab}\\0&0&m^q_{ba}&m^q_{bb}\end{pmatrix}.$$

Upon calculating $M=\alpha M'\alpha^{-1}$ one finds, in particular, $M_{34}=M_{43}=0$, as may well be expected even under the general conditions permitted here. Indeed, these zeros can be predicted as soon as it is recognized that $\boldsymbol{e}_3$ and $\boldsymbol{e}_4$ are of distinct symmetry species.

The fields $\boldsymbol{e}_4(=\boldsymbol{e}'_{p\alpha})$ and $\boldsymbol{h}_4(=\boldsymbol{h}'_{p\alpha})$ are both of species p (even); they satisfy $\boldsymbol{e}_4(x,y,z)=P_S\boldsymbol{e}_4(x,y,z)$, $\boldsymbol{h}_4(x,y,z)=P_S\boldsymbol{h}_4(x,y,z)$. The x,y,z components of these two equations are

$$e_{4x}(x,y,z)=-e_{4x}(-x,y,z), \qquad h_{4x}(x,y,z)=h_{4x}(-x,y,z),$$

$$e_{4y}(x,y,z)=e_{4y}(-x,y,z), \qquad h_{4y}(x,y,z)=-h_{4y}(-x,y,z),$$

$$e_{4z}(x,y,z)=e_{4z}(-x,y,z), \qquad h_{4z}(x,y,z)=-h_{4z}(-x,y,z),$$

where for $\boldsymbol{e}_4$ eq 24b is used, and for $\boldsymbol{h}_4$ eq 24c and 23 are used (cf also eq 25). The even symmetry with respect to the plane $x=0$ forces $e_{4x}\equiv 0$ and $h_{4y}\equiv h_{4z}\equiv 0$ on the plane. (For $\boldsymbol{e}_3$ and $\boldsymbol{h}_3$, which are odd, $e_{3y}\equiv e_{3z}\equiv 0$ and $h_{4x}\equiv 0$ on $x=0$.) Despite the differences in behavior among their components, the tensor entities $\boldsymbol{e}_4$, $\boldsymbol{h}_4$ are unambiguously classified as of the same species by eq 43.

Example B. For the junction shown in figure 5, the symmetry group $\{P_R\}$ is of order $g=3$ and consists of the identity P_I, a counter-clockwise rotation P_{C_3} of 120° around the indicated axis, and the inverse $P_{C_3}^{-1}$ of P_{C_3}. It is evident from the figure that $P_{C_3}\boldsymbol{e}_1=\boldsymbol{e}_2$, $P_{C_3}\boldsymbol{e}_2=\boldsymbol{e}_3$, etc., and one finds $\chi(I)=3$, $\chi(C_3)=\chi(C_3^{-1})=0$. The characters of the irreducible representations of the symmetry group (as well as the representations themselves) are furnished in the table

	P_I	P_{C_3}	$P_{C_3}^{-1}$
χ^p:	1	1	1
χ^q:	1	w	$\overline{w}$
χ^r:	1	$\overline{w}$	w,

where $w\equiv\exp(2\pi j/3)$. From eq 40, $c_p=c_q=c_r=1$: in this case there will be exactly one (electric or magnetic) basis field of each of the three possible symmetry species. One may easily verify that the fields

$$\boldsymbol{e}'_p=(\boldsymbol{e}_1+\boldsymbol{e}_2+\boldsymbol{e}_3)/\sqrt{3},$$

$$\boldsymbol{e}'_q=(\boldsymbol{e}_1+\overline{w}\boldsymbol{e}_2+w\boldsymbol{e}_3)/\sqrt{3},$$

$$\boldsymbol{e}'_r=(\boldsymbol{e}_1+w\boldsymbol{e}_2+\overline{w}\boldsymbol{e}_3)/\sqrt{3},$$

obey eq 43 and in fact constitute a symmetry basis. We list α, $\tilde{\alpha}\alpha$, and the necessary form of M'.

$$\alpha=\frac{1}{\sqrt{3}}\begin{pmatrix}1&1&1\\1&w&w\\1&w&w\end{pmatrix}, \qquad \tilde{\alpha}\alpha=\begin{pmatrix}1&0&0\\0&0&1\\0&1&0\end{pmatrix},$$

$$M'=\begin{pmatrix}m^p&0&0\\0&m^q&0\\0&0&m^r\end{pmatrix}.$$

It happens that M' is necessarily diagonal, so that M is certainly a normal matrix. In this example the reciprocity condition (eq 52) forces the degeneracy $m^q=m^r$. This degeneracy is technically accidental; it might well be termed reciprocity degeneracy.

Example C. The discussion of the waveguide Wheatstone bridge (fig. 6) is limited mainly to a sketch of results. The symmetry group of this junction is identical with that of a regular tetrahedron and is of order $g=24$. Of the five nonequivalent irreducible representations of this group, the two three-dimensional ones (D^p and D^q, say) are con-

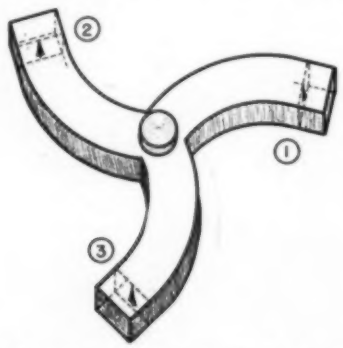

FIGURE 5. *Three-arm junction possessing a threefold axis but no plane of symmetry*

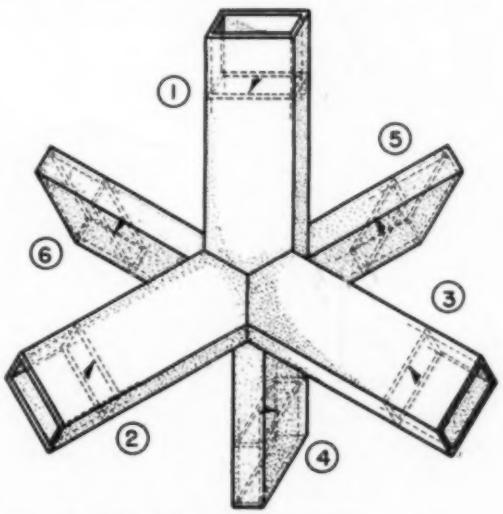

FIGURE 6. *Waveguide Wheatstone bridge.*

tained in D'. There are accordingly three fields (partners) of species p and three of species q in the symmetry basis; it can be shown that a symmetry basis is furnished by[31]

$$\begin{pmatrix} \boldsymbol{e}'_{p\pi} \\ \boldsymbol{e}'_{p\rho} \\ \boldsymbol{e}'_{p\sigma} \\ \boldsymbol{e}'_{q\pi} \\ \boldsymbol{e}'_{q\rho} \\ \boldsymbol{e}'_{q\sigma} \end{pmatrix} = \frac{1}{2} \begin{pmatrix} 1 & 1 & 0 & 1 & -1 & 0 \\ 1 & 0 & 1 & -1 & 0 & 1 \\ 0 & 1 & 1 & 0 & 1 & -1 \\ 1 & -1 & 0 & 1 & 1 & 0 \\ 1 & 0 & -1 & -1 & 0 & -1 \\ 0 & 1 & -1 & 0 & 1 & 1 \end{pmatrix} \begin{pmatrix} \boldsymbol{e}_1 \\ \boldsymbol{e}_2 \\ \boldsymbol{e}_3 \\ \boldsymbol{e}_4 \\ \boldsymbol{e}_5 \\ \boldsymbol{e}_6 \end{pmatrix}.$$

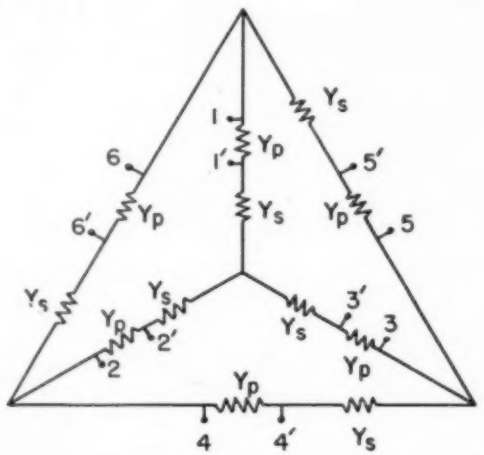

FIGURE 7. *Equivalent network.*

Sign convention: m' is the positive terminal for v_m at the terminal-pair mm'; positive i_m is into the network at m'.

(Note that this matrix equation is the transpose $\tilde{\boldsymbol{e}}'=\tilde{\alpha}\tilde{\boldsymbol{e}}$ of the equation $\boldsymbol{e}'=\boldsymbol{e}\alpha$.) Here, instead of considering impedance, admittance, and scattering matrices in common, we shall consider the admittance matrices particularly. From eq 51, Y' must be of the form

$$Y' = \begin{pmatrix} y^p & 0 & 0 & 0 & 0 & 0 \\ 0 & y^p & 0 & 0 & 0 & 0 \\ 0 & 0 & y^p & 0 & 0 & 0 \\ 0 & 0 & 0 & y^q & 0 & 0 \\ 0 & 0 & 0 & 0 & y^q & 0 \\ 0 & 0 & 0 & 0 & 0 & y^q \end{pmatrix}.$$

The eigen-admittances y^p, y^q are in general complex; the condition $\mathrm{Re}(W)\gtrless 0$ (mentioned on p. 271) requires $\mathrm{Re}(y^p)\gtrless 0$, $\mathrm{Re}(y^q)\gtrless 0$. A calculation of $Y=\alpha Y'\alpha^{-1}$ yields

$$Y = \begin{pmatrix} \lambda & \mu & \mu & 0 & -\mu & \mu \\ \mu & \lambda & \mu & \mu & 0 & -\mu \\ \mu & \mu & \lambda & -\mu & \mu & 0 \\ 0 & \mu & -\mu & \lambda & -\mu & -\mu \\ -\mu & 0 & \mu & -\mu & \lambda & -\mu \\ \mu & -\mu & 0 & -\mu & -\mu & \lambda \end{pmatrix},$$

where $\lambda\equiv(y^p+y^q)/2$, $\mu\equiv(y^p-y^q)/4$. The matrix Y is both normal and symmetric in virtue of the symmetry of the junction.

The six-terminal-pair network shown in figure 7 is a Wheatstone-bridge scheme of connections modified by the presence of the "parallel" and "series" elements Y_p and Y_s. If $Y_p=\lambda+2\mu=y^p$ and $Y^s=-4\mu=y^q-y^p$, then (with the scheme of signs noted under the figure) the admittance matrix of the network is the same as that of the junction, and the network is an "equivalent" network for the junction.

The particular values of y^p and y^q for a given structure depend upon the (common) distance of the terminal surfaces from the center of the junction. If the structure is nondissipative, it is always possible, and sometimes convenient, to assume terminal surfaces so located that $y^p=0$ or, alternatively, $y^q\to\infty$. In the first alternative the equivalent network is simplified by the absence of Y_p; in the second, by the virtual absence of Y_s (Y_s being replaceable by a perfect conductor). (This second case is the one presented in the reference in footnote 4.)

The author is greatly indebted to K. F. Herzfeld for valuable discussions and guidance in the course of this work. The writer is also very grateful to C. C. J. Roothaan for helpful discussions, and to H. Lyons for his wholehearted support of this work.

VI. Appendix

1. Transformation of Equation 9

The integral of $(1/2)(\boldsymbol{E}^1\times\overline{\boldsymbol{H}}^2)\cdot\boldsymbol{k}$ taken over the complete boundary of V (assuming an infinite domain) is equal to

$$[\boldsymbol{E}^1,\boldsymbol{H}^2]+(1/2)\int_{S_\infty}(\boldsymbol{E}^1\times\overline{\boldsymbol{H}}^2)\cdot\boldsymbol{k}\,dS=-(1/2)\int_V\nabla\cdot(\boldsymbol{E}^1\times\overline{\boldsymbol{H}}^2)dV,$$

where in the left-hand side the definition of the bracket (eq 9) and the boundary condition on the surfaces S'_∞ (p. 268) are used, and the right-hand side is given by the divergence theorem of vector analysis. From the above equation the desired express on,

$$\left.\begin{aligned}[\boldsymbol{E}^1,\boldsymbol{H}^2]=(\eta/2)\int_{S_\infty}\boldsymbol{E}^1\cdot\overline{\boldsymbol{E}}^2\,dS+(1/2)\int_V\boldsymbol{E}^1\cdot\sigma\cdot\overline{\boldsymbol{E}}^2\,dV\\ +(j\omega/2)\int_V(\overline{\boldsymbol{H}}^2\cdot\mu\cdot\boldsymbol{H}^1-\boldsymbol{E}^1\cdot\epsilon\cdot\overline{\boldsymbol{E}}^2)dV,\end{aligned}\right\}\quad(54)$$

may be obtained with the aid of further vector identity, Maxwell's equations (eq 1), and the following relations hold-

[31] This transformation represents an adaption of information contained in the tables on p. 638 of the reference in footnote 4.

ing (for both electromagnetic fields) on S_∞: $\boldsymbol{H}^2=\eta\boldsymbol{E}^2\times\boldsymbol{k}$ and $\boldsymbol{k}\cdot\boldsymbol{E}^2=0$, where $\eta\equiv\sqrt{\epsilon/\mu}$ and vacuum values of ϵ, μ may be assumed. Equation 54 applies also in the case of a finite domain provided merely that the S_∞-integral is omitted.

2. Additional Symmetry Properties

The complex conjugate of the element $Y'_{p\tau a, q\rho b}$ of the admittance matrix Y' is, from eq 12, equal to $[\mathbf{e}'_{p\tau a}, \mathfrak{H}(\mathbf{e}_{q\rho b})]$, so that, making appropriate substitutions in eq 54 and taking the complex conjugate, one obtains

$$\left.\begin{aligned} Y'_{p\tau a, q\rho b}&=(\eta/2)\int_{S_\infty}\bar{\mathbf{e}}'_{p\tau a}\cdot\mathbf{e}'_{q\rho b}dS+(1/2)\int_V\bar{\mathbf{e}}'_{p\tau a}\cdot\sigma\cdot\mathbf{e}'_{q\rho b}dV\\ &+(j\omega/2)\int_V\bar{\mathbf{e}}'_{p\tau a}\cdot\epsilon\cdot\mathbf{e}'_{q\rho b}dV-(j\omega/2)\int_V\mathfrak{H}(\mathbf{e}'_{q\rho b})\cdot\mu\cdot\overline{\mathfrak{H}(\mathbf{e}'_{p\tau a})}dV.\end{aligned}\right\}\quad(55)$$

We wish to show here that an equation of the form 51, which holds for the elements of Y', holds also for each of the four integrals making up the right-hand side of eq 55. It will suffice to consider the third and the fourth of these integrals. Since the structure is invariant with respect to P_R, and since P_R is unitary in the sense of eq 27, one may write

$$\int_V\bar{\mathbf{e}}'_{p\tau a}\cdot\epsilon\cdot\mathbf{e}'_{q\rho b}dV=\int_V(P_R\bar{\mathbf{e}}'_{p\tau a})\cdot\epsilon\cdot(P_R\mathbf{e}'_{q\rho b})dV,\quad(56)$$

$$\int_V\mathfrak{H}(\mathbf{e}'_{q\rho b})\cdot\mu\cdot\overline{\mathfrak{H}(\mathbf{e}'_{p\tau a})}dV=\int_V[P_R\mathfrak{H}(\mathbf{e}'_{q\rho b})]\cdot\mu\cdot\overline{[P_R\mathfrak{H}(\mathbf{e}'_{p\tau a})]}dV.\quad(57)$$

The right-hand side of eq 56 may immediately be expanded with the aid of eq 43a:

$$\int_V\bar{\mathbf{e}}'_{p\tau a}\cdot\epsilon\cdot\mathbf{e}'_{q\rho b}dV=\sum_{\sigma,\tau}\overline{D^p(R)}_{\sigma a}D^q(R)_{\tau b}\int_V\bar{\mathbf{e}}'_{p\sigma a}\cdot\epsilon\cdot\mathbf{e}'_{q\tau b}dV.\quad(58)$$

The right-hand side of eq 57 may be expanded similarly as soon as it is observed that $P_R\mathfrak{H}(\mathbf{e}'_{p\tau a})=\mathfrak{H}(P_R\mathbf{e}'_{p\tau a})$ (as is directly implied by eq 32) and that $\mathfrak{H}$ is a linear function of its argument. Equation 58 is of the form 48, and it is thus clear that an equation of this form holds for each of the integrals involved. The derivation in the text leading to eq 51 obviously applies. An equation of the type 55 may of course be written for $Z'_{p\tau a, q\rho b}$, and a similar argument leads to the same results for the integrals making up $Z'_{p\tau a, q\rho b}$.

WASHINGTON, June 7, 1950.

Journal of Research of the National Bureau of Standards Vol. 46, No. 4, April 1951 Research Paper 2196

Comparison of Viscosities of Rubbers from the McKee Worker-Consistometer and from the Mooney Viscometer [1]

A. B. Bestul, G. E. Decker, and H. S. White

Viscosities of three GR–S rubbers and three GR–I rubbers were measured at 100° C with the McKee worker-consistometer, a piston-type capillary viscometer, and with the standard Mooney viscometer, a rotating disk instrument. Rates of shear from several tenths to several hundred sec^{-1} were covered with the consistometer and from 0.1 sec^{-1} to several sec^{-1} with the Mooney viscometer. The procedure for preparing the samples and taking the measurements with the Mooney viscometer was selected as giving the best possible simulation of the conditions of the standard Mooney measurement, consistent with a valid indication of the temperature of the sample and as nearly as possible a like state of degradation at all rates of shear. The viscosities from the consistometer were calculated, using the Weissenberg-Rabinowitsch differentiation method for reducing observed flow data to fundamental quantities. The agreement of the results from the two instruments in their common range varies for the different rubbers, being better for the GR–S's. The best agreement is within about 2 percent, the uncertainty of the measurements, and the worst is within about 20 percent. The results from both instruments for X–518 GR–S agree with results obtained by Treloar for a "Standard GR–S" with a Piper and Scott biconical rotor modification of the Mooney viscometer. As the disagreements shown are not the same for all the rubbers they cannot be the result of constant instrumental differences, but must involve factors such as hydrostatic pressure, elasticity, and slippage at instrument surfaces.

I. Introduction

The McKee worker-consistometer [1],[2] which was recently adapted to measurements of the viscosities of raw rubbers [2, 3], is a piston-type capillary viscometer. Probably the most commonly used instrument for measuring such viscosities is the standard Mooney viscometer [4], which is based on a rotating disk. The results obtained with the two instruments for a given rubber should agree if, for both instruments, the method used for interpreting the observed data and for reducing them to fundamental quantities is truly applicable to the situation concerned. In order to check the applicability of the methods used it is necessary to compare results from the two instruments. Such comparison has been made with the results for three GR–S and three GR–I rubbers at 100° C.

II. Materials and Apparatus

The six rubbers for which viscosities were measured are listed, with descriptive data, in table 1.

The worker-consistometer used and its operation are described in reference [2, 3]. Rates of shear lower than those mentioned in reference [2, 3] were obtained by increasing the number of gears between the driving motor and worm gear.

The standard Mooney viscometer and its operation are described in reference [4]. However speeds other than the standard 2 rpm are reported here. In unreported measurements on the GR–S rubbers with this apparatus and with a biconical rotor Mooney viscometer [6], these two instruments gave identical viscosities for a given rubber if the samples were treated similarly in the two instruments.

[1] The work reported here was sponsored by the Reconstruction Finance Corporation, Office of Rubber Reserve.
[2] Figures in brackets indicate the literature references at the end of this paper.

TABLE 1. *Rubbers investigated*

Rubber	Origin	Polymerization temperature	Standard Mooney reading [a]
		°C	
X–518 GR–S	Standard reference lot	50	49
X–558 GR–S	do	5	59
X–478 GR–S	Production sample	5	64
Y–105 GR–I–17	Standard reference lot	−90	61
GR–I–18 B–13	Production sample	−90	78
GR–I–18 D	do	−90	81

[a] 100° C, 2 rpm, large rotor, 4-min readings, GR–S samples prepared according to Taylor [5], GR–I's tested as received.

For this reason it was felt that the standard Mooney viscometer was satisfactory for the present comparisons, and that it was not necessary to use the biconical instrument, which has a more nearly uniform rate of shear throughout the flow field.

III. Measurements and Treatment of Data

1. Worker-Consistometer

Measurements were made in the worker-consistometer with a 50-hole shearing element at reciprocal rates of piston travel from about 13.6 hr/in. to 1 min/in. These rates correspond to rates of shear from about 0.3 to 500 sec^{-1}. The procedure in these measurements is as follows: A fresh sample of rubber (not mill-massed) is placed in the instrument and forced through the shearing element 10 times at a nominal rate of shear of 100 sec^{-1}. During these passes the apparent viscosity of the rubber increases. Previous measurements [2] show that the viscosity of the rubber at a given rate of shear remains nearly constant for the second 10 passes. The data at all rates reported are obtained between the tenth and the twentieth passes on one

filling of the instrument. In this instrument the differences between results for GR–S samples mill-massed for 25 passes and samples that have not been mill-massed are small enough to be ignored.

The observed pressure drop across the capillary (P) and volume rate of flow (Q) are converted to shearing stress at the capillary wall (s_w) and nominal rate of shear (D) by the usual relations

$$s_w = RP/2L, \text{ and } D = 4Q/\pi R^3, \quad (1)$$

where R and L are the radius (0.0188 cm) and length (0.635 cm), respectively, of the capillary. The actual rate of shear at the capillary wall ($\dot{\gamma}_w$) is obtained from the relation

$$\dot{\gamma}_w = (D/4)\ (3 + d \log D/d \log s_w). \quad (2)$$

This relation is the result of the differentiation method for reducing observed data to fundamental quantities. This method is described by Mooney [7] and others. The term $d \log D/d \log s_w$ is obtained for a given value of D by plotting log D against log s_w over the range available and measuring the tangential slope at the point concerned. In this paper viscosity (η) is defined as the ratio of shearing stress to rate of shear, regardless of whether the flow is Newtonian. According to this usage the quantities called viscosities are not material constants for non-Newtonian substances, but are merely helpful ratios, the numerical values of which vary with the rate of shear or the shearing stress. This usage has been adopted by Burgers and Scott-Blair [8] and by Reiner [9], and has been used by numerous other authors. The ratio $s_w/\dot{\gamma}_w$ is thus the viscosity corresponding to the rate of shear $\dot{\gamma}_w$.

2. Mooney Viscometer

When a fresh sample of any of the GR-S rubbers used (mill-massed according to Taylor [5]) is placed in a Mooney viscometer and the instrument started, the viscosity first rises to a maximum and then decreases continually with further shearing. This decrease results from molecular degradation. Viscosity results varying by as much as a factor of 2 can be obtained, depending on the procedure used in taking the measurements [10, 11]. The data reported here for the GR-S rubbers in the Mooney viscometer were obtained by a procedure that meets the following three requirements: (1) the rubber should be allowed to come to the temperature of the instrument before data are taken; (2) the data at all rates of shear should be taken on material in as nearly as possible a uniform state of degradation; and (3) conditions should simulate as nearly as possible those of the standard Mooney measurement. The procedure selected is as follows. A fresh, mill-massed sample is placed in the instrument, which has previously been heated to 100° C. Ten minutes is allowed for the rubber to reach the temperature of the instrument. The viscometer is then started at 2 rpm. At the end of 4 min the gage reading is recorded, and the speed is reduced to 1.5 rpm. As soon as the gage reading becomes steady at the new speed (less than 1 min) it is recorded and the speed reduced again. Further readings are made at successive speeds of 1.0, 0.5, and 0.2 rpm. The speeds used correspond to rates of shear from 0.103 to 1.03 sec^{-1}. As GR-I rubbers do not show the above molecular degradation [5, 12], this procedure is not followed so exactly with them, and measurements are made at higher rates of shear.

For the Mooney viscometer the observed gage reading (G) and rate of revolution (W) are converted to a volume average viscosity (η) and rate of shear ($\dot{\gamma}$) by the approximate method given by Mooney [4]. Mooney found that a purely theoretical analysis had to be empirically corrected to give agreement with results from the "rubber rheometer" [13], a viscometer of more nearly uniform rate of shear developed by him. This correction is used here. The numerical relations used here are

$$\eta = 34{,}000G/W, \text{ and } \dot{\gamma} = 0.516W \quad (3)$$

IV. Results

Results on the six rubbers with the worker-consistometer and with the Mooney viscometer, used according to the procedures described above, are given in figures 1 through 6 as logarithmic plots of viscosity at 100° C versus rate of shear. These figures also show the viscosities calculated from the standard Mooney readings.

For X–518 GR-S (fig. 1) the two curves agree

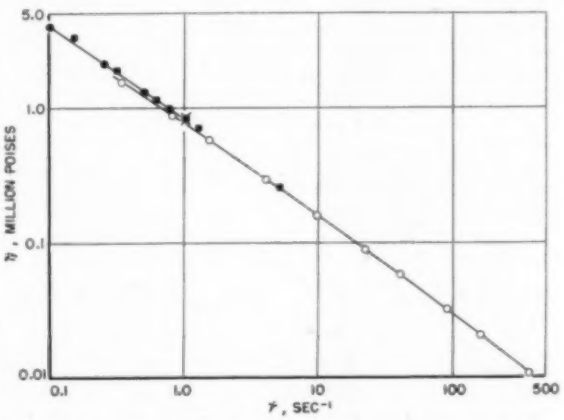

FIGURE 1. *Viscosity of X-518 GR-S versus rate of shear.*

■, Trelour; X, standard Mooney value; ○, worker-consistometer values; ●, Mooney values.

within 10 percent over their common range. The standard Mooney value indicated by the x agrees with the Mooney curve within 3 percent. The two curves have slightly different slopes in their common region. However, an extension of the Mooney curve to slightly higher rates of shear appears to show better agreement with the worker-consistometer curve.

For X–558 GR–S (fig. 2) all comparable data agree within the uncertainty of the measurements.

For X–478 GR–S (fig. 3) the only Mooney observation is the standard Mooney value. This value agrees with the worker-consistometer curve within the uncertainty of the measurements.

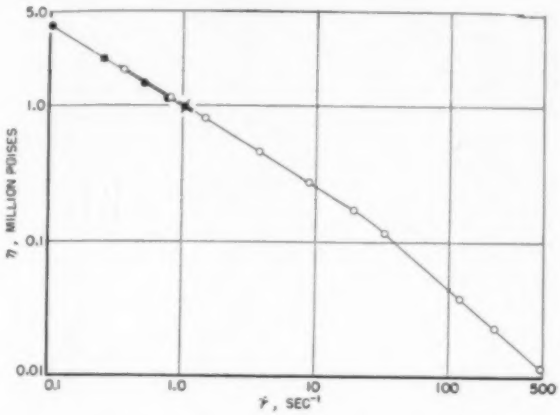

FIGURE 2. *Viscosity of X-558 GR-S versus rate of shear.*

X, Standard Mooney value; ○, worker-consistometer values; ●, Mooney values.

The results for the three GR–I rubbers (figs. 4, 5, and 6) are sufficiently similar so that they may be mentioned collectively. For these rubbers the standard Mooney values are in complete agreement with the present Mooney curves. This result would be expected since no degradation occurs under the conditions of the experiments [5, 12], and it is presumably degradation that causes discrepancies here for the GR–S rubbers. In the region around 1 sec^{-1} the Mooney values are all about 20 percent higher than the corresponding worker-consistometer values. A Mooney curve and a corresponding worker-consistometer curve do not have identical slopes over their common region in every case. However, from figure 5 it appears that an extension of the Mooney curve to higher rates of shear may coincide with the worker-consistometer curve.

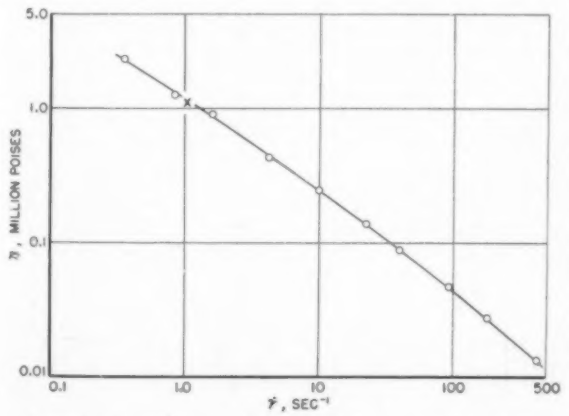

FIGURE 3. *Viscosity of X-478 GR-S versus rate of shear.*

X, Standard Mooney value; ○, worker-consistometer values.

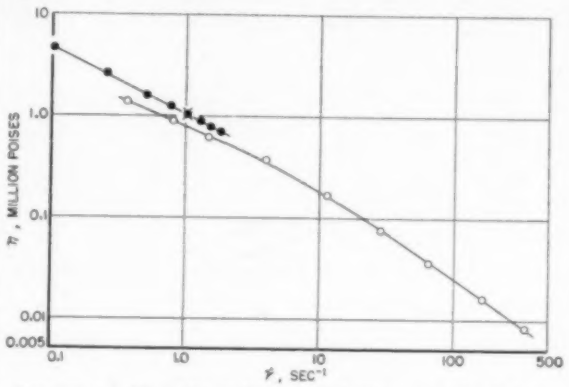

FIGURE 4. *Viscosity of Y-105 GR-I-17 versus rate of shear.*

X, Standard Mooney value; ○, worker-consistometer values; ●, Mooney values.

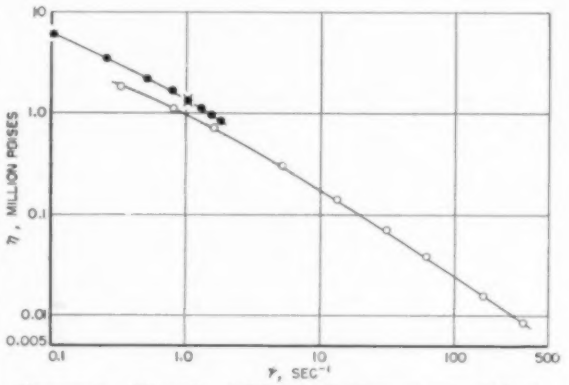

FIGURE 5. *Viscosity of GR-I-18 B-13 versus rate of shear.*

X, Standard Mooney value; ○, worker-consistometer values; ●, Mooney values.

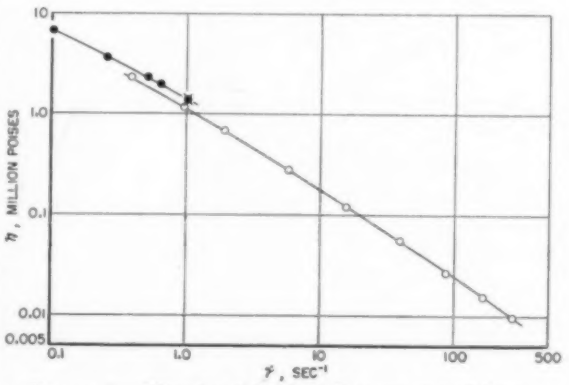

FIGURE 6. *Viscosity of GR-I-18 D versus rate of shear.*

X, Standard Mooney value; ○, worker-consistometer values; ●, Mooney values.

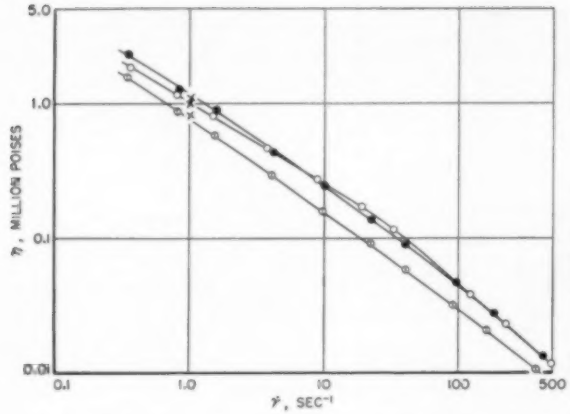

FIGURE 7. *Worker-consistometer data for GR-S rubbers.*

X, Standard Mooney values; 0, X-558 GR-S; ●, X-478 GR-S; ①, X-518 GR-S.

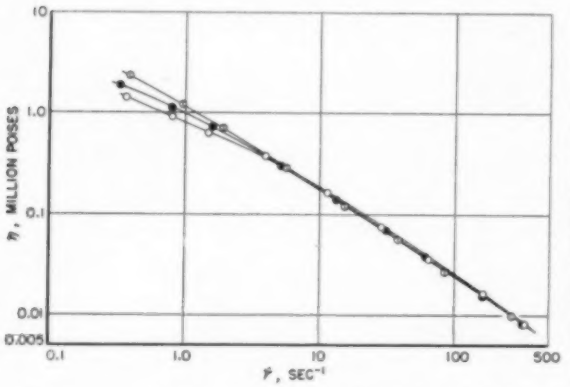

FIGURE 8. *Worker-consistometer data for GR-I rubbers.*

①, D GR-I; ●, B-13 GR-I; 0, Y-105 GR-I.

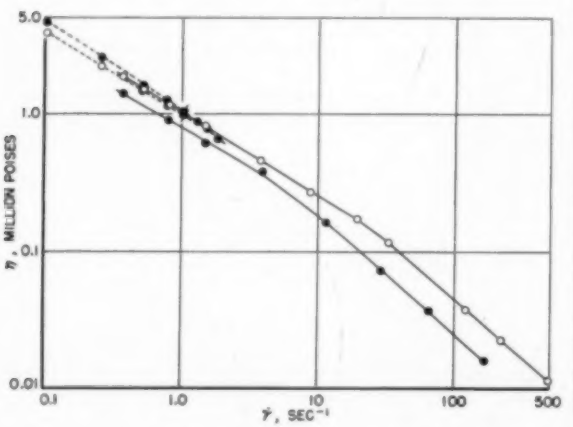

FIGURE 9. *Flow curves for GR-S and GR-I rubbers.*

○, X-558 GR-S; ●, Y-105 GR-I; ...., Mooney values; —, worker-consistometer values; x, standard Mooney values.

Figure 7 is a composite plot of the worker-consistometer data for the GR–S rubbers. It is included as a demonstration of the differences in the flow curves for GR–S rubbers. The plots for X–518 GR–S and for X–478 GR–S have approximately the same shapes, but different locations. The plots for X–558 GR–S and for X–478 GR–S have roughly the same locations, but different shapes.

Figure 8 is a similar composite plot for the GR–I rubbers. It is interesting that although the flow curves for these three rubbers are separated at lower rates of shear they are nearly coincidental at higher rates of shear.

In order to give a direct comparison of the data for a GR–S rubber with that for a GR–I, the results for X–558 GR–S and for Y–105 GR–I are plotted together in figure 9. The viscosity of the GR–I rubber shows the most rapid decrease at lower rates of shear than does that of the GR–S.

V. Discussion

Since the differences shown in figures 1 to 6 between the results from the two instruments for identical rubbers are not the same for all the rubbers, there is no constant instrumental difference between the instruments.

In the case of the GR–S rubbers the variation of the differences may represent varied degrees of degraduation produced in different rubbers by the same procedure. Treloar [10] shows what large variations may be produced in the location of a flow curve by procedural differences. Unreported data of our own confirm this fact and also show that large differences in the slopes may be thus produced.

The differences between the results from the two instruments for the GR–I rubbers show a large scale similarity within the group. In all three cases the Mooney values are about 20 percent higher than the worker-consistometer values. Degradation cannot be a factor in these differences. However, since the differences do not show, sufficient uniformity to be attributed completely to constant instrumental differences, they are apparently also contributed to by properties of the rubbers other than viscosity, such as elasticity, and adhesion to the viscometer surfaces. These properties may vary for the different rubbers and thus produce varied discrepancies. Known differences and variations in the hydrostatic pressures, and possible ones in the temperatures in the two instruments, would also result in differences that would not be related to the flow mechanics and that would vary for different rubbers having unlike pressure and temperature coefficients of viscosity. Another possible source of difference is the flow analysis for the Mooney viscometer, which is only approximate and may not take adequate account of the change of viscosity with rate of shear. Therefore the Mooney results on two rubbers having different flow curves may well compare differently with worker-consistometer results for the same two rubbers.

In the case of figure 1, a tentative comparison with literature can be made. Treloar [10] gives flow data obtained with a biconical rotor Mooney viscometer [6] for a rubber described as a "standard GR–S". Although this rubber is not described further, and the preparation of the sample is described only as "a preliminary light milling", the results probably represent a material similar to that treated in figure 1. Treloar's data have been expressed in the form of figure 1 and are plotted on that figure (■). Good agreement with the present results is shown, but it may be entirely fortuitous in view of the extreme dependence of results on the preparation of the sample.

VI. Conclusion

It can be concluded that in the worst cases there is agreement within about 20 percent between results from the worker-consistometer and those from the standard Mooney viscometer used according to the procedure described here. For two of the rubbers investigated the differences are within the limits of uncertainty of the measurements. The procedure used was selected as giving the best possible simulation of the conditions of the standard Mooney measurement, consistent with a valid indication of the temperature of the sample. The degree of agreement shown is within reasonable expectations in view of the confusing factors mentioned above.

It has also been demonstrated that the flow curves for different rubbers of a given type can be of noticeably different characters.

Many of the calculations and all of the drawings for this paper were made by Miss H. V. Belcher.

VII. References

[1] S. A. McKee and H. S. White, ASTM Bull. No. 153, 90 (1948).
[2] H. S. White, Technical Report to Reconstruction Finance Corporation, Office of Rubber Reserve (Feb. 2, 1950).
[3] S. A. McKee and H. S. White, J. Research NBS **46,** 18 (1951) RP2170.
[4] M. Mooney, Ind. Eng. Chem., Anal. Ed. **6,** 147 (1934); Rubber Chem. Tech. **7,** 564 (1934).
[5] R. H. Taylor, NBS Circular C451 (1945); India Rubber World **112,** 582 (1945); Rubber Chem. Tech. **19,** 808 (1946).
[6] G. H. Piper and J. R. Scott, J. Sci. Instr. **22,** 206 (1945); Rubber Chem. Tech. **19,** 822 (1946).
[7] M. Mooney, J. Rheol. **2,** 210 (1931).
[8] J. M. Burgers and G. W. Scott-Blair, Proc. Int. Cong. Rheol., Holland, 1948, p. V–28 (North-Holland Publishing Co., Amsterdam, 1949).
[9] M. Reiner, Deformation and flow, p. 54 (H. K. Lewis and Co., Ltd., London, 1949).
[10] L. R. G. Treloar, Trans. Inst. Rubber Ind. **25,** 167 (1949).
[11] R. H. Taylor, J. H. Fielding, and M. Mooney, Symposium on rubber testing, ASTM Publication 74 (1947); Rubber Age (N. Y.) **61,** 567 and 705 (1947).
[12] R. L. Zapp and F. P. Baldwin, Rubber Chem. Tech. **20,** 84 (1947).
[13] M. Mooney, Phys. **7,** 413 (1936); Rubber Chem. Tech. **10,** 214 (1937).

Washington, July 7, 1950.

Journal of Research of the National Bureau of Standards Vol. 46, No. 4, April 1951 Research Paper 219

Spectrophotometric Determination of Carboxyl in Cellulose[1]

Florence H. Forziati, John W. Rowen, and Earle K. Plyler

A method that uses the intensity of the absorption of the oxidized celluloses at 5.8 microns as a measure of their carboxyl content is described. The analyses are carried out on mineral oil slurries of 1:1 mixtures of finely divided polystyrene and cellulose. The absorption of the polystyrene at 6.2 microns is used as a reference band, thus obviating the necessity of accurately controlling the thickness of the absorption cell. The method gives results that agree fairly well with those obtained by the calcium acetate method and can be used to detect as little as 0.1 millimole of carboxyl per gram of cellulose.

I. Introduction

Cellulose products are frequently exposed to oxidative environments during manufacture and use. The oxidation of cellulose, commonly represented by the formula below is, therefore, of great technical importance.

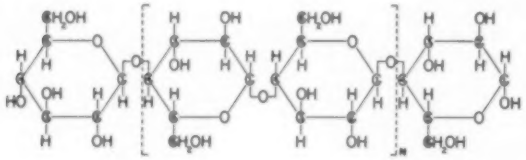

The types of oxidation theoretically possible for cellulose are:

Oxidation of primary alcohol groups (carbon 6 of the anhydroglucose units) to aldehyde or carboxyl groups.

Oxidation of secondary alcohol groups (carbon 2 or 3) to ketone groups.

Oxidation of glycol groups (carbons 2 and 3) to aldehyde or carboxyl groups with attendant cleavage of the carbon-to-carbon bond.

Oxidation of hemiacetal groups (carbon 1) to carboxyl groups. Although this type of oxidation is unimportant in undegraded celluloses where the number of terminal groups is extremely small, it may be of importance in certain degraded celluloses.

With few exceptions [1 to 5],[2] oxidants appear to be nonselective in their action on cellulose, giving rise to two or more of the above types of oxidation simultaneously. Accordingly, for the characterization of oxidized celluloses, methods capable of detecting, estimating, and allocating ketone, aldehyde, and carboxyl groups in the presence of each other are needed. Available chemical methods are not entirely satisfactory for this purpose.

The presence of carbon attached to oxygen by means of a double bond in the aforementioned groups suggests that oxidized celluloses will show the characteristic absorption of the C=O stretching vibrations in the 5.5- to 6.5-μ region of the spectrum. As the frequency and intensity of this absorption are normally influenced by the adjacent molecular structure [6, 7], ketonic, aldehydic, and carboxylic carbonyl groups of oxidized celluloses might reasonably be expected to absorb at different wavelengths. If such is the case, infrared spectrophotometry should be useful in the analysis and characterization of oxidized celluloses.

During earlier work in this laboratory, an absorption band at 5.8 μ was observed in the spectra of films of regenerated cellulose that had been subjected to moderate oxidation with nitrogen dioxide [8, 9]. Under the conditions used, this reagent is selective in its action on cellulose, resulting only in the conversion of primary alcohol groups to carboxyl groups [1, 2]. The absorption of these films at 5.8 μ was, consequently, attributed to carboxylic carbonyl. Subsequent examination of spectra of mineral oil slurries of cottons that had been treated with a variety of oxidants showed absorption at 5.8 μ to be of frequent occurrence. Although it was recognized that noncarboxylic carbonyl might be responsible for this absorption in some cases, the possibility of using the intensity of the absorption of the oxidized celluloses at 5.8 μ as a measure of their carboxyl content was investigated. The results of this investigation are presented in this report.

The use of the intensity of an absorption band as a measure of the concentration of the group or compound responsible for the band is based on Beer's law. This law states that $\log I_0/I = kcd$, where I_0 and I are the intensities, respectively, of the radiant energy of a given wavelength falling upon and passing through the sample, k is an absorption coefficient characteristic of the sample, c is a concentration, and d is the cell thickness. In the analysis of discontinuous solids, such as the oxidized celluloses, the necessity for measuring cell thickness is usually avoided by the addition of a properly chosen solid reference material in a fixed ratio to the total sample [7, 10]. Spectrophotometric measurements on mixtures of the reference material with samples containing varying and known amounts of the component of interest supply the data required

[1] A report of work done under cooperative agreement with the United States Department of Agriculture and authorized by the Research and Marketing Act. The work is being supervised by the Southern Regional Research Laboratory of the Bureau of Agricultural and Industrial Chemistry.

[2] Figures in brackets indicate the literature references at the end of this paper.

for the construction of a working curve to be used in the analysis of unknowns. The curve is obtained by plotting the concentration of the component of interest against the ratio of log I_0/I for the wavelength of interest in the sample to log I_0/I for a wavelength at which the reference material absorbs.

II. Construction of an Analytical Working Curve

In the present work, data for the construction of an analytical working curve were obtained from spectra of mineral oil slurries of 1:1 mixtures of cellulose samples of known carboxyl content with finely divided polystyrene, which provided a reference absorption band at 6.2μ. The polystyrene was obtained from the manufacturer, the Dow Chemical Co., in granular form. Prior to use, it was ground to a fine powder in a vibratory ball mill [11], washed with 95 percent ethanol and dried in air.

Empire cotton purified by a modification of the procedure described by Worner and Mease [12] and milled for 30 min in the vibratory ball mill, was used as a diluent in the preparation of cellulose samples of known carboxyl content. A nitrogen-dioxide-oxidized cotton prepared by the Tennessee Eastman Corp. was used as the source of carboxyl. This oxidized cellulose had been ground in a Wiley mill to pass a 100-mesh screen, freed of water-soluble material by repeated extraction with water, and dehydrated by successive treatments with absolute methanol and benzene. The benzene was removed by prolonged storage over paraffin in vacuum.

Before use, the cotton, oxidized cotton, and polystyrene were conditioned at 65-percent relative humidity at 21°C. The carboxyl contents of the conditioned cotton and nitrogen-dioxide-oxidized cotton as determined by the calcium acetate method [1] were 0.01 and 1.78 millimoles per gram. This sample of nitrogen-dioxide-oxidized cotton was used in preference to a more highly oxidized sample in order to keep the concentration of noncarboxylic carbonyl to a minimum [1,13]. The quantities of cotton and oxidized cotton used were such that the total weight of each cellulose sample was 100 mg.

The cellulose samples were dry-mixed with an equal weight of polystyrene and were then mulled with 0.5 ml of mineral oil between weighted ground glass plates. For the absorption measurements, the resulting slurries were injected into demountable rock-salt absorption cells equipped with silver or cellulose acetate spacers of approximately 25, 50, or 100 μ in thickness. The spacers were chosen in such a way that the values for the transmission at 5.8 μ ranged from 30 to 60 percent.

Spectra were obtained with a double-beam automatic recording Baird spectrophotometer [14] equipped with a sodium chloride prism. The performance of the instrument was checked frequently against a polystyrene film of known spectral characteristics. The single-cell rather than the double-cell method was used in securing spectra. In order to compensate for variations in the behavior of the spectrophotometer, four to six spectra were recorded for each absorption cell. Values for I_0 at 5.8 and 6.2 μ could not be obtained directly from the spectrograms. They were, therefore, assumed to be equal to the percentage transmission at nearby wavelengths at which neither oxidized cellulose nor polystyrene has absorption bands—namely, 5.5 and 6.4 μ. Average values for the ratio,

$$\frac{\log\,(I_0/I)_{5.8\mu}}{\log\,(I_0/I)_{6.2\mu}},$$

were used in the construction of the working curve and in spectrophotometric analyses.

In figure 1 are shown the 5.2- to 6.5-μ region of the spectra of mineral oil slurries of three of the polystyrene-cellulose mixtures. For comparison, spectra of mineral oil slurries of the polystyrene, cotton, and nitrogen-dioxide-oxidized cotton are given in figure 2. In table 1, the values of the ratio,

$$\frac{\log\,(I_0/I)_{5.8\mu}}{\log\,(I_0/I)_{6.2\mu}},$$

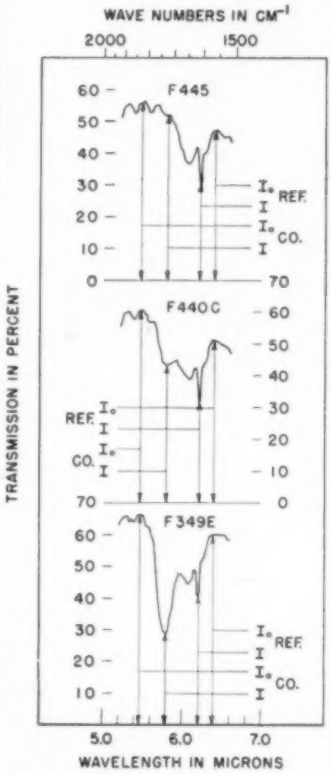

FIGURE 1. *Spectrograms of mineral oil slurries of 1:1 mixtures of polystyrene with cellulose samples of known carboxyl content showing method of obtaining values of I_0 and I for carboxylic carbonyl and reference bands.*

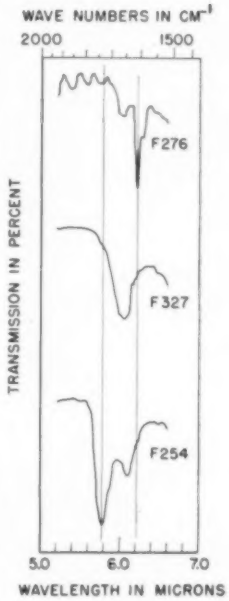

FIGURE 2. *Spectrograms of mineral oil slurries of F276, polystyrene; F327, cotton; F254, nitrogen-dioxide-oxidized cotton.*

F445, 0.01 millimoles COOH/g cellulose; F440C, 0.54 millimoles COOH/g cellulose; F349E, 1.78 millimoles COOH/g cellulose.

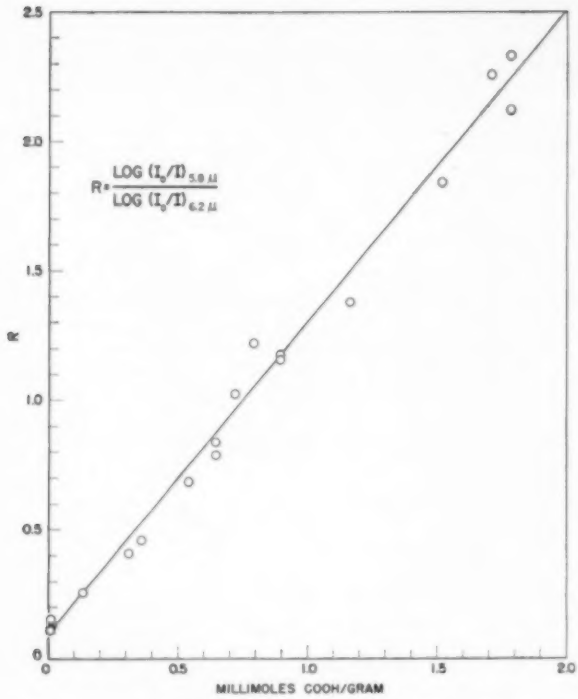

FIGURE 3. *Analytical working curve for determination of carboxyl in cellulose.*

are given with the carboxyl contents of the cellulose samples. A comparison of the plot of these these data with the straight line obtained by the application of the method of least squares to the experimental data, both presented in figure 3, shows that

$$\frac{\log (I_0/I)_{5.8\mu}}{\log (I_0/I)_{6.2\mu}}$$

is essentially a linear function of the concentration of carboxyl in the cellulose samples. The actual values of the points plotted have an uncertainty of about one-twentieth of a unit.

The failure of the straight-line plot to pass through the origin as required by Beer's law is the result of the arbitrary procedure employed in obtaining values for I_0 from the spectrograms. It should not affect the usefulness of the plot as an analytical working curve.

TABLE 1. *Spectrophotometric measurements on 1:1 mixtures of polystyrene with cellulose of known carboxyl content*

Carboxyl content of cellulose	$\frac{\log (I_0/I)_{5.8\mu}}{\log (I_0/I)_{6.2\mu}}$	Carboxyl content of cellulose	$\frac{\log (I_0/I)_{5.8\mu}}{\log (I_0/I)_{6.2\mu}}$
Millimoles/g		*Millimoles/g*	
0.01	0.15	0.79	1.22
.01	.12	.89	1.32
.01	.11	.89	1.18
.13	.26	.89	1.15
.31	.41	1.16	1.38
.36	.46	1.52	1.84
.54	.68	1.71	2.26
.64	.79	1.78	2.33
.64	.84	1.78	2.12
.72	1.02		

III. Analysis of Oxidized Celluloses

As a check on the general utility of the analytical working curve, it was used in the analysis of 11 oxidized celluloses. Using the procedure outlined above, values for the ratio,

$$\frac{\log (I_0/I)_{5.8\mu}}{\log (I_0/I)_{6.2\mu}},$$

were obtained for 1:1 mixtures of polystyrene with the oxidized celluloses. The concentrations of carboxyl in the oxidized celluloses were then read directly from the working curve.

The oxidants used in the preparation of the oxidized celluloses were air at 145° C, chromic oxide in a mixture of glacial acetic acid and acetic anhydride [15], hydrogen peroxide [16, p. 114], potassium dichromate in oxalic acid solution [16, p. 114], potassium permanganate in sulfuric acid solution [16, p. 112], bromine in the presence of excess barium carbonate [17], buffered periodic acid [18, 19], and nitrogen dioxide [1]. With the exception of the two nitrogen-dioxide-oxidized cottons and one of the periodate-oxidized cottons that were prepared, respectively, by the Tennessee Eastman Corp. and R. E. Reeves of the Southern Regional Research Laboratory, all of the oxidized cottons were prepared from purified Empire cotton that had been ground in a Wiley mill to pass a 20-mesh screen. The fact that the cotton was added to the oxidant without previous swelling probably accounts for the low degree of oxidation observed in most samples.

The results of the spectrophotometric analyses are given in table 2. Also given are the values obtained for carboxyl and noncarboxylic carbonyl by the calcium acetate [1] and hydroxylamine hydrochloride [15] methods. In table 3 are given the results of 13 analyses for carboxyl carried out on a single oxidized cotton over a 3-month period by 2 different analysts as a check on the precision of the spectrophotometric method. The values obtained for carboxyl by the spectrophotometric and calcium acetate methods agree fairly well. The greatest difference observed, 0.34 millimoles per gram for a nitrogen-dioxide-oxidized cotton, is of doubtful significance, as the yellow color of this oxidized cotton introduced considerable uncertainty in the determination of carboxyl by the calcium acetate method. Difficulty was also encountered in applying the calcium acetate method to the periodate-oxidized cottons. Thus, here also the value obtained by the spectrophotometric method may be the more reliable of the two. In general, the results indicate that the intensity of the absorption of the oxidized celluloses at 5.8μ constitutes a fairly satisfactory measure of their carboxyl content even in the presence of appreciable amounts of non-carboxylic

carbonyl. When measured according to the procedure described in this report, as little as 0.1 millimole of carboxyl per gram of cellulose can be detected.

TABLE 2. *Analyses of oxidized celluloses*

Oxidant used in preparation of oxidized cellulose	Carboxyl by calcium acetate method	Carboxyl by spectrophotometric method	Deviation	Noncarboxylic carbonyl by hydroxylamine hydrochloride method
	Millimole/g	*Millimole/g*	*Millimole/g*	*Millimole/g*
Air at 145° C	0.02	0.04	+0.02	0.40
CrO_3/acetic acid-acetic anhydride	.00	.02	+.02	.95
H_2O_2	.04	.06	+.02	.98
$K_2Cr_2O_7$/oxalic acid	.04	.02	−.02	.44
$KMnO_4/H_2SO_4$	.44	.56	+.12	.18
$Br_2/BaCO_3$	.38	.40	+.02	1.19
$Br_2/BaCO_3$	.66	.68	+.02	0.38
HIO_4	.02	.19	+.17	7.37
HIO_4	.09	.19	+.10	.....
NO_2	1.40	1.39	−.01	.....
NO_2	2.65	2.31	−.34	.....

TABLE 3. *Spectrophotometric analyses of potassium-permanganate-oxidized cotton*

Sample	Carboxyl	Deviation from mean
	Millimole/g	*Millimole/g*
1	0.46	−0.10
2	.59	+.03
3	.56	.00
4	.61	+.05
5	.55	−.01
6	.61	+.05
7	.52	−.04
8	.53	−.03
9	.53	−.03
10	.58	+.02
11	.53	−.03
12	.66	+.10
13	.59	+.03
	0.56 mean	±0.04 average deviation from mean

IV. Summary

Details of a spectrophotometric method for the quantitative estimation of carboxyl in cellulose are given. The method gives results that are in fair agreement with those obtained by the calcium acetate method and can be used to detect as little as 0.1 millimole of carboxyl per gram.

The authors express their appreciation to Walter K. Stone, Edith T. L. Voong, and Eva Estermann for technical assistance.

V. REFERENCES

[1] E. C. Yackel and W. O. Kenyon, J. Am. Chem. Soc. **64,** 121 (1942).
[2] C. C. Unruh and W. O. Kenyon, J. Am. Chem. Soc. **64,** 127 (1942).
[3] H. A. Rutherford, F. W. Minor, A. R. Martin, and M. Harris, J. Research NBS **29,** 131 (1942) RP1491.
[4] E. L. Jackson and C. S. Hudson, J. Am. Chem. Soc. **60,** 989 (1938).
[5] G. F. Davidson, Shirley Inst. Memoirs **18,** 69 (1941).
[6] H. M. Randall, R. G. Fowler, N. Fuson, and J. R. Dangl, Infrared determination of organic structures (D. Van Nostrand Co., Inc., New York, N. Y., 1949).
[7] R. B. Barnes, R. C. Gore, U. Liddel, and Van Z. Williams, Infrared spectroscopy (Reinhold Publishing Co., New York, N. Y., 1944).
[8] J. W. Rowen, C. M. Hunt, and E. K. Plyler, J. Research NBS **39,** 133 (1947) RP1816.
[9] J. W. Rowen and E. K. Plyler, J. Research NBS **44,** 313 (1950) RP2080.
[10] R. B. Barnes, R. C. Gore, E. F. Williams, S. G. Linsley, and E. M. Petersen, Anal. Chem. **19,** 620 (1947).
[11] F. H. Forziati, W. K. Stone, J. W. Rowen, and W. D. Appel, J. Research NBS **45,** 109 (1950) RP 2116.
[12] R. K. Worner and R. T. Mease, J. Research NBS **21,** 609 (1938) RP1146.
[13] P. A. McGee, W. F. Fowler, Jr., C. C. Unruh, and W. O. Kenyon, J. Am. Chem. Soc. **70,** 2700 (1948).
[14] W. S. Baird, H. M. O'Bryan, G. Ogden, and D. Lee, J. Opt. Soc. Am. **37,** 754 (1947).
[15] E. K. Gladding and C. B. Purves, Paper Trade J. **116,** 150 (1943).
[16] C. Doree, The methods of cellulose chemistry, 2d ed. (D. Van Nostrand Co., Inc., New York, N. Y., 1947).
[17] O. Faber and B. Tollens, Ber. deut. chem. Ges. **32,** 2592 (1899).
[18] D. H. Grangaard, E. K. Gladding, and C. B. Purves Paper Trade J. **115,** 75 (1942).
[19] R. Adams, Editor, Organic reactions, vol. II (John Wiley & Sons, New York, N. Y., 1944).

WASHINGTON, October 30, 1950.

Journal of Research of the National Bureau of Standards Vol. 46, No. 4, April 1951 Research Paper 219

Static Friction Tests with Various Metal Combinations and Special Lubricants

H. S. White and Dino Zei

An inclined-plane apparatus was used in obtaining static friction data for various lubricants with different metal combinations. Special lubricants, such as chlorinated and fluorinated hydrocarbons, were compared with a reference mineral oil. The effect of additives, such as graphite, molybdenum disulfide, zinc oxide, boron nitride, and an oxidized petroleum compound, was investigated. Metal combinations involving stainless steels, carbon steel, cast iron, aluminum alloy, and chromium plate were used.

It was found that the special chlorinated and fluorinated lubricants without additives gave higher friction than the Navy symbol 2110 reference oil. A lubricant containing the oxidized petroleum compound and one containing a silicone grease gave slightly less friction than the reference oil. With a mineral lubricating grease, with dry molydenum disulfide, and with lubricants containing graphite or molybdenum disulfide, the friction was about 50 percent less than with the reference oil. The remaining lubricants gave higher friction than the 2110 reference oil.

In general, the heat-treated stainless-steel combinations gave the lowest friction, whereas the combinations involving cast iron or aluminum alloy gave relatively high friction. Friction was less with lapped and polished surfaces than with ground surfaces.

I. Introduction

Static friction data were obtained for making a practical comparative evaluation of the oiliness of special lubricants when used with various metal combinations. Navy symbol 2110 oil was used as a reference lubricant for comparing the friction obtained with the special lubricants. The work was done at the request of the Naval Ordnance Laboratory, which furnished most of the lubricants and the unmachined metals and specified the metal combinations to be used. The time allotted did not permit a comprehensive investigation, but it is believed that the data may be helpful to those interested in the use of these types of lubricants and metal combinations.

II. Apparatus

An inclined-plane apparatus was used for making the static friction tests. The coefficient of friction, f, is defined as F/W, where F is the tangential force at the sliding surface, and W is the force normal to the surface. As is customary with this type of apparatus, the tangent of the angle with the horizontal when a rider on the incline starts to slide is used as a measure of f. For a given vertically applied load, the magnitude of W changes with the angle of the inclined plane, and the distribution of the load at the sliding surface varies with the angle. However, these variations are not important, as the coefficient of friction was found to be practically independent of load over a wide range.

The testing machine is shown in figure 1. An electric hot plate is mounted on transite between two journals. A handwheel acts through a 100-to-1 reduction gear to give slow tilting of the hot plate. A pointer, perpendicular to the hot plate, indicates on a calibrated scale the tangent of the angle between the surface of the hot plate and the horizontal. The heavy cylindrical weight at one corner of the transite mounting is used to load the reduction gear in one direction, thus eliminating backlash. The plate specimen is fastened to the hot plate with two screws. A loading yoke with a weight pan and weights gives the desired load on the rider specimen. Two steel bars (thicker than the plate specimen), fastened to the hot plate, have several pairs of tapped holes to allow fastening of cross bars at different positions. One of these cross bars (at the left in fig. 1) is pro-

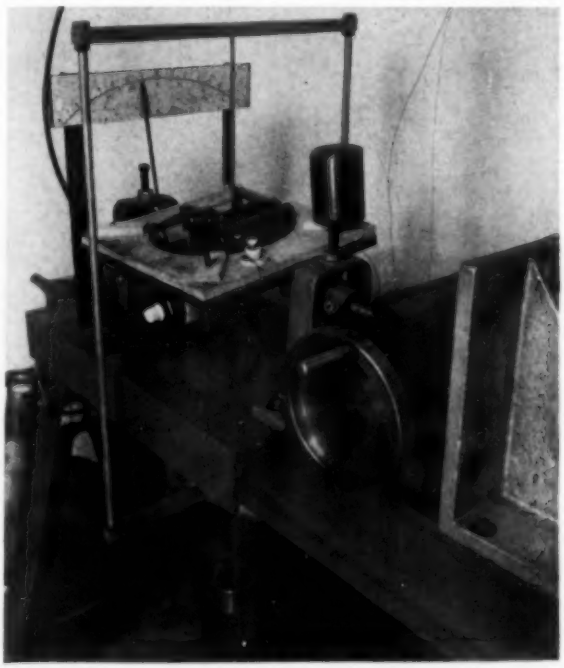

FIGURE 1. *Static friction machine.*

vided with an electrically insulated screw and needle that are connected in series with a dry cell, lamp, and rider. Connection from the lamp to the rider is made with a No. 38 copper wire in such a way as not to influence movement of the rider. When the rider contacts the needle, the completed circuit is indicated by the signal lamp. The temperature, controlled manually, is measured by a thermocouple fastened to the plate specimen.

Typical test specimens are shown in figure 2. The plate dimensions are ⅜ in. by 2 in. by 7 in., and the rider dimensions are ½ by 1 by 2 in. Each rider has a cone-shaped depression formed in the center of its upper surface for locating the point of the loading yoke. The central portion of the underside of each rider is undercut so as to leave a bearing surface ⅛ by 1 in. at each end. The tapped holes for fastening the thermocouple to the plates and the screws for fastening the signal light wire to the riders are shown in figure 2. The rider and plate shown in the background were finished by grinding. After the plate shown in the foreground was ground, it was lapped, and the contacting surfaces of the rider were finished by lapping and polishing.

III. Metal Combinations

The code numbers and descriptions of the plate specimens are given in the following tabulation.

Code No.	Material	Hardness, Rockwell C	Roughness, (rms)	Remarks
			μ in.	
431	431 stainless steel	42	9	Dry-ground.
431-L	do	42	1	Dry-ground and lapped.
440C-L	440C stainless steel	54	1	Do.
214	214 Alcoa alloy		4	Kerosine-ground.
214-L	do		3	Kerosine-ground and lapped.
2-L	cast iron		2	Oil-ground and lapped.

The code numbers and descriptions of the rider specimens are given in the following tabulation.

Code No.	Material	Hardness, Rockwell C	Roughness, (rms)	Remarks
			μ in.	
416S	416 stainless steel [a]	49	3	Dry-ground.
416S-LP	do. [a]	49		Dry-ground, lapped and polished.
3C-LP	Chromium plate			Do.
304	304 stainless steel		5	Dry-ground.
304-LP	do			Dry-ground, lapped and polished.
1050-LP	1050 steel			Do.

[a] Sulfurized for free machining.

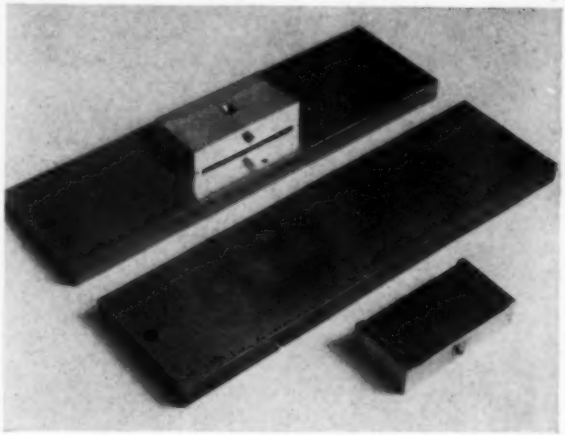

FIGURE 2. *Static friction machine specimens.*

The specimens of stainless steel 431, 440C, and 416 were hardened by heating to 1,850° F and quenching in oil, and tempered by heating at 500° F for 1 hr and cooling in air.

The sharp edges of the ⅛ by 1-in. contact surfaces of the riders were stoned and polished to prevent any shaving effect.

The values of roughness given are in microinches (rms) as determined by an Abbot Profilometer. With the lapped cast iron (2–L) the open pores gave erratic high readings above 2 μ in., but examination with an interference microscope indicated a roughness of about 2 μ in., if the pores were neglected. With the ground riders, roughness was measured on the backs of the specimens, which were ground in the same manner as the contacting surfaces. It is assumed that the lapped and polished surfaces of the riders had a roughness less than 1 μ in. In the code numbers, L means lapped, and LP means lapped and polished.

A cast iron plate with grids was used to charge a similar lead-tin-alloy plate, which was then rinsed and used to lap the test specimens. This method prevented charging of the specimens with abrasives. After lapping the riders were polished on 4/0 polishing paper resting on a surface plate.

The specimen combinations used in these tests are listed in the following tabulation.

Rider	Plate
416S	431.
304	214.
416S-LP	431-L and 440C-L.
3C-LP	431-L and 214-L.
304-LP	214-L.
1050-LP	2-L.

IV. Lubricants

The lubricants used in this investigation are listed in the following tabulation.

Series No.	Code No.	Lubricant
	7	Navy symbol 2110 oil (SAE 10).
1	13	Chlorinated hydrocarbon.
1	14	Organic phosphate ester.
1	15	Fluorinated hydrocarbon S (medium viscosity).
2	16	Fluorinated hydrocarbon S+1% commercial additive, oxidized petroleum compound.
2	17	Fluorinated hydrocarbon S+1% molybdenum disulfide.
3	18	Fluorinated hydrocarbon FS (light viscosity).
3	19	Fluorinated hydrocarbon S+1% graphite.
3	20	Perfluorokerosene.
4	21	Fluorinated hydrocarbon FS+0.5% copper phthalocyanine.
4	22	Silicone DC-200 (100 centistokes at 25° C).
4	23	Fluorinated hydrocarbon FS+2% silicone grease DC-44 (medium).
4	24	Fluorinated hydrocarbon KEL-F.
4	25	Fluorinated hydrocarbon FS+5% fluorinated grease (light).
5	26	Grease G (23.5% sodium soap).
5	27	Grease G+5% molybdenum disulfide.
5	28	Molybdenum disulfide (dry).
5	29	2110 oil+1% molybdenum disulfide.
5	30	Fluorinated hydrocarbon FS+1% zinc oxide.
6	31	Fluorinated hydrocarbon S+2% molybdenum disulfide concentrate.
6	32	Fluorinated hydrocarbon S+0.75% boron nitride (amorphous).

Lubricant 7 was selected as the reference oil for comparing the frictional characteristics of the samples, most of which were furnished by the Naval Ordnance Laboratory. The lubricants were received in groups and each group was assigned a series number.

V. Test Procedure

For cleaning the test specimens, five solvents were used in the following order: Stoddard solvent; carbon tetrachloride; benzene, cp; acetone, cp; ethyl alcohol, 95 percent. Absorbent cotton was used for scrubbing the specimens with the first two solvents. This was followed by rinsing with the other three and drying with clean cotton.

The liquid lubricants were applied to the plates and riders by means of small clean cotton swabs. Grease samples were applied with a finger tip and dry molybdenum disulfide by dusting.

With the plate horizontal, the rider was placed in position, contacting the insulated needle, and the load was applied. The needle was retracted 0.006 in. (¼ turn of the screw), and the plate was tilted slowly until the rider moved sufficiently to contact the needle and light the signal lamp. The tangent of the angle of tilt was recorded. A second reading was obtained by leveling the plate, retracting the needle another 0.006 in., and again tilting the plate until the signal lamp was lighted. This was repeated, usually until eight readings were obtained, giving a total movement of the rider of 0.048 in. This procedure and series of readings were considered as one test. Between tests the specimens were cleaned and the needle was returned to its original position so that the next lubricant could be tested on the same area of the plate specimen. Because of the variation in static friction resulting from such things as the presence of the oxide films, microscopic irregularities of the metal surfaces, and contamination from the atmosphere, tests with the reference oil (Navy symbol 2110) were made in conjunction with each series of special lubricants. For example, with series No. 1 and one needle bar position, tests were made with lubricants in the following order of Code Nos.: 7, 7, 13, 7, 14, 7, 15, 7. After all the lubricants of a series had been tested at one plate area, the needle bar was moved to another position, the rider was lapped and polished again, and the series was tested at the new plate area. In general, these comparative tests were made at three different areas of the plate specimens. With each new surface area, two or more tests were made with the 2110 oil to assure reasonable reproducibility before testing the series of lubricants. After three areas had been used on a plate specimen, it was lapped again before being used with the next series of lubricants.

VI. Test Results

Some preliminary testing was done in order to study reproducibility and the effects of temperature and load. The effect of temperature was small and was within probable experimental error for the range of 80° to 120° F. Tests with loads of 5, 10, and 15 lb. indicated that variation in the load had no effect on the coefficient of friction, that is, the tangent of the angle when sliding occurred. This was checked later with the 2110 reference oil and special lubricants 16 and 17, with the 416S–LP rider on the 431–L plate. All the values of coefficient of friction reported herein were obtained at a nominal temperature of 100° F and with a 10-lb. load (40 lb/in.² average).

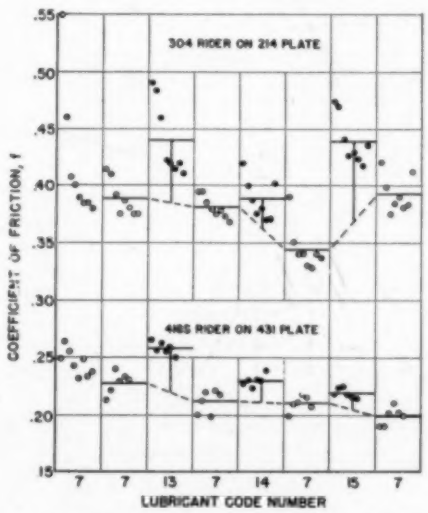

FIGURE 3. *Representative friction data at 10-lb load and 100° F, with ground surfaces.*

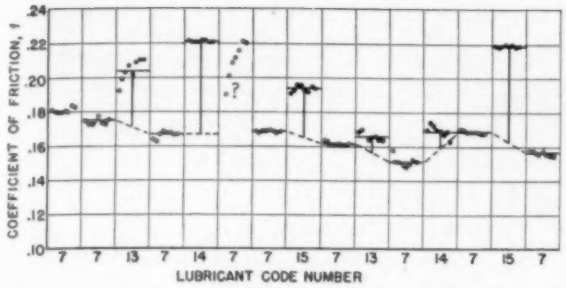

FIGURE 4. *Representative friction data at 10-lb load and 100° F, with 416S–LP rider on 431–L plate (first series of lubricants).*

Some tests were made with ground surfaces on the metal specimens. Typical data for the 2110 reference oil and lubricants 13, 14, and 15 are shown in figure 3. The horizontal lines represent the averages for each group of data obtained in a test. The averages for the reference oil are connected by broken lines from which vertical lines are drawn to the averages for the special lubricants.

Due to the large spread of data on ground surfaces and the fact that lapped or lapped-and-polished surfaces are more easily reproduced and are more commonly used for machine parts involving small clearances, subsequent tests were made with lapped plates and lapped-and-polished riders. The lapping and polishing processes have already been described.

Figure 4 shows typical data for the first series of lubricants with the 416S lapped-and-polished stainless-steel rider on the 431 lapped stainless steel plate. Where a test was obviously not representative it was ignored, as indicated by the question mark for one of the tests with oil 7. Otherwise, the spread of data in figure 4 is much less than in figure 3.

Representative data for the second and fifth series of lubricants are shown in figures 5 and 6, respectively.

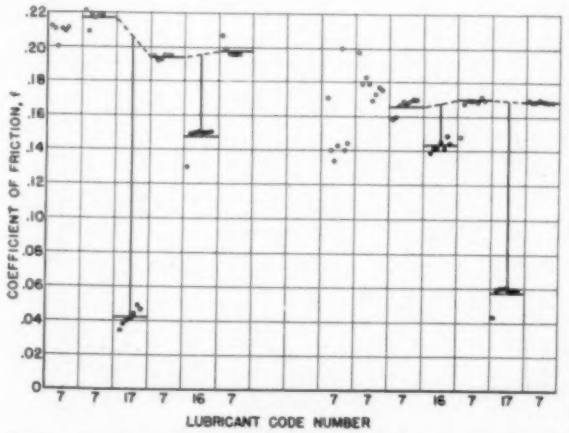

FIGURE 5. *Representative friction data at 10-lb load and 100° F, with 416S–LP rider on 431–L plate, at two locations on the plate (second series of lubricants).*

The data for all the lubricants with this particular metal combination are given in table 1. These were obtained from plots similar to figures 4, 5, and 6. The position number refers to the position of the needle bar, and hence each different position means a different location of the rider on the plate specimen. The spread of data is indicated by giving the maximum and minimum readings for each test, and the average corresponds to the horizontal mean lines as in figures 4, 5, and 6. The percentage increase in friction corresponds to the vertical lines connecting the means to the broken lines for the 2110 reference oil. The percentage increase is indicated as negative when the friction is less than with the reference oil. The reference values of f used for the 2110 oil in connection with each special lubricant test is given in the last column.

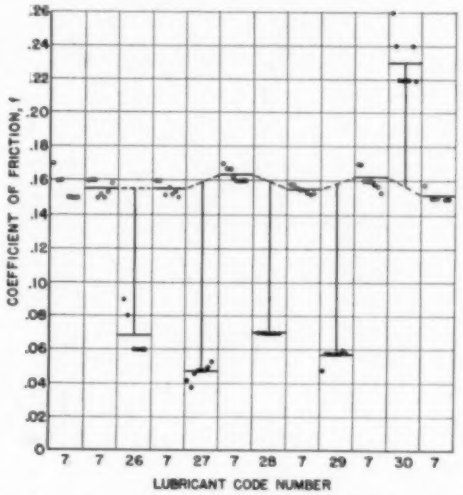

FIGURE 6. *Representative friction data at 10-lb load and 100° F, with 416S–LP rider on 431–L plate (fifth series of lubricants).*

TABLE 1. *Static friction data at 10-lb. load and 100° F, for 416 stainless steel (416S–LP) on 431 stainless steel (431–L)*

Test No.	Position No.	Lubricant Code No.	f (tangent)			Percentage increase [a]	f 2110 Oil
			Maximum	Minimum	Average		
61	7	13	0.210	0.192	0.204	19	0.172
68	7	13	.190	.184	.186	19	.156
78	5	13	.160	.146	.153	10	.138
63	7	14	.222	.221	.221	32	.167
72	7	14	.220	.218	.219	34	.163
80	5	14	.190	.178	.182	34	.136
66	7	15	.196	.191	.194	17	.166
70	7	15	.174	.164	.169	6	.160
76	5	15	.141	.138	.139	−2	.142
213	3	16	.167	.162	.165	−13	.186
221	5	16	.150	.130	.147	−25	.196
226	7	16	.149	.139	.143	−15	.168
215	3	17	.089	.078	.086	−52	.179
219	5	17	.049	.034	.042	−80	.205
228	7	17	.060	.043	.057	−67	.170
353	3	18	.219	.194	.203	18	.172

[a] Percentage increase in average f relative to tests with 2110 oil.

TABLE 1. *Static friction data at 10-lb. load and 100° F. for 416 stainless steel (416S–LP) on 431 stainless steel (431–L)*—Continued

Test No.	Position No.	Lubricant Code No.	*f* (tangent)			Percentage increase *	*f* 2110 Oil
			Maximum	Minimum	Average		
365	5	18	.171	.160	.164	3	.159
371	7	18	.154	.137	.142	−1	.144
355	3	19	.087	.077	.079	−52	.164
363	5	19	.081	.069	.071	−57	.166
369	7	19	.101	.070	.078	−49	.152
357	3	20	.176	.168	.170	8	.158
361	5	20	.171	.166	.167	0	.167
373	7	20	.160	.149	.152	7	.142
503	3	21	.240	.190	.222	29	.172
519	5	21	.230	.200	.216	27	.170
529	7	21	.170	.150	.160	−5	.168
505	3	22	.240	.190	.215	26	.171
515	5	22	.211	.179	.195	5	.185
531	7	22	.220	.180	.200	15	.164
507	3	23	.124	.105	.118	−28	.164
517	5	23	.130	.106	.125	−28	.174
527	7	23	.160	.100	.130	−24	.172
509	3	24	.220	.200	.215	31	.164
521	5	24	.180	.170	.177	−1	.178
533	7	24	.230	.220	.225	36	.166
511	3	25	.170	.166	.168	11	.152
523	5	25	.190	.176	.179	1	.178
535	7	25	.190	.180	.181	−1	.182
575	3	26	.090	.060	.068	−56	.155
597	5	26	.130	.070	.000	−45	.165
603	7	26	.100	.040	.058	−62	.154
577	3	27	.053	.038	.047	−70	.159
599	5	27	.060	.036	.052	−68	.163
605	7	27	.040	.030	.037	−77	.158
579	3	28	.070	.070	.070	−56	.159
591	5	28	.094	.086	.000	−46	.167
607	7	28	.100	.070	.000	−40	.149
581	3	29	.060	.048	.057	−64	.158
593	5	29	.049	.030	.045	−73	.165
609	7	29	.052	.050	.052	−64	.143
583	3	30	.260	.220	.230	47	.156
595	5	30	.230	.200	.212	30	.163
611	7	30	.160	.150	.159	12	.142
625	3	31	.050	.040	.049	−68	.151
634	5	31	.070	.048	.058	−58	.138
638	7	31	.070	.050	.067	−57	.156
627	3	32	.210	.190	.198	32	.150
631	5	32	.210	.198	.200	24	.161
640	7	32	.198	.180	.184	16	.158

* Percentage increase in average *f* relative to tests with 2110 oil.

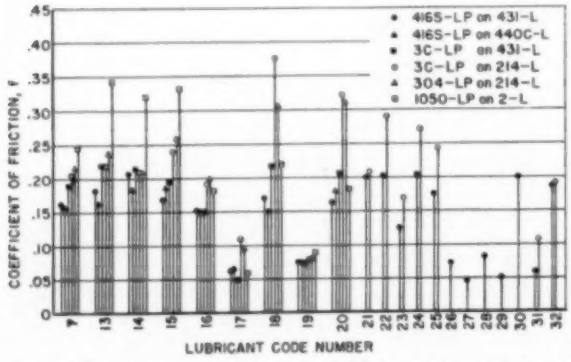

FIGURE 7. *Summary of friction data for various lubricants with different metal combinations, at 10-lb load and 100° F.*

Tables 2, 3, 4, 5, and 6 present similar data for the other metal combinations.

The data in the above tables are summarized in figure 7. The average values of *f* for lubricant 7 (2110 reference oil) and special lubricants 13 to 20 are given for six metal combinations. The averages for lubricants 21 to 25 and 31 and 32 are given for the two metal combinations used with them. Lubricants 26 to 30 were prepared at this Bureau and were tested with one metal combination only.

TABLE 2. *Static friction data at 10-lb load and 100° F. for 416 stainless steel (416S–LP) on 440C stainless steel (440C–L)*

Test No.	Position No.	Lubricant Code No.	*f* (tangent)			Percentage increase *	*f* 2110 oil
			Maximum	Minimum	Average		
86	5	13	0.163	0.158	0.160	7	0.150
92	7	13	.180	.159	.166	15	.144
88	5	14	.189	.179	.183	22	.150
94	7	14	.188	.182	.185	23	.150
84	5	15	.184	.180	.181	19	.152
96	7	15	.195	.184	.188	24	.152
233	7	16	.170	.163	.167	−5	.176
241	5	16	.174	.160	.165	−7	.178
245	3	16	.124	.121	.122	−25	.162
235	7	17	.097	.091	.095	−49	.175
239	5	17	.064	.052	.060	−66	.179
247	3	17	.044	.029	.039	−76	.160
377	7	18	.161	.147	.154	3	.149
390	5	18	.169	.130	.138	−1	.139
397	3	18	.179	.148	.158	11	.142
379	7	19	.085	.070	.074	−50	.148
386	5	19	.081	.070	.072	−50	.144
399	3	19	.096	.079	.081	−43	.143
382	7	20	.190	.170	.184	15	.160
398	5	20	.200	.169	.192	41	.136
395	3	20	.170	.158	.162	17	.139

* Percentage increase in average *f* relative to tests with 2110 oil.

TABLE 3. *Static friction data at 10-lb load and 100° F. for chromium plate (3C–LP) on 431 stainless steel (431–L)*

Test No.	Position No.	Lubricant Code No.	*f* (tangent)			Percentage increase *	*f* 2110 oil
			Maximum	Minimum	Average		
155	3	13	0.278	0.214	0.252	15	0.219
165	5	13	.210	.201	.205	40	.146
175	7	13	.210	.200	.202	19	.170
157	3	14	.242	.221	.237	12	.212
167	5	14	.217	.207	.211	37	.154
171	7	14	.211	.196	.199	21	.164
159	3	15	.233	.209	.226	24	.182
163	5	15	.166	.157	.161	13	.143
173	7	15	.199	.190	.195	14	.171
269	7	16	.172	.168	.170	−19	.210
278	5	16	.171	.110	.150	−13	.175
283	3	16	.139	.121	.130	−37	.207
271	7	17	.058	.050	.053	−74	.205
276	5	17	.061	.039	.056	−68	.173
285	3	17	.050	.032	.044	−78	.204
429	7	18	.239	.198	.213	10	.193
441	5	18	.270	.238	.253	17	.216
448	3	18	.196	.174	.184	8	.171
431	7	19	.088	.078	.084	−58	.200
437	5	19	.077	.070	.072	−67	.220
450	3	19	.080	.070	.073	−58	.175
433	7	20	.216	.200	.206	6	.194
439	5	20	.243	.238	.240	11	.216
446	3	20	.184	.178	.179	−4	.187

* Percentage increase in average *f* relative to tests with 2110 oil.

TABLE 4. *Static friction data at 10-lb load and 100°F, for chromium plate (3C–LP) on 214 Alcoa alloy (214–L)*

Test No.	Position No.	Lubricant code No.	*f* (tangent)			Percentage increase *	*f* 2110 oil
			Maximum	Minimum	Average		
179	7	13	0.239	0.182	0.221	12	0.198
190	5	13	.248	.187	.221	19	.186
200	3	13	.230	.199	.215	7	.201
182	7	14	.211	.200	.204	9	.188
192	5	14	.228	.199	.211	10	.191
196	3	14	.231	.200	.214	3	.207
184	7	15	.230	.199	.214	14	.188
188	5	15	.346	.267	.296	58	.187
198	3	15	.223	.196	.212	3	.206
289	3	16	.211	.172	.192	−4	.200
299	5	16	.200	.180	.185	−15	.218
303	7	16	.200	.180	.192	−10	.214
326	3	17	.068	.048	.062	−71	.214
297	5	17	.200	.174	.195	−12	.245
305	7	17	.137	.049	.077	−63	.210
454	3	18	.367	.253	.292	36	.214
467	5	18	.460	.340	.406	79	.226
473	7	18	.470	.360	.425	109	.203
456	3	19	.084	.080	.080	−58	.192
463	5	19	.090	.073	.082	−60	.204
475	7	19	.090	.078	.081	−62	.216
458	3	20	.420	.300	.355	70	.209
465	5	20	.430	.216	.310	41	.220
471	7	20	.420	.196	.303	52	.200
539	7	21	.260	.220	.242	17	.206
555	5	21	.220	.190	.200	2	.197
565	3	21	.190	.170	.180	−16	.214
541	7	22	.330	.320	.323	63	.198
551	5	22	.290	.270	.279	28	.217
567	3	22	.270	.260	.265	26	.210
543	7	23	.180	.150	.169	−11	.190
553	5	23	.180	.150	.169	−21	.213
563	3	23	.190	.140	.165	−25	.221
545	7	24	.280	.230	.261	33	.196
557	5	24	.300	.260	.284	46	.195
569	3	24	.270	.250	.265	35	.196
547	7	25	.260	.220	.245	32	.185
559	5	25	.280	.230	.256	27	.202
571	3	25	.234	.220	.225	18	.190
645	7	31	.140	.040	.111	−49	.219
653	5	31	.120	.070	.099	−52	.206
657	3	31	.140	.070	.114	−37	.181
647	7	32	.212	.196	.201	0	.201
651	5	32	.230	.180	.195	−4	.204
659	3	32	.180	.170	.173	−14	.201

* Percentage increase in average *f* relative to tests with 2110 oil.

TABLE 5. *Static friction data at 10-lb load and 100° F, for 304 stainless steel (304–LP) on 214 Alcoa alloy (214–L)*

Test No.	Position No.	Lubricant Code No.	*f* (tangent)			Percentage increase *	*f* 2110 Oil
			Maximum	Minimum	Average		
108	7	13	0.223	0.182	0.214	1	0.212
116	5	13	.232	.217	.223	8	.206
148	3	13	.293	.237	.277	14	.239
110	7	14	.211	.196	.200	−7	.216
118	5	14	.222	.201	.208	0	.207
150	3	14	.233	.216	.221	−8	.238
112	7	15	.219	.181	.208	2	.203
125	5	15	.307	.252	.285	26	.217
146	3	15	.316	.272	.289	27	.227
309	7	16	.234	.192	.210	−7	.226
317	5	16	.180	.176	.179	−19	.220
321	3	16	.226	.205	.215	−12	.245
311	7	17	.180	.120	.168	−21	.214
315	5	17	.060	.040	.057	−75	.227
323	3	17	.070	.045	.060	−75	.240
403	3	18	.310	.250	.277	31	.211
414	5	18	.360	.250	.309	47	.210
422	7	18	.350	.298	.325	78	.183
405	3	19	.082	.070	.072	−64	.201
412	5	19	.122	.083	.092	−59	.222
424	7	19	.085	.073	.078	−58	.185
407	3	20	.367	.250	.311	50	.207
416	5	20	.380	.319	.359	64	.219
420	7	20	.290	.250	.258	39	.185

* Percentage increase in average *f* relative to tests with 2110 oil.

TABLE 6. *Static friction data at 10-lb load and 100° F, for 1050 steel (1050–LP) on cast iron (2–L)*

Test No.	Position No.	Lubricant Code No.	*f* (tangent)			Percentage increase *	*f* 2110 Oil
			Maximum	Minimum	Average		
130	5	13	0.360	0.326	0.340	19	0.286
138	7	13	.357	.317	.344	18	.292
132	5	14	.378	.292	.318	10	.290
140	7	14	.386	.297	.324	6	.305
134	5	15	.367	.329	.353	19	.298
142	7	15	.318	.308	.312	4	.302
251	3	16	.173	.148	.160	−23	.207
259	5	16	.192	.171	.177	−43	.308
263	7	16	.210	.192	.198	−13	.227
253	3	17	.078	.060	.070	−67	.213
257	5	17	.088	.038	.057	−81	.299
265	7	17	.082	.045	.057	−76	.237
479	7	18	.240	.220	.222	25	.178
491	5	18	.220	.168	.189	10	.172
497	3	18	.270	.240	.249	23	.202
481	7	19	.090	.090	.090	−51	.186
487	5	19	.085	.074	.078	−59	.191
499	3	19	.100	.090	.098	−60	.246
483	7	20	.210	.194	.201	14	.176
489	5	20	.200	.196	.198	4	.190
495	3	20	.150	.150	.150	−13	.173

* Percentage increase in average *f* relative to tests with 2110 oil.

VII. Conclusion

For static friction under the conditions used for these tests, the following indications have been obtained:

1. Polished surfaces sliding on lapped surfaces tend to give lower friction and less variation than ground surfaces sliding on ground surfaces.

2. For the metal specimens tested, with most of the lubricants, the heat-treated stainless steel combinations gave the lowest friction. The chromium-plated rider on the heat-treated stainless steel plate also gave correspondingly low friction with lubricants 16, 17, and 19. For the chromium-plated rider and the 304 stainless steel rider on the Alcoa 214 alloy plate, and for the 1050 steel rider on the cast iron plate, the relative friction varied greatly with the lubricant. Each of these combinations gave high friction with one or more lubricants while giving low friction with other lubricants.

3. The lubricants containing molybdenum disulfid gave the lowest friction, whereas mineral lubricatin grease, dry molybdenum disulfide, and the lubrican containing graphite gave friction nearly as low With the above lubricants the friction was about 5 to 60 percent less than with the 2110 reference oil The lubricant containing an oxidized petroleum compound and the one containing a silicone grease gav slightly less friction than the 2110 oil. The chlorinated and fluorinated lubricants without additives and the remaining special lubricants gave higher friction than the 2110 reference oil.

These relative evaluations of friction apply only for static conditions as used in these tests. Any significance with respect to kinetic boundary lubrication is questionable, except possibly in those cases where the velocity approaches zero.

Washington, October 9, 1950.

Journal of Research of the National Bureau of Standards Vol. 46, No. 4, April 1951 Research Paper 2199

Apparatus for the Preparation of Anhydrous Titanium (III) Chloride and Titanium (III) Bromide

J. M. Sherfey

An improved method is described for the preparation of titanium (III) chloride or titanium (III) bromide from the corresponding tetrahalide. The apparatus consists essentially of a reaction kettle, in the upper half of which is suspended a hot tungsten filament. A mixture of hydrogen and the vapor of the refluxing tetrahalide reacts at the surface of the filament, and the resulting solid product collects at the bottom of the vessel.

The laboratory preparation of anhydrous titanium (III) chloride has been described by several workers. The method described by Georges and Stahler [1] has been perhaps the most satisfactory. A stream of hydrogen is saturated with titanium (IV) chloride, and the mixture is passed through an annular space formed by two concentric tubes. The inner wall is electrically heated, and the outer wall is cooled by a water jacket. The mixture reacts at the hot surface, and the resulting trichloride collects on the cold surface. It was found that the rate of production of titanium (III) chloride in the apparatus described was only a few grams per hour and that the yield, particularly with regard to the hydrogen used, was very poor. The product was contaminated with tetrachloride, especially if the temperature of the tetrachloride saturator was high.

The apparatus described below, utilizing the same reaction ($2TiCl_4+H_2 \rightleftharpoons 2TiCl_3+2HCl$), has been found very satisfactory, and 150 to 200 g can be produced in 1 day. The product is about 98 percent pure and can be further purified.

The essential parts of the apparatus are shown in figure 1. The 4-liter reaction kettle, A, has a flanged top with four female standard taper openings, one (34/45) centrally located with three (24/40) joints symmetrically spaced around it. For simplicity these are shown in the drawing as if they were in a straight line.

The center joint, B, of the reaction kettle is fitted with a chimney, C, in the top of which is a rubber stopper, D. Two tungsten rods, E, about 6 mm in diameter, pass through this stopper and support a tungsten filament, F. The diameter and length of this filament are fixed by the power supply available. A filament 1 mm in diameter and 30 cm long requires 38 amperes at 8.6 volts to heat it to 1,000° to 1,100° C, a satisfactory temperature range. Thinner filaments should not be used because they are apt to burn out during a run.

A run is started by flushing the entire apparatus

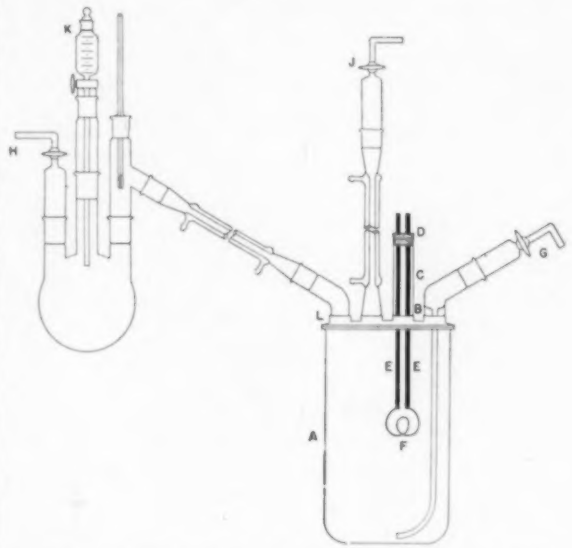

FIGURE 1. *Apparatus for the preparation of anhydrous titanium (III) chloride and titanium (III) bromide.*

A, Pyrex reaction kettle; B, central standard taper joint of reaction kettle; C, chimney; D, rubber stopper; E, 6-mm tungsten rods; F, 1-mm tungsten filament; G, hydrogen inlet; H, initial hydrogen outlet; J, final hydrogen outlets; K, burette.

with dry oxygen-free hydrogen, purified by passing it over hot copper turnings and then over a desiccant such as magnesium perchlorate. After purification the hydrogen should pass through copper tubing or, if necessary, a minimum length of sound rubber tubing. The purified hydrogen is introduced at G and passes through the distillation assembly and out through the stopcock, H, until all the air has been removed. This will also remove moisture and thus prevent the formation of hydrolysis products.

The hydrogen stream is continued while stopcock H is closed and that at J is opened. About 1,500 ml of titanium (IV) chloride is run into the distilling flask through the burette, K, and distillation is started. About 1,000 to 1,500 ml is distilled over into the reaction kettle. The distilling apparatus can then be removed from the reaction kettle and the opening, L, quickly stoppered. The hydrogen

[1] Ber. deut. chem. Ges. **42**, 3200 (1909); see also, Stahler and Bachran, Ber. deut. chem. Ges. **44**. 2906 (1911).

926633—51——3

stream should be very rapid during this operation.

A hemispherical heating mantle is now used to reflux the tetrachloride over the tungsten filament. A heating mantle that entirely encloses the reaction kettle must not be used, as this will cause the tetrachloride to reflux too rapidly and flood the condenser. This situation is detrimental because, after the reduction is started, solid trichloride will be carried out of the apparatus by the hydrogen stream. Most, if not all, of the tetrachloride should be condensed on the walls and top of the reaction flask. Jets of air directed against the upper part of the flask will aid in this.

When the boiling of the tetrachloride has reached equilibrium, the filament is turned on and brought to a bright red heat. Reduction begins with the formation of a dark purple smoke of titanium (III) chloride which collects on the walls of the reaction vessel. Most of these particles are washed down to the bottom by the refluxing tetrachloride.

If for any reason the vessel is cooled, for instance by turning off the filament, the hydrogen flow must be momentarily increased to prevent influx of air as a result of the partial vacuum formed. This influx would cause hydrolysis and oxidation. A length of rubber tubing on outlet J minimizes this danger.

The reaction is continued until the tetrachloride no longer refluxes freely down the sides of the vessel. The filament is then turned off, and the whole reaction kettle is heated to drive off the residual tetrachloride, which tends to be absorbed in the cake of solid trichloride. To condense and remove the tetrachloride, a still head and horizontal condenser must be substituted for the reflux condenser.

The hydrogen stream is continued while the apparatus cools. The flask should be opened and the product bottled in an inert atmosphere. Titanium (III) chloride thus formed often ignites spontaneously when exposed to moist air and invariably does so when gently heated.

In a typical run, 1 liter (1,700 g) of titanium (IV) chloride was distilled into the reaction flask and yielded 154 g of titanium (III) chloride, a conversion of 10 percent. Based on the tetrachloride consumed, the yield of trichloride was about 90 percent.

Analysis of the product gave

	Ti	Cl	Reducing power
Found (percent)	31. 9	67. 6	97. 2, 98. 7
Calculated (percent)	31. 0	68. 9	100. 0

The reducing power was determined by titration with potassium dichromate. The crude product was heated in a vacuum at 200° C, and a small quantity of a volatile impurity was driven off. After this treatment a reduction value of 101.5 percent was obtained, indicating the presence of a small amount of titanium (II) chloride.

It is possible to obtain a much higher percentage conversion, particularly if the whole flask is heated, but two factors must be borne in mind. First, a solid reaction mass at the bottom is no longer being stirred by its own ebullition, and second, the solid cake on the sides, if no longer washed down by the refluxing tetrachloride, tends to build out toward the filament. Either of these factors could result in localized overheating and consequent disproportionation of trichloride into dichloride and tetrachloride.

The rate of formation of titanium (III) chloride is largely determined by the size of the filament. This limitation could be circumvented if a sheet of tungsten, preferably in the shape of a cylinder, were heated by induction.

Titanium (III) bromide has been prepared in the same apparatus. As the tetrabromide is solid at room temperature, hot water or steam is used as a coolant for the condensers (instead of the cold water used in the preparation of trichloride). The tetrabromide is poured hot into the distilling flask and allowed to solidify before flushing with hydrogen. The yield and purity of the product are very similar to those reported for the trichloride.

In some runs a multiple collecting device was used, which made it possible to discard the first fraction of distilled tetrachloride without opening the apparatus. It has not been shown that this is either necessary or beneficial.

WASHINGTON, November 17, 1950

Journal of Research of the National Bureau of Standards Vol. 46, No. 4, April 1951 Research Paper 2200

An Apparatus for Studying Autoignition of Engine Fuels: Results with Normal Heptane and Normal Hexane

William J. Levedahl and Frank L. Howard

A single-cylinder ASTM–CFR fuel-testing engine with a variable compression ratio has been modified to facilitate the study of compression-ignition of homogeneous fuel-air mixtures. An investigation of this type of combustion may lead to a better understanding of engine knock. A cylinder-pressure limiter is described that permits firing a small number of cycles, the first of which is uncontaminated by exhaust gases. Pressure-crank angle oscillograms of the process are shown. The combustion of *n*-heptane and *n*-hexane was found to take place in two distinct stages over a wide range of fuel-air ratios. The pressure at which the first-stage reaction begins is relatively unaffected by the mixture composition throughout the firing range. The second, or firing, stage occurs most readily at fuel-air ratios near stoichiometric, and ionization during firing is highest in this range of mixture compositions. No ionization was observed during the first stage of combustion with either fuel.

I. Introduction

Many investigators have recognized two major stages in the combustion of hydrocarbons. The first stage is characterized by a relatively slow reaction following an induction period whose duration depends on experimental conditions such as temperature, pressure, fuel-air ratio, presence of additives, and the condition and area of the surface exposed to the mixture. Cold flames, blue luminescence, and relatively small changes in pressure are some of the physical phenomena associated with the first-stage reactions.

From a chemical standpoint the first isolable material from this reaction is peroxidic in character, and hydroperoxides have been identified. The exact mechanism of peroxide formation is unknown, but it is presumed to result first from the formation of short-lived free radicals from the hydrocarbon molecules, which in turn react with oxygen to form peroxides. Decomposition of these hydroperoxides gives rise to new oxygenated free radicals that act as carriers for the propagation of a chain reaction, some of whose intermediate products have been identified as aldehydes, ketones, and acids.

The progress of the first-stage reaction is governed by experimental conditions and by the molecular configuration of the fuel. It is unlikely that it ever reaches a condition of equilibrium in an engine, or even that a concept of equilibrium could be applied to the reaction. Possibly the first-stage reaction influences the second or "firing" stage of combustion by providing certain essential chain carriers. It may be that the second stage will not occur until the first stage has progressed to a certain point.

In a spark-ignition engine, normal combustion is initiated at the spark plug, and a flame front travels through the mixture from this point of origin, compressing the unburned mixture of fuel and air ahead of it. This unburned portion of the charge is frequently called the "end gas." The temperature of the end gas is increased due to adiabatic compression by the burning gases in and behind the flame front and by motion of the piston. This temperature rise, accompanied by increases of pressure and density, sometimes causes first-stage reactions to occur, often followed by a very rapid second-stage reaction, which may cause combustion knock if it takes place with sufficient rapidity. It is thought that investigation of the characteristics of these reactions may prove helpful in obtaining a better understanding of combustion knock.

In 1947–48 Levedahl and Sargent [1] [1] studied the autoignition characteristics of diethyl ether, *n*-heptane, and other fuels in a single-cylinder CFR [2] engine in which a well-mixed charge was ignited by compression in the cylinder. Diagrams of this indicated pressure versus crank angle showed very marked and reproducible evidence of a two-stage combustion reaction. Diagrams made at lower compression ratios showed results similar to those obtained by Peletier [2] and Muhlner [3] in that only the first stage occurred. Peletier made a number of runs at compression ratios low enough to preclude firing and measured the extent of the first stage reaction by measuring the temperature of the exhaust gas. Mulner went further with this method, making graphs of the rise of temperature and the torque obtained at many fuel-air ratios and compression ratios with several gasolines, and obtaining some pressure diagrams.

Retailliau, Ricards, and Jones [4] extended this technique by making analyses of the exhaust-gas and other refinements. Pastell [5] carried out experiments with the same general type of apparatus and added a photomultiplier tube to detect the radiation from cool-flames during the (first-stage) reactions. He also measured the energy liberated by these reactions.

A number of single-cycle rapid-compression machines [6 to 15] have been built for the purpose of studying autoignition. Most productive of these has been the MIT rapid compression machine with which Leary and coworkers [12 to 15] have obtained significant results from measurements of the delay

[1] Figures in brackets indicate the literature references at the end of this paper.
[2] The Motor Fuels Division of the Cooperative Fuel Research Committee developed the CFR engine for knock testing of engine fuels.

time in the ignition of several fuels under many conditions.

In order to extend and augment work previously reported on compression ignition studies, a program has been initiated to determine how the structure of the fuel affects the duration of preflame reactions and the pressure developed by these reactions. It is planned to use several six-carbon hydrocarbons as fuels. These compounds have a variety of structures; paraffins, naphthenes, olefins, and an aromatic being included. This paper describes the apparatus and the methods of operation, and presents the results of preliminary experiments in which *n*-heptane and *n*-hexane were used as fuels.

II. Apparatus

Engine. Figure 1 shows the ASTM supercharge method fuel-rating engine [16], modified for the present work, together with the accessory equipment used. A special cylinder was obtained with three holes for 18-mm spark plugs around its circumference and one ⅞-in. hole in the top. The springs beneath the cylinder were removed and the zero setting on the micrometer used to measure the cylinder height was changed 0.3 in. so that compression ratios in excess of 18:1 could be obtained. An alternating-current dynamometer was used to maintain the engine speed at 600, 900, 1,200, or 1,800 rpm.

Cooling system. Immediately before entering the cylinder jacket, the cooling water passed through the central tube of a heat exchanger consisting of ¼-in. copper tubing within a ⅝-in. tube. Either steam or water could be passed through the annular space. In this way the temperature of the cylinder jacket could be maintained constant at any desired temperature between 150° and 212° F when the engine was in operation under either motoring or firing conditions. A motor-driven vane pump circulated the cooling water through the jacket from a coolant tower (A, fig. 1) used as a reservoir. The exhaust system was cooled by passing water through coils wound on the exhaust pipe, B, and by water sprayed directly into the gases.

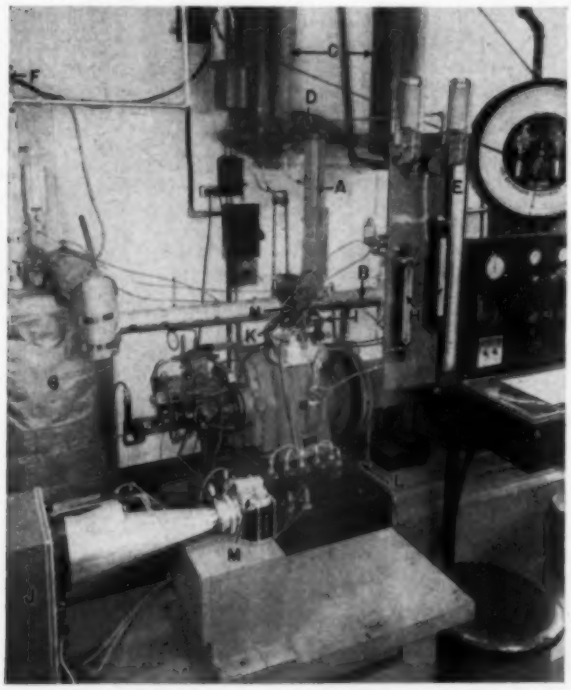

FIGURE 1. *Engine and auxiliary equipment.*

Induction system. Air for the mixture was supplied at high pressure, passed through a water trap and was then throttled to 40 psig. A pair of surge tanks, C, and a thermostatically controlled air heater insured a steady flow of air through an ASME sharp-edged orifice plate, D. The drop in pressure across the orifice was read directly on a manometer, E, calibrated in pounds of air per hour. Following another throttle valve, which automatically maintained inlet pressure at the desired level, the air passed over a 3,000-w electric heater, F. Fuel was injected into the airstream as it left the heater; vaporization and thorough mixing took place in a large steam-jacketed mixing tank, G. The charge then flowed over a thermometer and through a copper-tube flame trap into the engine. The fuel was metered by one of two calibrated flowmeters, H, with a combined range of approximately 0.5 to 20 lb of fuel per hour, and the rate was controlled manually with a needle valve. The composition of the fuel-air mixture is expressed throughout this paper as fraction of stoichiometric fuel, and is given the symbol S in the figures.

Pressure-measuring equipment. In order to obtain records of the variation of pressure with time during combustion cycles it was necessary to use a sensitive and sturdy pressure pickup with a rapid response and a stable calibration. A Draper-Li strain-gauge unit, I, with an extra-heavy catenary diaphragm and strain-generating tube was selected. A direct-current bridge circuit, of which the pickup formed two legs, and an electronic amplifier fed a voltage that varies linearly with cylinder pressure to an oscilloscope, J, with direct-current amplification on the deflection plates. A resistor in parallel with one leg of the bridge was automatically cut into the circuit once each cycle by a microswitch and caused a calibration mark to be made on the screen at a known pressure. As the indicator operated at a voltage well above ground, a 22½-v battery-potentiometer circuit was used to put a steady opposited bias on the *y*-axis input, and to permit use of the direct-current amplifier on the oscilloscope.

Ionization-detecting equipment. Ionization of the gases in a spark ignition engine has been observed in both knocking and nonknocking combustion [17,18]. In order to investigate the relationship between ionization and time in autoignition cycles, a standard 18-mm spark plug, K, was used as the ionization gap

in a circuit formed by a 135-v battery and a 250,000-ohm resistor. The voltage drop across the resistor was proportional to the ionization current and was fed to the vertical amplifier of the oscilloscope.

Timing and recording equipment. In order to correlate the pressure-time and ionization-time traces on the oscilloscope with crank angle, it was desirable to have the beam sweep across the face of the tube once each revolution and have the trace marked to indicate known crank positions. These two functions were performed by a photoelectric cell, L, which reacted to a beam of light reflected from fine strips of tinfoil located on the black flywheel so as to register top center, 30°, 60°, and 90° before top center. The strip at 90° before top center triggered the sweep, and the others produced small vertical marks. The oscilloscope traces were photographed with a camera, M, whose exposure time was set to expose the desired number of consecutive cycles. The shutter was tripped at a selected time in the cycle by a microswitch and solenoid actuated by a projection on the engine camshaft.

Cylinder-pressure limiter. It is often desirable to record combustion cycles in the absence of residual exhaust gases and hot spots in the combustion chamber. This can be done without disturbing the flow of fuel and air to the engine by keeping the pressure in all except a few chosen cycles from rising enough to cause appreciable chemical reaction. A pressure limiting device was developed for this purpose and mounted in the upper cylinder hole (N, fig. 1). It is shown in assembly and layout in figure 2.

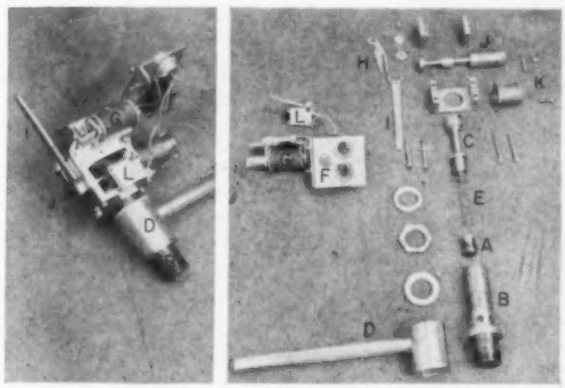

FIGURE 2. *Cylinder-pressure limiter.*

When the pressure in the cylinder exceeds 10 psig, the valve (A, in fig. 2) leaves its seat in the body, B, and moves upward until stopped by the piston, C. The gases in the cylinder can then escape through the annular space between A and B, through holes to the exhaust collector, D, and thence to an exhaust system. On the power stroke, when the pressure again drops below 10 psig, the limiter valve, A, is closed by the spring, E, and remains closed throughout the exhaust and intake strokes, thus permitting the induction of a full charge of combustible mixture.

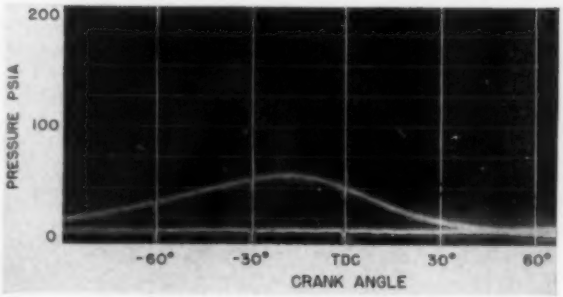

FIGURE 3. *Pressure—crank-angle diagram made with pressure limiter open at a compression ratio of 6.59.*

In this way the mixture can pass through the engine without being burned.

When it is desired to fire the mixture the switch, F, is closed, and at top center on the next exhaust stroke a microswitch actuated by the engine camshaft completes the circuit to the solenoid, G, which pulls the trigger, H. The lever, I, which is attached to the camshaft, J, is released, permitting the torsion spring, K, to rotate the cam against the piston, C. After the cam has rotated about 60° the piston is locked firmly against the valve, A, by the cam, permitting the pressure in the cylinder to rise to that of full compression.

When the lever, I, rotates, it operates the microswitch, L, and when bottom center on the inlet stroke is reached another microswitch is closed by the camshaft to complete the circuit to the recording camera. Thus the film is exposed during the first cycle after closing the pressure limiter and for subsequent cycles until the shutter is closed. Figure 3 is a typical pressure record made at 900 rpm with a compression ratio of 6.6 and with the pressure limited in the manner just described. The pressure reached a maximum of about 47 psig at approximately 20° before top center and dropped off rapidly thereafter.

III. Experimental Procedure

Steady firing conditions. The vaporizing tank was preheated by steam, and the engine was motored (driven by the dynamometer) until the inlet air temperature reached the desired value. With the compression ratio set at about 8:1, the fuel was introduced at a rate to give mixtures from 0.5 to 0.7 of stoichiometric. Firing usually started immediately; if not, the compression ratio was increased until it did occur. When the rates of flow of the fuel and air and the temperatures had been adjusted to the desired values, the oscilloscope trace of one cycle was photographed.

Cylinder-pressure limiter. The engine was motored at full compression without fuel, and hot water was circulated through the cooling jacket until the temperatures were stabilized. The pressure limiter was placed in operation, the desired flow of fuel was established, and all temperatures were again allowed to stabilize. The exposure time

of the camera was set to expose three cycles, and the limiter switch, F, was closed. The limiter lever was raised manually after three firings. As the temperature equilibrium is virtually undisturbed by three firings, series of observations can be made in rapid succession.

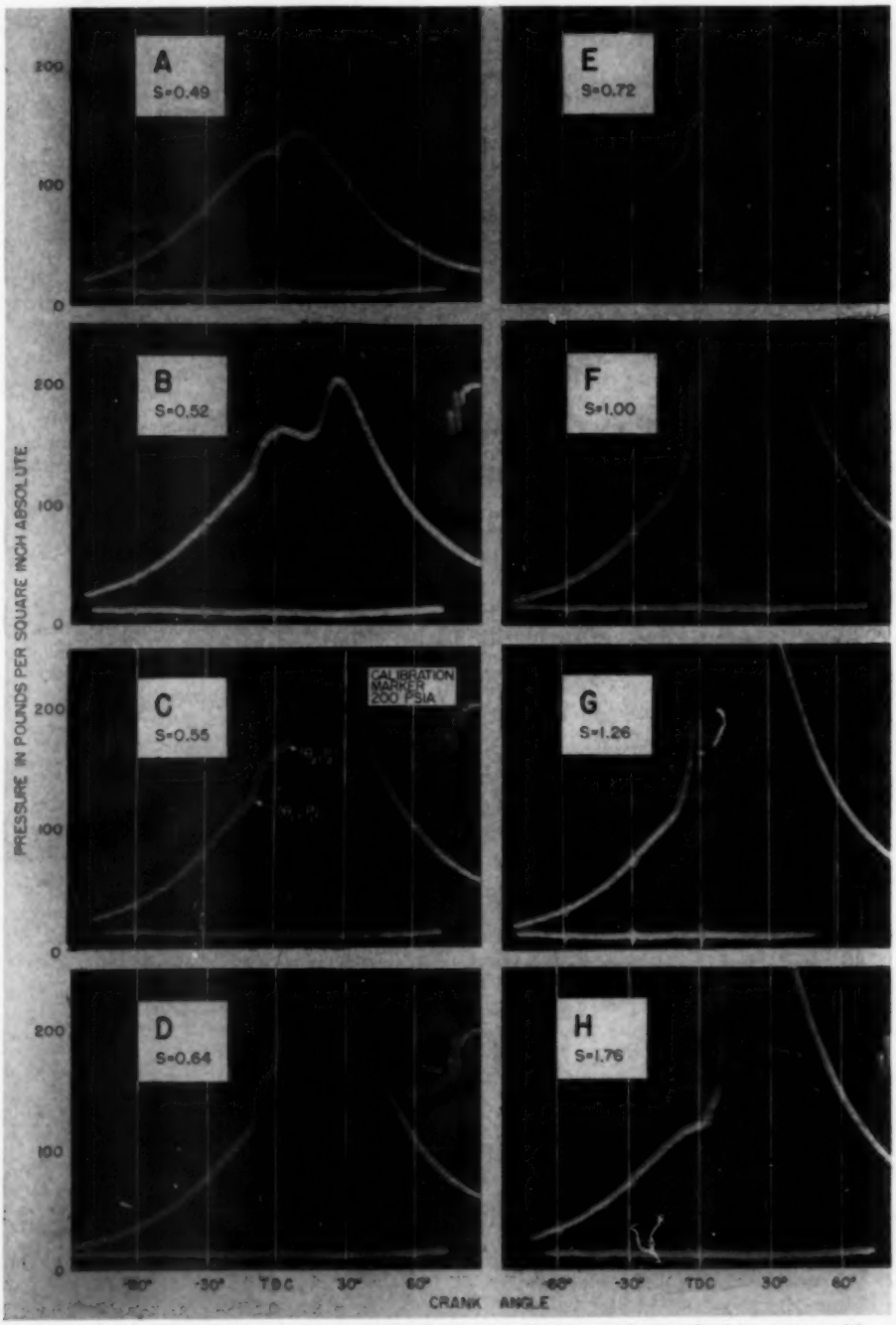

FIGURE 4. *Pressure-crank angle diagrams of n-heptane combustion with several mixture compositions at 600 rpm, 220° F inlet temperature, 180° F jacket temperature, air consumption 18 lb/hr, and compression ratio 5.68*

IV. Results and Discussion

1. Steady Firing of n-Heptane

Effect of mixture composition. The engine was operated on *n*-heptane over a wide range of mixtures and compression ratios under the following conditions: inlet temperature, 220° F; jacket temperature, 180° F; air rate 18 lb/hr; speed, 600 rpm. At a compression ratio of 7:1, the engine ran steadily at all fuel mixtures between 0.3 and 2.5 times stoichiometric. No knocking was observed with the leanest mixtures, but all those richer than about 0.5 of stoichiometric knocked violently. Decreasing the compression ratio reduced both the knock intensity and the range of fuel-air ratios that would fire. Figure 4 shows one set of typical diagrams of pressure versus crank angle taken at a compression ratio of 5.68 and at various fuel compositions in the range 0.49 to 1.76. The occurrence of two reactions, as indicated by sudden changes in the slope of the pressure curve, are first evident in figure 4, B. The coordinates of pressure and crank angle at which these changes in slope occur are designated by P_1 and θ_1 and by P_2 and θ_2 for the first and second stages, respectively, in figure 4, C.

Firing was steady and reproducible from cycle to cycle at all mixture ratios. In figure 4, A, only the first-stage reaction took place. In figure 4, B, the mixture was at the "critically lean" point, that is, a very small decrease in the fuel concentration would prevent the second- or firing-stage of the reaction from occurring. Conversely, a very small increase in fuel would cause steady firing.

Observations of pressure and crank angle made from figure 4 are plotted as functions of mixture composition in figures 5 and 6, respectively. Figure 5 shows that the pressure, P_1, necessary to start the first-stage reaction is nearly constant over a wide range of mixtures above the critically lean value of 0.52. The pressure at which the second stage begins is lowest near stoichiometric and highest for lean mixtures. Figure 6 shows that the time θ_1 (in terms of crank angle) at which reaction begins is nearly constant, except for very lean and very rich mixtures. It is possible that the reaction starts later in rich mixtures because of their lower specific heat ratio; the temperature and pressure required to start the reaction are not reached until later in the piston stroke. The crank angle at which firing occurs (θ_2) decreases sharply as the fuel-air ratio is increased in the very lean range, flattens out between about 0.6 and 0.8 stoichiometric then drops more gradually as S is increased. The duration of the first-stage reaction ($\theta_2 - \theta_1$) decreases sharply in the lean range, then decreases more gradually as the mixture becomes richer.

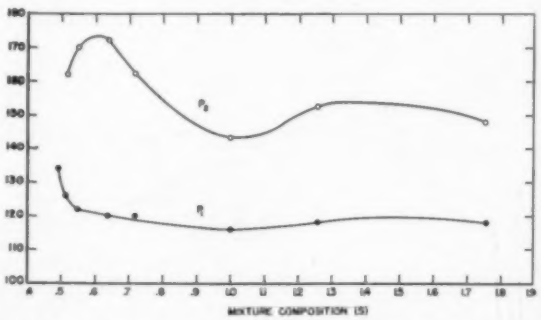

FIGURE 5. *Plot of data from figure 4: Effect of mixture composition on pressures for beginning of first (P_1) and second (P_2) stages of combustion.*

Mixture composition is expressed as fraction of stoichiometric fuel.

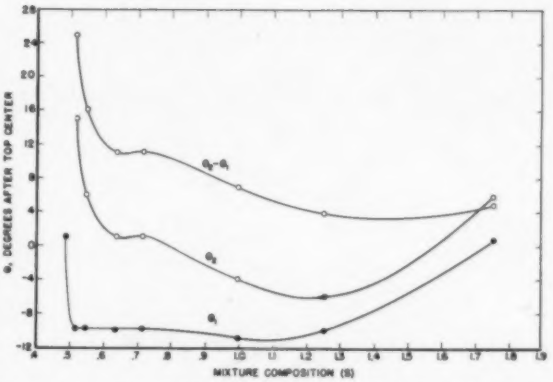

FIGURE 6. *Plot of data from figure 4: Effect of mixture composition on crank angles at which the first stage (θ_1) and second stage (θ_2) of combustion begin, and duration of the first-stage reaction ($\theta_2 - \theta_1$).*

Mixture composition is expressed as fraction of stoichiometric fuel.

2. Ionization as an Indication of Firing

Diagrams of ionization versus crank angle. The engine was operated under several combinations of mixtures, engine speed, and inlet temperature to determine the relation between the ionization at one location in the cylinder and the corresponding pressure. In no case was any ionization detected during the first-stage reaction, but a sharp rise in ionization was always noted exactly at the onset of the second stage of combustion. Typical ionization curves for experiments in which *n*-hexane was used are shown in figure 7. Figure 7, A, shows a low wide peak characteristic of lean mixtures, and figure 7, B, shows a curve typical of richer mixtures. Figure 7, C, shows three consecutive cycles, in each of which the sudden rise in ionization current occurred at the same crank angle. The maxima (not shown in this curve) show cycle-to-cycle variations as high as 20 percent. After passing the peak, the traces show considerable oscillation.

Figure 8 shows the effect of mixture composition on peak ionization current, using *n*-hexane as fuel. In every case the compression ratio was set to cause the onset of ionization at exactly top center. When the fuel content of the mixture was increased from 0.5 to 1.1 stoichiometric, the ionization increased about 200 times. Points taken at three engine speeds and two inlet temperatures lie very nearly

on the same curve, and data taken with *n*-heptane under comparable conditions have shown similar results. From this it would appear that peak ionization in autoignition is primarily a function of mixture composition, whereas the changes in other variables cause only secondary effects.

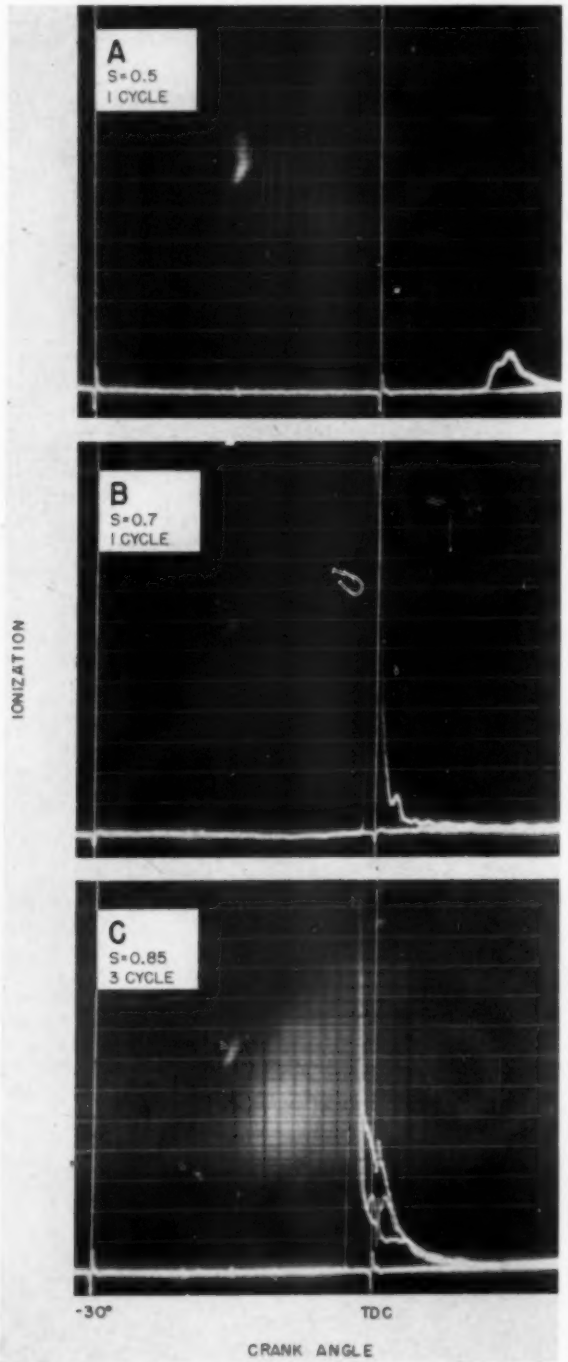

FIGURE 7. *Oscillograms of ionization current at three mixture compositions with n-heptane as fuel.*

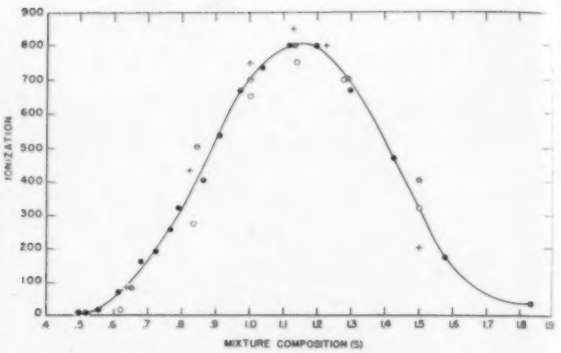

FIGURE 8. *Effect of mixture composition on ionization with n-hexane as fuel.*

The compression ratio was varied to maintain firing at top center. ○, 600 rpm, T inlet = 220° F; ●, 900 rpm, T inlet = 220° F; +, 1,200 rpm, T inlet = 220° F; –, 900 rpm, T inlet = 150° F. Ionization is expressed as tenths of an inch deflection on the oscilloscope, at full gain. Higher readings were made possible by attenuation. Mixture composition is expressed as fraction of stoichiometric fuel.

Effect of mixture composition on the compression ratio required to cause firing at top center. The compression ratios used to obtain the points in figure 8 are plotted against mixture composition in figure 9.

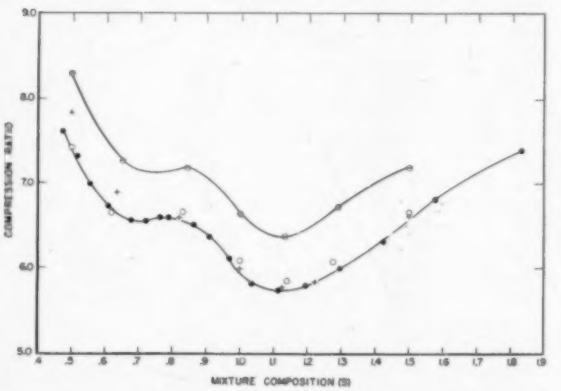

FIGURE 9. *Effect of mixture composition on compression ratio required to maintain continuous firing at top center, with n-hexane as fuel.*

○, 600 rpm, T inlet = 220° F; ●, 900 rpm, T inlet = 220 °F; +, 1200 rpm, T inlet = 220° F; –, 900 rpm, T inlet = 150° F. Mixture composition is expressed as fraction of stoichiometric fuel.

The effect of engine speed on the required compression ratio is slight, decreased inlet temperature consistently raises the requirement throughout the mixture range. The effects of fuel composition are great, however, with the minimum requirement being at a point slightly richer than stoichiometric. With mixtures between 0.6 and 0.8 stoichiometric there is a reversal of curvature that is comparable to the reversal in the firing angle curve (θ_2) of *n*-heptane in figure 6. The reasons for this are not yet understood.

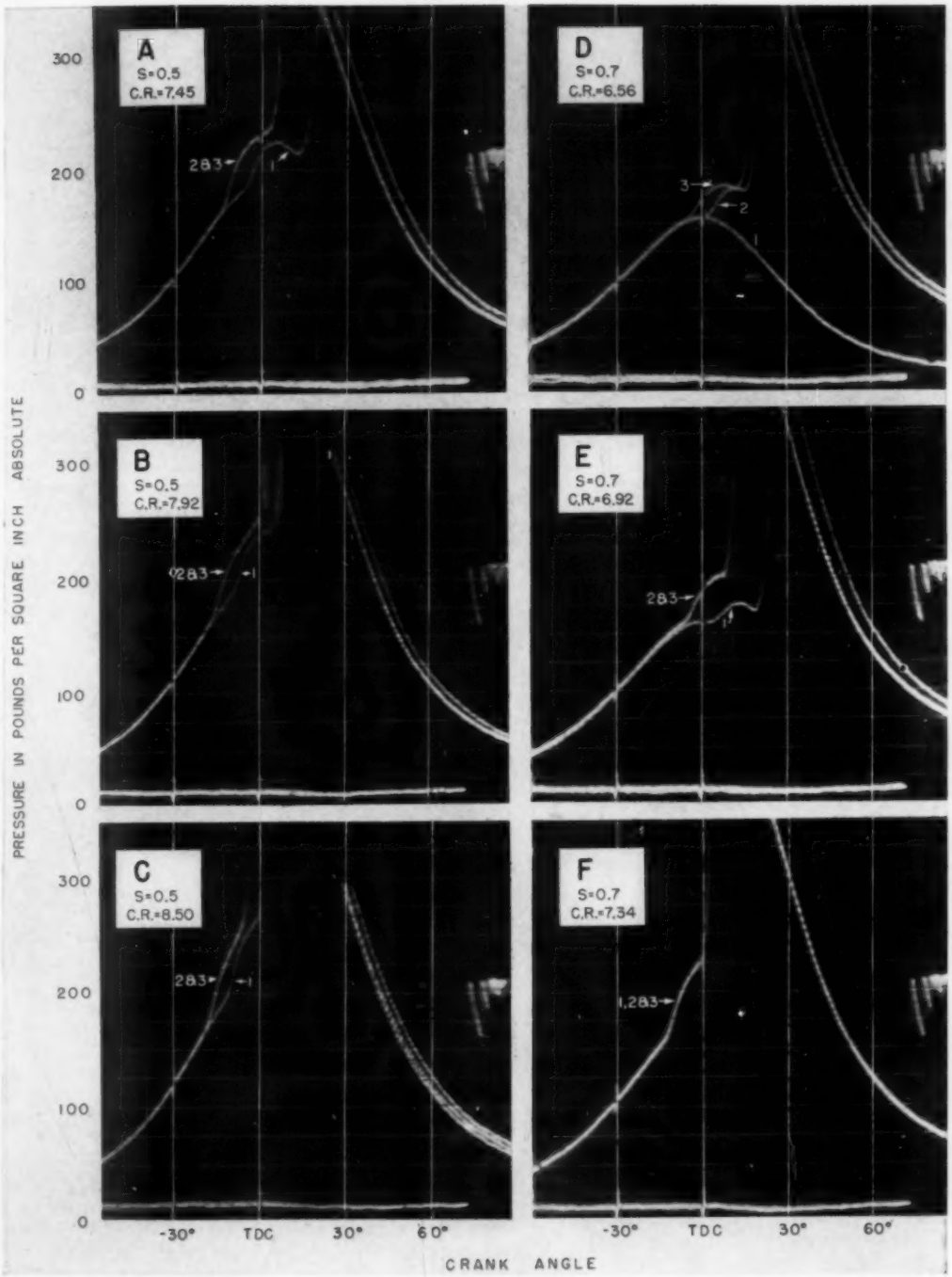

FIGURE 10. *Pressure-crank angle oscillograms, showing effect of compression ratio on combustion of n-hexane at two mixture compositions.*

The first three cycles after closing the pressure limiter are shown. Other conditions: 900 rpm, 220° F inlet temperature, 212° F jacket temperature, 30 lb/hr air consumption.

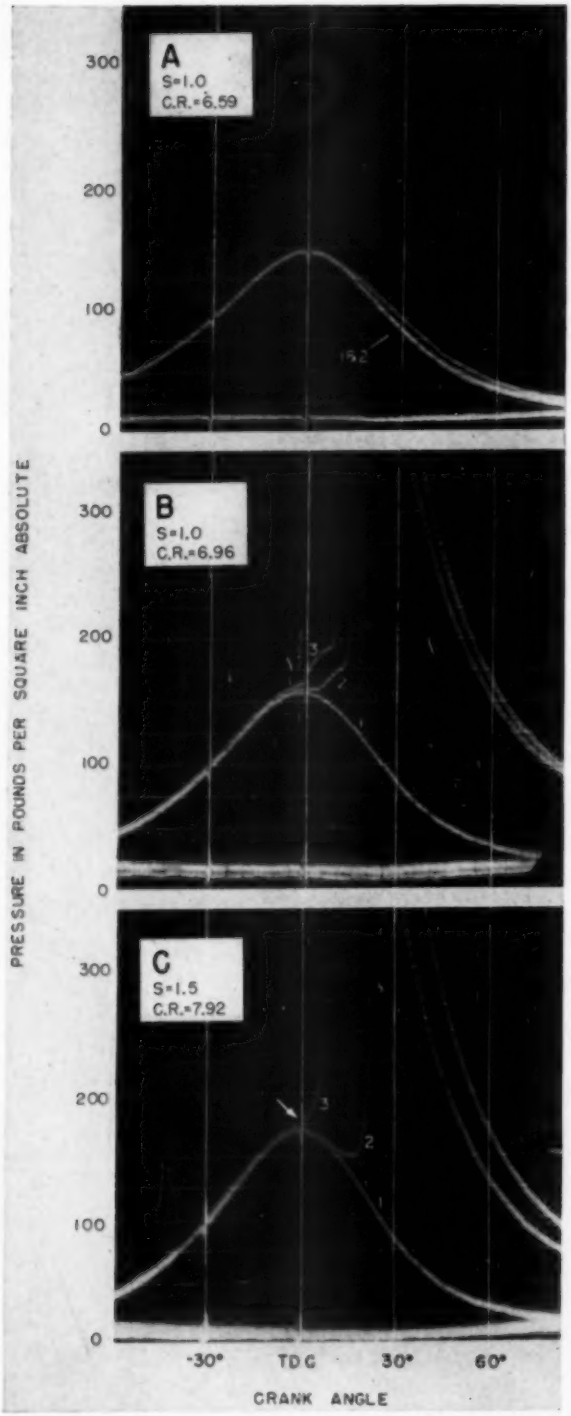

FIGURE 11. *Pressure-crank angle oscillograms at richer mixture.*

Continuation of figure 10.

3. Experiments with n-hexane with the cylinder pressure limiter

The cylinder-pressure limiter was installed for the rest of the work with *n*-hexane. Figures 10 and 11 show diagrams of pressure versus crank angle made at 900 rpm, 212° F jacket temperature, 220° F inlet temperature, and 30-lb/hr air consumption. At each mixture the first set of observations was made at the compression ratio that caused firing at top center under steady-firing conditions (see fig. 9). Subsequent observations were made at progressively higher compression ratios, and each was repeated to determine reproducibility. Average differences amounted to less than 1° of crank angle and 1 psi for θ_1 and P_1, respectively. An accurate determination of the pressure at which firing begins is difficult because the slope of the curve at that point is steep enough to cause considerable reading error.

The oscillograms in figure 10 (A, B, and C) were made at progressively increased compression ratios with a mixture of 0.5 stoichiometric. The superposed pressure curves of the second and third cycles show earlier firing than in the first cycle at all three compression ratios. This fact seems to indicate that residual exhaust gases from one cycle had an accelerating effect on combustion in the next cycle. At a richer mixture the first cycle in figure 10, D, showed no perceptible reaction, but the second and third cycles fired. At higher compression ratios (fig. 10, E, and F) all three cycles fired.

Figure 11, A, shows a slight first-stage reaction beginning at about 10° after top center on the third cycle with a stoichiometric mixture. Several cycles later (not shown in the figure) the engine began to fire. When the compression ratio was raised (fig. 11, B), no firing occurred on the first cycle, but the second and third cycles fired progressively earlier. It appears that the residual gases from a motored cycle may have an accelerating effect on the reactions in the next cycle even though no perceptible reaction took place in the first.

With a very rich mixture, 1.5 times stoichiometric, figure 11, C, shows that firing began very late on the second cycle and near top center on the third. Only a slight evidence of a first-stage reaction is apparent; in the third cycle it appears as a fillet (shown by arrow) between the compression and firing parts of the pressure trace.

The pressure rise due to first-stage reactions decreases as the mixture becomes richer; with the leaner mixtures it is apparently necessary for the first stage to progress farther before the second stage can begin. At the higher fuel concentration it was necessary to use much higher compression ratios to cause firing when the engine is being motored than those shown in figure 9 for steady firing conditions. This phenomenon may be attributed to the large difference between the temperatures in a motoring and a heavily knocking engine.

V. Conclusions

1. *n*-heptane and *n*-hexane both evidence a pronounced two-stage autoignition reaction over a wide range of operating conditions.

2. When all other conditions are held constant, the pressure and crank angle at which the first-stage reaction begins in a steadily firing engine are nearly constant over a range of mixture compositions from critically lean to 1.2 times stoichiometric.

3. The duration of the first stage of the reaction decreases as the mixture is made richer up to about 1.2 stoichiometric, then remains nearly constant.

4. Considerable ionization occurs in the cylinder during firing, but none was observed during the first-stage reaction. The ion concentration is affected greatly by fuel-air ratio and is relatively unaffected by changing other operating variables.

5. When residual gases from either a first- or second-stage combustion are in the cylinder, the charge will burn earlier than when uncontaminated.

The authors are grateful to E. F. Fiock, Chief of the Combustion Section, for his advice and assistance in preparing the manuscript of this report.

VI. References

[1] W. J. Levedahl and G. W. Sargent, Jr., Auto-ignition in an internal combustion engine, Thesis, B. S., Mech. Eng., MIT (1948).

[2] L. A. Peletier, S. G. van Hoogstraten, I. Smittenberg, and L. P. Kooymann, Reactions chemique prealables dans un moteur a essence, Chaleur et Industrie **20,** 120 (1939).

[3] E. Muhlner, Researches on preliminary chemical reactions in spark-ignition engines, NACA Tech. Note 1049 (June 1943).

[4] E. R. Ratailliau, H. A. Ricards, Jr., and M. C. K. Jones, Precombustion reactions in the spark ignition engine, SAE Quarterly Trans. (July 1950).

[5] D. L. Pastell, Precombustion reactions in a motored engine, Preprint of paper presented at SAE Summer Meeting (1950).

[6] H. T. Tizard and D. R. Pye, Experiments on the ignition of gases by sudden compression, Phil. Mag. **44,** 179, 121 (July 1922).

[7] H. T. Tizard and D. R. Pye, Ignition of gases by sudden compression, Phil. Mag. **1,** 1094 (May 1926).

[8] W. Jost, Reactions of adiabatically compressed hydrocarbon-air mixtures. Third Symposium on Combustion, Flame and Explosion Phenomena, p. 424 to 432 (Williams & Wilkins Co., Baltimore, Md., 1949).

[9] von H. Teichmann, Reaktionskinetische untersuchungen zum klopfvorgang. II., Z. Elektrochem **47,** No. 4, 297 (April 1941).

[10] W. Jost, Explosion and combustion processes in gases (Julius Springer, Berlin, 1939).

[11] F. A. F. Schmidt, Bericht uber die grundsatzlichen forschungsarbeiten uber den zundvorgang, Schriften der Deutschen Akademie der Luftfahrtforschung **54,** 77 (1942).

[12] W. A. Leary, E. S. Taylor, C. F. Taylor, and J. U. Jovellanos, A rapid compression machine suitable for studying short ignition delays, NACA Tech. Note 1332 (Feb. 1948).

[13] W. A. Leary, E. S. Taylor, C. F. Taylor, and J. U. Jovellanos, The effect of fuel composition, compression pressure, and fuel-air ratio on the compression-ignition characteristics of several fuels, NACA Tech. Note 1470 (March 1948).

[14] J. U. Jovellanos, E. S. Taylor, C. F. Taylor, and W. A. Leary, An investigation of the effect of tetraethyl lead and ethyl nitrate on the auto-ignition characteristics of iso-octane and triptane, to be published by NACA.

[15] C. F. Taylor, E. S. Taylor, J. C. Livengood, W. A. Rusell, and W. A. Leary, The ignition of fuels by rapid compression, SAE Quarterly Trans. (April 1950).

[16] ASTM Manual of engine test methods for rating fuels (American Society for Testing Materials, Philadelphia, Pa., March 1948).

[17] Charles E. Hastings, Ionization in the knock zone of an internal combustion engine, NACA Tech. Note 774 (Sept. 1940).

[18] R. Vicknievsky, Trans. Faraday Soc. XLII, No. 268, 322 (March–April 1946).

WASHINGTON, October 2, 1950.

Journal of Research of the National Bureau of Standards Vol. 46, No. 4, April 1951 Research Paper 2211

Creep of High-Purity Aluminum

William D. Jenkins

A study was made of cold-drawn aluminum at 105° F, to determine the effects of variations of creep rate on the mechanism of deformation. Strain-hardening was found to decrease monotonically with increase in strain during first stage of creep. The extension on loading and the extension at the beginning of the third stage both increased with increase in stress. Cyclic temperature changes appeared to increase the ductility. Discontinuous flow was evidenced in constant-load creep tests at 105° F and in tensile tests conducted at 80° F. Conformance to Andrade's law of transient flow was found within a limited range of strain rates. Sigmoidal curves were produced that depicted the relationship between stress and creep rate. A mechanism of flow based on observed structural changes is proposed.

I. Introduction

Many empirical formulas have been developed and used with rather limited success to evaluate the relationships between temperature, stress, and creep rate of metals and alloys. Interpretations of these relations are complicated by the various types of flow occurring during the first, second, and third stages of creep. Some investigators, however, agree that movement can occur both at the grain boundaries and within the grains in creep, and that the parent grains break up into crystallites whose dimensions are dependent on such factors as chemical composition, temperature, strain rate, and the stage of the creep test [1, 2].[1]

Discontinuous flow has been observed in creep tests made at this Bureau on annealed high-purity copper [3] and on cold-drawn ingot iron [4]. Further evidence of this phenomenon, observed in the tests with high-purity aluminum, will be discussed in this paper.

II. Material and Testing Procedure

All specimens were cut from a ⅝-in. round bar of high-purity aluminum that had been cold drawn to 40-percent reduction of area. This aluminum contained the following percentages of other elements as determined spectrochemically.

Cu	0.012	Mg	0.004
Si	.011	Ti	$<$.003
Fe	.007	Mn	$<$.002

Some properties, at room temperature (80° F), of the cold-drawn aluminum are as follows:

Yield strength, 0.2-percent offset, psi	14,000
Tensile strength, psi	17,500
Elongation in 2 in., percent at maximum load	1.4
Elongation in 2 in., percent at fracture	20
Reduction of area, percent at maximum load	1.3
Brinell number, 500-kg load; 10-mm-diameter ball	34

[1] Figures in brackets indicate the literature references at the end of this paper.

The creep tests were made on round specimens having a gage length of 4 in. and a gage diameter of 0.505 in. These tests were carried out in air at a temperature of 105° F, with the exception of one test for which the temperature was changed from 105° to 95° F and back to 105° F. The specimens were held at the test temperature for 48 hr before loading, and the rate of loading was controlled so that an average rate of extension of 30 to 50 percent per 1,000 hr was maintained until the desired creep load was obtained. Thereafter the load was not changed until the test was discontinued. The creep-testing equipment has been described in a previous paper [5].

Tension tests also were made at room temperature on specimens similar to those used for the creep tests, and true stress-strain values were determined from simultaneous load and diameter measurements made during these tests. Usual procedures were used in preparing the specimens and in carrying out the metallographic examinations.

III. Results and Discussion

1. Influence of Stress on Plastic Extension During Loading

A composite stress-extension curve for different specimens loaded at rates of extension of 30 to 50 percent per 1,000 hr is shown in figure 1. The homogeneity of the material is indicated by the lack of appreciable scatter of the observed values. With this rate of loading the change of strain hardening with strain decreases continuously with increase in stress. These conditions are evidence of the fact that the course of the reaction to a more stable state is speeded as the stress is increased. Similarity to chemical-rate reactions should be noted as the ability of metals to flow is increased by increase in strain-energy. The subsequent work-hardening characteristics are described in succeeding sections.

2. Extension-Time Characteristics as Influenced by Stress

The general relation between extension and time during creep of metals and alloys tested in tension at a constant load and a constant temperature can be simply represented by an extension-time curve. For

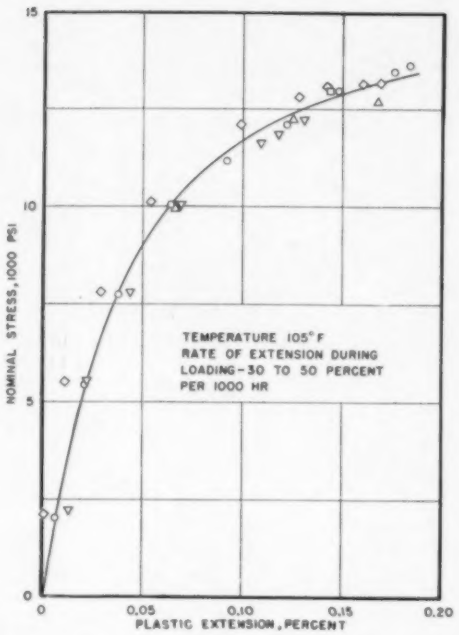

FIGURE 1. *Effect of nominal stress on plastic extension during loading.*

Each symbol represents values obtained in individual tests.

ideal conditions, the course of such a curve is divided into parts as follows: (1) An initial extension (elastic and plastic), which occurs on the application of load, (2) a stage of decreasing rate of extension (designated as primary or first stage of creep), (3) a stage of nearly constant rate that attains a minimum (designated as secondary, minimum rate, or second stage of creep), and (4) a stage of increasing rate eventually leading to complete fracture (designated as tertiary or third stage of creep).

The family of extension-time curves for various applied stresses are shown in figure 2. A general examination of these curves shows that, as the applied stress is increased, the time for initiation of each of the stages is decreased, and the initial extension on loading and the extension at the beginning of the third stage are increased. The variation of stress with time to attain some equal value of strain apparently conform to a power relationship; however, no simple qualitative relationship could be established between stress and extension at the beginning of the second stage nor the intercept extension produced by extrapolating the second stage extension-time curve to zero time due to the existing work-hardening and recovery characteristics of the material at various stress levels.

A suggested partial explanation for these phenomena is that the deformation occurs in part by the breaking up of some of the parent crystals into smaller units designated as subcrystals [3], which for a fixed temperature are smaller, the greater the initially applied stress. The factors that produce the smaller units, tend to cause greater hardness and thus increase the rate of strain-hardening; however, due to the randomness of the adjacent subcrystals (figs., 10, A and B) the tendency to recover is more apparent than in larger crystals, and thus greater ductility at the beginning of the third stage is obtained. At this point the atoms are in a more stable position than at any previous strain state, and the increase in free energy of the system with time is at a minimum. The shape of the extension-time curves is further influenced by local imperfections due to plastic deformation in addition to the inherent structural stability of the material and the distribution of the parent grains that did not fragment during deformation. These factors account in part for the transient effects observed when some of the test conditions were altered and then returned to their original state.

3. Effect of Cyclic Temperature Changes on Creep Characteristics

The extension-time and creep-rate time diagrams for a specimen tested in creep with a stress of 13,200 psi (consecutively at temperatures of 105°, 95° and 105° F) are shown in figure 3. The average creep rate before lowering the temperature was 0.37 percent per 1,000 hr. The change to the lower temperature did not cause an immediate steady-state rate condition, but rather a gradual reduction in the slope of the extension-time curve. This indicates the presence of a first stage under these conditions. After the attainment of approximately constant rate at 95° F, the subsequent creep rate on raising the temperature to 105° F appeared to be unaffected by previous test temperature. These findings confirm the results presented in a previous investigation with copper [3], which showed that other disturbances could produce entirely different results. The conclusion in such cases was that the subsequent creep rate after temperature change depends essentially on the prior history of the material, despite the fact that changes in test conditions may be expected to alter the flow mechanism. As would be predicted, the creep rate-time cycles, illustrated in the upper portion of figure

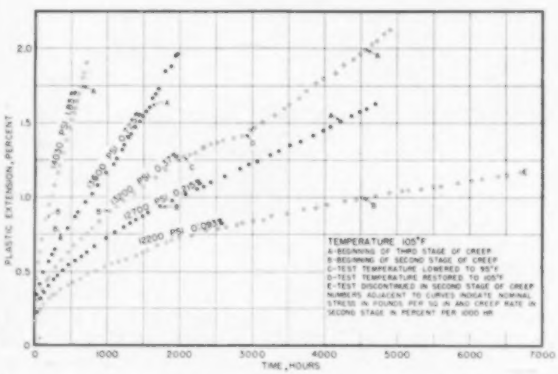

FIGURE 2. *Extension-time curves for specimens tested in creep with different initially applied loads.*

3, are more prominent in the range of lower temperature. The deformation at lower temperature and the thermal gradients set up as a result of the temperature change altered not only the deformation process as reflected in the strain rate-time diagram, but also caused an increase in extension at the beginning of the third stage as was shown in figure 2. Thus the range at which the free energy of the process is at a minimum is shifted to a higher extension value. Concepts of this type must be accounted for in physical interpretations of the deformation process, as it has been shown previously [3, 4] that neither recrystallization on a macro scale nor increase in average true stress is necessarily a prerequisite for initiation of the third stage of creep.

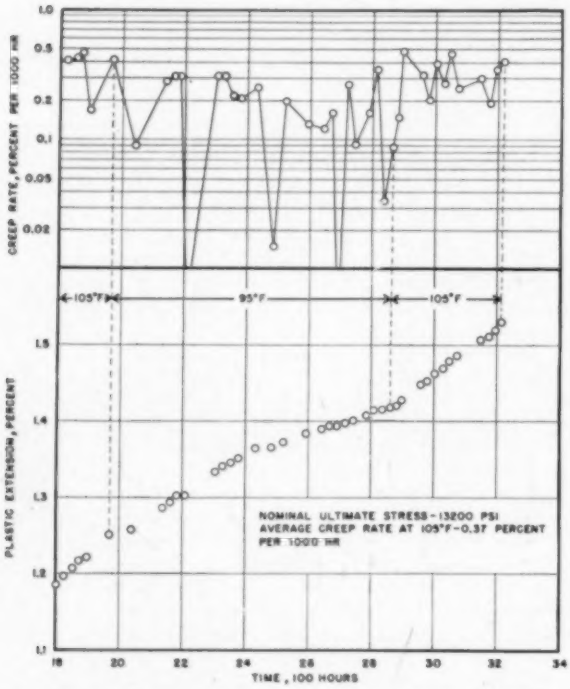

FIGURE 3. *Extension-time and creep rate-time relations for a specimen tested with constant nominal stress of 13,200 psi, and temperature cycled between 105° and 95° F.*

4. Variation of Creep Rate With Plastic Extension

The creep rate-plastic extension curves for two specimens tested with different initial stresses are illustrated in figure 4. The values are plotted on a semilog basis. It is evident that the magnitude of the creep rate-strain cycles, when the data are plotted in this manner, is greater in the specimen strained at the lower stress (extension readings were made at equivalent time intervals). Furthermore, as is shown in the upper curve, after an initial adjustment period, the amplitude of the cycles becomes less until third stage conditions are approached. The strain-hardening process tends to

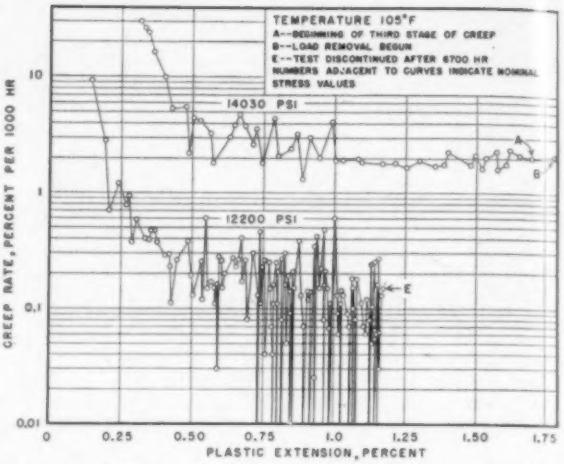
TEMPERATURE 105°F
A--BEGINNING OF THIRD STAGE OF CREEP
B--LOAD REMOVAL BEGUN
E--TEST DISCONTINUED AFTER 6700 HR
NUMBERS ADJACENT TO CURVES INDICATE NOMINAL STRESS VALUES
14030 PSI
12200 PSI
CREEP RATE, PERCENT PER 1000 HR
PLASTIC EXTENSION, PERCENT

FIGURE 4. *Variation in creep rate with plastic extension.*

cause an increase and the recovery a decrease in the activation energy necessary for flow. Thus the time for attainment of each stage of creep is shorter as the applied stress is increased, and the deformation produced as a result of the metastable state adjusting itself toward a condition of lower free energy is greater. (For example, see fig. 2). In order for a decrease in free energy to occur, this system must undergo considerable atomic rearrangements. The mechanics of this process are illustrated by the serrations in these curves (fig. 4) and confirmed by subsequent metallographic examinations. The activation energy of the process is supplied in part by heat gain, the externally applied stress and localized internal thermal fluctuations. The cycling is also due in part to nucleation and growth of fracture sites.

Log-log creep rate-time curves for the intial stage of creep of two specimens tested with nominal stresses of 12,700 and 13,600 psi are shown in figure 5. It is evident that both curves have approximately the same slope although at different levels. Such an equivalence tends to show that when the applied

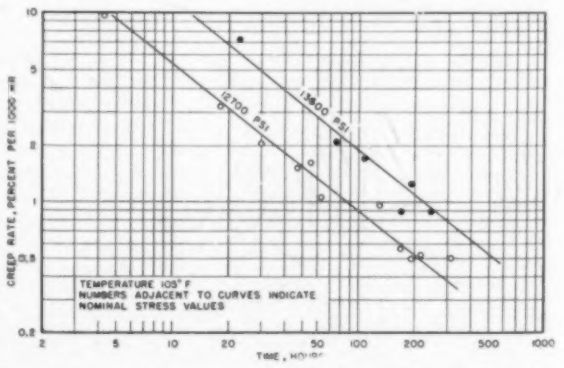

FIGURE 5. *Variation in creep rate with time during first stage of creep.*

stresses are of the same order of magnitude, the mechanism of deformation is similar during the initial stage. Andrade [6], in his analysis of first stage conditions, concluded that with this type of plot, the curves should have a slope of minus ⅔ when transient flow was the predominating characteristic. These two curves have a slope of about minus ⅗, although such good agreement could not be obtained for the specimens at other stresses. Until the many types of flow have been clearly delineated, the application of these physical theories should be used with caution. Several competing and supporting mechanisms, dependent on the material, grain and crystallite size, total deformation and prior strain history, may be operating simultaneously.

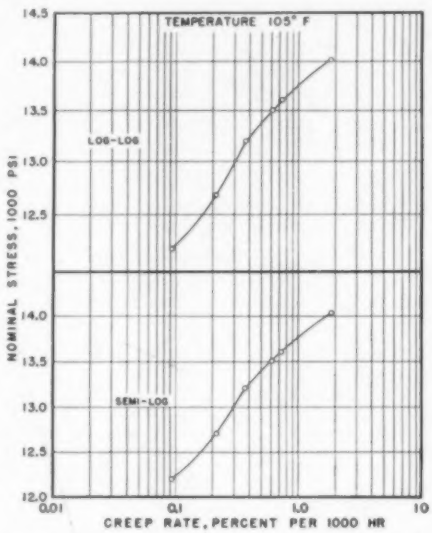

FIGURE 6. *Relationship between nominal stress and average creep rate during second stage of creep.*

5. Effect of Stress on Creep Rate in the Second Stage

The relationship between the applied nominal stress and the average creep rate during the second stage is illustrated in figure 6. Sigmoidal curves are produced when these values are plotted on either a log-log or semilog basis. It seems probable that either type of representation reflects the flow characteristics of the material. Only in those regions of stress in which the mechanism of deformation and the subsequent modes of fracture, transcrystalline or intercrystalline, are nearly equivalent, would linear relationships between the variables of stress and creep rate exist. Previously, it has been shown [3] that the size of the subcrystals produced as a result of plastic deformation vary inversely with the creep rate, and the tendency toward transcrystalline separation of the parent grains is greater the faster the speed of the process. Transcrystalline fracture predominates above the point of reversal in the stress-strain rate curve.

6. Stress-Strain Relationships at Room Temperature

McReynolds [7] in an analysis of stress-strain curves of aluminum tested in tension noted that macroscopic measurements almost invariably show a smooth curve of stress versus strain. Such homogeneity would indicate that discontinuities in strain on slip planes occur in increments too small to be recorded individually and in some manner independent of one another. However, as illustrated by a portion of the autographic stress-strain curve (fig. 7), inhomogeneity of deformation is reflected by the serrations (S) in this diagram for a tensile test conducted at 80° F with a rate of extension of 60,000 percent per 1,000 hr. This test was interrupted at various extensions and the load dropped to zero in order to evaluate the effects of the healing of the internal surfaces previously ruptured due to strain, on the subsequent work-hardening characteristics of the material. The test specimen was held at zero load during each interval for 10 mins before reloading at the same rate at which the specimen was originally loaded. The consequence of the ability of the atoms to rearrange themselves into a more stable system during the rest period was reflected after reapplication of load in the production of a "kink" (K, fig. 7) in the stress-strain curve. This phenomenon was observed and described previously by Farren and Taylor [8]. After the appearance of the kink, there appears to be a lag in stress before a continuous increase in rate of change of load with extension is noted (fig. 7). This lag extends over greater extension values the less the strain to which the specimen was subjected before the rest period. The rate of change of load with extension in the last part of the test appears to be independent of the load; however, multiaxial stresses due to the formation of a "neck" make further analysis difficult.

Whereas the above observations were based on nominal stress values, the true stress-strain curve reveals other interesting results, as is illustrated by figure 8. The values are shown only to a true strain of about 0.9 due to the fact that beyond this strain, the specimen deformed with a quadrilateral contour at the base of the neck and microscopic cracks occurred at the axis of the specimen. These factors prevented quantitative determinations of the remaining area of the material. In figure 8, A, the points at which the load was dropped to zero are indicated. The extension at maximum load was 1.4 percent—a value that was slightly less than the extensions obtained during the creep tests at the beginning of the third stage. It should be noted that the curve at 80° F becomes approximately horizontal for a limited range of true strain values immediately after maximum load. This indicates that the strain hardening in this strain range is zero. However, the contour of the curve between true strain values of 0.2 and 0.9 indicates that the strain-hardening increases slightly or becomes approximately constant. Some of these findings appear to confirm the conclusion of Farren and Taylor [8] that the ratio of the increase in internal energy to the work done is a

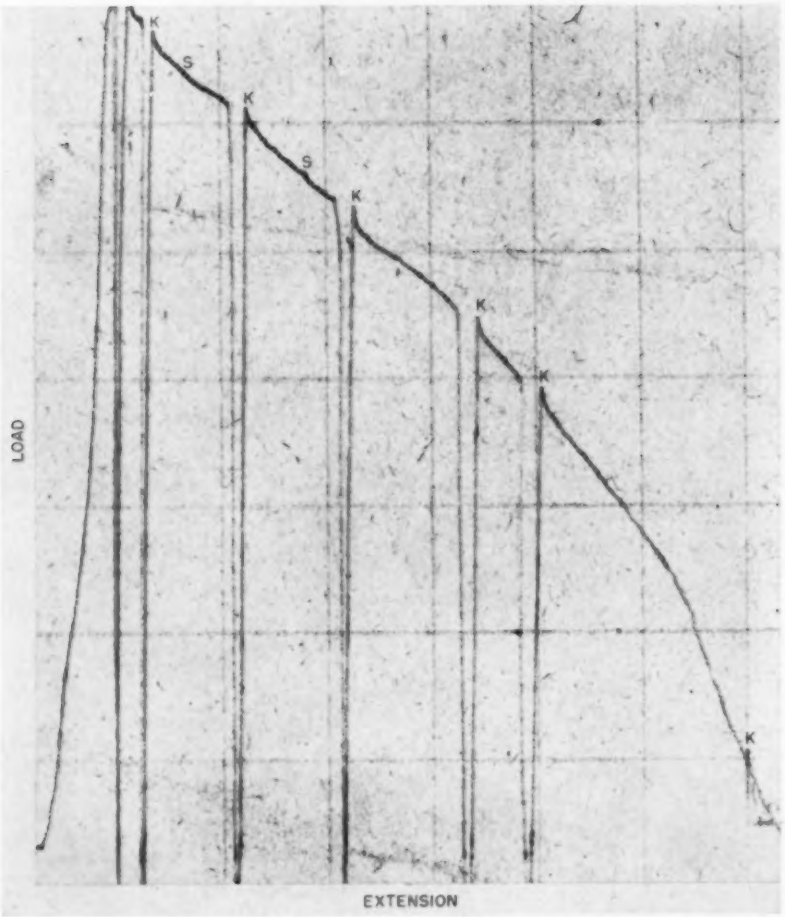

FIGURE 7. *Autographic stress-strain diagram for interrupted tensile test at 80° F.*

constant. Enlarged scales were employed for plotting the data in the regions in which the specimen was unloaded and subsequently reloaded. These curves are reproduced in figure 8, B, C, D, E, and F. It is obvious that in spite of the occurrence of the kinks in the nominal stress-strain curve of figure 7, the yield stress on reloading was lowered. In an analogous investigation, Cherian, Pietrokowsky, and Dorn [9] concluded that during the rest periods two types of recovery were evident. In one type, flow stress values on reloading are below those of the virgin material for all values of total strain. Fast reattainment of flow stress was evident in the test conducted with the creep specimen at two different temperatures (fig. 3). Slow reattainment of the original flow stress is apparent for the present tensile test (fig. 8). The change in extension at which the maximum flow stress is reattained after reloading is greater the higher the strain values at which the specimen was unloaded. Self recovery of the parent grains after deformation becomes more evident as the strain is increased.

7. Microstructure and Fracture Characteristics

The appearance of a fracture and some of the structural features accompanying deformation that led eventually to fracture of an aluminum specimen deformed at 80° F with a rate of extension of 60,000 percent per 1,000 hr are shown in figures 9, 10, and 11. Necking of the specimen commenced immediately after maximum load was reached, and the cross-sectional area at the base of the neck continuously decreased to the end of the test. The appearance of the outer surfaces at fracture is shown in figure 9, A. The general direction of granular elongation is outlined by the strain lines appearing at the surface. During the process of deformation the stress distribution was such that cracks (fig. 9, B) were nucleated at the axis of the specimen and propagated to the surface. As this process of deformation continued toward total fracture, the specimen finally exhibited a rim effect characterized by the extreme outer surface being the last portion to separate after considerable widening of the macro crack

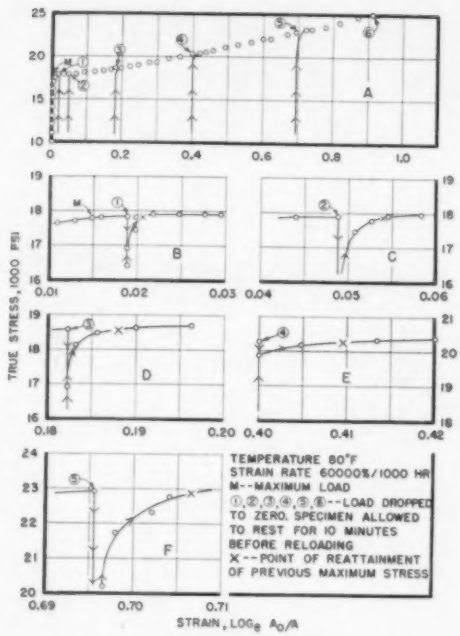

FIGURE 8. *True stress-strain relationships for a specimen stressed interruptedly at 80° F.*

formed by the linking up of a number of microcracks in the interior. Figure 10, A, illustrates the structure representative of the original cold-drawn aluminum; the direction of the drawing is evident from the strain pattern. Some of the elongated grains appear to have broken up into small fragments due to the severity of the deformation, others are intact. As a result of testing in tension at a fast rate, the mode of fracture is essentially transcrystalline, as illustrated by figure 10, B. Transcrystalline cracks that did not link up to form the main fracture course are shown at various points in this region.

Figure 11 illustrates some of the etched patterns developed in areas near the axis of the specimen. The reduction of area in the region in which these photomicrographs were made was approximately 90 percent. Figure 11, A, shows some of the grains elongated in the direction of the applied stress and containing subcrystals. These substructures, according to Heidenreich [10], are fully developed reorientation domains corresponding to self-recovery after cold work. The absence of fracture through the grains in which these substructures were observed in the present study suggest that these grains are in a rather stable state; however, conditions in all grains were not favorable for the development of this substructure. Figure 11, B, illustrates the etch patterns developed in some of the grains that were not resolved into subcrystals. The strain markings, as shown, indicate that during the course of deformation a number of slip systems were active as would be predicted from the serrated stress-strain curves previously shown. The geometry and quantitative

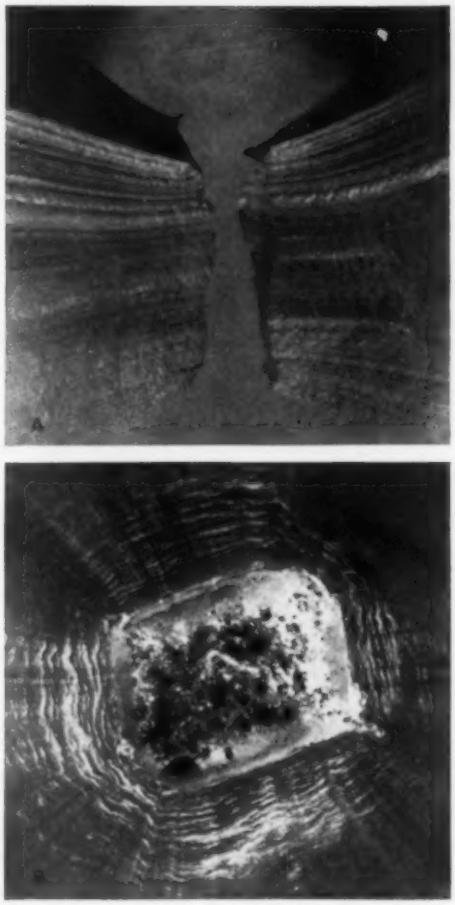

FIGURE 9. *Photograph of the necked portion of a specimen after testing in tension at 80° F.*

A, ×10 at fracture, longitudinal view; B, ×10 at fracture, transverse view.

studies of the nucleation and growth of strain markings of this nature have been made by Barrett [11], Banerjee [12], Rosi and Mathewson [13] and Yen and Hibbard [14].

IV. Summary

Tension tests were made on cold-drawn aluminum at 105° F at various creep rates.

Plastic extension at the beginning of the third stage was greater the higher the rate of extension in the second stage.

Cyclic temperature changes appeared to affect the mechanism of deformation and ductility at the beginning of the third stage to a greater degree than the second-stage creep rate.

Discontinuous flow was indicated by graphs obtained by plotting the logarithm of the creep rate against extension occurring during the course of each creep test. Discontinuous flow also was illustrated

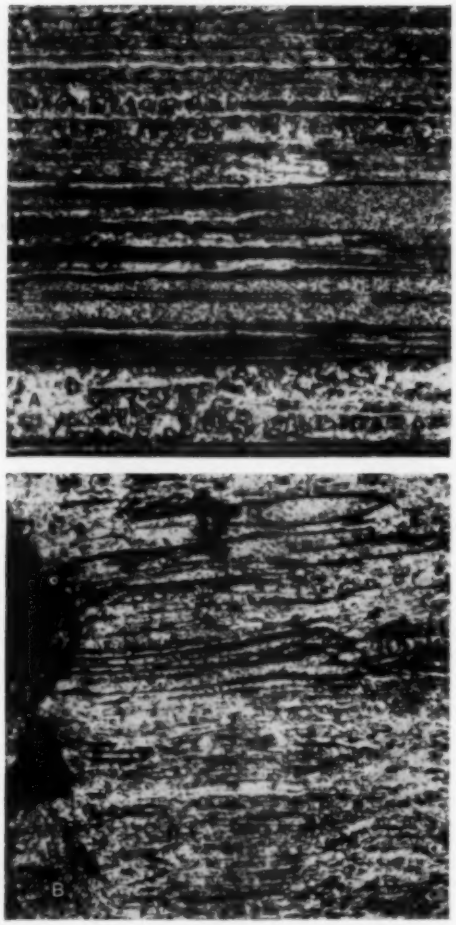

FIGURE 10. *Structure before and after testing in tension at 80° F.*

A, Photomicrograph, ×100, representative of structure before testing in tension, longitudinal section, etched in 10 parts nitric acid (concentrated), 10 parts hydrochloric acid (concentrated), 3 parts hydrofluroic acid (47%), and 77 parts water; B, photomicrograph, ×100, showing transcrystalline nature of fracture; longitudinal section; same etchant as A.

by serrated stress-strain curves for a specimen tested at 80° F.

Within a limited range of strain rates a slope of about minus ⅔ was obtained in first-stage creep curves when transient flow was the predominant characteristic that is essentially in agreement with Andrade's conclusions.

Sigmoidal stress-creep rate curves were obtained when the data were plotted on either a log-log or semilog basis.

Yield point lowering as evidence of recovery at room temperature in an interrupted tensile test served to confirm the results of previous investigations in this respect.

Self-recovery processes during deformation were illustrated by the breaking up of some of the parent grains into subcrystals of microscopic dimensions

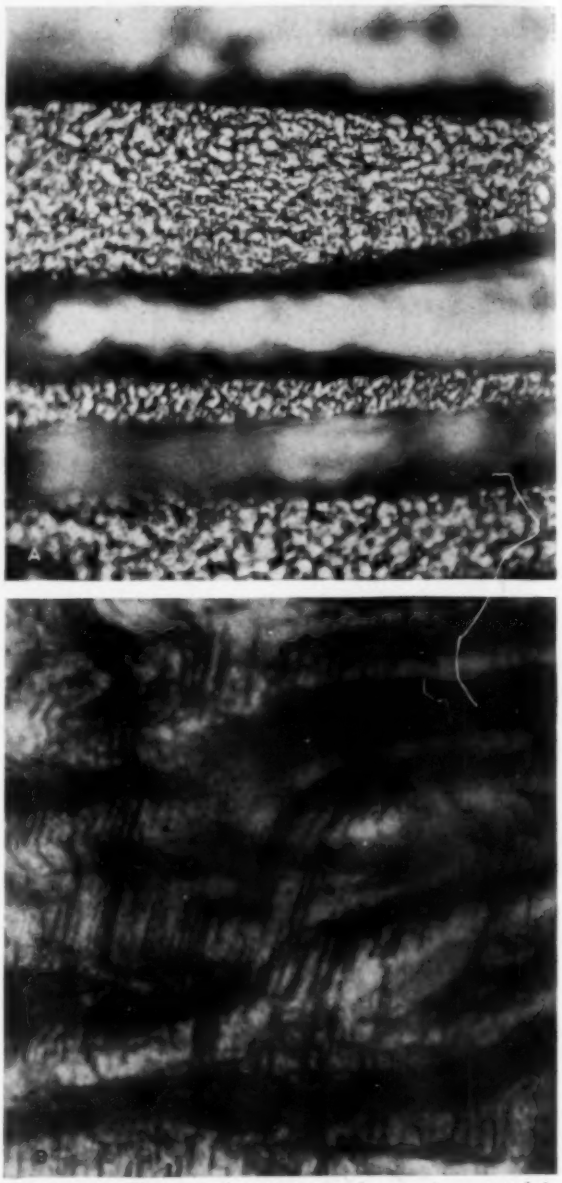

FIGURE 11. *Intragranular structure of a specimen tested in tension at 80° F with a strain rate of 60,000 percent per 1,000 hr; longitudinal sections, 0.1 in. from complete fracture, etched in 10 parts nitric acid (concentrated), 10 parts hydrochloric acid (concentrated), 3 parts hydrofluoric acid (47%), and 77 parts water.*

A, ×750 showing subcrystallite structure; B, ×2,000 showing slip bands and other strain markings.

and the occurrence of slip indicated by strain markings on other grains.

The author acknowledges the assistance of R. W.

Mebs for his helpful discussion and of C. R. Johnson for making some of the measurements.

V. References

[1] P. Lacombe and L. Beaujard, The application of etch figures on pure aluminum to the study of some micrographic problems, J. Inst. Metals **LXXIV,** 1 (1948).
[2] G. R. Wilms and W. A. Wood, Mechanism of creep in metals, J. Inst. Metals, **75,** 693 (1949).
[3] W. D. Jenkins and T. G. Digges, Creep of high-purity copper, J. Research NBS **45,** 153 (1950) RP2121.
[4] W. D. Jenkins and T. G. Digges, Influence of strain rate and temperature on the creep of cold-drawn ingot iron, J. Research NBS **43,** 117 (1949) RP2013.
[5] J. A. Bennett and D. J. McAdam, Jr., Creep rates of cold drawn nickel-copper alloy (Monel metal), J. Research NBS **28,** 417 (1942) RP1462.
[6] E. N. da C. Andrade, The creep of metals, Report of a Conference on the Strength of Solids, Phys. Soc. **20** (1948).
[7] A. W. McReynolds, Plastic deformation waves in aluminum, J. Met. (Jan. 1949); Trans. AIME **185,** 32 (1950).
[8] M. A. Farren and G. I. Taylor, The heat developed during plastic extension of metals, Proc. Roy. Soc. **107,** 422 (1925).
[9] T. V. Cherian, P. Pietrokowsky, and J. E. Dorn, Some observations on the recovery of cold-worked aluminum, J. Met. (Dec. 1949); Metals Trans. **185,** 948 (1950).
[10] R. D. Heidenreich, Structure of slip bands and cold-worked metal, Seminar on the cold working of metals, Trans. Am. Soc. Metals **41–A,** 57 (1949).
[11] C. S. Barrett, The crystallographic mechanisms of translation, twinning and banding, Seminar on the cold working of metals, Trans. Am. Soc. Metals **41–A,** 65 (1949).
[12] B. R. Banerjee, A study of strain markings in aluminum, J. Met. (Sept. 1950); Trans. AIME **188,** 1126 (1951).
[13] F. D. Rosi and C. H. Mathewson, A study of the plastic behavior of high-purity aluminum single crystals at various temperatures, J. Met. (Sept. 1950); Trans. AIME **188,** 1159 (1951).
[14] M. K. Yen and W. R. Hibbard, Jr., The transverse bending of single crystals of aluminum, J. Met. Oct. (1949); Metals Trans. **185,** 710 (1950).

Washington, November 1, 1950.

Journal of Research of the National Bureau of Standards Vol. 46, No. 4, April 1951 Research Paper 220

Standard X-Ray Diffraction Patterns

Howard E. Swanson and Eleanor Tatge

Improvement of the X-ray diffraction pattern file of the American Society for Testing Materials is the basis for work being done at the National Bureau of Standards with the cooperation of the Joint Committee on Chemical Analysis by X-ray Diffraction Methods of the American Society for Testing Materials, the American Crystallographic Association, and the British Institute of Physics. The equipment used in obtaining the data presented here comprises a Geiger-counter spectrometer with a 180° arc calibrated with the calculated patterns of substances whose lattice constants are known with high precision. Separate charts are prepared to obtain data for interplanar spacing and intensity measurements so that special attention can be paid to mounting the sample for the best results in each case. Tables are included to compare the patterns with those recorded in the literature.

Tables and discussion follow for X-ray diffraction data based on four compounds not listed in the American Society for Testing Materials file and on four represented there. The patterns of zinc borate, ZnB_2O_4; selenium oxide, SeO_2; magnesium silicate (forsterite), Mg_2SiO_4; and magnesium tungstate, $MgWO_4$, are recommended as additions to the file. The patterns of strontium nitrate, $Sr(NO_3)_2$; barium nitrate, $Ba(NO_3)_2$; lead fluochloride (matlockite), PbFCl; and mercuric chloride, $HgCl_2$, are recommended to replace the present patterns in the file.

I. Introduction

The National Bureau of Standards is undertaking a systematic review of published X-ray powder diffraction patterns and an experimental investigation planned to revise and supplement them. The work is being performed in cooperation with the Joint Committee on Chemical Analysis by X-ray Diffraction Methods, composed of members from the American Society for Testing Materials, the American Crystallographic Association, and the British Institute of Physics. The basis for the work is the card file of X-ray diffraction data published by the ASTM [1].[1] The information in the file was assembled from all available sources by a subcommittee, under the chairmanship of W. P. Davey, representing the organizations noted above. Data for inorganic and organic chemicals and minerals, as given in the cards, include interplanar spacings, relative intensities of the diffracted beams, and, where available, planar indices, unit-cell dimensions, specific gravity, and optical properties.

The objectives of the project are to record standard X-ray diffraction patterns for compounds of high purity comparable to the best patterns produced by other types of apparatus for the ASTM file. These patterns are used as a basis for comparing and evaluating duplicate file patterns, and as new information to be added to the file. For this purpose X-ray diffraction equipment utilizing a Geiger-counter spectrometer with a 160° effective arc is used.

Considerable progress has been made since 1920 in the production of X-ray diffraction patterns. In most older patterns the interplanar spacings are fewer in number and the precision of the measurements less than that obtainable with present equipment. In some instances the first low-angle line or lines are missing, and in other cases they do not fit the unit-cell dimensions determined from the more accurate high-angle lines or from data obtained by other techniques. In addition, many of the patterns appearing on the ASTM diffraction pattern file cards are combinations of several sets of published and previously unpublished data, and the resulting patterns are consequently difficult to evaluate. The present program to improve and clarify the ASTM file should add to its usefulness.

[1] Figures in brackets indicate the literature references at the end of this paper.

II. Equipment

The spectrometer assembly is based on X-ray equipment of the type designed for film cameras, modified for Geiger-counter recording. A Machlett X-ray tube is mounted horizontally, so that the focal spot has an effective focusing cross section of approximately 1.0 by 0.2 mm. For most work a copper target and nickel filter are used. Two rectifying valves contribute to linear Geiger-counter response. An arc of 180° was made by joining two 90° Geiger-counter spectrometer arcs [2]. The specimen holder is designed to allow oscillation or rotation of the specimen in the plane of its surface to increase the number of contributing crystal particles. The diffracted X-ray beam is received in the Geiger counter as it is moved along the arc by a synchronous motor. The Geiger-counter response represents the diffraction maxima as peaks on a potentiometer chart.

Auxiliary equipment includes a small blower directed on the specimen holder, and, in summer, an air-conditioning unit, which aid in maintaining the temperature of the specimen close to 26° C. A dry-box permits specimens of low stability to be mounted in dry air, or in an atmosphere of nitrogen or helium. Many unstable samples can be mounted satisfactorily as flat specimens if the powder is mixed with enough petrolatum to coat each particle and the mixture smoothed into the holder. Samples that are affected by petrolatum may be sealed into a cell with a thin cellophane window.

The Geiger-counter diffraction spectrometer is capable of greater precision in determining interplanar spacings if patterns of a few well-known materials are used to construct calibration curves for the full extent of the Geiger-counter arc travel. The unit-cell measurements given by Jette and Foote [3] are particularly useful as a basis for the calculation of spacings suitable for calibration. Aluminum, silver, gold, silicon, and tungsten dimensions are given at 25° C. Sodium chloride [4] is also a good calibration standard, but the coefficient of expansion is relatively large, so that temperature is a critical factor. Diamond [5] dust is useful because its coefficient of expansion is low enough to be disregarded.

III. Procedures

Interplanar spacings and intensity measurements are obtained from separately prepared charts, because the type of sample mount that gives the most precise interplanar spacing data is the one least suitable for satisfactory intensity data.

For the spacing measurements the powder sample is packed flat on a glass slide, where it is confined within a thin plastic ring cemented to the glass. Special care is given to obtaining a smooth flat surface, which facilitates close alinement with the spectrometer center. An error of 0.05 mm in the position of the specimen surface relative to the spectrometer arc center causes a change in the apparent diffraction angle 2θ of 0.032° at 0° of arc, which decreases to zero at 180° of arc. Errors due to such surface alinement difficulty may be compensated by corrections based on a few lines from a calibration substance used as an internal standard. Errors due to the penetration of the X-rays into samples containing elements of low atomic number may be corrected in the same manner. A small amount of the standard suffices, as few lines are needed for comparison. Tungsten contributes few lines to complicate the pattern, and its back reflection lines are unusually strong; less than 5 percent of the powder added to the sample is usually sufficient. In running the spacing charts a motor speed of ½ rpm is used to move the Geiger-counter arm ½°/min, covering the 160° of arc in about 5 hr. The recorder charts are run so that 1° of arc is equivalent to 1 in. on the chart paper. The interplanar spacings are obtained from the reflection angles directly by reference to spacing tables [6]. In general, the angles are measured with an accuracy well within ±0.04°. With copper radiation the largest measurable interplanar spacing is 44 A. The definition of the diffraction peaks is such that those due to the $K\alpha_1$ and $K\alpha_2$ wavelengths are usually resolved at angles greater than 70° with copper radiation.

For intensity measurements an additional chart is run. Random orientation of the crystal particles is achieved by loosely drifting the powdered sample, the particles of which are usually less than 0.025-μ diameter, into a cell fronted by a window of 0.005-mm cellulose acetate. The cell is wide enough to intercept the full width of the X-ray beam at the lowest angles of the pattern and thick enough to accommodate the greatest penetration of X-rays at high angles. For most materials 1 mm is thick enough. The specimen preparation outlined avoids the packing associated with many types of flat specimen mountings, which usually modifies the peak intensities so that they do not compare well with those made from a randomly oriented cylindrical mounting. In preparing the charts from which the intensity measurements of the patterns given here were made, the Geiger-counter motor was run at 1 rpm. Recent work indicates that a motor speed of ¼ rpm reproduces peak heights somewhat better. As the amplitude record of the instrument has been found linear for the counting rates used, the heights of the peaks are regarded as close approximations to the actual intensities of the diffracted X-ray beams. Measurements at diffraction angles less than about 70° include the intensities of both the $K\alpha_1$ and $K\alpha_2$ peaks. The peaks are measured vertically from a base line drawn at background height and are valued relative to the line of strongest intensity. Repeated intensity measurements for the stronger lines are found to vary less than 5 percent with separate samples of the same material. The resulting data are comparable to those from both the Debye-Scherrer type of camera and the usual Geiger-counter spectrometer procedures, if absorption errors introduced by the round specimen of the first are kept small and if random orientation is attained in the flat specimen of the latter.

Table 1 includes a comparison of intensity measurements from film camera and Geiger-counter equipment. The data for MgO in column (a) are based on careful film measurements made by Frevel [7], using molybdenum radiation. Column (c) comprises Frevel's calculated intensity values. In columns (b) and (d) both sets were converted to measurements based on copper radiation by means of the conversion chart in the Index to the ASTM diffraction pattern file in order to compare them with the NBS measurements of columns (e) and (f). A portion of a large single crystal of MgO was ground to pass a 325-mesh sieve. This powder, pressed lightly into the ring on the glass slide, formed a highly oriented specimen. The effect of the pressed sample on the intensity pattern, as shown in column (e), is typical of that of powder mountings used in many laboratories for routine identification with Geiger-counter diffraction equipment. The packing of the crystal particles is influenced by the prominent cleavage of magnesium oxide parallel to 100, and causes a reflection of considerably higher relative intensity for this plane than occurs with a randomly oriented sample. When the same sample powder was remounted by pouring the powder into the cell used in this laboratory for intensity measurements, the data shown in column (f) were obtained. The agreement of this pattern with Frevel's intensity measurements is well within the limit of the experimental error.

In addition to the tabulated interplanar spacings and intensity measurements, the standard patterns are accompanied by other pertinent data. The

Miller indices of the diffraction planes are calculated from published unit-cell dimensions. From the indexed lines the unit-cell measurements of the specimen used for the pattern are precisely determined and the density calculated. The phase purity of the specimens is checked by the petrographic microscope, and the indices of refraction of the material are determined when possible. Effort is made to obtain specimens of high purity upon which to base standard patterns, although, in general, small amounts of impurities do not significantly affect the pattern. Indeed, temperature variation may be just as important, for the presence of 0.01 percent of a foreign material in solid solution may produce, at most, a barely perceptible change in the size of the unit cell, whereas the change of a few degrees produces in some materials a substantial difference.

TABLE 1. *Comparison of intensity measurements for magnesium oxide*

Radiation	Film camera, Frevel		Calculated values, Frevel		Pressed sample, highly oriented, NBS	Same powder as (e) poured into cell, NBS
	Mo	Converted to Cu	Mo	Converted to Cu	Cu	Cu
hkl	(a)	(b)	(c)	(d)	(e)	(f)
111	8	8	8	8	3	9
200	100	100	100	100	100	100
220	50	45	55	50	21	51
311	4	4	6	6	2	5
222	12	11	15	13	4	11
400	4	4	6	6	4	6
331	1	1	3	4	1	2
420	.....	.....	.....	.....	6	12
422	.....	.....	.....	.....	4	11
511	.....	.....	.....	.....	1	2

The patterns prepared are checked with all available patterns previously made by other workers. References to the published literature are obtained by systematic search through Wyckoff's compilations [8], the Strukturbericht [9], Chemical Abstracts [10], and the ASTM cards [1]. The type of equipment used, radiation, unit-cell dimensions derived, space groups, density, and other data are noted for comparison. Patterns usually are published in a variety of forms, requiring recalculation for comparison. The values of θ, $\sin\theta$, or $\sin^2\theta$ may be listed, rather than interplanar spacings. Intensity measurements may be given as absolute values, as relative values on the basis of 1, 10, or 100 for the strongest line, or as visual estimates. In the preparation of the following comparison tables, these are reduced to interplanar spacings, d, and relative intensities, I, to the base 100, except that visual estimates not expressed numerically are retained.

Interplanar spacings and unit-cell dimensions for published patterns may appear in kX units or in angstrom units variously defined, depending on the accepted value of the radiation wavelength used at the time the pattern was made, which may or may not be given. In general, the difference is small; however for accurate comparison, the interplanar spacings and unit-cell dimensions are recalculated to the angstrom unit adopted in 1946 [11], which is used for the standard patterns. In tables 2 to 9 the recalculation of published patterns was usually made by dividing the spacings by the wavelength of the radiation originally used and multiplying by the wavelength now in use. In many cases the wavelength was not specified; then for data published between 1930 and 1947 it has been assumed that kX units were employed, and conversion to angstroms was made by use of the factor 1.00202; conversion of earlier data without specified radiation wavelengths was not possible, due to the variety of wavelengths in use. The interplanar spacings of each pattern previously published are not rounded off, although in many instances it is plain from the variation in the unit-cell calculations, particularly with cubic patterns, that one or more of the figures is not significant. For the sake of simplicity and uniformity of treatment, the practice was adopted of averaging the unit-cell dimensions from the last five lines, those of smallest interplanar spacing, of any set. This has generally given a serviceable figure. For the tetragonal patterns a was determined from as many $h00$ and $hk0$ lines as possible, and the average used to calculate c from the remaining lines. These were averaged after eliminating the more divergent values.

IV. Patterns

The following X-ray diffraction patterns for exceptionally pure chemicals available to the National Bureau of Standards were measured. Interplanar spacings and intensities are listed in the accompanying tables, in which they are compared with the results of other investigators. *Cubic:* Zinc borate, ZnB_2O_4; strontium nitrate, $Sr(NO_3)_2$; barium nitrate, $Ba(NO_3)_2$. *Tetragonal:* Lead fluochloride (matlockite), PbFCl; selenium dioxide, SeO_2. *Orthorhombic:* Mercuric chloride, $HgCl_2$; magnesium silicate (forsterite), Mg_2SiO_4. *Monoclinic:* Magnesium tungstate, $MgWO_4$. There are no patterns in the ASTM file for ZnB_2O_4, SeO_2, Mg_2SiO_4, or $MgWO_4$. It is recommended that the following patterns in the ASTM powder diffraction pattern file be replaced by National Bureau of Standards standard patterns:

Compound	Old file number	New file number	Index lines	Author	Year
$Sr(NO_3)_2$	732	0733	4.50	Hanawalt, Rinn, and Frevel.	1938
		1-0336	2.35		
		1-0336	2.24		
$Ba(NO_3)_2$	2022	3111	2.44	....do.....	1938
		1-1144	4.69		
		1-1144	2.34		
PbFCl	II-856	1310	3.54	British Museum	
		2-0388	2.25		
		2-0377	1.77		
PbFCl		3928	1.22	Nieuwenkamp and Bijvoet.	1932
		3-1184	1.29		
		3-1182	1.79		
$HgCl_2$	812	0852	4.35	Hanawalt, Rinn, and Frevel.	1938
		1-0377	3.00		
		1-0365	2.70		
$HgCl_2$	II-524	0826	4.34	Brükken and Harang	1928
		2-0249	4.08		
		2-0255	3.36		

1. Zinc Borate, ZnB_2O_4

No published pattern for zinc borate was found. The sample used for the pattern of table 2 was one of the phosphor preparations of the Radio Corporation of America [12], sample XII-17, of high purity. The unit-cell edge derived from an average of the values obtained from the last five lines is 7.4726 A, at 26° C. The lattice derived from the powder pattern is body-centered cubic, with two molecules in the unit cell. The density is 1.2017, from the X-ray data. The index of refraction for the sample was determined as 1.739.

TABLE 2. *Zinc borate:* ZnB_2O_4

Copper radiation, λ = 1.5405. Temperature, 26° C

hkl	d	I	a	hkl	d	I	a
110	5.29	6	7.48	444	1.0788	1	7.474
200	3.74	3	7.48	710	1.0598	1	7.473
211	3.048	100	7.466	640	1.0365	1	7.474
310	2.364	23	7.476	721	1.0169	3	7.473
222	2.158	1	7.476	642	0.9991	1	7.477
321	1.907	20	7.472	730	.9812	2	7.4726
400	1.869	13	7.476	732	.9490	1	7.4724
411	1.761	38	7.471	811	.9198	3	7.4725
420	1.672	2	7.477	820	.9062	1	7.4727
332	1.594	3	7.477	653	.8932	1	7.4730
422	1.526	25	7.476	822	.8807	1	7.4730
510	1.466	5	7.475	831	.8687	3	7.4728
521	1.364	8	7.471	662	.8573	1	7.4738
440	1.321	4	7.473	752	.8462	1	7.4734
530	1.282	3	7.475	910	.8252	1	7.4725
600	1.246	1	7.476	842	.8153	1	7.4723
611	1.213	2	7.477	921	.8058	1	7.4727
620	1.1817	1	7.474	664	.7996	1	7.4728
541	1.1531	3	7.473	930	.7877	1	7.4728
631	1.1025	1	7.478				
				Average last 5 lines			7.4726

2. Strontium Nitrate, $Sr(NO_3)_2$

A pattern for strontium nitrate is compared in table 3 with two previously published patterns. The first, by Vegard [13] in 1922, was well indexed and misses few lines, although it is of less precision than the later patterns. The copper radiation used was assigned a wavelength of 1.54 A, close to the currently accepted value for the angstrom. The data were published as sin θ values and estimated intensities. The former were converted to interplanar spacings for table 3. The pattern by Hanawalt, Rinn, and Frevel [14], 1938, is included in the diffraction pattern file of the ASTM. It was obtained with molybdenum radiation with the wavelength given as 0.708 *kX*. The sample for the National Bureau of Standards pattern was a specially purified material supplied by the Mallinckrodt Chemical Works. A spectrographic analysis shows Ba $<$ 0.01 percent and Na $<$ 0.01 percent as the only impurities greater than traces.

From the intensity measurements of the NBS pattern, the three strongest lines are the 111, 311, and 222, consistent with the index lines of the ASTM card for the Hanawalt, Rinn, and Frevel pattern. The unit-cell edges derived for the three patterns, 7.81, 7.799, and 7.779 A, show considerable variation. Other published unit-cell determinations include 7.80 A, by Jaeger and Van Melle [15] in 1928, given without stating the radiation used; and 7.811 A by Ringdal [16] in 1932, measured from a chart showing unit-cell variations in solid solutions, iron radiation, and with no wavelength given. Vegard and Roer [17] in 1942, studying the coefficient of expansion of nitrates, gave the unit-cell dimension of strontium nitrate at 10° C as 7.7629 A, the coefficient of expansion between 10° and 70° as 2.58×10^{-5}. They state that the unit-cell edge of sodium chloride used for calibration was 5.628 A. Thus, assuming that the values of Ringdal and of Vegard and Roer are in *kX* units, the following table shows comparative values, after conversion to angstroms:

TABLE 3. *Strontium Nitrate:* $Sr(NO_3)_2$

	1922, Vegard Cu, 1.54 A			1938 Hanawalt, Rinn and Frevel Mo, 0.709 A			1951, Swanson and Tatge Cu, 1.5405 A 26° C		
hkl	d	I	a	d	I	a	d	I	a
111	4.54	m	7.86	4.51	100	7.81	4.48	100	7.76
200	3.92	m	7.84	3.92	33	7.84	3.88	13	7.76
210	3.53	w	7.89	3.49	33	7.80	3.474	21	7.768
211	3.22	w	7.89	3.19	33	7.81	3.175	14	7.777
220	2.78	w	7.87				2.749	19	7.775
311	2.37	s	7.86	2.36	100	7.83	2.346	72	7.781
222	2.27	s	7.85	2.24	100	7.76	2.246	54	7.780
400	1.96	m	7.84	1.94	17	7.76	1.945	12	7.780
411							1.836	2	7.789
331	1.80	m	7.86	1.78	17	7.76	1.785	16	7.781
420	1.75	m	7.84	1.75	17	7.83	1.740	12	7.782
422	1.60	m	7.81	1.58	17	7.74	1.589	10	7.784
333	1.51	m	7.84	1.50	17	7.79	1.498	12	7.784
521							1.420	2	7.778
440	1.39	m	7.84	1.379	17	7.801	1.376	11	7.784
531	1.32	s	7.83	1.318	17	7.797	1.315	10	7.780
600	1.30	w	7.81				1.296	4	7.776
620	1.24	w	7.82				1.231	2	7.786
533	1.20	m	7.84				1.1867	4	7.782
622	1.176	m	7.80				1.1736	1	7.785
444	1.128	w	7.82				1.1235	2	7.784
711	1.094	m	7.81				1.0893	3	7.779
642	1.045	m	7.82				1.0396	3	7.780
731	1.017	s	7.81				1.0128	5	7.780
732							0.9878	2	7.778
820	0.951	s	7.84				.9435	4	7.780
422	.927	s	7.86				.9168	4	7.779
751	.902	s	7.81				.8983	5	7.780
840	.873	m	7.80						
911	.857	s	7.81						
842	.851	s	7.80						
664	.833	w	7.81						
Average unit-cell edge from last 5 lines			7.81			* 7.799			7.779

* Average of last 2 lines only.

Unit-cell dimensions, angstroms

		a
1922	Vegard	7.81
1932	Ringdal	7.827
1938	Hanawalt, Rinn, and Frevel	7.799
1942	Vegard and Roer (26° C)	7.7818
1951	Swanson and Tatge (26° C)	7.779

The lattice of strontium nitrate is simple cubic, four molecules to the unit cell. The space group according to Jaeger and Van Melle is T_h^6 (*Pa3*); Vegard and Bilberg [16] confirm this, but indicate

the possibility of $T^4(P2_13)$. The patterns of table 3 show $hk0$ only if h is even, adding confirmation of the T_h^6 $(Pa3)$ group. The density from the NBS unit-cell edge value is 2.974. The index of refraction is 1.587.

3. Barium Nitrate, $Ba(NO_3)_2$

The pattern for barium nitrate closely parallels that for strontium nitrate. Vegard [13] and Hanawalt, Rinn, and Frevel [14] published patterns, of which the latter is included in the ASTM file. In Vegard's paper the copper radiation was assigned, as for his strontium nitrate pattern, a wavelength of 1.54 A, and the data were published as sin θ values. For comparison with the data in table 4, they were converted to interplanar spacings. Hanawalt, Rinn, and Frevel used molybdenum radiation with a wavelength of 0.708 kX, converted in table 4 to 0.709 A. The National Bureau of Standards sample was specially purified material supplied by the Mallinckrodt Chemical Works. Spectrographic analysis indicates the following impurities: Al<0.01 percent, Na<0.01 percent, and Sr<0.01 percent. Copper radiation with a wavelength of 1.54050 A was used.

TABLE 4. *Barium nitrate:* $Ba(NO_3)_2$

	1922 Vegard Cu, 1.54 A			1938 Hanawalt, Rinn and Frevel Mo, 0.709 A			1951 Swanson and Tatge Cu, 1.5405 A, 26° C		
hkl	*d*	*I*	*a*	*d*	*I*	*a*	*d*	*I*	*a*
111	4.70	s	8.14	4.70	75	8.14	4.68	95	8.11
200	3.93	s	7.86	4.07	30	8.14	4.06	40	8.12
210				3.63	15	8.12	3.63	11	8.12
211				3.32	10	8.13	3.313	14	8.115
220	2.87	m	8.12	2.88	40	8.15	2.870	35	8.118
311	2.45	vs	8.13	2.45	100	8.13	2.448	100	8.119
222	2.34	s	8.11	2.35	50	8.14	2.343	55	8.116
400	2.03	m	8.12	2.02	20	8.08	2.029	17	8.116
411							1.914	21	8.120
331	1.86	m	8.11	1.86	40	8.11	1.862	21	8.116
420	1.81	m	8.09	1.81	30	8.09	1.815	20	8.117
422	1.66	m	8.13	1.65	30	8.08	1.657	15	8.118
333	1.56	m	8.11	1.56	30	8.11	1.562	15	8.116
440	1.44	m	8.15	1.436	15	8.123	1.435	5	8.118
531	1.37	vs	8.11	1.373	40	8.123	1.372	18	8.117
600				1.354	10	8.124	1.353	7	8.118
611				1.321	1	8.143			
620	1.29	w	8.16	1.283	8	8.114	1.284	1	8.121
533				1.240	13	8.131	1.238	1	8.118
622	1.23	m	8.16	1.224	13	8.119	1.224	2	8.119
444	1.17	w	8.11	1.172	4	8.120	1.1721	2	8.121
711				1.139	10	8.134	1.1370	3	8.120
640				1.128	6	8.134	1.1261	1	8.120
642				1.087	13	8.134	1.0849	1	8.119
731				1.058	20	8.127	1.0566	5	8.116
800							1.0150	1	8.120
733							0.9918	1	8.118
820							.9843	1	8.117
822							.9567	1	8.118
751							.9374	3	8.118
662							.9312	1	8.118
840							.9078	1	8.120
911							.8911	7	8.118
842							.8858	3	8.119
931							.8512	4	8.120
933							.8159	5	8.118
10.2.0							.7960	3	8.118
Average unit cell edge from last five lines			8.14			8.130			8.119

The three strongest lines, used as index lines for the ASTM cards, are the same for the NBS and the Hanawalt, Rinn, and Frevel patterns: 311, 111, and 222 lines. The unit-cell edges derived for the three patterns compared in table 4 are 8.14, 8.130, and 8.119 A, respectively. Other published unit-cell determinations include 8.10 A by Jaeger and Van Melle [15] in 1928, radiation not stated; 8.111 by Ringdal [16] in 1932, measured from a chart showing unit-cell variations in solid solutions, iron radiation, no wavelength given. Vegard and Roer [17] in 1942, studying the coefficient of expansion of nitrates, gave the unit-cell dimension of barium nitrate at 10° C as 8.0985 A, the coefficient of expansion between 10° and 70° as 1.75×10^{-5}. They state that the unit-cell edge of sodium chloride used for calibration was 5.628 A. Assuming that the values of Ringdal and of Vegard and Roer are in kX units, the following table compares the various lattice constants after converting them to angstrom units:

Unit-cell dimensions, angstroms

		a
1922	Vegard	8.14
1932	Ringdal	8.127
1938	Hanawalt, Rinn, and Frevel	8.130
1942	Vegard and Roer (26° C)	8.1172
1951	Swanson and Tatge (26° C)	8.119

The lattice of barium nitrate is, like that of strontium nitrate, simple cubic, four molecules to the unit cell. As found for strontium nitrate, the patterns of table 4 confirm the determination of the space group T_h^6 $(Pa3)$ by Jaeger and Van Melle [15] and by Vegard and Bilberg [18]. The density calculated from the NBS unit-cell edge dimension is 3.244. The index of refraction is 1.570.

4. Lead Fluochloride, PbFCl

The new ASTM X-ray diffraction file includes two patterns for lead fluochloride, one, also in the old file, of natural matlockite from the type locality of Matlock, Derbyshire, Eng., furnished by the British Museum (Natural History), London, the other, in the second supplement, from artificial material, published in 1932 by Nieuwenkamp and Bijvoet [19]. In 1933 Nieuwenkamp [20] compared the patterns of matlockite, whose formula was then given as Pb_2OCl_2, and artificial PbFCl, showing their identity. In table 5 these two patterns are compared with one prepared at this Bureau from material of high purity obtained from the NBS chemical laboratory, which had been prepared as part of a project for the precise determination of fluorine compounds.

TABLE 5. *Lead fluochloride:* PbFCl

	1932 Nieuwenkamp and Bijvoet Cr, 2.290		No date British Museum		1951 Swanson and Tatge Cu, 1.5405, 26° C	
hkl	*d*	*I*	*d*	*I*	*d*	*I*
001	.....	.....	7.2	40	7.22	20
002	.....	.....	.....	.....	3.61	70
101	3.58	48	3.55	100	3.56	100
110	2.905	28	2.90	70	2.904	47
102	2.719	28	2.70	70	2.714	35
003	2.410	6	2.40	20	2.409	6
112	2.262	51	2.25	80	2.263	38
103	2.074	20	2.07	70	2.079	14
200	2.052	34	1.99	60	2.053	24
201	1.954	23	1.98	40	1.974	1
113	1.852	17	1.84	60	1.855	4
004	.....	.....	.....	.....	1.808	1
211	1.780	66	1.77	80	1.780	36
104	1.654	40	1.65	70	1.654	11
212	1.635	28	1.63	60	1.637	7
203	1.560	14	1.558	20	1.564	1
213	1.462	31	1.461	60	1.461	4
220	.....	.....	.....	.....	1.452	3
005	1.447	34	1.443	60	1.448	1
221	1.417	37	.....	.....	.....	.....
105	1.363	23	.....	.....	.....	.....
222	}					
301	} 1.344	66	1.343	60	1.346	3
310	1.298	68	.....	.....	1.299	4
115	.....	.....	.....	.....	1.293	3
214	1.285	89	.....	.....	1.289	5
302	}					
311	} 1.281	17	1.276	70	1.281	1
223	.....	.....	1.240	20	1.244	1
312	1.220	100	1.222	60	1.223	2
006	.....	.....	.....	.....	1.2041	1
203	.....	.....	.....	.....	1.1911	2
205	.....	.....	1.181	60	1.1826	2
106	.....	.....	1.156	60	1.1565	2
313	.....	.....	1.142	40	1.1443	2
320	.....	.....	.....	.....	1.1386	1
321	.....	.....	1.126	50	1.1254	1
304	.....	.....	.....	.....	1.0922	1
322	.....	.....	1.089	50	1.0863	1
323	.....	.....	.....	.....	1.0300	1
400	.....	.....	1.027	60	1.0265	1
216	.....	.....	1.008	60	1.0078	2
402	.....	.....	.....	.....	0.9872	2
117	.....	.....	.....	.....	.9735	1
330	.....	.....	.....	.....	.9664	2
324	.....	.....	.....	.....	.9639	3
412	.....	.....	.....	.....	.9608	2
207	.....	.....	.....	.....	.9223	1
413	.....	.....	.....	.....	.9203	1
420	.....	.....	.....	.....	.9185	2

Chromium radiation was used for the Nieuwenkamp and Bijvoet pattern, but the wavelength is not recorded. The data published do not include interplanar spacings; for table 5 they were calculated from the $\sin^2\theta$ values listed, using the wavelength 2.2896 A for chromium radiation. The interplanar spacings of the British Museum pattern, presumably in *kX* units, were multiplied by the conversion factor 1.002 for recording in angstroms. While the interplanar spacings of the patterns check closely, the intensity measurements vary. The NBS and British Museum patterns agree that 101 is the strongest line, but the Nieuwenkamp and Bijvoet pattern shows the last line (312) strongest, with the second and third strongest in close proximity. The 002, the second strongest line of the NBS pattern, is unresolved in the others. The third and fourth strongest lines of the NBS pattern appear as second and third strongest in the British Museum pattern. The intensity measurements of the latter show effects due to absorption and to variable focusing common with the Debye-Scherrer procedure when using long wavelength radiation.

Frevel, Rinn, and Anderson [21] in 1946 repeated the 1932 Nieuwenkamp and Bijvoet determination of $a=4.09$, $c=7.21$ *kX*, which, converted to angstroms compares thus with the NBS determination:

Unit-cell dimensions, angstroms

		a	*c*
1932	Nieuwenkamp and Bijvoet	4.09	7.21
1951	Swanson and Tatge (26° C)	4.106	7.23

Bannister [22] in 1934 gave the structure as tetragonal, space group D_{4h}^{7} (*Pnmm*), two molecules in the unit cell, indices of refraction $\omega_D=3.145$, $\epsilon_D=2.006$. The NBS pattern yields a density of 7.13. The sample was too finely powdered for us to determine the indices of refraction.

5. Selenium Dioxide, SeO_2

A pattern was prepared from specially purified material supplied by the Mallinckrodt Chemical Works. Spectrographic analysis showed no impurities greater than 0.001 percent. The lines are indexed in accordance with the structure and unit-cell dimensions determined by McCullough [23] in 1937. The material is hygroscopic; lines from the monohydrate are omitted from the pattern given in table 6. Although the crystals generally have been described as monoclinic [24], the NBS pattern confirms the work of McCullough, showing a tetragonal structure. McCullough gives the unit cell dimensions $a=8.353$, $c=5.051$, the probable space group D_{14}^{15} (*P4/mbc*), or C_{4v}^{8} (*C4cb*), with eight molecules in the unit cell. Frevel, Rinn, and Anderson [21] in 1946 used these same values. An average of 13 cell-edge values based on *hk*0 lines yields $a=8.35$ A for the NBS pattern; an average of 11 values for c, after eliminating the more divergent ones, yields 5.08 A. Converting the McCullough values to angstrom units, they compare with the NBS determinations as follows:

Unit-cell dimensions, angstroms

		a	*c*
1937	McCullough	8.370	5.061
1951	Swanson and Tatge (26° C)	8.35	5.08

The material proved too unstable for a determination of the indices of refraction. The density is 4.16.

TABLE 6. *Selenium dioxide:* SeO_2

1951 Swanson and Tatge Cu, 1.5405, 26° C			1951 Swanson and Tatge Cu, 1.5405, 26° C		
hkl	*d*	*I*	*hkl*	*d*	*I*
110	5.92	13	322	1.711	25
200	4.17	85	500	1.673	9
210	3.73	100	510	1.640	9
201	3.227	11	431	1.588	3
211	3.009	88	511	1.559	14
220	2.998	38	332	1.556	10
300	2.789	2	213	1.538	4
310	2.640	14	422	1.503	3
002	2.533	2	440	1.478	4
311	2.343	3	530	1.437	4
112	2.320	15	313	1.421	5
202	2.252	14	432	1.394	8
321	2.105	6	512	1.379	20
400	2.090	14	522	1.324	9
330	1.973	10	620		
401	1.933	17	540	1.305	4
411	1.895	14	413	1.292	3
420	1.871	14	621	1.278	12
312	1.831	17	004	1.264	15
421	1.755	13	612	1.209	13

6. Mercuric Chloride, $HgCl_2$

One of the two patterns for mercuric chloride in the X-ray diffraction file of the American Society for Testing Materials was published in 1928 by Bräkken and Harang [25], the other by Hanawalt, Rinn, and Frevel [14] in 1938. Unfortunately, the Hanawalt, Rinn, and Frevel pattern is omitted from the index. Instead, the index lines 4.35, 3.00, 2.70 belonging to mercuric chloride are assigned to mercuric chlorate. (See "Alphabetical Index of X-ray diffraction patterns, covering original set of cards" for June 1945, p. 53.) In table 7 the two patterns are compared with one more recently prepared at this Bureau. The Bräkken and Harang pattern was prepared with iron radiation for which a wavelength of 1.932 is given; for the Hanawalt, Rinn, and Frevel pattern molybdenum radiation with a wavelength 0.708 *kX* was used. The NBS material was obtained from the J. T. Baker Chemical Co., No. 101742. Spectrographic analysis showed no impurity greater than 0.01 percent.

The data of Bräkken and Harang were published as a table of *hkl* indices, $\sin^2\theta$ values, and intensity values visually estimated. For our comparison table the $\sin^2\theta$ values were converted to interplanar spacings, using the iron radiation wavelength 1.93597 A. The spacings of Hanawalt, Rinn, and Frevel were converted from *kX* units to angstroms by applying the factor 1.002. The 120 line is the strongest for all three patterns. The second strongest is the 200, but this line is not resolved from the 031 line by Hanawalt, Rinn, and Frevel, so that their intensity measurement is a combination of the two intensities. The 011 and 111 are third and fourth strongest in the Hanawalt, Rinn, and Frevel pattern, reversed for the NBS pattern. The difference in intensity is probably too small to be significant; it is not due to the radiation used, as the conversion factor for molybdenum to copper radiation is close to 1 in this range.

TABLE 7. *Mercuric chloride:* $HgCl_2$

	1928 Bräkken and Harang Fe, 1.936		1938 Hanawalt, Rinn, and Frevel Mo, 0.709		1951 Swanson and Tatge Cu, 1.5405, 26° C	
hkl	*d*	*I*	*d*	*I*	*d*	*I*
120	4.34	vs	4.36	100	4.35	100
011	4.08	s	4.11	25	4.10	38
021	3.57	w	-----	-----	3.58	3
101	3.488	w	-----	-----	-----	-----
111	3.368	s	3.41	38	3.383	31
040	3.172	w	3.21	13	3.188	11
121	3.056	vw	-----	-----	3.066	2
031	3.019	w	3.01	75	3.033	21
200	2.976	s			2.986	48
131	2.692	s	2.70	50	2.707	36
220						
211	2.403	m	2.41	25	2.420	14
141	2.348	w	-----	-----	2.366	2
221	2.281	vw	-----	-----	2.297	4
051	2.194	w	2.18	13	2.182	6
002	2.158	vw	-----	-----	-----	-----
012	2.120	m	2.12	25	2.132	9
231						
060						
151	2.056	m	2.06	25	2.065	13
112	1.997	m	2.00	50	2.004	16
241	-----	-----	1.94	25	1.940	11
122	1.929	m	-----	-----	-----	-----
061	1.895	w	1.90	13	1.902	8
132	1.829	w	-----	-----	1.837	1
301	1.806	vw	-----	-----	1.810	1
042	1.784	m	1.79	13	1.791	6
311						
251	1.762	w	-----	-----	1.769	4
202	1.745	vw	-----	-----	1.765	1
071	1.674	vw	1.67	13	1.686	4
331	1.658	w	-----	-----	-----	-----
052	1.643	m	-----	-----	-----	-----
232	-----	-----	1.62	13	1.619	3
080	1.589	m	1.59	13	1.595	1
341	1.569	vw	-----	-----	1.572	1
180	1.531	m	1.54	13	1.539	2
081	1.489	w	-----	-----	1.496	1
312	-----	-----	1.455	13	1.454	4
013	-----	-----	-----	-----	1.431	1
023	-----	-----	-----	-----	1.406	3

In indexing the pattern the unit-cell dimensions were taken in the Dana convention, $c<a<b$, although the reverse order is given by Wyckoff [8]. The unit cell dimensions published in 1934 by Braekken and Scholten [26], 5.963, 12.735, 4.325, converted from *kX* to angstroms compare thus with those derived from the NBS pattern:

Unit-cell, angstroms

		a	*b*	*c*
1934	Braekken and Scholten	5.975	12.761	4.334
1951	Swanson and Tatge (26° C)	5.96	12.76	4.32

The presence of *hk*0 lines only for *k* even, and *h*0*l* lines only for $h+l$ even, agrees with the generally accepted orthorhombic space-group determination D_{2h}^{16} (*Pmnb*) for the crystal orientation used here. The density of the material calculated from the NBS X-ray data is $D=5.49$. The indices of refraction are very high.

7. Magnesium Silicate, Mg_2SiO_4

A sample of magnesium silicate (forsterite) of high purity, labeled X–9, was furnished by the Radio Corporation of America. It was prepared in connection with their phosphor project [12], by heating at 1,500° C for 1 hr. The indexed pattern is compared in table 8 with a pattern published by Clark [27] in 1946. Clark's pattern was made with cobalt radiation, for which he specified a wavelength of 1.786 A (*kX*), that of the NBS with copper, of wavelength 1.54050 A. The large unit cell of magnesium silicate furnishes a large number of possible planar reflections. Thus indexing becomes increasingly difficult with increasing Bragg angle. As θ increases, Clark's interplanar spacings diverge more and more widely from calculated values. The last 17 lines of his pattern were omitted from the table because the divergence combined with the multiplicity of possible lines makes indexing purely arbitrary. The Geiger-counter intensity measurements of the NBS pattern show 112 to be the strongest line, 131 second, and 222 third, rather than the order 222, 131, and 112 estimated by Clark.

TABLE 8.

Magnesium silicate: Mg_2SiO_4

	1946, Clark Co, 1.789		1951, Swanson and Tatge Cu, 1.5405, 26° C	
hkl	*d*	*I*	*d*	*I*
020	5.1	vvw	5.11	26
021	3.86	ms	3.88	69
101	3.71	vw	3.73	25
111	3.49	vw	3.487	21
120				
121	2.98	vw	3.000	17
002	2.87	vvw		
130	2.75	ms	2.768	53
131	2.50	s	2.513	73
112	2.45	s	2.458	100
041	2.34	vvw	2.348	9
210	2.31	vvw	2.316	9
122	2.26	w	2.268	20
140	2.24	w	2.250	33
211	2.15	vw	2.161	15
132	2.03	vvw	2.034	5
042	1.934	vvw	1.945	4
150	1.864	vvw	1.878	5
113	1.798	vvw	1.811	2
151	1.776	vvw	1.792	3
222	1.737	vs	1.748	60
240	1.729	vvw		
241	1.661	vw	1.670	13
061	1.624	vw	1.636	12
133	1.607	vw	1.618	15
152			1.589	2
300	1.579	vvw		
043	1.560	vvw	1.572	10
301	1.523	vvw	1.531	1
311	1.504	vvw	1.514	10
213				
320				
004	1.487	w	1.497	27
062	1.471	ms	1.479	30
330	1.424	vvw	1.438	4
170	1.385	vw	1.396	12
233			1.394	9
322	1.341	w	1.351	17
134	1.305	vw	1.316	9
332	1.285	vvw	1.295	2
204			1.266	1
214			1.256	1
262				

Magnesium silicath: Mg_2SiO_4—Con.

	1946, Clark Co, 1.789		1951, Swanson and Tatge Cu, 1.5405, 26° C	
hkl	*d*	*I*	*d*	*I*
163			1.246	2
081				
270			1.242	2
351			1.226	1
400	1.181	vvw	1.189	1
401	1.159	vvw	1.166	2
352	1.148	vvw	1.155	1
272	(*)		1.1476	1
263			1.1369	2
421				
430			1.1225	1
412			1.0987	1
334			1.0360	3
055				
0.10.0			1.0201	3
283			0.9797	1
381				
462				
414			.9266	1
2.10.1				
531			.9061	1
444			.8748	1
3.10.1			.8495	1
0.12.0				
533			.8331	7
326				
365				
552			.8281	9
1.11.3				
037				

* The remaining 17 lines could not be indexed and are omitted.

Although several sets of unit-cell dimensions are available for the closely related mineral olivine (iron-bearing), only one was found for forsterite. Rinne [28] in 1923 examined a natural forsterite from Vesuvius, for which he found the dimensions $a=4.74$, $b=10.26$, $c=5.99$, using molybdenum radiation, wavelength 0.7076 A, which compares very closely with olivine measurements. Converting from *kX* to angstrom units, his values compare with those derived from the NBS pattern thus:

Unit cell, angstroms

		a	*b*	*c*
1923	Rinne	4.75	10.28	6.00
1951	Swanson and Tatge (26° C)	4.76	10.20	5.99

From the NBS data the cell dimensions were calculated only from spacings of planes parallel to one or more axes.

Forsterite is orthorhombic with a space group presumably the same as that specified by Bragg and Brown [29] for olivine, V_h^{16}, or D_{2h}^{16} (*Pnma*). The density calculated from the cell dimensions of the NBS determination, allowing four molecules per unit cell, is 3.213. The material was too finely powdered for us to determine the indices of refraction.

8. Magnesium Tungstate, $MgWO_4$

Five patterns of magnesium tungstate are compared in table 9. Two are by Broch [30], published in 1928 and 1930, one by Fonda [31], 1944, and one by Dunning and Megaw [32], 1946. To Broch we owe most of the indices. He used copper radiation for the first pattern, iron for the second. In addition to the indices his data include diffraction, angles and, for the second pattern, estimated intensities. The interplanar spacings listed in table 9 were computed from his reflection angles with recent wavelength values, so that they appear in angstroms. Fonda used molybdenum radiation, other workers copper. The Fonda and the Dunning and Megaw interplanar spacings are converted from presumed kX units to angstroms. For the NBS pattern, material of exceptionally high purity was obtained from the Radio Corporation of America, marked No. 4, prepared at 1,000° C. The NBS pattern includes the first accurately measured intensities.

TABLE 9. *Magnesium tungstate:* $MgWO_4$

hkl	1928 Broch Cu, 1.54	1930 Broch Fe, 1.936		1944 Fonda Mo, 0.709		1946 Dunning and Megaw Cu, 1.540		1951 Swanson and Tatge Cu, 1.5405, 26°C	
	d	d	I	d	I	d	I	d	I
010	5.60	5.69	s	5.60	s	5.66	w	5.68	21
100	4.64	4.69	s	4.65	s	4.68	s	4.68	91
011	3.72	3.71	s	3.72	s	3.70	ms	3.70	97
110	3.60	3.60	m	3.61	f	3.60	m	3.607	39
111	2.91	2.91	s	2.91	s	2.94	ms	2.928	100
$\bar{1}11$	.....	2.90	s	.....	..	2.92	ms	2.902	86
020	2.84	2.89	m	.....	..	2.84	m	2.841	20
002	2.46	2.47	s	2.46	m	2.46	ms	2.462	47
021		2.45	s						
120	2.43	2.42	vw	.....	..	2.42	mw	2.426	11
200	2.34	2.34	w	2.34	m	2.34	m	2.346	10
012	2.26	2.27	w	.....	..	2.26	vvw	2.260	<1
102	2.18	2.19	s	.....	..	2.20	mw	2.194	26
121	2.17	2.17	s	2.18	m	2.17	ms	2.173	28
$\bar{1}02$	.....	.....	.....	.....	..	.....	..	2.170	27
210	2.16	2.15	vvw	.....	..	.....	..	.....	.....
112	2.03	2.04	vw	.....	..	2.05	w	2.047	5
$\bar{1}12$		2.03	vw	.....	..	2.02	w	2.026	4
211	1.98	1.99	m	.....	..	1.991	mw	1.993	13
$\bar{2}11$	1.98	1.97	m	1.97	w	1.975	m	1.975	15
030	1.89	1.89	s	.....	..	1.892	mw	1.892	3
022	1.86	1.86	m	1.88	w	1.861	m	1.862	5
220	1.81	1.81	s	1.80	w	1.813	m	1.806	10
130	1.75	1.75	vvs	1.75	m	1.754	ms	1.754	21
122	.....	.....	.....	.....	..	1.738	w	1.735	2
$\bar{1}22$	1.73	.....	.....	.....	..	1.726	vw	1.724	3
031	.....	.....	.....	.....	..	1.712	ms	.....	.....
202	.....	1.71	s	.....	..	1.705	ms	1.708	16
221						.....	..	1.702	16
$\bar{2}21$	1.69	1.69	vs	1.696	m	1.692	s	1.689	22
131	1.65	..	..	.....	..	1.659	vw	1.652	1
$\bar{1}31$									
003	.....	..	..	.....	..	1.639	vw	1.639	<1
212	1.62	..	..	.....	..	1.622	vw	1.617	<1
$\bar{2}12$									
013	1.58	..	..	1.574	f	1.581	mw	1.578	4
300	.....	..	..	.....	..	1.566	w	1.565	1
032	1.50	..	..	.....	..	1.505	ms	1.502	10
113	1.493	..	..	1.497	m	1.494	m	1.499	5
$\bar{1}13$	1.480	..	..	.....	..	1.477	m	1.491	1
230	1.470	..	..	.....	..	1.466	w	1.473	2
222	.....	..	..	.....	..	1.465	w	1.465	3
$\bar{2}22$	1.454	..	..	.....	..	1.451	ms	1.448	8

TABLE 9. *Magnesium tungstate:* $MgWO_4$—Continued

hkl	1928 Broch Cu, 1.54	1930 Broch Fe, 1.936		1944 Fonda Mo, 0.709		1946 Dunning and Megaw Cu, 1.540		1951 Swanson and Tatge Cu, 1.5405, 26°C	
	d	d	I	d	I	d	I	d	I
311	1.438	..	..	.....	..	1.438	ms	1.434	13
$\bar{3}11$									
132	1.428	..	..	1.427	m	1.427	ms	1.426	10
$\bar{1}32$	1.426	..	..	.....	..	.....	..	1.423	12
320	1.365	..	..	1.365	w	.....	..	1.364	5
041	1.363	..	..	.....	..	.....	..	.....	.....
302	1.320	..	..	.....	..	.....	..	1.325	1
321									
321	1.315	..	..	.....	..	.....	..	1.317	1
$\bar{3}02$									
141	1.309	..	..	1.313	m	.....	..	1.311	5
$\bar{1}41$									
213									
$\bar{2}13$	1.306	..	..	.....	..	.....	..	.....	.....
232	.....	..	..	.....	..	.....	..	1.269	2
$\bar{2}32$	1.261	..	..	1.262	f	.....	..	1.260	1
004	.....	..	..	.....	..	.....	..	1.231	1
223	1.215	..	..	.....	..	.....	..	.....	.....
$\bar{2}23$	1.211	..	..	.....	..	.....	..	.....	.....
330	1.202	..	..	1.204	f	.....	..	1.206	3
322	1.1933	..	..	.....	..	.....	..	.....	.....
$\bar{3}22$									
142	.....	..	..	.....	..	.....	..	1.1897	1
$\bar{1}42$	.....	..	..	.....	..	.....	..	1.1805	2
241	1.1776	..	..	1.177	f	.....	..	1.1778	1
$\bar{2}41$	1.1764	..	..	.....	..	.....	..	.....	.....
400	.....	..	..	.....	..	.....	..	1.1743	1
050	.....	..	..	.....	..	.....	..	1.1397	1
024	1.1273	..	..	.....	..	.....	..	.....	.....
411	1.1149	..	..	1.114	f	.....	..	1.1186	1
$\bar{4}11$									
150	1.1019	..	..	1.102	f	.....	..	1.1034	3
124	1.0990	..	..	.....	..	.....	..	1.0987	1
$\bar{1}24$									
420	1.0818	..	..	1.080	f	.....	..	1.0853	<1
043	1.0726	..	..	.....	..	.....	..	1.0768	1

The unit-cell constants of the monoclinic magnesium tungstate crystals were given by Broch from his first pattern as $a=4.67$, $b=5.66$, $c=4.92$, $\beta=89°35'$, from his second pattern as $a=4.68$, $b=5.66$, $c=4.93$, $\beta=89°40'$. Converted from kX to angstroms, the later values compare with those derived from the NBS pattern thus:

Unit cell, angstroms

		a	b	c
1930	Broch	4.69	5.67	4.94
1951	Swanson and Tatge (26° C)	4.69	5.68	4.92

Broch's 1930 paper gives the space group as $C_{2h}^{4}(P2/c)$ two molecules in the unit cell; the NBS pattern conforms to this determination. The density calculated from the NBS data is 6.897. The material was too finely powdered to work with satisfactorily in determining the indices of refraction, but it is known that they are very high.

V. References

[1] American Society for Testing Materials, X-Ray Diffraction Data Cards, Philadelphia, Pa. (1939?); first supplement (1944); second edition, including second supplement (1950). For a description of this file see Bull. Am. Soc. Testing Materials No. **135,** 64 (1945); No. **160,** 18 (1949).

[2] H. Friedman, Geiger-counter spectrometer for industrial research, Electronics **18,** 132 (1945).
[3] Eric R. Jette and Frank Foote, Precision determination of lattice constants, J. Chem. Phys. **3,** 605 (1935).
[4] H. van Bergen, Präzisionsmessung von Gitterkonstanten mit einer Kompensationsmethode II, Ann. Phys. **39,** 553 (1941).
[5] Kathleen Lonsdale, Divergent-beam X-ray photography, Nature **153,** 22 (1944).
[6] National Bureau of Standards Applied Mathematics Series 10, Tables for conversion of X-ray diffraction angles to interplanar spacing. (Government Printing Office, Washington, D. C., 1950.)
[7] Ludo K. Frevel, Chemical analysis by powder diffraction, Ind. & Eng. Chem., Anal. Ed. **16,** 209 (1944).
[8] Ralph W. G. Wyckoff, The structure of crystals, 2d ed., (The Chemical Catalog Company, Inc., New York, N. Y., 1931); Supplement (Reinhold Publishing Corp., New York, N. Y., 1935); Crystal structures (Interscience Publishers Inc., New York, N. Y., 1948).
[9] Strukturbericht (Akademische Verlagsgesellschaft M. B. H., Leipzig).
[10] Chemical abstracts (American Chemical Society, Easton, Pa.).
[11] The conversion factor for kX units to angstrom units, J. Sci. Inst. 24, 27 (1947).
[12] H. W. Leverenz, Phosphors versus the periodic system of the elements, Proc. Inst. Radio Engineers **32,** 256 (1944).
[13] L. Vegard, Die Struktur der isomorphen Gruppe $Pb(NO_3)_2$, $Ba(NO_3)_2$, $Sr(NO_3)_2$, Z. Phys. **9,** 395 (1922).
[14] J. D. Hanawalt, H. W. Rinn, and L. K. Frevel, Chemical analysis by X-ray diffraction; classification and use of X-ray diffraction patterns, Ind. & Eng. Chem., Anal. Ed. **10,** 457 (1938).
[15] F. M. Jaeger and F. A. van Melle, On the symmetry and structure of the cubic nitrates of calcium, strontium, barium, and lead, Akad. Wetens. Amsterdam, Proc. Sec. Sci. **31,** 651 (1928).
[16] H. Th. Ringdal, Über Mischkristalle von Erdalkalinitraten, Z. Krist. **82,** 50 (1932).
[17] L. Vegard and K. I. Roer, Verfahren zur röntgenometrischen Bestimmung des Temperatureinflusses auf Kristallgitter mit Verwendung auf Nitraten zweiwertiger Metalle, Avhandl. Norske Vidensk.-Akad. Oslo I, Mat.-Naturv. Klasse **1941,** No. 17 (1942).
[18] L. Vegard and Leif Bilberg, Die Kristallstruktur der Nitrate von Ca, Sr, Ba und Pb, Avhandl. Norske Vidensk.-Akad. Oslo, I, Mat.-Naturv. Klasse **1931,** No. 12, 22 pp. (1932).
[19] W. Nieuwenkamp and J. M. Bijvoet, Die Kristallstruktur von Bleifluochlorid PbFCl, Z. Krist. **81,** 469 (1932).
[20] W. Nieuwenkamp, Die chemische Zusammensetzung von Matlockite, Z. Krist. **86,** 470 (1933).
[21] L. K. Frevel, H. W. Rinn, and H. C. Anderson, Tabulated diffraction data for tetragonal isomorphs, Ind. & Eng. Chem., Anal. Ed. **18,** 83 (1946).
[22] F. A. Bannister, The crystal structure and optical properties of matlockite (PbFCl), Miner. Mag. **23,** 587 (1934).
[23] James D. McCullough, The crystal structure of selenium dioxide, J. Am. Chem. Soc. **59,** 789 (1937).
[24] G. R. Waitkins and C. W. Clark, Selenium dioxide; preparation, properties and use as oxidizing agent, Chem. Rev. **36,** 235 (1945).
[25] H. Bräkken and L. Harang, Zur Kristallstruktur einiger rhombischer Verbindungen MX_2; I, Z. Krist. **68,** 123 (1928).
[26] H. Braekken and W. Scholten, Die Kristallstruktur des Quecksilber Chlorids $HgCl_2$, Z. Krist. **89,** 448 (1934).
[27] C. Burton Clark, X-ray diffraction data for compounds in the system CaO–MgO–SiO_2, J. Am. Ceramic Soc. **29,** 25 (1946).
[28] F. Rinne, Bemerkungen und röntgenographische Erfahrungen über die Umgestaltung und den Zerfall von Kristallstrukturen, Z. Krist. **59,** 230 (1923).
[29] W. L. Bragg and G. B. Brown, The structure of olivine, Z. Krist. **63,** 538 (1926).
[30] Einar Broch, Über die Gitterart einiger monoklinen Verbindungen vom Typus $MgWO_4$, Z. Phys. Chem. [B] **1,** 409 (1928); Untersuchungen über Kristallstrukturen des Wolframittypus und des Scheelittypus, Skrifter Norske Videns.-Akad. Oslo I, Mat.-Nat. Klasse **1929,** No. 8 (1930).
[31] Gorton R. Fonda, The magnesium tungstate phosphor, J. Phys. Chem. **48,** 303 (1944).
[32] N. J. Dunning and Helen D. Megaw, The crystal structure of magnesium tungstate, Trans. Faraday Soc. **42,** 705 (1946).

WASHINGTON, October, 31, 1950.

Journal of Research of the National Bureau of Standards Vol. 46, No. 4, April 1951 Research Paper 220

The Half-Life of Carbon 14[1]

George G. Manov[2] and Leon F. Curtiss

The half-life of carbon 14 has been determined by gas counting of $C^*O_2+CS_2$ mixtures (where C^*O_2 is used to designate inert carbon dioxide containing some $C^{14}O_2$) by using pairs of counters that are identical in construction except for the length of the cathodes. The suitability of various equations proposed for calculating the true counting rate, C_T, from the resolving time, t_r, and the observed counting rate, C_o, is evaluated from experimental measurements of C_o and t_r and is presented graphically. A value of $5,370 \pm 200$ years for the half-life of C^{14} is obtained from these measurements. By comparison with the results of other workers, it is estimated that the most probable value for the half-life of carbon 14 is $5,400 \pm 200$ years.

I. Introduction

The half-life of carbon 14 has been the subject of many determinations, the values of which have ranged from a high of 7,200 to a low of 4,700 years. Two general methods have been used: end-window counting of solid barium carbonate, and counting of gaseous carbon dioxide, in which the radioactive carbon is either a minor or a major portion of the filling gas of the counter. In general, larger and more numerous corrections are necessary to the experimental measurements if solid counting is employed.

Libby [1][3] and Jones [2] have introduced the radioactive carbon dioxide as a minor constituent of the gas filling of Geiger-Müller counters containing the customary alcohol-argon mixture. The technique employed by Brown and Miller [3] of counting $C^{14}O_2+CO_2+CS_2$ (abbreviated as $C^*O_2+CS_2$) mixtures represents a notable advancement in the analysis of radiocarbon.

The National Bureau of Standards has prepared, and is in the process of certifying, standard sources of activity of C^{14}. The process of standardization consists of three parts: (1) A collaborative determination by mass spectrograph of the isotopic ratio of C^{14} in carbon dioxide prepared at the Bureau from active barium carbonate, (2) conversion at the Bureau of a weighed amount of barium carbonate into active sodium carbonate solution containing 0.1-M inactive sodium carbonate as carrier and approximately 0.0001-M free sodium hydroxide, (3) collaborative analysis of the solution by absolute gas counting. The standards after certification will be available * in the form of glass ampoules containing 25 ml of the above solution and having an activity of the order of 1,000 disintegrations per second per milliliter. A full account of the collaborative analyses will be presented when all the results of the determinations have been received. The purpose of the present paper is to offer preliminary values obtained at the Bureau for this intercomparison.

[1] Presented at the Chicago meeting of the American Chemical Society Petroleum Division on Sept. 6, 1950.

[2] Present address, Isotopes Division, Atomic Energy Commission, Oak Ridge, Tenn.

[3] Figures in brackets indicate the literature references at the end of this paper.

* The ampoules referred to above are now available for distribution by the National Bureau of Standards.

The value in this paper for the half-life of C^{14} was calculated from the equation

$$T_{\frac{1}{2}}=0.693\ N/(dN/dt), \tag{1}$$

where N, the number of atoms of C^{14}, was determined by mass-spectographic analysis, and dN/dt (the rate of radioactive decay) was measured by gas counting of mixtures of $C^*O_2+CS_2$.

II. Determination of the Number of Active Carbon Atoms

Radioactive carbon dioxide was obtained by heating active barium carbonate[4] to approximately 1,100° C in a quartz tube. Analysis of the isotopic ratio was made by Fred L. Mohler and Vernon H. Dibeler, of the Bureau's Mass Spectrometry Section. The average value obtained from 10 determinations was 3.876 $\pm$0.002 percent of C^{14}, with an estimated accuracy of $\pm$0.04 percent (absolute), based on known limits to calibration and other procedural errors. The probable error was computed from the formula

$$0.8453\Sigma d/n\sqrt{n-1}.$$

A quantity of active barium carbonate weighing 0.1066 $\pm$0.0001 g was transferred to a small round-bottomed flask containing 1.40 g of inert barium carbonate. (The exact quantity used is not critical.) The mixture was treated with an excess of perchloric acid in an evacuated system and the carbon dioxide absorbed in a tenfold excess of 2-M sodium hydroxide. The large amount of inactive CO_2 evolved aided in sweeping over the active carbon dioxide. (It should be noted that neither the perchloric acid nor the sodium hydroxide were required to be carbonate-free.) Quantitative transfer was accomplished by boiling the acidified solution several times. Examination of the resulting sodium carbonate solution by means of a Tyndall beam indicated that no barium ion was carried over.

The sodium carbonate portion was diluted gravimetrically to a volume of 39.00 liters at 25° C with

[4] The BaC^*O_3 was made available by the Atomic Energy Commission through the Oak Ridge National Laboratory, and had been especially purified by W. J. Skraba of the ORNL Chemistry Division.

the appropriate quantity of inert Na_2CO_3 dissolved in water to form a solution that contained all the active carbon as $Na_2C^{14}0_3$, 0.100-*M* inert Na_2CO_3 as carrier, and free sodium hydroxide to the extent of approximately 0.001 *M*. The accuracies in weighing the active barium carbonate and in preparing the large volume of solution were each of the order of 0.1 percent. One milliliter of the above solution was therefore equivalent to 2.733 $\pm$0.005 mg of barium carbonate. Analysis by R. A. Paulson, of the Bureau's Chemistry Division, of the original barium carbonate for carbon dioxide indicated a purity of 97.1 percent (with an absolute error of $\pm$0.4 percent), and 1 ml of the solution contained[5] (3.132 $\pm$0.050) $\times 10^{14}$ atoms of C^{14}. Bureau calibrated weights and volumetric glassware were used throughout. Experiments made with A. Schwebel, using an ionization chamber and a vibrating-reed electrometer, demonstrated that 0.1-*M* sodium carbonate carrier was sufficient to prevent the loss of any significant quantity of active carbonate by adsorption on the walls of the container.

III. Apparatus and Experimental Technique

1. Apparatus

The counter, a sketch of which is shown in figure 1, consists of an outer Pyrex jacket in which are assembled, in order, a 1-in. glass spacer, a disk of aluminum approximately 1 mm in thickness, a copper cathode with a passivated surface, a 1-in. glass spacer, a second disk of aluminum, and finally a 1-in. glass spacer. The outermost spacers are sealed to the glass jacket and prevent movement within the assembly. The aluminum disks define

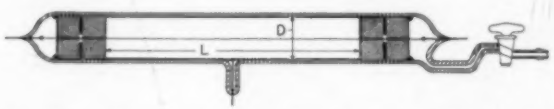

FIGURE 1. *Cross section of carbon dioxide counter showing effective length (L) and diameter (D).*

the active volume of the counter, and a small hole is drilled in each, through which passes a center wire of 3-mil tungsten. The ends of the center wire are sealed to the ends of the outer Pyrex envelope. The inner spacers are identical in length ($\pm$0.01 in.); they serve to insulate the copper cathode from the aluminum disk and to make the ends of the counter identical. It has been shown [4] that the efficiency of these counters is 97 $\pm$1 percent. The number of observed counts per second is, therefore, very nearly equal to the disintegration rate.

A number of experimental counters were built, and a total of six was used for the C^{14} measurements. Their nominal dimensions (inside diameter and length) were 1 in. by 12 in. and 1 in. by 6 in.; ¾ in. by 12 in. and ¾ by 6 in.; and ½ in. by 12 in. and ½ in. by 6 in. Four measurements of the diameter and two of the length were made of each cathode, and the averages are listed in table 1.

[5] The accuracy in the determination of *N*, of *dN/dt*, and of the half-life is given in section V.

TABLE 1. *Dimensions of copper cathodes used in counters*

Counter	Length	Inside diameter	Cathode volume	Difference in cathode volume	Length / diameter
	cm	*cm*	*cm*³	*cm*³	
1	29.868 $\pm$0.001	2.357 $\pm$0.004	130.34 $\pm$0.31		12.7
2	15.049 $\pm$0.002	2.351 $\pm$0.001	65.33 $\pm$0.04	65.01 $\pm$0.31	6.4
3	30.162 $\pm$0.002	1.925 $\pm$0.004	87.87 $\pm$0.26		15.7
4	15.079 $\pm$0.010	1.928 $\pm$0.001	44.02 $\pm$0.03	43.85 $\pm$0.27	7.8
5	30.480 $\pm$0.003	1.278 $\pm$0.002	39.10 $\pm$0.08		23.9
6	15.186 $\pm$0.003	1.269 $\pm$0.003	19.21 $\pm$0.06	19.89 $\pm$0.10	12.0

The preparation line (fig. 2) consisted of a 25-ml round-bottomed Pyrex bulb in which the carbon dioxide was generated; a calibrated mixing bulb (146.8$\pm$0.1 ml) equipped with a freeze-out tube, a small flask with a stopcock through which pure CS_2 vapor could be admitted into the mixing bulb, a mercury manometer with a ½-in. bore, and lastly, a pair of counters that could be detached from the system by means of standard-taper glass joints.

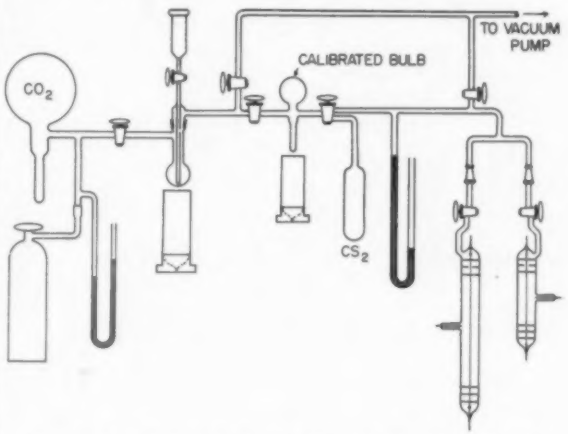

FIGURE 2. *Glass train for preparation of carbon dioxide samples and filling counters.*

The total volume of the system (mixing bulb, counters, manometer, etc.) was readily determined by noting the change in pressure produced by expanding nitrogen gas from the known volume of the mixing bulb (146.8 ml) into the entire system. The total volume ranged from 390 to 650 ml, depending upon the pairs of counters used and could be determined to $\pm$0.2 percent.

The counting system used included a preamplifier and quench circuit of the type used by Mann and Parkinson [5] and a conventional scaler. The resolving time applied to the counter was measured by an oscilloscope and could be varied from 300 to 1,400 microseconds.

2. Experimental Technique

A definite quantity of active sodium carbonate solution (0.5 to 1 ml, measured to $\pm$0.002 ml) was pipetted into the generating flask. The solution was frozen by means of liquid air and the flask evacuated.

The vacuum was shut off, and a large excess (25 to 30 ml) of concentrated sulfuric acid was added slowly and frozen in a layer above the solidified carbonate solution. The liquid air was then removed and the flask allowed to warm to room temperature. The sulfuric acid, because of its lower melting point, was the first to liquefy and, as the carbonate began to melt, the evolution of carbon dioxide proceeded very smoothly. This technique of adding the sulfuric acid served not only to generate the carbon dioxide, but completely to remove the water from it as the reaction progressed. (This technique can also be used with barium carbonate; the barium sulfate is soluble in excess of concentrated sulfuric acid.) The necessity for the quantitative separation of the water from the carbon dioxide, as would have been required had the customary procedure of adding the acid dropwise to the carbonate solution been used, was therefore avoided, and a considerable simplification in the construction of the gas train was rendered possible.

The carbon dioxide was admitted to the calibrated mixing bulb, which contained a pressure of carbon disulfide (approximately 2 cm) requisite for the operation of the counters. The generating bulb was warmed and flushed with a quantity of inactive carbon dioxide that would be sufficient to yield a final pressure between 8 and 15 cm within the counters. The contents of the mixing bulb was frozen by means of liquid air, and any trace of permanent gas removed by pumping. The pump was then shut off, the liquid air removed, and the gases allowed to mix by thermal diffusion, after which the counter assembly and the manometer system were filled. The counters were then removed from the preparation line and placed within a 2-in. lead shield.

3. Correction for Resolving Time

It is well known that the use of CO_2 as a filling gas may result in counters having resolving times as high as 1,000 microseconds and, further, that CO_2+CS_2 counters are not self-quenching. In this respect, such counter fillings are inferior to alcohol-argon, to which is added a small amount of carbon dioxide. The advantage of using the CO_2+CS_2 mixture, on the other hand, is that it eliminates the necessity of working with very small volumes of CO_2 (0.01 to 0.1 ml) and diminishes any concern regarding the possibility of absorbing some of the CO_2 on the comparatively large surfaces of the sample preparation line and on the walls of the counter.

Various equations have been proposed to correct the observed counting rate, C_o, to a "true" one, C_T.

$$C_T=C_o e^{C_T t_r}, \tag{2}$$

$$C_T=C_o(1+C_o t_r), \tag{3}$$

$$C_T=C_o\left(1+C_o t_r+\frac{(C_o t_r)^2}{2!}+\frac{(C_o t_r)^3}{3!}+\cdots\right), \tag{4}$$

and

$$C_T=\frac{C_o}{(1-C_o t_r)}. \tag{5}$$

Equations 2 [6, 7, 8] and 5 [10] have been derived from theoretical considerations. Equations 3 [9] and 4 represent expansions of eq 5 and 2, respectively.

So long as the resolving time, t_r, is small (approximately 300 microseconds), eq 2 to 5 all lead to approximately the same percentage corrections even at fairly high rates of counting, but if the resolving time is of the order of 1,000 microseconds, not all of them are equally suitable. The differences in these equations will be accentuated for high values of t_r and of C_o.

An experimental test of the suitability of eq 2 through 5 was made by observing the counting rate obtained for a mixture of $C^*O_2+CS_2$ as the resolving time applied to the counter was increased systematically. All other variables, including the voltage applied to the counter, were kept constant, and the measurements were made at a point approximately in the center of the plateau. Since C_o is measured experimentally for each setting of t_r, the equation that is the most nearly suitable for obtaining a true counting rate is that which yields calculated values for C_T that show no trend with t_r. The results of such a test are presented in table 2 and in figure 3. Figure 3 shows that eq 2 overcorrects and that eq 3 and 4 undercorrect. Equation 5 appears to be the most suitable, and it was therefore selected for correcting all observed counting rates, C_o, to a true value, C_T. The accuracy in the correction for resolving time is estimated at ± 1 percent.

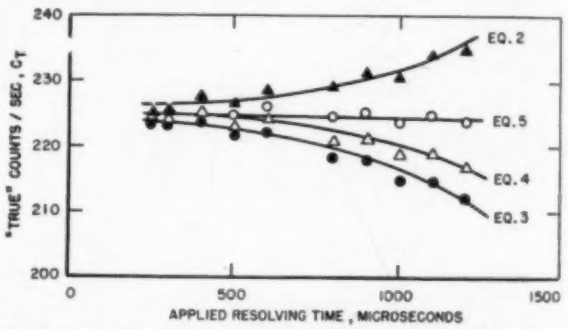

FIGURE 3. *Curves showing the results of application of various resolving time correction formulae to data.*

▲, eq 2; ●, eq 3; △, eq 4; ○, eq 5.

TABLE 2. *Suitability of various equations proposed for correcting observed counting rate, C_o, at a resolving time, t_r*

Applied resolving time	Observed counting rate, C_o	Corrected counting rate obtained by equation			
		2	3	4	5
Microseconds	*Counts/sec*				
350	208.7	225.9	223.4	224.6	225.1
400	206.2	225.6	223.2	223.9	224.7
500	203.5	228.1	224.2	225.3	226.6
600	198.1	227.0	221.7	223.0	224.8
700	195.6	229.0	222.4	224.3	226.0
900	186.7	229.5	218.1	220.9	224.4
1,000	183.9	231.9	217.7	221.0	225.3
1,100	179.4	231.3	214.8	218.5	223.5
1,200	177.1	234.7	214.7	219.0	224.9
1,300	173.2	235.1	212.2	216.8	223.5

4. Effect of Resolving Time on Length of Plateau

The effects of varying the total pressure within the system, the ratio of carbon disulfide to carbon dioxide, the resolving time applied to the counters, etc., were determined. The effect on the plateau of varying the applied resolving time is particularly worthy of mention.

In figure 4 are plotted typical plateaus (for a given mixture of CS_2 and C^*O_2) corresponding to different values of the applied resolving time, t_r. It is evident that longer plateaus are associated with larger values of t_r. As the correction for the effect of the resolving time can be applied by use of eq 5, and a comparatively long plateau is desirable, most of the subsequent experimental work was performed by using $t_r = 1{,}000$ microseconds, with two measurements being made by using $t_r = 1{,}400$ microseconds.

A typical plateau obtained by using a resolving time of 1,000 microseconds applied to a pair of counters (1 in.×12 in. and 1 in.×6 in.) filled with CS_2 and active CO_2 is shown in figure 5. The lowest curve represents the differences in the two counting rates. The flatness of the plateaus indicates that the distortion of the electric field of the ends of the counters is small. A counter 1 in. in diameter and 3 in. in length did not give a flat plateau, presumably because the distortion of the field at the ends of the counter amounted to an appreciable fraction of the length of the cathode. Counters whose ratio of length to diameter was 6 or more were found to be satisfactory.

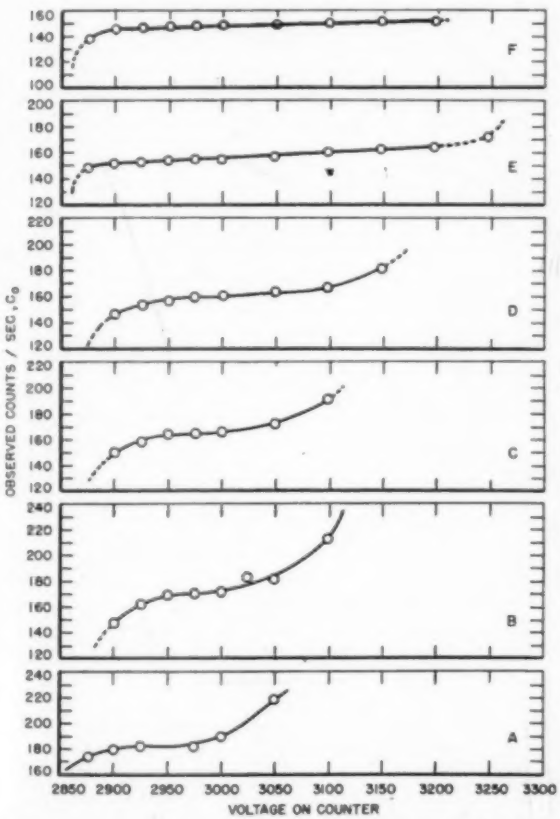

FIGURE 4. *Curves showing the effect of various resolving times on the length of the plateau of the counter.*

A, t_r=325 microseconds; B, t_r=600 microseconds; C, t_r=800 microseconds; D, t_r=1,000 microseconds; E, t_r=1,200 microseconds; F, t_r=1,400 microseconds.

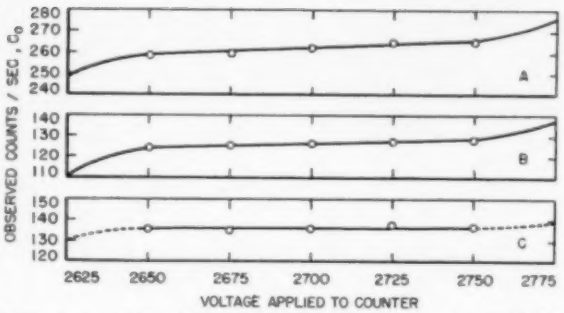

FIGURE 5. *Typical plateau for two sizes of counters with the curve representing the differences in counting rate.*

A, 1 in. by 12 in. counter; B, 1 in. by 6 in. counter; C, difference in counts per second; t_r=1,000 microseconds; PCS_2=2.2 cm; PC^*O_2=8.6 cm.

IV. Determination of the Rate of Decay, *dN/dt*

The rate of decay of the solution containing $Na_2C^{14}O_3$ was measured as follows. The number of counts per second was determined as a function of the applied voltage for each of a pair of counters filled with a definite mixture of CS_2 and active CO_2. Between 100,000 and 200,000 counts were totalized at each voltage setting to obtain a standard deviation $\left(\frac{\sqrt{\text{total counts}}}{\text{total counts}}\right)$ between 0.3 and 0.2 percent. Corrections were then applied to each point for the resolving time (eq 5) and for the background to yield a net counting rate, C_n. The difference in C_n for the long and short counters were averaged. The activity of the solution in disintegrations per second per milliliter was calculated from

$$(\text{dis/sec})/\text{ml} = \frac{\Delta C_n \times V}{\Delta V \times \text{ml} \times 0.97}, \qquad (6)$$

where ΔC_n is the average difference in net counting rate for the pair of counters used, ΔV is the difference in their cathode volumes (table 1), V is the total volume of the system, ml is the number of milliliters of the active solution taken, and 0.97 is the efficiency [4] of the counting system.

In table 3 is presented a condensation of the data that were obtained. In columns 1, 2, 3, 4, 5, and 6 are shown, respectively, the nominal dimensions of the pairs of counters used, the differences in their cathode volumes, the volume of active Na_2CO_3 solution taken, the applied resolving time in microseconds, the total volume of the system, and the average net difference in counting rate. In column 7 is computed the activity of the carbonate solution in disintegrations per second per milliliter. The aver-

age value is 1,280 (dis/sec)/ml with a probable error of the mean $\left(E=\frac{0.845\Sigma d}{n\sqrt{n-1}}\right)$ or ± 8 (dis/sec)/ml.

TABLE 3. *Condensation of data obtained for the activity of a solution of* Na_2CO_3 *containing* C^{14}

Counter	Difference in cathode volume	Volume of Na_2CO_3 taken	Applied l_T	Total volume of system	Average net difference in rate	Activity of solution
in.	*ml*	*ml*	*μ seconds*	*ml*	*Counts/sec*	*dis/sec/ml*
1 by 12 and 1 by 6	65.01	0.502	1,000	637.9	63.7	1,284
1 by 12 and 1 by 6	65.01	1.013	1,000	620.4	135.9	1,320
1 by 12 and 1 by 6	65.01	0.388	1,000	639.5	49.9	1,304
1 by 12 and 1 by 6	65.01	1.013	1,400	637.8	130.7	1,300
¾ by 12 and ¾ by 6	43.85	1.013	1,000	559.4	96.9	1,258
¾ by 12 and ¾ by 6	43.85	1.013	1,400	558.3	102.6	1,282
½ by 12 and ½ by 6	19.89	1.013	1,000	394.5	60.5	1,221
½ by 12 and ½ by 6	19.89	1.013	1,000	391.5	63.5	1,272
Average						1,280
$\left(E=\frac{0.845\Sigma d}{n\sqrt{n-1}}\right)$, probable error						±8

V. Sources of Error

The accuracy in the determination of the half-life of radiocarbon can be estimated as follows. The accuracies in the determination of N involve ($\pm$ 0.04/3.876) or ± 1.0 percent in the isotopic ratio, ± 0.1 percent each in the weighing of the barium carbonate and in preparation of the solution, and ± 0.4 percent in the analysis of the barium carbonate. The accuracy [6] in N is therefore ± 1.6 percent.

The accuracy in dN/dt involves the error in the gas counting ($\pm 8/1280$) or ± 0.6 percent; in the determination of the total volume of the counting system, ± 0.2 percent; in the application of the correction for the resolving time, ± 1.0 percent; and for the efficiency of the counting system, ± 1.0 percent. The accuracy in dN/dt is therefore ± 2.8 percent. The combination of ± 1.6 percent in N and of ± 2.8 percent in dN/dt corresponds to an accuracy of ± 4.4 percent in the half-life of radiocarbon.

VI. Calculation of the Half-Life of C^{14}

The half-life of C^{14} was computed according to eq 1. N has been previously calculated to be 3.132×10^{14} atoms of C^{14}/ml of solution, and dN/dt from table 3 is 1,280 dis/sec/ml. The half-life of C^{14} is therefore 5,370 $\pm$200 years.

VII. Comparison With Other Determinations

The half-life obtained here, 5,370 $\pm$200 years, is in fair agreement with that obtained by Jones [2] (5,589 $\pm$75 years) and by Libby [1] (5,580 $\pm$45 years), but differs from that reported by Mann and coworkers [12] (6,360 $\pm$200 years) and by Yaffe and Grunlund [13] (7,200 $\pm$500 years). A summary of the values for the half-life is presented in table 4.

[6] The accuracy is $|a_1|+|a_2|+\ldots|a_n|$, where $|a|$ represents the numerical value of the accuracy without regard to sign.

TABLE 4. *Comparison of values obtained for the half-life of* C^{14}

Year	Reference	Authors	Method used for determination of—		$T_{½}$
			Isotopic ratio	Activity	
					Years
1946	[14]	Reid, Dunning, Weinhouse, Grosse	Mass spectrometer (1.71% of C^{14})	End-window	4,700 ±(235 to 470)
1948	[15]	Norris and Ingham	Mass spectrometer (3.23 and 3.35% of C^{14}).	do	5,100 ±200
1948	[13]	Yaffe and Grunlund	Mass spectrometer (6.21% of C^{14})	do	7,200 ±500
1949	[12]	Hawkins, Hunter, Mann, Stevens	do	$C^*O_2+CS_2$	6,360 ±200
1949	[1]	Engelkemeir, Hamill, Inghram, Libby.	Mass spectrometer (1.28 to 6.14% of C^{14}).	C^*O_2+alcohol-argon	5,580 ±45
1949	[2]	Jones	Mass spectrometer (39.4% of C^{14})	do	5,589 ±75
1950	This paper	Manov and Curtiss	Mass spectrometer (3.876% of C^{14}).	$C^*O_2+CS_2$	5,370 ±200

The measurements of Libby and of Jones were performed by using single counters in which the major constituent of the filling was alcohol-argon, with the carbon dioxide introduced in a small quantity. End effects were determined for counters of various sizes, and corrections were applied to the data, and the assumption was made that alcohol-argon-$C^{14}O_2$ counters were 100-percent efficient.

The value for the half-life of radiocarbon would be decreased if the barium carbonate were not entirely pure, or if the gas counters were not 100-percent efficient. Adsorption of a small amount of CO_2 on the walls of the glass system prior to entering the counter would tend to increase the value obtained for the half-life.

The value found by Yaffe and Grunlund was obtained by using an aliquot of the same Na_2CO_3 solution as used by Hawkings, Hunter, Mann, and Stevens, except that the counting was performed by using barium carbonate and an end-window counter.

VIII. Summary

The isotopic ratio of C^{14} in a mixture of inert and radioactive $BaCO_3$ was determined by a mass-spectrometric analysis of the carbon dioxide prepared therefrom. A known quantity of this barium carbonate was used to prepare a solution containing active Na_2CO_3, the activity of which was determined by using internal Geiger-Müller counters. The value for the half-life of C^{14} was found to be 5,370$\pm$200 years.

Acknowledgment is made to W. B. Mann for helpful discussions during the early experimental work, to Louis Costrell for construction of the electric equipment, and to Churchill Eisenhart for estimating the accuracy of the measurements.

IX. References

[1] A. G. Engelkemeir, W. H Hamill, M. G. Inghram, and W. F. Libby, Phys. Rev. **75,** 1825 (1949); A. G. Engelkemeir and W. F. Libby, Rev. Sci. Instr. **21,** 550 (1950).
[2] W. M. Jones, Phys. Rev. **76,** 885 (1949).
[3] S. C. Brown and W. W. Miller, Rev. Sci. Instr. **18,** 496 (1947).
[4] R. C. Hawkings, R. F. Hunter, and W. B. Mann, Can. J. Research **B27,** 555 (1949).
[5] W. B. Mann and G. B. Parkinson, Rev. Sci. Instr. **20,** 41 (1949).
[6] H. Volz, Z. Physik **93,** 539 (1935).
[7] L. I. Schiff, Phys. Rev. **50,** 88 (1936).
[8] D. E. Hull, Rev. Sci. Instr. **11,** 404 (1940).
[9] T. P. Kohman, Phys. Rev. **65,** 63 (1944).
[10] A. E. Ruark and F. E. Brammer, Phys. Rev. **52,** 322 (1937).
[11] Johnson and Street, J. Franklin Inst. **215,** 239 (1939).
[12] R. C. Hawkings, R. F. Hunter, W. B. Mann, and W. H. Stevens, Can. J. Research **B27,** 545 (1949); Phys. Rev. **74,** 696 (1948).
[13] L. Yaffe and J. M. Grunlund, Phys. Rev. **74,** 696 (1948).
[14] A. F. Reid, J. R. Dunning, S. Weinhouse and A. V. Grosse, Phys. Rev. **70,** 431 (1946).
[15] L. D. Norris and M. G. Inghram, Phys. Rev. **73,** 350 (1948).

WASHINGTON, April 5, 1950.

926653—51——6

Journal of Research of the National Bureau of Standards Vol. 46, No. 4, April 1951 Research Paper 220

Heat Capacity of Liquid Mercury Between 0° and 450° C; Calculation of Certain Thermodynamic Properties of the Saturated Liquid and Vapor

Thomas B. Douglas, Anne F. Ball, and Defoe C. Ginnings

The enthalpy of liquid mercury was measured from 0° to 450° C by the "drop" method. These and other precise published data were used to calculate a number of thermodynamic properties of liquid and gaseous mercury at the vapor pressures from the triple point, −38.88°, to +500° C. The entropy calculated from data on the vapor and liquid was compared with that derived from published low-temperature heat-capacity data for the solid. The calculated values of vapor pressure, also using data on the vapor and liquid, were found to agree over a wide temperature range with certain published experimental values when independently derived gas-imperfection and published temperature-scale corrections were applied.

I. Introduction

It is of considerable practical and theoretical importance that the physical properties of mercury be known accurately. The element has found an important use as the fluid in certain heat engines operating at high temperatures. Furthermore, it can be highly purified, perhaps more easily than almost any other commonly available substance. Because of their reproducibility, the physical properties of mercury have often been used as standards.

The accuracy of the values of many thermodynamic properties, over a temperature range, often depends on how accurately the heat capacity is known. As various past observers have shown considerable disagreement above room temperature in their values for the heat capacity of mercury, the measurements reported in this paper were undertaken primarily to furnish accurate values of this property up to a vapor pressure of 4 atm. This investigation is the second in a current series of measurements at this Bureau of the heat capacities of liquid metals.

II. Experimental Procedure

1. Method and Apparatus

The method and apparatus have been described previously [1, 2, 3].[1]

In brief, the method consists in heating the sample in a furnace to a known temperature and dropping it into an ice calorimeter, thereby measuring the heat evolved in cooling the sample to 0° C. The calibration factor of the calorimeter was determined electrically to be 270.46 ±0.03 absolute joules per gram of mercury. The samples were sealed in cylindrical containers of stainless steel. The heat capacities of the empty containers were accounted for by "blank" experiments employing them, these experiments being carried out at the same temperatures as with the filled containers. The temperature of the sample in the furnace was measured by a platinum resistance thermometer that had been calibrated at this Bureau.

2. Samples

Two samples of mercury of about 130 g each were sealed in the containers made of stainless steel No. 347, each having about 10-cm³ capacity. The capsules had the same mass (17 g) and composition as those used in the sodium investigation [3]. The samples, purified and sealed, were furnished by the Knolls Atomic Power Laboratory, of Schenectady, N. Y. Commercially pure mercury that was believed to have been triply distilled was redistilled four more times in vacuum. The samples were sealed in the containers under a pressure of helium of about 1/30 atm. The sealing process [4] was completed by a pulse of high-frequency current induced locally at the top of the container. It was found possible to seal the containers in this manner without changing their weight by more than a milligram. The "empty" containers were sealed in the same manner with the same pressure of helium. The containers filled with mercury were tested for tightness at 450° C and were found to have a leakage rate of about 0.1 microgram of mercury per hour at this temperature, an amount that is without significant effect on the enthalpy measurements.

The mercury sample actually used for most of the thermal measurements was examined spectrochemically at this Bureau. Of 34 elements looked for as possible impurities, only copper and nickel were detected by this means, and these were found to be present only in traces amounting to less than 0.01 percent of the mass of the sample. The stock supply of mercury from which the sample for the thermal measurements had been taken was analyzed by the Knolls Atomic Power Laboratory. The total nonvolatile impurity found, mostly silver, amounted to 0.00001 percent. A mass-spectrographic examination by them for "volatile" impurities indicated the possible presence of traces of aluminum, manganese,

[1] Figures in brackets indicate the literature references at the end of this paper.

iron, cobalt, nickel, zinc, and rhodium; the total amount of these, however, was shown not to exceed 0.001 percent.

III. Experimental Results

A total of 111 measurements of enthalpy was made, from 0° to 450° C (to about 4 atm pressure). Of these, 66 were made with the two empty capsules and 45 with the two capsules containing mercury. The average deviation of a single measurement from the mean at a given temperature was 0.03 percent. One of the mercury samples, measured at only 250° C (to ensure that no systematic error in mass was present), gave a mean value for the enthalpy of mercury that differed from that obtained when using the other sample by only 0.01 percent. The detailed results of individual runs are given in table 1.

No corrections for impurities were made, as these were undoubtedly so small as to lie well within the accidental error. All weights were corrected for buoyancy. No corrections for temperature were made, as the thermometer reading was held to within ± 0.01 deg of the stated temperature in each case. The ice point of the resistance thermometer changed so slightly during the course of the measurements as to indicate a negligible error in computing the temperatures. Corrections were applied to account for small differences in masses of capsule and exterior oxide coatings. In addition, corrections were made at the higher temperatures for the small heats evolved in condensing some mercury vapor inside the container, in order that the results would refer to the liquid alone.

This last-mentioned correction, and that needed to evaluate the enthalpy change that would have resulted under maintenance of saturation from the heat measurements made on the system maintained at constant volume, were conveniently calculated by an equation given by Osborne [5],

$$[Q]_1^2=[q-PV+mH_{(l)}+(V-mv)L/(v'-v)]_1^2, \quad (1)$$

where $[Q]_1^2$ is the heat evolved in cooling a closed container in which there is a liquid in equilibrium with its vapor from temperature 2 to temperature 1; $[q]_1^2$ is the contribution to $[Q]_1^2$ made by the empty container, shields, and suspension wire; P is the vapor pressure of the liquid; V is the internal volume of the container; m is the total mass of liquid and vapor; $H_{(l)}$ is the enthalpy, per unit mass, of the "saturated" liquid (i. e., at pressure P); v' and v are the specific volumes of saturated vapor and liquid, respectively; and L is the enthalpy of vaporization per unit mass.

The total of the various corrections did not exceed 0.03 percent of the enthalpy, except in the case of some of the first runs, where a correction of approximately 0.2 percent was necessitated by the use of a shield system that was later broken and so had to be replaced by one of different heat capacity.

TABLE 1. *Corrected heat and enthalpy values of individual experiments*

Furnace temperature	Measured heat		[a] Enthalpy change of mercury, H_t-H_0		
	Blank	With mercury	Observed	Calculated	Difference
°C	*abs j*	*abs j*	*abs-j g⁻¹*	*abs-j g⁻¹*	*abs-j g⁻¹*
50.00	400.5				
	403.4				
	401.6	[b](1269.3)			
	397.1	1298.7			
	401.1	1298.7	6.942	6.946	−0.004
	400.8	1298.1			
	[c] 401.0				
	[c] 401.0				
	[c] 399.2				
100.00	814.3				
	814.0				
	815.6				
	[c] 816.5	2905.0			
	[c] 815.9	2903.8	13.835	13.831	+0.004
	[c] 816.2	2904.8			
	813.2				
	814.4				
	814.6				
150.00	1238.6	3913.6			
	1242.0	3914.9	20.672	20.669	+0.003
	1239.9	3914.8			
	1241.9				
200.00	1676.6				
	1673.5	5223.9			
	1678.8	5228.9			
	1678.1	5226.4			
	1674.9	5223.0	[d] 27.461	27.470	−0.009
	1676.3	5230.2			
	1677.5	5227.4			
	[c] 1674.1	5228.6			
	[c] 1674.2	5228.1			
	[c] 1675.6				
250.00		6548.5			
	2117.5	6548.0			
	2121.5	6549.3	34.250	34.250	0.000
	2120.2	[e] 6484.0			
	2119.4	[e] 6481.9			
		[e] 6482.8			
300.00	2571.3				
	2567.0				
	2572.2	[b](7808.3)			
	2570.0	7875.9			
	2570.0	7874.8	41.027	41.019	+0.008
	2568.8	7877.9			
	[c] 2571.6	7875.3			
	[c] 2569.6				
	[c] 2569.1				
350.00	3030.5	9205.5			
	3028.0	9209.5	47.791	47.790	+0.001
	3028.2	9211.0			
	3029.1	9207.8			
400.00	3496.6				
	3493.5				
	3494.3	10548.9			
	3490.6	10544.6			
	3493.4	10550.8	[d] 54.569	54.577	−0.008
	3493.7	10553.0			
	3492.8	10548.2			
	[c] 3489.5	10547.5			
	[c] 3489.4				
	[c] 3491.2				
450.00	[b](3957.4)	11900.7			
	3964.1	11902.0			
	3965.6	11900.9			
	3964.1	11902.8	[d] 61.396	61.392	+0.004
	[c] 3965.0	11897.3			
	[c] 3965.9	11900.7			
	[c] 3964.3				

[a] Values apply to saturation (i. e., at the vapor pressure).
[b] Rejected by Chauvenet's criterion.
[c] On alternate capsule of same mass.
[d] This mean obtained by weighting each set proportionately to the number of measurements in the set and inversely proportionately to the average deviation from the mean of the set.
[e] On alternate capsule, containing 127.411 g Hg. The other capsule had the same mass of container but contained 129.344 g Hg.

Within the accidental error the heats of the empty containers ("blank" experiments) were found to vary perfectly smoothly with temperature up to 450° C. By plotting against t(°C) the function

$$\frac{H_t - H_0}{1.86t + 0.0025t^{1.73}} \tag{2}$$

which varied only 1 percent between 50° and 450°, these blank values were thereby smoothed. The net enthalpies of mercury given in table 1 have been calculated by using the smoothed values for the empty container, although the heat values listed for the empty containers in the table are those actually obtained.

The experimental values of the enthalpy of liquid mercury (at saturation pressure), less the enthalpy at 0° C, are represented by the following equation, whose constants were fitted by least squares:

$$\left.\begin{aligned} H_t - H_0 = {} & 0.139612t - 1.4673\,(10^{-5})\,t^2 \\ & + 1.6874\,(10^{-8})\,t^3 \qquad (0° \text{ to } 450°\text{C}) \end{aligned}\right\}, \tag{3}$$

where H is in absolute joules per gram and t in deg C (International Temperature Scale). The values in the fifth column of table 1 were calculated from this equation.

IV. Calculation of Thermodynamic Properties

1. General Procedure

The more common thermodynamic properties of liquid and gaseous mercury, at the existing vapor pressures, were accurately calculated as a function of temperature over the range from the triple point, —38.88°, to 500° C. Except for what may be considered as minor but unavoidable correction terms, the calculated values of most of these properties rest on three sets of precise experimental data, namely, (1) the enthalpy measurements of the liquid reported in this paper, (2) a previously published series of vapor pressure measurements covering a 13-deg temperature range in the vicinity of the normal boiling point, and (3) the experimental values of the fundamental physical constants that made possible the statistical evaluation of the entropy of the ideal vapor. The additional experimental data employed, whose accuracy is of secondary effect on the accuracy of the calculated properties, are (1) those giving certain fundamental constants of the Hg_2 molecule (used to arrive at data of state for mercury vapor), (2) accurate gas-thermometer measurements of one laboratory (used to make corrections from the International to the thermodynamic temperature scale), and (3) PVT data for the liquid (necessary in an accurate evaluation of the heat capacities from the measured enthalpy).

The procedure of calculation followed will now be outlined. The heat capacities of liquid mercury were calculated from the enthalpy data by the usual thermodynamic relations. The changes with temperature of the entropy of the saturated liquid were next calculated from the values of heat capacity, and were combined with the statistically calculated value of the entropy of the vapor (at the vapor pressure) to give the absolute entropy of the liquid. The heat capacity (C_p) of the vapor was calculated by first assuming it to be an ideal monatomic gas and then making small corrections for imperfections of the gas. By integration of the resulting heat capacity equation and evaluation of the integration constant by using the value of the heat of vaporization at the normal boiling point calculated from the vapor-pressure data and the Clapeyron equation, values of enthalpy of the vapor (relative to the liquid at a fixed temperature) were obtained. The free energies of the liquid and vapor followed from the calculated entropy and enthalpy values. By equating the expressions for these free energies of "saturated" liquid and vapor, a vapor-pressure relation was obtained that is applicable over a much larger temperature range than the supporting vapor-pressure data.

At the present time, the uncertainty in the corrections for gas imperfection and temperature scale, referred to above, limit slightly the accuracy of the calculated properties. Because of these uncertainties it was considered advisable merely to indicate these two corrections in the equations derived. The values of the properties tabulated (in tables 3, 4, and 5) were arrived at, however, by assigning to the corresponding correction terms, on the basis of what are judged to be the best existing data, specific values that are separately listed (in tables 6 and 7 and in the text preceding them). This procedure facilitates an estimation of the uncertainties introduced into the present values and also should simplify any future desired revision of the values, should more accurate corrections become available.

2. Nomenclature and General Assumptions

In what follows, energy will be expressed in calories (1 cal=4.1840 abs j); all extensive properties, per gram-atom of mercury (atomic weight=200.61); and temperature (T), in degrees absolute (0° C=273.16° K), unless otherwise stated. Each value calculated from the equations applies at the existing vapor pressure, except in those cases where pressure is an explicit variable in the equations given. In addition, the subscripts in the heat capacities C_p, C_v, and C_s signify that the respective heat changes are those occurring under the maintenance of constant pressure, constant volume, and liquid-vapor equilibrium, respectively. The equations for relative enthalpy and relative free energy contain the term $H_{TP(l)}$, the enthalpy of the liquid at the triple point, —38.88° C. Liquid and vapor are distinguished by the subscripts l and g, respectively. In the numerical equations (i. e., those in which some or all of the numerical constants have dimensions), P, the pressure, is to be expressed in millimeters of mercury (760 mm=1 standard atm); and V, the volume, in cm^3 $g\text{-}atom^{-1}$.

Log and *ln* indicate logarithms to the bases 10 and e, respectively.

Saturated mercury vapor at pressures not exceeding 2 atm has been found experimentally to have densities that differ from those calculated for an ideal gas by less than 2 percent (the uncertainty of the measurements). It is therefore permissible to assume that practically all of the gas imperfection arises from binary collisions only. Statistical mechanics shows that under this circumstance the correct form for the equation of state of the vapor is

$$PV_{(g)}=RT\left[1+\frac{B}{V}\right], \tag{4}$$

where B, the so-called "second" virial coefficient, is a function of temperature only. However, for convenience it will be used here in the approximately equivalent form

$$PV_{(g)}=RT+PB. \tag{5}$$

In the numerical equations of this paper, B is to be expressed in cm^3 g-atom^{-1}. The values of dB/dT and d^2B/dT^2 at the temperature at which the equation is applied will be designated by B' and B'', respectively, and the corresponding values at the normal boiling point, 629.74° K, will be designated by B_0, B_0', and B_0''.

θ and T will be used to designate the values of a given temperature on the International and thermodynamic absolute temperature scales, respectively.

3. Enthalpy and Heat Capacity of the Liquid

By extrapolating the experimental enthalpy values (represented by eq 3) to the triple point, −38.88° C (234.28° K), and changing to the units as indicated above (to cal, g-atom, deg K), the enthalpy of the liquid $H_{(l)}$ at any temperature θ, relative to the enthalpy $H_{TP(l)}$ at the triple point, becomes

$$H_{(l)}-H_{TP(l)}=7.25939\theta-1.36651\ (10^{-3})\theta^2 +8.0906(10^{-7})\theta^3-1636.13. \tag{6}$$

The heat capacity equations that are derived from eq 6 must be multiplied by $d\theta/dT$ to account for the difference between thermodynamic (T) and International (θ) temperature scales. However, in the temperature range in which the equations are applicable, the heat capacity varies by only 3 percent. Since $d\theta/dT$ is, at all these temperatures, very close to unity, an error negligible in comparison with the experimental errors of the supporting data is introduced by the more convenient procedure of multiplying by $d\theta/dT$ only the average value of $(\partial H_{(l)}/\partial\theta)_s$, taken to be 6.55. This is equivalent to adding as a correction term $6.55[(d\theta/dT)-1]$.

The "saturation" heat capacity ($C_{s(l)}$) can be found from the thermodynamic equation

$$C_{s(l)}=\left(\frac{\partial H_{(l)}}{\partial\theta}\right)_s\frac{d\theta}{dT}-V_{(l)}\left(\frac{\partial P}{\partial\theta}\right)_s\frac{d\theta}{dT}. \tag{7}$$

For mercury below 500° C the last term is small and therefore may be approximated with sufficient accuracy by replacing $d\theta/dT$ by 1 and by substituting for $V_{(l)}$ the constant value 15.9 cm^3 g-atom^{-1}, equal to the volume of the saturated liquid at 400° C [6]. A simple vapor pressure equation, sufficiently accurate for the present purpose, is

$$P=6.345(10^7)e^{-7136.5/\theta}. \tag{8}$$

(This was derived from the values of P and $dP/d\theta$ given at the normal boiling point by eq 19, and provides on differentiation an equivalent of $(\partial P/\partial\theta)_s$). With these substitutions, together with the equivalent of $(\partial H/\partial\theta)_s$ obtained by differentiating eq 6, eq 7 becomes

$$\left.\begin{aligned}C_{s(l)}=7.25939-2.73302(10^{-3})\theta+2.42718(10^{-6})\theta^2\\ -\frac{2.294(10^8)}{\theta^2}e^{-\frac{7136.5}{\theta}}+6.55(d\theta/dT-1).\end{aligned}\right\} \tag{9}$$

The heat capacity at constant pressure may be found from the thermodynamic relation

$$C_p=C_s+T(\partial V/\partial T)_p(\partial P/\partial T)_s. \tag{10}$$

The last term is small in this case and need not be highly accurate. In fact, it will be used with T replaced by θ. Deriving $(\partial P/\partial\theta)_s$ from eq 8 as before, and substituting as a constant value for the slowly changing $(\partial V_{(l)}/\partial\theta)_p$ the value at 400° C [6], $3.09(10^{-3})$ cm^3 g-atom^{-1} deg^{-1}, eq 10 becomes

$$C_{p(l)}=C_{s(l)}+\frac{44585}{\theta}e^{-\frac{7136.5}{\theta}} \tag{11}$$

The heat capacity at constant volume may in turn be calculated from the thermodynamic relation

$$C_v=C_p-\frac{\alpha^2VT}{\beta}, \tag{12}$$

where α and β are the coefficients of isobaric thermal expansion and isothermal compressibility, respectively.

In the use of eq 12 to calculate C_v, use was made of the following equation for the liquid (t being in deg. C):

$$V_{(l)}=14.756+2.678(10^{-3})\,t+1.36(10^{-7})\,t^2 +9.8(10^{-11})t^3+9.93(10^{-13})t^4. \tag{13}$$

This equation was derived from the equation of Sears [6,7] for the relative volume and from the mean experimental value of the density of the liquid at 0° C. Sears' equation seems to be based on data covering the range 0° to 300° C only. However, it fits well the available data for temperatures below 0° C. Its use in this paper between 300° and 500° does not introduce an appreciably increased uncertainty to any of the thermal properties calculated, as

the affected terms in the equations are relatively small.

For the isothermal compressibility, the values of Smith and Keyes [8], extrapolated to zero pressure (the approximate vapor pressure up to 200° C), were used. The values of C_v tabulated in this paper extend only up to 200° C, because reliable values of the compressibility above this temperature are not now available.

4. Entropies of Liquid and Vapor

The entropy of the saturated liquid is

$$S_{(l)}=\int_{T_0}^{T}\frac{C_{s(l)}}{T}dT+S_{0(l)}, \tag{14}$$

where T_0 is the thermodynamic temperature of the normal boiling point ($\theta=629.74$), $S_{0(l)}$ is the absolute entropy of the saturated liquid at that temperature, and C_s is the heat capacity given by eq 9. Of the terms in the second member of eq 9, the sum of all except $6.55000\ d\theta/dT$ is always relatively small, as discussed in the preceding section and may thus, without appreciable error, be conveniently divided by and integrated with respect to θ instead of T. The remaining term must be divided by and integrated with respect to T, giving

$$6.55000\int_{629.74}^{\theta}\frac{d\theta}{T},$$

and this will be replaced by

$$6.55000\ \ln\frac{\theta}{629.74}+6.55\int_{629.74}^{\theta}\left(\frac{1}{T}-\frac{1}{\theta}\right)d\theta,$$

in order that again the term including the correction will be small. Upon integrating, it is found that

$$\left.\begin{aligned}S_{(l)}=&16.71536\ \log\ \theta-2.73302(10^{-3})\theta\\&+1.21359(10^{-6})\theta^2\\&-4.511\left(\frac{7136.5}{\theta}+1\right)e^{-\frac{7136.5}{\theta}}\\&+6.55\int_{629.74}^{\theta}\left(\frac{1}{T}-\frac{1}{\theta}\right)d\theta\\&-45.548507+S_{0(l)}.\end{aligned}\right\} \tag{15}$$

The value of the entropy of the liquid at the normal boiling point, $S_{0(l)}$, will now be evaluated as a function of the corrections for gas imperfection and temperature-scale divergence. The result is eq 24.

The entropy of the ideal vapor (S°), with ideality assumed to imply monatomicity as well, is given by the well-known statistical mechanical (so-called Sackur-Tetrode) equation. (The ground state of the mercury atom is singlet. As for all values of entropy in this paper, nuclear-spin and isotopic contributions are omitted.) The equation is as follows:

$$S^0=R\ln\left(\frac{2\pi m}{h^2}\right)^{3/2}\frac{(kT)^{5/2}}{P}+\frac{5}{2}R, \tag{16}$$

where R is the gas constant, m is the mass of the atom, h is Planck's constant, k is Boltzmann's constant, and P is the pressure. The entropy of the real gas at the same pressure can be shown thermodynamically to be less by PB' (see eq 5). Subtracting this and adding the temperature-scale correction lead to

$$S_{(g)}=R\ln\left(\frac{2\pi m}{h^2}\right)^{3/2}\frac{(k\theta)^{5/2}}{P}+\frac{5}{2}R+\frac{5}{2}R\ln\frac{T}{\theta}-PB'. \tag{17}$$

Making the substitutions $R=1.98719$ cal g-atom^{-1}, $m=3.3308(10^{-22})$[2] g-molecule^{-1}, $h=6.624(10^{-27})$ erg-sec, $k=1.38047(10^{-16})$ erg molecule^{-1} deg^{-1}, and 1 cm^3-mm (of mercury)$=3.186484(10^{-5})$ cal, eq 17 becomes, for any pressure P,

$$\left.\begin{aligned}S_{(g)}=&11.439185\log\theta-4.575674\log P+26.6702\\&+11.44\log\frac{T}{\theta}-3.186(10^{-5})PB'.\end{aligned}\right\} \tag{18}$$

Beattie, Blaisdell, and Kaminsky [9] have accurately measured the vapor pressure of mercury from 349° to 362° C. They have given the normal boiling point ($P=760$) as 356.58° C, and in this temperature range the vapor pressure equation (t=deg C International),

$$\left.\begin{aligned}t=&356.580+7.30951(10^{-2})(P-760)\\&-3.9866(10^{-5})(P-760)^2\\&+3.191(10^{-8})(P-760)^3\end{aligned}\right\}, \tag{19}$$

from which their individual determinations vary by only 0.001 deg on the average. Equation 19, which will be adopted in what follows, gives a value of 13.6808 (mm deg^{-1}) for $dP/d\theta$ at the normal boiling point. This value will be substituted into the Clapeyron equation to obtain a value for the entropy of vaporization at this temperature. Substituting for the vapor volume its equivalent from eq 5, the Clapeyron equation may be written

$$S_{(g)}-S_{(l)}=\frac{RT}{P}\left(\frac{\partial P}{\partial T}\right)_s+(B-V_{(l)})\left(\frac{\partial P}{\partial T}\right)_s. \tag{20}$$

If T be replaced by θ, only the first term of the second member is large enough at the boiling point to require the addition of a correction term, which is obviously

$$\frac{R}{P}\left(\frac{\partial P}{\partial\theta}\right)_s\left(T\frac{d\theta}{dT}-\theta\right).$$

[2] Mean molecular mass for the naturally occurring isotopic mixture. The strictly correct procedure of using in eq 17 the weighted mean of the logarithms of the isotopic masses would have resulted, in the case of mercury, in a value of the entropy of the vapor that is only 0.00005 cal g-atom deg^{-1} different.

Equation 20 then becomes

$$S_{(g)}-S_{(l)}=\left(\frac{R\theta}{P}+B-V_{(l)}\right)\left(\frac{\partial P}{\partial\theta}\right)_s + \frac{R}{P}\left(\frac{\partial P}{\partial\theta}\right)_s\left(T\frac{d\theta}{dT}-\theta\right). \quad (21)$$

Letting $\theta=629.74$, at which temperature $V_{(l)}=15.748$ [6], applying the subscript "0" to designate this temperature, and substituting the above value 13.6808 mm deg^{-1} for $(\partial P/\partial\theta)_s$, eq 21 gives

$$\left.\begin{aligned}S_{0(g)}-S_{0(l)}&=22.519887+4.359(10^{-4})B_0\\&\quad+0.03577(T-\theta)_0\left(\frac{d\theta}{dT}\right)_0\\&\quad+22.53\left(\frac{d\theta}{dT}-1\right)_0.\end{aligned}\right\} \quad (22)$$

At $\theta=629.74$, eq 18 gives

$$S_{0(g)}=45.508660+11.44\log\left(\frac{T}{\theta}\right)_0-0.02422\,B_0'. \quad (23)$$

Substituting for $S_{0(g)}$ from eq 23 into 22 gives

$$\left.\begin{aligned}S_{0(l)}&=22.988773-0.02422\,B_0'-4.359(10^{-4})\,B_0\\&\quad+11.44\log\left(\frac{T}{\theta}\right)_0-0.03577\,(T-\theta)_0\left(\frac{d\theta}{dT}\right)_0\\&\quad-22.53\left(\frac{d\theta}{dT}-1\right)_0.\end{aligned}\right\} \quad (24)$$

And finally, the value of $S_{0(l)}$ may be substituted into eq 15 to give an equation for the absolute entropy of the "saturated" liquid at any temperature in the range covered:

$$\left.\begin{aligned}S_{(l)}&=16.71536\log\theta-2.73302(10^{-3})\theta\\&\quad+1.21359(10^{-6})\theta^2-4.511\left(\frac{7136.5}{\theta}+1\right)e^{-\frac{7136.5}{\theta}}\\&\quad-22.559734-0.02422B_0'-4.359(10^{-4})B_0\\&\quad+6.55\int_{629.74}^{\theta}\left(\frac{1}{T}-\frac{1}{\theta}\right)d\theta+11.44\log\left(\frac{T}{\theta}\right)_0\\&\quad-0.03577(T-\theta)_0\left(\frac{d\theta}{dT}\right)_0-22.53\left(\frac{d\theta}{dT}-1\right)_0.\end{aligned}\right\} \quad (25)$$

5. Enthalpy of the Vapor; Free Energy; General Vapor Pressure Equation

The relative Gibbs free energy of the liquid may next be found from the entropy and the relative enthalpy, by using the thermodynamic definition

$$F=H-TS. \quad (26)$$

For this purpose eq 26 may be written in the form

$$-(F_{(l)}-H_{TP(l)})=\theta S_{(l)}-(H_{(l)}-H_{TP(l)})+(T-\theta)S_{(l)} \quad (27)$$

From the thermodynamic relation

$$C_P=T\left(\frac{\partial S}{\partial T}\right)_p \quad (28)$$

and eq 18, there is obtained for the heat capacity of the gas at constant pressure

$$C_{p(g)}=4.96797-3.186(10^{-5})P\theta B''. \quad (29)$$

Integration of eq 29 with respect to T at constant pressure yields the enthalpy of the gas at pressure P,

$$H_{(g)}=4.96797\theta+3.186(10^{-5})[B-\theta B']P+4.97(T-\theta)+A. \quad (30)$$

The integration constant A may be expressed in terms of $H_{TP(l)}$ the constant used in the case of the liquid, by utilizing the value obtained from eq 22 for the enthalpy of vaporization at the boiling point. Multiplying eq 22 by the temperature $T_0(=629.74+(T-\theta)_0)$ and neglecting the very small terms as before, there results:

$$\left.\begin{aligned}H_{0(g)}-H_{0(l)}&=14181.674+0.2745B_0\\&\quad+22.53(T-\theta)_0\left(\frac{d\theta}{dT}+1\right)_0\\&\quad+1.419(10^4)\left(\frac{d\theta}{dT}-1\right)_0.\end{aligned}\right\} \quad (31)$$

Evaluating eq 6 at $\theta=629.74$ gives

$$H_{0(l)}-H_{TP(l)}=2595.531. \quad (32)$$

By evaluating eq 30 at $\theta=629.74$ and substituting the resulting equivalent of $H_{0(g)}$ into the sum of eq 31 and eq 32, an equivalent of the constant A in terms of $H_{TP(l)}$ is provided that when substituted for A into eq 30 gives

$$\left.\begin{aligned}H_{(g)}-H_{TP(l)}&=13648.676+4.96797\theta\\&\quad+2022e^{-7136.5/\theta}[B-\theta B']+0.2503B_0\\&\quad+15.25B_0'+22.53(T-\theta)_0\left(\frac{d\theta}{dT}+1\right)_0\\&\quad+1.419(10^4)\left(\frac{d\theta}{dT}-1\right)_0\\&\quad+4.97[(T-\theta)-(T-\theta)_0].\end{aligned}\right\} \quad (33)$$

In this equation, the vapor pressure has been evaluated (with sufficient accuracy, for the correction

term, from eq 8) and has been substituted for P. Subtraction of eq 6 from eq 33 will give the heat of vaporization at any temperature in the range studied.

The relative Gibbs free energy of the gas, as does that for the liquid, now follows by the use of eq 26, which may now be written in the form

$$-(F_{(g)}-H_{TP(l)})=\theta S_{(g)}-(H_{(g)}-H_{TP(l)})+(T-\theta)S_{(g)}. \tag{34}$$

By equating the free energies of saturated liquid and gas from eq 27 and 34; substituting for the enthalpy and entropy of vapor and liquid from eq 33, 18, 6, and 25; and solving for $\log P$ contained in S_g, the following vapor pressure equation is obtained:

$$\left.\begin{aligned}\log P=11.259839&-\frac{3340.449}{\theta}-1.153092\log\theta\\&+2.98647(10^{-4})\theta-8.8409(10^{-8})\theta^2\\&+9.526(10^{-5})\left(\frac{\theta-629.74}{\theta}\right)(B_0+55.56B_0')\\&-\frac{6.963(10^{-5})}{\theta}(PB-760B_0)\\&+0.9860\left(\frac{7136.5}{\theta}+1\right)e^{-\frac{7136.5}{\theta}}\\&+2.500\log\frac{T/\theta}{(T/\theta)_0}-1.431\int_{629.74}^{\theta}\left(\frac{1}{T}-\frac{1}{\theta}\right)d\theta\\&+7.817(10^{-3})\left(\frac{\theta-629.74}{\theta}\right)\\&\left[629.74\left(\frac{d\theta}{dT}-1\right)_0+(T-\theta)_0\left(\frac{d\theta}{dT}\right)_0\right]\\&+\frac{1}{\theta}\left[\left\{1.8705-1.1531\log\theta+\frac{3099.3}{\theta}\right.\right.\\&+5.973(10^{-4})\theta\\&\left.\left.-2.652(10^{-7})\theta^2\right\}(T-\theta)-3.838(T-\theta)_0\right].\end{aligned}\right\} \tag{35}$$

(In the part of the last bracketed term which represents the entropy of vaporization, all minor terms have been omitted, since they would be multiplied by the very small factor $(T-\theta)$. In this bracketed term, P (contained in the equivalent of $S_{(g)}$) has been replaced by its equivalent in terms of θ, by using eq 8.)

If the specific corrections for gas imperfection and temperature-scale differences described in the next two sections be adopted, eq 35 may be approximated by the following more readily applicable vapor pressure equation:

$$\left.\begin{aligned}\log P=11.257555&-\frac{3339.202}{\theta}-1.153092\log\theta\\&+2.95697(10^{-4})\theta-7.4588(10^{-8})\theta^2\\&-1.5605(10^{-11})\theta^3+3.600e^{-5360/\theta}.\end{aligned}\right\} \tag{36}$$

Between 100° and 500° C, this equation reproduces the vapor pressures of eq 35 to within 0.01 percent. Below 100°, however, it gives lower values, the discrepancy amounting to 0.1 percent at 25° and 0.6 percent at −39°, the triple point.

6. Calculation of the Second Virial Coefficient; Corrections for Gas Imperfection

Smith and Menzies [10] found the density of mercury vapor to be ideal between 360° and 400° C to within their probable experimental error, about 2 percent. Apparently no one has measured such densities with much greater accuracy.

Approximate values for the degrees of gas imperfection at various temperatures have been calculated for many gases by the use of some equation of state, such as Berthelot's. To employ the last equation, the critical constants must be known. In the case of mercury, however, the values that have been reported for the critical temperature (around 1,500° C) and critical pressure (from 1,000 to 3,500 atm) show such wide variations that this method is hardly applicable.

There is abundant spectroscopic evidence that mercury vapor contains appreciable amounts of the dimer Hg_2, which is known to possess a singlet ground state. Adopting suitable constants for this molecule as described below, values of the second virial coefficient B of mercury vapor, treated as an imperfect monatomic gas in which only binary collisions are important below 500° C, were calculated from the following statistical mechanical equation [11]:

$$B(T)=-2\pi N\int_0^{\infty}(e^{-U(r)/RT}-1)r^2dr, \tag{37}$$

where N is Avogadro's number, and $U(r)$ is the potential energy of a mole of Hg_2 molecules, all at an interatomic separation of r. $U(r)$ was calculated from a Morse potential function in which it was assumed that the equilibrium separation is $3.2(10^{-8})$ cm, and that the first vibrational constant ω_e is 36 cm^{-1}. The former figure, derived from data on liquid mercury, has been generally accepted as approximately correct. The latter figure, considered by Kuhn [12] to be the most likely choice among alternative multiples for which there is spectroscopic evidence, is supported by the theoretical calculation of a value of 35 cm^{-1} by Heller [13], whose values for a number of other diatomic molecules are in good agreement with well-established experimental values.

The third parameter needed in the use of the Morse function is the molar dissociation energy of the Hg_2 molecule in its ground state. Evidence for various values has been described in the literature. London [14] made a theoretical calculation of the polarization

force and arrived at 2.0 kcal mole^{-1}; however, Kuhn [12] points out that this is undoubtedly too high because of the neglect of repulsion forces. Kuhn measured the total absorption in the discrete band system (2,540 A) at 175° C and calculated a value for the concentration of Hg_2. He claims that the extrapolation to 0° K (giving a dissociation energy of 2.1 kcal) yields too high a value because of the neglect of vibrational anharmonicity. If this be true, then, as he claims, the values obtained by measuring the decrease in absorption with rising temperature are too low. By the latter method and with the assumption of vibrational harmonicity, Koernicke [15] found a dissociation energy of 1.4 kcal, Kuhn and Freudenberg [16] found 1.6 kcal, and Winans and Heitz [17] found 1.38 ±0.07 kcal. Gaydon [18] recommends the latter value for the dissociation energy, whereas Herzberg [19] lists 1.84 kcal.

Equation 37 was solved graphically by the authors for values of B at the temperatures T=430, 530, 630, and 730, by using for each temperature values of 1.4, 1.5, 1.6, and 1.7 kcal for the molar dissociation energy of Hg_2. In these ranges the calculated value of B for a given temperature varies almost linearly with the value of the dissociation energy used. The thermodynamic properties of mercury listed in this paper were calculated assuming a value of 1.5 kcal as a reasonable weighted mean of the above values of the dissociation energy. This particular value was adopted partly because of the support it receives in figure 4, where calculated and experimental vapor pressures are compared. The following empirical equation represents the corresponding values of the second virial coefficient B, in cm^3 g-atom^{-1}, in this temperature range:

$$B=56.4-43.82e^{\frac{655}{\theta}}, \tag{38}$$

which agrees with the directly calculated values to within 0.5 percent from θ=430 to θ=730. On differentiation with respect to temperature, eq. 38 gives:

$$B'=\frac{655}{\theta^2}(56.4-B). \tag{39}$$

Values calculated from eq 38 and 39 are listed in table 2.

TABLE 2. *Second virial coefficient (B) and its temperature derivative (B') for mercury vapor*

Temperature	B	B'	Temperature	B	B'
°C	cm^3 g-atom^{-1}	cm^3 g-atom^{-1} deg^{-1}	°C	cm^3 g-atom^{-1}	cm^3 g-atom^{-1} deg^{-1}
100	−197	+1.19	320	−76	+0.25
120	−175	0.98	340	−71	.22
140	−158	.82	356.58(bp)	−68	.20
160	−142	.69	360	−67	.20
180	−130	.59	380	−63	.18
200	−118	.51	400	−60	.17
220	−109	.45	420	−56	.15
240	−101	.39	440	−53	.14
260	−93	.34	460	−51	.13
280	−87	.31	480	−48	.12
300	−81	.27	500	−46	.11

7. Corrections to Basis of Thermodynamic Temperature Scale

The results of recent investigations [20] of the differences between the thermodynamic and International temperature scales have been formulated by an equation [21] equivalent to the following:

$$T-\theta=0.6381-4.809(10^{-4})\theta+1.1096(10^{-5})\theta^2 -7.481(10^{-9})\theta^3 \tag{40}$$

(The value of $(T-\theta)$ is so small and changes so slowly with temperature that when desirable, θ may be replaced by T in the second member of eq 40 without appreciably changing the corrections calculated.)

It is believed that the differences given by eq 40 are the most probable values in the light of the evidence now available, and that their uncertainties may be considered to correspond to probable errors of about half their respective values. All thermodynamic properties given in this paper have been corrected by this equation to units involving deg K thermodynamic, though for convenience of usage the tabulated values of these properties have been calculated for rounded temperatures on the International scale of 1948.

By use of eq 40 it may be shown that the integral appearing in eq 25 and 35 is approximately as follows

$$\left.\begin{aligned}\int_{629.74}^{\theta}\left(\frac{1}{T}-\frac{1}{\theta}\right)d\theta=0.01107\ \log\ \theta+\frac{0.6381}{\theta}\\ -1.1096(10^{-5})\theta\\ +3.7405(10^{-9})\theta^2-0.0264958\end{aligned}\right\} \tag{41}$$

V. Tables

1. Thermodynamic Properties

In tables 3, 4, and 5, values calculated from preceding equations are given for saturated liquid and gaseous mercury at temperatures from the triple point, −38.88° C [22], to 500° C. The numbers in parentheses given under the symbols heading the various columns indicate the particular equations from which the values were calculated.

Though the tabulated values of the heat capacities of the liquid were calculated to apply at the vapor pressures, the corresponding values of $C_{p(l)}$ at any small fixed pressure are practically identical. For it may be readily shown by using eq 13 that $C_{p(l)}$ varies by not more than 0.001 percent in this temperature range when the pressure varies by 1 atm.

It will be noted that the free-energy values calculated from eq 27 and listed in table 5 apply to either the saturated liquid or vapor.

TABLE 3. *Relative enthalpy; heat of vaporization; compressibility factor*

Temperature	Relative enthalpy		Heat of vaporization, $H_{(g)}-H_{(l)}$	Compressibility factor of vapor, $pV_{(g)}/RT$
	Liquid, $H_{(l)}-H_{TP(l)}$	Vapor, $H_{(g)}-H_{TP(l)}$		
	(6)	(33)	(6, 33)	(5)
°C Int	cal g-atom^{-1}	cal g-atom^{-1}	cal g-atom^{-1}	
−38.88° (tp)	0.00	14800.8	14800.8	1.0000
−20	127.20	14894.5	14767.3	1.0000
0	261.37	14993.8	14732.4	1.0000
20	394.98	15093.1	14698.1	1.0000
25	428.29	15118.0	14689.7	1.0000
40	528.06	15192.5	14664.4	1.0000
60	660.65	15291.8	14631.2	1.0000
80	792.80	15391.2	14598.4	1.0000
100	924.54	15490.6	14566.1	1.0000
120	1055.91	15590.0	14534.1	1.0000
140	1186.96	15689.4	14502.4	1.0000
160	1317.71	15788.8	14471.1	1.0000
180	1448.21	15888.1	14439.9	1.0000
200	1578.49	15987.5	14409.0	0.9999
220	1708.60	16086.8	14378.2	.9999
240	1838.58	16186.0	14347.4	.9998
260	1968.46	16285.1	14316.6	.9997
280	2098.28	16384.1	14285.8	.9996
300	2228.08	16482.9	14254.8	.9994
320	2357.90	16581.6	14223.7	.9992
340	2487.78	16679.9	14192.1	.9989
356.58 (bp)	2595.53	16761.2	14165.7	.9987
360	2617.76	16778.0	14160.2	.9986
380	2747.88	16875.7	14127.8	.9982
400	2878.17	16973.1	14094.9	.9978
420	3008.67	17070.0	14061.3	.9972
440	3139.42	17166.4	14027.0	.9966
460	3270.47	17262.3	13991.8	.9959
480	3401.85	17357.7	13955.8	.9950
500	3533.59	17452.4	13918.8	.9942

TABLE 4. *Heat capacity*

Temperature	Heat capacity			
	Liquid			Vapor
	$C_{v(l)}$	$C_{p(l)}$	$C_{s(l)}$	$C_{p(g)}$
	(9)	(11)	(12)	(29)
°C Int	cal g-atom^{-1} deg^{-1}	cal g-atom^{-1} deg^{-1}	cal g-atom^{-1} deg^{-1}	cal g-atom^{-1} deg^{-1}
−38.88° (tp)	6.7578	6.7578	5.969	4.968
−20	6.7272	6.7272	5.900	4.968
0	6.6967	6.6967	5.831	4.968
20	6.6683	6.6683	5.769	4.968
25	6.6615	6.6615	5.752	4.968
40	6.6419	6.6419	5.708	4.968
60	6.6176	6.6176	5.650	4.968
80	6.5954	6.5954	5.594	4.968
100	6.5752	6.5752	5.544	4.968
120	6.5571	6.5571	5.494	4.968
140	6.5410	6.5410	5.449	4.968
160	6.5270	6.5270	5.403	4.968
180	6.5150	6.5150	5.364	4.969
200	6.5050	6.5050	5.335	4.969
220	6.4970	6.4970	.....	4.970
240	6.4909	6.4910	.....	4.970
260	6.4867	6.4869	.....	4.971
280	6.4845	6.4847	.....	4.973
300	6.4840	6.4843	.....	4.975
320	6.4853	6.4858	.....	4.977
340	6.4884	6.4890	.....	4.980
356.58 (bp)	6.4922	6.4930	.....	4.983
360	6.4931	6.4940	.....	4.984
380	6.4993	6.5005	.....	4.988
400	6.5071	6.5087	.....	4.993
420	6.5164	6.5186	.....	4.999
440	6.5270	6.5288	.....	5.005
460	6.5390	6.5426	.....	5.013
480	6.5522	6.5567	.....	5.021
500	6.5666	6.5723	.....	5.030

° Triple point.

TABLE 5. *Entropy; relative free energy; vapor pressure*

Temperature	Absolute entropy		Relative free energy (liquid or vapor), $-(F-H_{TP(l)})$	Vapor pressure, P
	Liquid, $S(l)$	Vapor, $S(g)$		
	(25)	(18)	(27)	(35)
°C Int.	cal g-atom^{-1} deg^{-1}	cal g-atom^{-1} deg^{-1}	cal g-atom^{-1}	mm Hg
−38.88° (tp)	16.5045	79.6736	3867.1	$2.191(10^{-6})$
−20	17.0267	75.3563	4183.4	$2.336(10^{-5})$
0	17.5367	71.4701	4529.0	$1.996(10^{-4})$
20	18.0088	68.1470	4884.4	$1.268(10^{-3})$
25	18.1215	67.3906	4974.7	$1.935(10^{-3})$
40	18.4480	65.2766	5248.9	$6.340(10^{-3})$
60	18.8584	62.7760	5622.0	0.026048
80	19.2436	60.5809	6003.2	.090954
100	19.6065	58.6409	6391.8	.27710
120	19.9494	56.9161	6787.6	.75213
140	20.2745	55.3742	7190.0	1.8499
160	20.5836	53.9894	7598.9	4.1795
180	20.8781	52.7401	8013.8	8.7734
200	21.1594	51.6086	8434.4	17.273
220	21.4286	50.5798	8860.6	32.147
240	21.6870	49.6414	9292.1	56.931
260	21.9351	48.7828	9728.6	96.481
280	22.1741	47.9949	10169.9	157.234
300	22.4045	47.2699	10615.9	247.413
320	22.6270	46.6013	11066.4	377.27
340	22.8421	45.9828	11521.2	559.22
356.58 (bp)	23.0153	45.5047	11901.4	760.00
360	23.0505	45.4098	11980.2	808.00
380	23.2525	44.8776	12443.1	1140.65
400	23.4486	44.3824	12909.9	1576.64
420	23.6391	43.9207	13380.4	2137.76
440	23.8246	43.4895	13854.6	2848.09
460	24.0051	43.0861	14332.2	3733.8
480	24.1812	42.7080	14813.2	4822.9
500	24.3529	42.3531	15297.5	6145.4

° Triple point.

2. Effects of Gas Imperfection and Temperature Scale

The values listed in tables 3, 4, and 5 contain contributions from the small terms (in the equations) that contain B, or its derivatives, or T and that thus correct for gas imperfection of mercury vapor and for the deviations between the thermodynamic and International temperature scales. When these contributions for a given property vary appreciably with temperature, they are listed separately in tables 6 and 7 for a number of temperatures. (Except for vapor pressure these are listed in the same units as the values in tables 3, 4, and 5.) The magnitudes of these contributions depend in most cases on the particular way in which the properties have been calculated in this paper, as well as on what basic data have been used. Consequently, they are not intrinsically characteristic of the properties themselves.

Table 3. There are no contributions to the relative enthalpy of the liquid, as the values used are those measured essentially directly. The contributions are hence identical for the relative enthalpy of the vapor and for the heat of vaporization. These are listed in tables 6 and 7.

Table 4. The three calculated heat capacities of the liquid have no contribution from gas imperfection. At a given temperature they have identical contributions from the temperature-scale correction, as listed in table 7. The contribution to $C_{p(g)}$ from gas imperfection is the deviation from $5/2\ R$ (i. e., from 4.968 cal g-atom^{-1}deg^{-1}).

TABLE 6. *Contributions to thermodynamic properties from gas imperfection of mercury vapor*

Temperature	To $H_{(g)}-H_{TP(l)}$ and $H_{(g)}-H_{(l)}$	To $S_{(g)}$	To $-(F-H_{TP(l)})$	To vapor pressure
°C	cal g-atom^{-1}	cal g-atom^{-1} deg^{-1}	cal g-atom^{-1}	Percent
−38.88	−13.8	0.0000	+5.7	+1.73
0	−13.8	.0000	+6.7	+1.31
40	−13.8	.0000	+7.7	+0.98
80	−13.8	.0000	+8.6	+.73
120	−13.8	.0000	+9.6	+.53
160	−13.9	−.0001	+10.6	+.37
200	−14.0	−.0003	+11.6	+.24
240	−14.3	−.0007	+12.6	+.14
280	−15.1	−.0015	+13.5	+.061
320	−16.5	−.0030	+14.5	+.015
356.58	−18.6	−.0049	+15.4	.000
360	−18.8	−.0052	+15.5	.000
400	−22.4	−.0085	+16.5	+.021
440	−27.8	−.0129	+17.4	+.082
480	−35.1	−.0186	+18.4	+.18
500	−39.7	−.0218	+18.9	+.25

TABLE 7. *Contributions to thermodynamic properties from correction to thermodynamic temperature scale*

Temperature	To $H_{(g)}-H_{TP(l)}$ and $H_{(g)}-H_{(l)}$	To $C_{s(l)}$, $C_{p(l)}$, $C_{v(l)}$	To $-(F-H_{TP(l)})$	To vapor pressure
°C	cal g-atom^{-1}	cal g-atom^{-1} deg^{-1}	cal g-atom^{-1}	Percent
−38.88	+2.0	+0.0955	+1.0	−0.29
0	+1.9	+.0028	+0.7	−.47
40	+1.8	+.0004	+0.6	−.49
80	+1.8	−.0015	+0.8	−.43
120	+1.9	−.0029	+1.1	−.33
160	+2.0	−.0039	+1.7	−.23
200	+2.2	−.0044	+2.3	−.14
240	+2.3	−.0044	+3.0	−.077
280	+2.4	−.0039	+3.6	−.031
320	+2.5	−.0030	+4.2	−.006
356.58	+2.6	−.0017	+4.6	.000
360	+2.6	−.0016	+4.6	+.002
400	+2.6	+.0003	+4.8	−.009
440	+2.6	+.0026	+4.6	−.035
480	+2.4	+.0054	+4.1	−.075
500	+2.4	+.0070	+3.7	−.100

Table 5. To the entropy of the liquid the contribution from gas imperfection is the same at all temperatures, +0.0245 cal g-atom^{-1}deg^{-1}. The contribution to the entropy from the temperature-scale correction is practically constant, being equal to +0.002 cal g-atom^{-1}deg^{-1} at all temperatures in the case of the liquid and not lying outside the range 0.000 to +0.001 in the case of the vapor. The other contributions to the entropy of the vapor, the free energy, and the vapor pressure are listed in tables 6 and 7.

VI. Discussion of Results

1. Reliability

An index to the reproducibility, or "precision", of the enthalpy measurements on liquid mercury is afforded by the deviations from the means, as shown by the results of the individual measurements, which are recorded in table 1. Another index is provided by the deviations (also listed in table 1) from the smoothed values as represented by the empirical equation adopted. All the results lead to an average probable error of the mean of about 0.02 percent on enthalpy, and a corresponding magnitude of about 0.1 percent on the derived heat capacity values ($C_{s(l)}$ or $C_{p(l)}$).

One check on the over-all accuracy of the apparatus in measuring enthalpy was made by measuring the heat delivered to the ice calorimeter by a Monel capsule containing water and dropping from 250° C. By thus determining in several measurements the difference in heats for two amounts of water differing by about 6 g, a mean value of 1042.05 abs j g^{-1} for $\alpha]_0^{250}$ of water, an enthalpy function defined elsewhere [23], was obtained. This figure differs by only 0.02 percent from the value of 1041.85 published in the latest report [24] on the thermal properties of water as accurately measured earlier in this laboratory by an adiabatic calorimeter.

The various sources of appreciable systematic error were examined in order to estimate their likely contributions. As measurements by the General Electric Co. [24a] of Nitralloy and of Swedish iron in mercury at various temperatures indicate a solubility of less than 1 part in 100,000,000 at 500° C, no error in the enthalpy should be caused by the dissolving of the container. Considering the uncertainty in each possible error, the authors believe that the values of the enthalpy of the liquid given in table 3 are accurate to 0.1 percent, except below 100° C, where small errors in measurement become relatively more important as 0° C is approached. As a consequence, it is believed that the corresponding uncertainties in the heat capacity values $C_{s(l)}$ and $C_{p(l)}$ (table 4) may be as large as 0.3 percent between 25° and 425° C. Outside this temperature range the values given should be considered much more uncertain, as they resulted from the extrapolation of an empirical function beyond the range of experimental measurements.

The calculated properties other than the enthalpy and heat capacity of the liquid are, as pointed out earlier in this paper, subject to varying uncertainties caused by uncertainties in the corrections for gas imperfection and temperature scale. The values in tables 6 and 7 should aid in estimating such uncertainties in specific cases. In many cases the difference between the values at two temperatures for a given property will be much more accurate than the listed absolute magnitude of the property itself.

The value of the absolute entropy as calculated here may be compared with that arrived at through use of low-temperature heat-capacity data for solid mercury. For liquid mercury at the triple point, for example, table 5 gives a value of 16.50 cal g-atom^{-1}deg^{-1}, based principally on vaporization data. If eq 19, representing the vapor pressure data of Beattie, Blaisdell, and Kaminsky [9], can be accepted as having an accuracy comparable to that which they claim, the entropy value just quoted should not be uncertain beyond a very few hundredths of a cal g-atom^{-1}deg^{-1}. This estimate includes the consideration of the aforementioned uncertainty in the extrapolated heat capacity of the liquid between 0° C and the triple point.

Pickard and Simon [25] have recently measured the heat capacity of solid mercury down to 3° K.

By using their data and those of others, the authors have computed a value of 14.34 cal g-atom^{-1}deg^{-1} for the entropy of solid mercury at the triple point. Addition of the entropy of fusion, 2.38 cal g-atom^{-1}-deg^{-1} [26, 27], gives a value of 16.72 for the liquid at the same temperature. This is 0.2 cal g-atom^{-1}-deg^{-1} higher than the value in table 5. The discrepancy seems to the authors as more likely due to errors in the low-temperature heat-capacity data than to any other source.

The effect of certain possible errors on the accuracy of vapor pressures as calculated by eq 35 will now be examined. As stated earlier, this equation has been adjusted to agree with the empirical eq 19 at, and in the immediate vicinity of, the normal boiling point, which both equations give as 356.58° C. (However, according to the experimental results on which eq 19 is based, there may be an absolute error of 0.01 deg in this temperature, corresponding to an error of 0.02 percent in the vapor pressure at any neighboring temperature.) Equation 19 gives values of vapor pressure at 350° and 362° C (temperatures near the extremes of the range of claimed validity of the equation) that are higher by 0.004 and 0.001 percent, respectively, than those given by eq 35. These divergences are within the precision of the data on which eq 19 is based.

The small uncertainty in the temperature assumed for the normal boiling point will affect all vapor pressures calculated from eq 35 by the same percentage. There are four other factors contributing significant uncertainty to these calculated pressures, and as the temperature becomes increasingly higher or lower than the boiling point, the effect of each of these four factors becomes acceleratingly greater. These factors are (1) degree of gas imperfection, (2) thermodynamic temperature scale, (3) heat of vaporization at the normal boiling point, and (4) average heat capacity of the liquid between the boiling point and the temperature in question. Taking the uncertainty in the last factor to be 0.1 percent, as estimated above, it was computed that the resulting uncertainties in the calculated vapor pressures would be as follows: At −39° C, 0.7 percent; at 100°, 0.15 percent; and at 250° or 500°, 0.02 percent.* The assumption of these and reasonable uncertainties in each of the other factors has led to the assignment of the following uncertainties in individual values of vapor pressure calculated from eq 35 and listed in table 5: At −39° C, 1.5 percent; at 100°, 0.5 percent; at 250° or 500°, 0.2 percent; and at 357° (the boiling point), 0.03 percent. These figures were arrived at without consideration of agreement of the calculated vapor pressures with any direct measurements, except those represented by eq 19.

A number of investigators [28 to 33] have directly measured the vapor pressure of mercury in this temperature range. The deviations of most of the more precise of these experimental values from those given by eq 35 are shown in figure 1. In most of these measurements there was an average variation of several times the uncertainties just stated.

2. Comparison of Liquid Heat Capacity Values With Those of Other Experimental Investigations

A number of other investigators [34 to 47] have measured the heat capacity of mercury above 0° C. Most of these results are shown in figure 2 for comparison with the results reported in this paper. The experimental points labeled NBS were calculated by dividing by the temperature interval the differences in the mean unsmoothed experimental heats for pairs of successive furnace temperatures. A very small correction for curvature was applied.

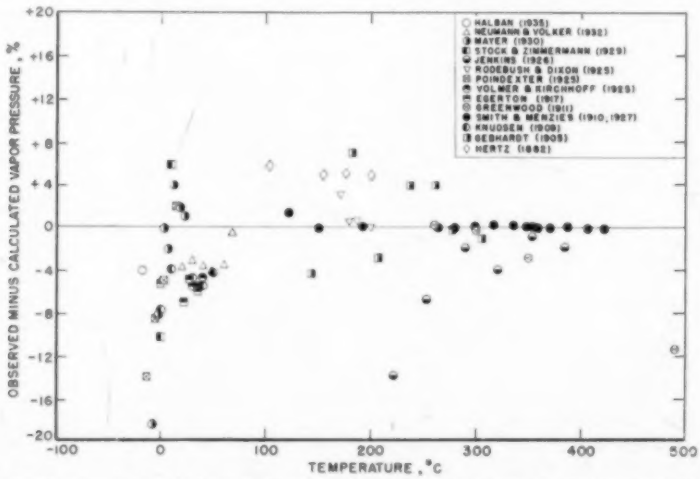

FIGURE 1. *Comparison between values of vapor pressure of mercury observed by various workers and values calculated from eq 35.*

To avoid confusion, only representative data of each worker are shown. The temperatures of Smith and Menzies have been corrected by table 8.

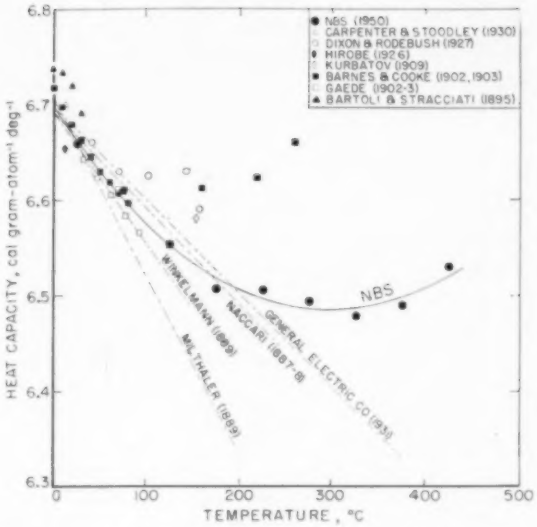

FIGURE 2. *Saturation heat capacity (C_s) of liquid mercury, as found by various investigators.*

Most observers are in substantial agreement below 100° C, but those who extended their measurements to higher temperatures show considerable disagreement. Gaede [42] employed an essentially adiabatic calorimeter; Hirobe [46] used an isothermal one; and Dixon and Rodebush [41], claiming an accuracy of approximately 1 percent, resorted to adiabatic compression. The observations of Milthaler [39], Naccari [37], and Winkelmann [38], all of whom employed the method of mixtures, agree approximately, as to a value of the negative temperature coefficient, with the later measurements of the General Electric Co. [45]. The measurements of Barnes and of Barnes and Cooke [34] were made, apparently, with considerable care by using a continuous flow method previously employed in measuring the specific heat of water. They considered their measurements below 100° to be accurate to 0.1 percent. However, above 150° their values differ markedly from those of all other observers, including the present authors. In spite of this difference, their values have often been considered by some in the past to have a reliability superior to the heat-capacity values of mercury of the other observers.

Recently Kleppa [48] has used an electronic pulse-circuit technique to measure ultrasonic velocities in mercury at 50° and 150° C, obtaining a precision of about 1 percent. When these velocities were combined with the coefficients of thermal expansion given by eq 13 and with the values of $C_{p\,(l)}$ interpolated from table 4, they gave values of $C_{v\,(l)}$ of 5.72 ±0.01 and 5.49 ±0.01 cal g-atom^{-1}-deg^{-1}, respectively, at these two temperatures. The corresponding values of $C_{v\,(l)}$ interpolated from table 4, based on the directly measured compressibilities of Smith and Keyes [8], are 5.68 and 5.43, respectively.

3. Isobaric and Isochoric Heat Capacities of the Liquid

The values of the heat capacities of the liquid C_p and C_v that are given in table 4 are represented graphically in figure 3 as multiples of the gas constant R. It is of interest that the curve for C_p shows a minimum at a temperature somewhat below the boiling point. This is analogous to the results obtained by the authors for two other liquid metals, sodium [3] and potassium [49], whose values of C_p were found to exhibit even deeper minima than mercury, and at temperatures somewhat below their respective normal boiling points.

It is well known that the theoretical interpretation of C_v is simpler than that of C_p. The curve for C_v of liquid mercury in figure 3, in contrast to that for C_p, shows no definite evidence of extrapolating to a minimum below the critical temperature, indicating that the distinct minimum in C_p is caused by the increasing difference between C_p and C_v as the temperature rises. (Though Smith and Keyes [8] measured the compressibility of mercury up to 300° C, their values above 200° show a very rapid and unexpected increase, which would lead to a minimum in the calculated curve for C_v above this temperature. However, they discredited their results above 200° because of invalidating experimental circumstances.)

It is of interest that the value of C_v calculated in this paper (table 4) for liquid mercury at its triple point is only 0.1 percent different from $3R$, which is the value predicted at this temperature by a recent fairly successful theoretical treatment of liquid mercury [50]. According to some recently published theories [51], a liquid exhibits a fairly continuous transition from the crystalline to the gaseous state as the temperature rises. The heat capacity C_v of a monatomic liquid, taken at small pressures, may be expected to vary from approximately $3R$ at the triple point and approach $\frac{3}{2}R$ near the critical point. The decrease in C_v as the temperature rises may be interpreted as being due to a decreasing contribution to disorderliness in the liquid. The curve for C_v of mercury shown in figure 3 is consistent with this picture.

4. Vapor Pressure

Near the normal boiling point, 357° C, the terms for gas imperfection have very little influence on the values calculated for the vapor pressure from eq 35. However, as pointed out in an earlier section, the effect is many times as great at much higher or lower temperatures. If the calculated vapor pressures at such temperatures agree with corresponding measured values, there is thus afforded an independent experimental check on the adopted value of the principal parameter determining the gas-imperfection corrections in the various equations for thermodynamic properties. This assumes, of course, that the experimental values of vapor pressure have sufficient accuracy and precision.

The vapor pressure of mercury has been measured by various workers [52] from the triple point to 1400° C. Though at very low and very high temperatures in this range the percentage accuracy of the vapor pressure measurements need not be very great, the precision of most of these results is so relatively poor as to exclude their use for this test.

In 1910 Smith and Menzies [53] carefully measured the vapor pressure of mercury from about 250° to 435° C with a precision of about ±0.1 percent. The temperatures were recalculated by Menzies [52] in 1927 on the basis of the new value for the sulfur boiling point. Menzies added three more experimental points between 120° and 200° C and derived the following equation to represent the data:

$$\log P = 9.957094 - \frac{3283.92}{\theta'} - 0.665240 \log \theta', \quad (42)$$

where

$$\theta' = t' + 273.1, \quad (43)$$

t' being deg C Int as measured by the platinum thermometer of Smith and Menzies.

The authors have recalculated Menzies' centigrade temperatures, as given by eq 43, in accordance with the present knowledge of the platinum-thermometer scale. Smith and Menzies [54] had reported for their thermometer a δ value of 1.6147, on the basis of their assumed sulfur boiling point of 445° C. Correcting this to the basis of the temperature assumed by Menzies in 1927, 444.6°, yields a value of δ of 1.5919. Equation 42 gives a mercury normal boiling point of 356.711° C, which is 0.13 deg higher than reported by Beattie, Blaisdell, and Kaminsky [9]. Waidner and Burgess [55] and Beattie, Blaisdell, and Kaye [56] have found independent evidence that a platinum thermometer accurately calibrated at the ice, steam, and sulfur points indicates for the mercury boiling point a temperature depending fairly systematically on the δ value of the thermometer. In fact, Beattie et al. have argued that by adding the mercury boiling point as a fourth calibration point and using a cubic temperature-resistance relation, the platinum-thermometer scale will be approximately independent of the thermometer constants.

This recommendation has been followed here. A cubic temperature-resistance equation has been derived that gives the same temperatures for the ice, steam, and sulfur points but a value of 356.58° C for the mercury boiling point when there are substituted the resistances given for these four temperatures by a Callendar equation with $\delta = 1.5919$, and with the mercury boiling point taken as 356.711° C. Equating the resistances given by the two equations indicates that the Centigrade temperatures given by eq 42 should be changed by the amounts shown in table 8 to accord with a four-point calibration. Though a fourth calibration point is obviously, in itself, an asset toward greater accuracy, it is believed that considerably more uncertainty should be attached to the interpolations of temperature provided by a thermometer with such a high δ value than to those by thermometers meeting present-day standards.

After correcting the Centigrade temperatures of eq 42 by the values of table 8, figure 4 was obtained for the differences between the experimental vapor pressures of Smith and Menzies and those calculated from eq 35. The four curves represent the differences obtained depending on what dissociation energy is made the basis of calculating the gas-imperfection terms in the latter equation. This equation has been derived to give the experimentally measured normal boiling point regardless of the magnitudes of the gas imperfections assumed. For a range of 200 deg below the boiling point, the best agreement between experimental and calculated vapor pressures is seen to correspond to a gas imperfection equivalent to a dissociation energy of 1.5 kcal mole^{-1} of Hg_2. This value was claimed earlier in this paper to be a reasonable weighted mean of those indicated by independent spectroscopic evidence. However, in view of the smallness of the

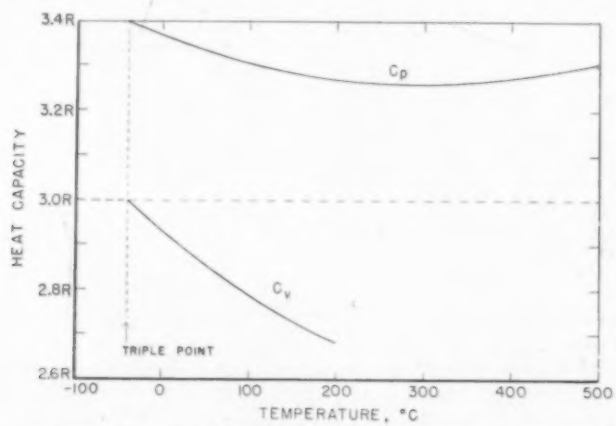

FIGURE 3. *Heat capacities of liquid mercury at constant pressure and constant volume.*

deviations of figure 4 and the uncertainties in some of the small corrections applied to both experimental and calculated vapor pressures, the agreement may be somewhat fortuitous.

TABLE 8. *Correction of temperature values of a platinum thermometer with $\delta = 1.5919$ to accord with a four-point calibration in which the mercury boiling point is changed from 356.711° to 356.58° C*

Temperature	Correction
°C Int.	*°C Int.*
100	0.000
150	−.033
200	−.076
250	−.115
300	−.138
330	−.140
356.58	−.131
400	−.089
430	−.034
444.6	.000

It will be noted that above the boiling point all four curves indicate lower experimental than calculated vapor pressures. This may be attributed quantitatively, in large part, to the fact that as the temperature rises the saturated vapor becomes denser, and as a result the empirical eq 42, derived to fit the data well near the boiling point and at lower temperatures, is too simple to represent the increasing importance of gas imperfection and liquid volume.

The ordinate differences in figure 4 are of the same order of magnitude as the absolute uncertainties assigned in an earlier section to the vapor pressures calculated from eq 35. However, the several factors named there as affecting the accuracy of this equation have effects that vary in roughly comparable ways with temperature. Therefore, errors in the adopted magnitudes of their effects on the calculated vapor pressures at various temperatures would be capable of being compensated considerably by the choice of a single somewhat erroneous value for the dissociation energy of Hg_2 for calculating the effects of gas imperfection. It is thus possible that the choice of 1.5 kcal per mole (made partly on the basis of the apparent agreement in fig. 4 between observed and calculated vapor pressures when this value is selected) is of this nature.

Nevertheless, it is believed that the comparison afforded by figure 4 provides confirmatory evidence that the values of dissociation energy and second virial coefficient of mercury that were selected in this paper are not far from the correct ones. That this comparison between observed and calculated vapor pressures has such significance is due in no small degree to the accuracy of the experimental values of liquid heat capacity recently measured and reported in this paper. For a given temperature, an error in the heat capacity produces an approximately proportional error in the vapor pressure calculated in this manner. The previously available heat capacity values, because of their disagreement in the region above and below the boiling point, would no doubt have been considered up to 10 times as uncertain. Therefore had it been necessary to rely on these previous values, the relatively small differences of such a comparison graph as figure 4 would have had very much less significance.

The heat-capacity measurements were greatly expedited by the commendable cooperation of Leo F. Epstein and his associates, of the Knolls Atomic Power Laboratory, Schenectady, N. Y. Under his direction the mercury samples were painstakingly prepared and supplied in a state of very high purity and ready for the thermal measurements. Collaborating with him in this work were L. W. Hibbs, Jr., who purified the mercury, filled and sealed the containers, and tested them; George Strichman, who tested the containers for tightness; and R. E. Schofield, who performed the mass-spectrometer analyses.

The authors express their special indebtedness also to certain members of this Bureau. B. F. Scribner and his associates performed a spectrochemical

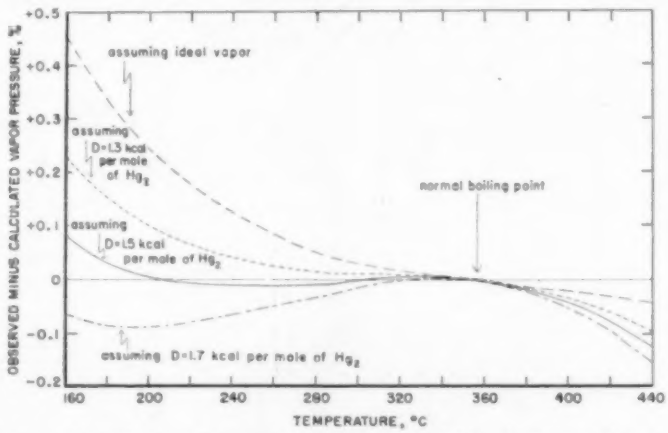

FIGURE 4. *Comparison between observed vapor-pressure values of Smith and Menzies (corrected to present temperature scale) and values calculated from eq 35, taking as a parameter several degrees of gas imperfection.*

examination of the mercury sample used, and in the course of the calculations of thermodynamic properties there were very helpful discussions with W. S. Benedict and H. F. Stimson.

VII. References

[1] D. C. Ginnings and R. J. Corruccini, J. Research NBS **38,** 583 (1947) RP1796.
[2] D. C. Ginnings and R. J. Corruccini, J. Research NBS **38,** 593 (1947) RP1797.
[3] D. C. Ginnings, T. B. Douglas, and Anne F. Ball, J. Research NBS **45,** 23 (1950) RP2110.
[4] R. J. Bondley, GE Research Laboratory Report No. RL-269 (1949).
[5] N. S. Osborne, BS J. Research **4,** 609 (1930) RP168.
[6] International Critical Tables **II** 457 (McGraw-Hill Book Co., Inc., New York, N. Y., 1927).
[7] F. W. Sears, Proc. Phys. Soc. London **26,** 95 (1913).
[8] L. B. Smith and F. G. Keyes, Proc. Am. Acad. Adv. Sci. **69,** 313 (1933–34).
[9] J. A. Beattie, B. E. Blaisdell, and J. Kaminsky, Proc. Am. Acad. Arts Sci. **71,** 361, 375 (1937).
[10] A. Smith and A. W. C. Menzies, J. Am. Chem. Soc. **32,** 1541 (1910).
[11] S. Glasstone, Theoretical chemistry, p. 441 (D. Van Nostrand Co., Inc., New York, N. Y., 1944).
[12] H. Kuhn, Proc. Royal Soc. London **A158,** 230 (1937).
[13] R. Heller, J. Chem. Phys. **9,** 154 (1941).
[14] F. London, Z. physik. Chem. **B11,** 222 (1930).
[15] E. Koernicke, Z. Physik **33,** 219 (1925).
[16] H. Kuhn and K. Freudenberg, Z. Physik **76,** 38 (1932).
[17] J. G. Winans and M. P. Heitz, Phys. Rev. **65,** 65 (1944).
[18] A. G. Gaydon, Dissociation energies, p. 209 (Chapman and Hall, Ltd., London, 1947).
[19] G. Herzberg, Molecular spectra and molecular structure: I. Diatomic molecules, p. 488 (Prentice-Hall, Inc., New York, N. Y., 1939).
[20] J. A. Beattie, M. Benedict, B. E. Blaisdell, and J. Kaye, Proc. Am. Acad. Arts Sci. **77,** 255 (1949).
[21] H. F. Stimson, J. Research NBS **42,** 209 (1949) RP1962.
[22] Temperature, p. 1322 (Reinhold Publishing Corp., New York, N. Y., 1941).
[23] N. S. Osborne, Trans. Am. Soc. Mech. Eng. **52,** 221 (1930).
[24] N. S. Osborne, H. F. Stimson, and D. C. Ginnings, J. Research NBS **23,** 261 (1939) RP1229.
[24a] A. L. Marshall, L. F. Epstein, and F. J. Norton, J. Am. Chem. Soc. **72,** 3514 (1950).
[25] G. L. Pickard and F. E. Simon, Proc. Phys. Soc. 6 , 7 (1948).
[26] F. Pollitzer, Z. Elektrochem. **17,** 5 (1911); **19,** 53 (1913).
[27] P. W. Bridgman, Proc. Am. Acad. Sci. **47,** 347 (1911).
[28] R. W. Ditchburn and J. C. Gilmour, Rev. Mod. Phys. **13** (No. 4), 310 (1941).
[29] H. Hertz, Ann. Physik [3] **17,** 193 (1882).
[30] A. Gebhardt, Ber. physik. Ges. **7,** 184 (1905).
[31] M. Knudsen, Ann. Physik **29,** 179 (1909).
[32] H. C. Greenwood, Z. physik. Chem. **76,** 484 (1911).
[33] A. C. Egerton, Phil. Mag. **33,** 33 (1917).
[34] H. T. Barnes, Rep. Brit. Assoc. Winnipeg **1909,** 403; H. T. Barnes and H. L. Cooke, Rep. Brit. Assoc. Adv. Sci. **1902,** 530; Phys. Rev. **16,** 65 (1903).
[35] Bartoli and Stracciati, Rend. reale estit. Lombardo sci. e lettere **28,** 469 (1895).
[36] J. N. Brönsted, Z. Elektrochem. **18,** 714 (1912).
[37] A. Naccari, J. phys. radium **8,** 612 (1889); Atti. Torini **23,** 107, 594 (1887–88).
[38] Winkelmann, Ann. Physik **149,** 1 (1873).
[39] J. Milthaler, Wied. Ann. **36,** 897 (1889).
[40] L. G. Carpenter and L. G. Stoodley, Phil. Mag. [7], **10,** 249 (1930).
[41] A. L. Dixon and W. H. Rodebush, J. Am. Chem. Soc. **49,** 1162 (1927).
[42] W. Gaede, Phys. Z. **4,** 105 (1902–03).
[43] S. Lussana, Nuovo cimento **4,** 207 (1912).
[44] V. Kurbatov, Russ. Phys.-Chem. Soc. **40,** 811 (1909).
[45] Research Laboratory, General Electric Company, private communication (1931).
[46] H. Hirobe, J. Fac. Sci. Imp. Univ. Tokyo **1** (Part 4), 155 (1926).
[47] O. Pettersson and E. Hedelius, J. prakt. Chem., N. F. **24,** 135 (1881).
[48] O. J. Kleppa, J. Chem. Phys. **17,** 668 (1949).
[49] T. B. Douglas, Anne F. Ball, and D. C. Ginnings (publication pending).
[50] J. F. Kincaid and H. Eyring, J. Chem. Phys. **5,** 587 (1937).
[51] J. Walter and H. Eyring, J. Chem. Phys. **9,** 393 (1941).
[52] A. W. C. Menzies, Z. physik. Chem. **130,** 90 (1927).
[53] A. Smith and A. W. C. Menzies, J. Am. Chem. Soc. **32,** 1434 (1910).
[54] A. Smith and A. W. C. Menzies, J. Am. Chem. Soc. **32,** 1412 (1910).
[55] C. W. Waidner and G. K. Burgess, Bul. BS **6,** 149 (1909) S124.
[56] Temperature, p. 127 (Reinhold Publishing Corp., New York, N. Y., 1941).

WASHINGTON, August 9, 1950.